HEAT TRANSFER ENHANCEMENT IN RECTANGULAR CHANNELS USING AUTONOMOUS, AERO-ELASTICALLY FLUTTERING REEDS

A Dissertation
Presented to
The Academic Faculty

by

Sourabh Kumar Jha

In Partial Fulfillment
Of the Requirements for the Degree
Doctorate of Philosophy in Mechanical Engineering

Georgia Institute of Technology
George W. Woodruff School of Mechanical Engineering

May 2021

HEAT TRANSFER ENHANCEMENT IN RECTANGULAR CHANNELS USING AUTONOMOUS, AERO-ELASTICALLY FLUTTERING REEDS

Approved by:

Professor Ari Glezer, Advisor
School of Mechanical Engineering
Georgia Institute of Technology

Professor Marc. K. Smith
School of Mechanical Engineering
Georgia Institute of Technology

Professor Donald R. Webster
School of Civil and Environmental Engineering
Georgia Institute of Technology

Dr. Tom Crittenden
School of Mechanical Engineering
Georgia Institute of Technology

Professor Yogendra Joshi
School of Mechanical Engineering
Georgia Institute of Technology

Date Approved: [April 19, 2021]

Dedicated to my mother and my wife

Meena Jha and India Hayes

ACKNOWLEDGEMENTS

I would like to offer my sincere gratitude to all who have helped me throughout my graduate school experience. Financially, this work was possible with the support of Air Force Office of Scientific Research, National Science Foundation, Electrical Power Research Institute and Department of Energy. This work would not have been possible without the support and guidance of my advisor Professor Ari Glezer who has constantly motivated me to find simple and elegant solutions to challenging problems in my research and personal life. I would like to quote Professor Glezer on one of his many nuggets of wisdom which have guided me: “While it is easy to look for your lost wallet in well-lit areas, you should also pay attention to the dark to find the wallet”. While I have not lost my wallet in the graduate school, I have gained a wealth of wisdom over the years of interactions with Professor Glezer.

I would also like to thank my thesis committee members for their time and patience in evaluating my research work throughout my proposal and until my defense. I would like to thank Dr. Tom Crittenden for sharing his valuable time and expertise in design and testing of fin array experiments. Most importantly, many thanks for the abundant supply of mechanical components on your workbench which you have graciously shared. I would like to express my gratitude to Professor Donald Webster, Professor Yogendra Joshi and Professor Marc Smith for the insightful discussions about my research work and methodologies.

I would like to express my sincere gratitude to the research engineers in FMRL lab: Dr. Pablo Hidalgo, Dr. Svyatoslav Yorish, and Dr. Bojan Vukasinovic who shared their

expertise and experiences and from whom I have learnt the skills of the trade. I would also like to thank the alumni and graduate students from FMRL lab from whom I have learnt how to navigate my way through the graduate school as an international student and understand the American culture. To the alumni and Drs. Abe Gissen, George Woo, John Kearney, Mark Simpson, Thomas Boziuk, Thomas Lambert, Travis Burrows and Mr. Zicheng Gong who were kind enough to share their experiences and offer help whether it was mock orals for qualifiers or troubleshooting DaVis, Matlab and Labview codes or understanding the turbulent world of fluid dynamics. I have enjoyed the company and conversations of my fellow graduate members in FMRL: Curtis Peterson, Edward Lee, Derek Nichols, Gabriel Peyredieu Du Charlat, Yuehan Tan and You Huang. I would like to offer my gratitude to Drs. Rajat Mittal, Kouroush Shoele and Arne Pearlstein for sharing the research insights they obtained through their numerical simulations on reeds in channel flows. Many thanks to Tom Lestina from HTRI whose advice was helpful in the design of the fin arrays.

A special thanks goes to my friends in Atlanta and India who have made the graduate school experience enjoyable for me. Finally, and most importantly, I would like to thank my mother without whom I would not have even thought of entering graduate school and my wife who has kept me balanced through several tumultuous experiences in graduate school.

TABLE OF CONTENTS

		Page
ACKNOWLEDGEMENTS		iv
LIST OF TABLES		xi
LIST OF FIGURES		xii
LIST OF SYMBOLS AND ABBREVIATIONS		xxx
SUMMARY		xxxiv
I:A	Overview of Inlet Flow in Rectangular Channels	1
1.1	Flow Evolution within the Inlet Region of Rectangular Channels	1
1.2	Heat Transfer Characteristics within the Inlet Flow Domain of Rectangular Channels	4
1.3	Passive Approaches to Heat Transfer Enhancement in Inlet Flows	5
1.4	Active Approaches to Heat Transfer Enhancement	7
I:B	Enhanced Heat Transfer Using Fluttering Reeds	9
1.5	Flow Physics of Fluttering Flags	10
1.6	Heat Transfer Enhancement using Fluttering Flags	12
1.7	The Goals of the Present Research	14
II	Experimental Setup	16
2.1	Isolated Channel Configurations	16

	2.1.1	The Low Aspect Ratio Channel	18
	2.1.2	The High Aspect Ratio Channels	19
2.2		Flow and Heat Transfer Diagnostic Techniques	22
	2.2.1	Pressure and Mass Flow Measurements	22
	2.2.2	Spectral Measurements using Hotwire Sensors	22
	2.2.3	Particle Image Velocimetry	23
	2.2.4	Range Finder Measurements of the Reed Motion	26
	2.2.5	Heat Transfer Measurements	28
2.3		The Self-Oscillating Reeds	34
	2.3.1	Reeds Development	34
	2.3.2	Position-Locked Reed Motion Analysis	36
2.4		Processing of PIV Data	38
	2.4.1	Time-Averaged Velocity Measurements	38
	2.4.2	Velocity Measurements Position-Locked to the Reed Motion	40
III		Dynamics Of Reed Flutter In A Rectangular Channel Flow	44
		Overview	44
3.1		Review of Mechanisms of Reed Flutter	44
3.2		Reed Fluttering in Channel Flow	49
3.3		Flow Dynamics in the Presence of Reed in Low Aspect Ratio Channels	56

	3.4	Some Aspects of Reeds Flow Dynamics in High Aspect Ratio Channels	72
IV		Characteristics Of Reed Driven Small-Scale Motions In High Aspect Ratio Channels	81
		Overview	81
	4.1	Introduction	81
	4.2	Phase-Locked Measurements of the Reed-Induced Flow Field	83
	4.3	The Time-Averaged Reed-Flow Interactions (Re = 2,000)	95
	4.4	The Role of the Reynolds Number	119
	4.5	The Role of the Reed Oscillation Strouhal Number	136
V		Heat Transfer Enhancement Using Self-Oscillating Reeds	147
		Overview	147
	5.1	Heat Transfer Analysis in the High Aspect Ratio Channel	147
	5.2	Characteristics of Reed-Driven Heat Transfer Enhancement at Re = 2,000	150
	5.3	The Role of the Reynolds Number in the Reed-Enhanced Heat Transfer	155
	5.4	The Role of the Reed Strouhal Number in the Balance Between Heat Transfer Enhancement and Flow Losses	162
	5.5	Variation of the Channel Width	174
VI:A		Implementation of Reeds in Fin Arrays	180
		Overview	180
	6.1	The Fin Array Setup	180
	6.2	Calculations of the Heat Transfer in the Fin Array	184

6.3	Scaling between Isolated Channels and Fin Arrays	187
6.4	Limited Investigations of External Reed Mounting	197
VI:B	System Level Performance Enhancement	201
6.5	Estimated Reed-Enabled Reduction in ACC Losses	202
VII	Conclusions	208
7.1	Summary of Findings	208
7.2	Summary of Insights	219
Appendix A	Kinetic Energy Budget Analysis	224
A.1	Simplifications for Obtaining Mean Kinetic Energy Budget using 2-D PIV Data	224
A.2	Simplifications for Obtaining Fluctuating Kinetic Energy Budget using 2-D PIV Data	226
Appendix B	Supplemental Parametric Investigations	229
B.1	Spanwise Variations in the Base Flow	229
B.2	Limited Investigations on Streamwise Location of Reed at Re = 5,000	230
B.3	Limited Investigations on Reed Span	236
Appendix C	Effect of Multiple Reeds and Limited Variations in ITD_{max}	243
C.1	Effect of Multiple Reeds	243
C.2	Comparisons between $ITD_{max} = 40^0$C and 60^0C in the 5 mm Isolated Channel	246
	REFERENCES	248
	VITA	260

LIST OF TABLES

Table 2.1	Error estimates of the measured velocity and vorticity distributions in the H/W=1 and 5 channels	25
Table 6.1	Details of losses inside and outside fin array (cf. Figure 6.10) for base flow and reeds (as discussed in Figure 6.13) at identical fin *ITD* and heat dissipation	205
Table C.1	Global Nusselt number, channel friction factor increments over the base-flow, and thermal enhancement factor, Nu/Nu_b, f/f_b and η for the reed configurations discussed in Figure C.1	244

LIST OF FIGURES

Figure 2.1 CAD drawings of the diffuser without (a) and with installed partitions (b) and an isometric view of the contraction (c). 17

Figure 2.2 CAD drawings of the 25 x 25 mm channel (flow from left to right) including the diffuser, contraction, and the channel test section with the spanwise-cantilevered reed (shown in red) and its mounting fixture 18

Figure 2.3 Top views of the high aspect ratio channels (channel dimensions not to scale) down stream of the primary contraction: a) The heat transfer channel showing the modular secondary contraction and the side wall inserts, and b) The PIV channel with integrated secondary contraction elements along the side walls. The air gap between the side wall inserts and the outer side walls in (a) are sealed. 19

Figure 2.4 Variation of channel friction factor, f with Re in the heat transfer (■) and PIV (●) $H/W = 5$ channels. Solid black and red lines represent the laminar and turbulent channel flow data by Kakac et al.,1987 and Hartnett et al., 1962 respectively for a 5 mm channel of similar aspect ratio. 20

Figure 2.5 Schematic of overlapping PIV views (at z=0) in the H/W = 1 channel (flow is from left to right). The trace of reed centerline is shown in black and its shadow is shown in gray. A reference point near the reed tip is monitored using a laser based **range finder** for determining the instantaneous position of the reed 24

Figure 2.6 *a)* Top view of the heat transfer channel configuration, including a **2-D contraction**, **cantilevered reed**, and **thin-film heater** mounted on **aluminum surfaces** instrumented with arrays of **thermocouple sensors** and insulated on the sides using air gap and **styrofoam plugs** [an **elementary panel** marked between two adjacent thermocouple sensor was used for measurements of the local heat transfer (cf. §2.6 and 5.1)]; b) Front view of the channel 28

Figure 2.7 a) Streamwise variation of wall temperature $T_w(x)$ at Re = 1,500 in the presence of a reed (planform 22 x 50 mm and thickness, t_s = 12.7 μm) measured over the left ($\hat{y}$ = 0.5, ■) and right ($\hat{y}$ = -0.5, ■) walls as shown in in Figure 2.6**,** and b) spanwise variations of T_w measured at the bottom wall near the channel exit (x = 0.25 m). The reed tip location is shown using a vertical dashed line 29

Figure 2.8 a) Front view of the heat transfer test section showing the air cavities formed by the walls, the **heater** and **Styrofoam plugs** and the location of the thermocouple sensors in the cavity for measuring the heat flux losses through the cavity and walls; and b) Top view of the channel showing streamwise stations of the thermocouple sensors 31

Figure 2.9 Variation of the total heat flux losses $\dot{Q}_{ins}''$ from the H/W=5 channel with average channel wall temperature ITD_{avg}, whose slope yields the insulation heat transfer coefficient. 31

Figure 2.10 Front (streamwise, a) and top (b) views of the reed clamping assembly and side view (c) of the assembled reed fixture in the channel. The spanwise recess of the left clamp in (a) spans the height of the channel to minimize blockage. Single-sided reed mounting fixtures using a plat plate and a cylinder are shown in (d) 34

Figure 2.11 Conditionally-averaged and normalized oscillation cycle **($\hat{y}$-$\hat{t}$)** of a reference point at the spanwise center of the reed and 5 mm upstream of its tip (at rest) based the range finder measurements (●) and the digitized centerline images (■) 36

Figure 2.12 Cross-stream distributions of the normalized time-averaged streamwise velocity $\hat{\bar{u}}$ (at z = 0, -0.5<$\hat{y}$<0) for the base-flow in the H/W=5 channel at $\hat{x}$ = 18 (●), 36 (●) and 48 (●) for Re = 2,000 (a), 5,000 (b), 7,000 (c) and 12,000 (d) The solid lines are a comparison with the data of Sparrow et al.(1967). 39

Figure 2.13 a) Superimposed 3000 **instantaneous cycles of the reed position** inferred from the range finder measurements and the **time-averaged cycle**, and b) the cross stream center (●) of each data 41

bin based on a sine function that is fitted to the **time-averaged cycle**.

Figure 2.14 Example of sorted PIV data acquired for a reed ($L_s/W = 10$, $H_s/H = 0.9$) oscillating at 65 Hz at Re=2,000 at $\hat{y} = 18$, $\hat{z} = 0$: Cross stream distributions of instantaneous spanwise vorticity, $\hat{\omega}_z$ corresponding to sorted PIV image (a) and bin-average(b) 42

Figure 3.1 a) The centerline of the reed's planform surface $y(x, t)$ at $z = 0$ of a reed measuring $L_s \times W_s \times t_s$ and oscillating in a uniform cross flow with speed U; and b) The projection of the reed in x-z plane 45

Figure 3.2 Soap film flow visualization (the flow is from left to right) around an undulating silk reed by Zhang et. al. (2000). The interference fringes were produced using monochromatic light to represent instantaneous streamlines 46

Figure 3.3 The stability boundary of a reed cantilevered at the root in a uniform cross flow derived from the potential flow model of Shelley et al (2005). For reed of given mass ratio M^*, the domains below and above the curve correspond to flow speeds U^* for which the reed is stable or unstable to flutter, respectively 47

Figure 3.4 a) Schematic of a section of a channel showing the placement of a thin-film reed cantilevered on a thin (5 mm) stainless-steel plate mounted between the top and bottom wall of the channel at downstream of the channel's entrance; and b) A cross section of the reed in the x-y plane $z = 0$. The motion of the reed is monitored along its centerline using a laser range-finder **(marked by a green line segment)** 49

Figure 3.5 a) The variation with time of reed's oscillation as the channel speed increases between 4.72 and 4.88 m/sec (the reed offset at $t = 0$ from the channel center is about $0.01W$); and b) The variation of reed oscillation frequency with increasing/decreasing air speed in the channel 50

Figure 3.6 a) Variation of the critical flow speed $U_{critical}$* with the reed mass ratio M*: t_s = 13 μm (■), 25 μm (◆), 38 μm (▲), 50 μm (●) and for L_s = 45 and 30 mm. The solid black line is the critical speed of a 2-D reed in uniform stream based on the potential flow model of Shelley et al. (2005) (cf. Figure 3.3). The variance of the measured critical speed are shown by a bar for each reed 52

Figure 3.7 Variation of the reed Strouhal Number St_L (L_s = 45mm) with the reduced velocity U* for t_s = 25 μm (◆), 38 μm(●), and 50 μm(▲). 53

Figure 3.8 Variation of the channel friction factor, f with the Re in the absence (○) and presence of reeds: t_s = 25 μm(◆), 38 μm(●), and 50 μm(▲). 54

Figure 3.9 Overlaid traces of the centerline of a reed measuring 22 x 45 (38 μm thick) in a 25 mm channel at 39 equally spaced positions of a **reference point** y_{ref} near its tip (cf. Figure 3.4b) for U = 4.8 m/sec. The centerlines are conditionally averaged from ensembles that are acquired position-locked to the motion of the reference point 56

Figure 3.10 Color raster plot of the variation of the reed kinetic energy in the 25 mm channel along its centerline s during the nominal oscillation period T_{cycle} = 0.02 sec (L_s = 45 mm, t_s = 38 μm). At t_{w-1} and t_{w-2} (marked by dotted lines) the reed tip touches the channel left (1) and right (2) walls, respectively 57

Figure 3.11 Color raster strips of the spanwise vorticity flux, $u \cdot \omega_z$ across the width of the channel during the reed oscillation cycle. Each strip is plotted at sequential time steps as a reference point near the reed-tip passes through 39 positions across the width of the channel (the cross-stream position of the reed tip is indicated by white line segments) 59

Figure 3.12 Color raster plots showing distributions of position-averaged spanwise vorticity concentrations superposed with cross-stream velocity vectors in the cross-stream x-y plane z = 0 left of the surface of the reed in Figure 3.9 and in its near wake. The trace 62

of the reed's centerline is shown for reference (the velocity field under the reed which is not illuminated by the PIV laser sheet is marked in gray). These images are locked to 39 equally-spaced positions of the reed reference point y_{ref} (cf. Figure 3.9) near the reed tip ($\hat{y}_{tip}$ marked at the bottom of each image). The spanwise vorticity flux in Figure 3.11 is extracted at AB and shown for reference

Figure 3.13 Color raster plots of the position-averaged spanwise vorticity, ω_z in the x-y plane ($z = 0$) downstream of the reed ($3.1 < \hat{x} < 9.7$) as the reed (cf. Figure 3.15) moves from the right to left wall (a-e). The **reed centerlines** and its tip location $\hat{y}_{tip}$ are shown for reference. Velocity vector of magnitude 5m/s is shown for reference in (a) 64

Figure 3.14 Color raster plots of the position-averaged fractional fluctuation kinetic energy , $\hat{k}_{ci}$ in the $\hat{x} - \hat{y}$ plane ($z = 0$) downstream of the reed ($3.1 < \hat{x} < 9.7$) as the reed (cf. Figure 3.13) moves from the channel's right to left wall (a-e). The **reed centerlines** and tip-locations $\hat{y}_{tip}$ are shown for reference 66

Figure 3.15 Color raster plots of the fluctuating kinetic energy $\hat{k}_f$ ($Re = 7{,}200$) in the $\hat{x} - \hat{y}$ plane ($3.1 < \hat{x} < 9.7$, $z = 0$) in the absence (a) and presence of the reed (b, cf. Figure 3.15) 67

Figure 3.16 Power spectra of the streamwise velocity measured along: the channel's centerline (a) and $0.08W$ leftwards from the right wall (b) at the streamwise stations: $\hat{x} =$ **3.08**, **5.08**, and **7.08**. The spectra at $\hat{x} =$ **5.08** and **7.08** are shifted down by four and eight decades, respectively and the spectrum at $\hat{x} =$ **3.08** is repeated (in gray) for reference. The solid black line depicts -5/3 slope 69

Figure 3.17 Overlaid traces of centerlines of 38 μm thick reeds in 25 (a) and 5 mm (b) high channels in which the respective reed lengths are 45 and 50 mm and the air flow is set at each reed's critical speeds. Each set of data are scaled with the corresponding channel width and reed length. The streamwise location of the reed root is x_o 72

Figure 3.18 Reconstructions of reed traces based on first and second POD modes of the reed's centerline motion in the 25 (a.1, a.2) and 5 mm (b1, b2) channels (cf. figure 3.17) 75

Figure 3.19 Color raster plots of the variation of the reed's kinetic energy along its length s during the nominal oscillation period T_{cycle} in the 25 (a) and 5 (b) mm channels (cf. figure 3.17). The times $t_{w\text{-}1}$ and $t_{w\text{-}2}$ correspond to the times at which the reed tip first touches the channel's left (1) and right (2) walls 76

Figure 3.20 Variation of the normalized kinetic energy during a nominal oscillation cycle of the reeds in the 25 mm (●) and 5 mm (●) channels. The cycle shown starts at the time at which the reed tip first touches the channel left wall ($t_{w\text{-}1}$) and the time it touches the right wall ($t_{w\text{-}2}$) is marked by a dashed line 77

Figure 3.21 Streamwise variation of the normalized bulk mean fluctuation kinetic energy $\hat{k}_m$ measured in the *x*-*y* plane $z = 0$ downstream of the reed tip x_{tip} in the 25 (○) and 5 (●) mm channels for the reeds discussed in connection with Figure 3.20 79

Figure 4.1 Superimposed 3000 **instantaneous cycles of the reed position** inferred from the range finder measurements along with the **ensemble-averaged cycle**, and b) the cross-stream center (●) of each data bin based on a sine function that is fitted to the **ensemble-averaged cycle** 83

Figure 4.2 Color raster strips of the spanwise vorticity flux across the width of the channel during the reed oscillation cycle. The strips are plotted at sequential, equal phase steps as the reed tip passes through the 38 increments across the width of the channel (the cross stream positions of the reed tip offset for the convection time delay are indicated by white line segments across each strip). The bin numbers are marked for reference along the top of the figure 85

Figure 4.3 Color raster plots of distributions of bin-averaged cross-stream spanwise vorticity, $\hat{\omega}_z$ (superposed with the velocity vectors) downstream of the reed tip, ($\hat{x}_{tip} = 16$) for $17.6 < \hat{x} < 18.4$ at the channel's mid-span $z = 0$. Selected cross-stream locations of the tip $-0.3 < \hat{y}_{tip} < 0.3$ are shown when the tip is moving towards 88

channel's left wall ($\hat{y}$ = 0.5) from bins 1 to 8 (a1 to b4, $\pi/38 < \alpha < 15\pi/38$, cf. Figure 4.2) and towards right wall ($\hat{y}$ = -0.5) from bins 19 to 26 (c.1 to d.4, $37\pi/38 < \alpha < 51\pi/38$). The location of the reed tip (corrected for the advection delay of the flow) is shown upstream of each image. The dashed line segment AB is the location where the vorticity fluxes in Figure 4.2 are extracted

Figure 4.4 Similar to Figure 4.2, spanwise variations of cross-stream, phase-averaged distributions of phase-averaged vorticity flux during the reed oscillation cycle (the cross-stream position of the reed tip offset for the advection time delay is indicated by white line segments) at the spanwise locations $\hat{z}$ = 0 (a.1), 0.5 (a.2), 1 (a.3), 1.5 (b.1), 2 (b.2) (as shown schematically below 4.2-b.2). 91

Figure 4.5 Streamwise variations (*Re* = 2,000) of phase-averaged cross-stream distributions of vorticity flux as in Figure 4.2 (column 1) and the corresponding time-averaged vorticity flux in the presence (column 2) and absence (column 3) of the reed at $\hat{x}$ = 23.7 (a), 35.7 (b), and 47.7 (c) shown schematically above Figure 4.5a 94

Figure 4.6 Streamwise variation of the channel static pressure coefficient, $C_p(\hat{x})$ in the absence (■) and presence of the reed (●) at *Re* = 2,000 95

Figure 4.7 Instantaneous Cross stream distributions ($\hat{x}$ = 36, $\hat{z}$ = 0) of streamwise and cross stream velocity components ($\hat{u}$ in a.1 and b.1 and $\hat{v}$ in a.2 and b.2, respectively) in the absence and presence of the reed (columns a and b, respectively) at *Re* = 2,000 in the 5 mm channel. The scale of $\hat{v}$ is enlarged (the black dotted line is $\hat{v}$ = 0). 96

Figure 4.8 Cross stream distributions (at z = 0) of the time-averaged streamwise and cross streamwise velocity components ($\hat{\bar{u}}$ in row 1 and $\hat{\bar{v}}$ in row 2, respectively) and of the magnitude of spanwise vorticity ($\hat{\bar{\omega}}$ in row 3) in the absence and presence of reed (columns a and b, respectively) at $\hat{x}$ = **18**, **24**, **30**,**34**, **42**,**48** for 99

Re = 2,000. Column c shows the differences between the presence and absence of the reed.

Figure 4.9 Cross stream distributions at $z = 0$ of $\widehat{u'u'}$ (a), $\widehat{v'v'}$ (b) and $\widehat{u'v'}$ (c) in the presence of the reed at $\hat{x}$ = **18**, **24**, **30**, **34**, **42**, **48** for *Re* = 2,000 101

Figure 4.10 Line plots of cross stream distributions of the terms in the dimensionless mean kinetic energy budget (Equation 4.1) terms including the material derivative, $\widehat{\boldsymbol{M}}$, transport of mean kinetic energy by mean pressure $\widehat{\boldsymbol{T}}_{\mathbf{p}}$ (●), mean viscous stress $\widehat{\boldsymbol{T}}_{\mathbf{v}}$ (■), and second moment of velocity fluctuations, $\widehat{\boldsymbol{T}}_{\mathbf{R}}$ (♦), mean viscous dissipation, $\widehat{\boldsymbol{D}}_{\mathbf{v}}$ and shear production of fluctuation kinetic energy, $\widehat{\boldsymbol{P}}$. The measurements are acquired at $\hat{x}$ = 18 for *Re* = 2,000 in the absence (a.1) and presence of the reed (a.2). Column b shows the sum of the terms on the right hand side of Equation 4.3 (gray line) along with $\widehat{\boldsymbol{M}}$ in the absence (b.1) and presence (b.2 of the reed). 106

Figure 4.11 As in Figures 4.10-a.1 and a.2 in the absence and presence of the reed (columns a and b, respectively) for $\hat{x}$ = 18 (row 1), 36 (row 2) and 48 (row 3). 110

Figure 4.12 Line plots of cross stream distributions of the terms in the dimensionless fluctuating kinetic energy budget (Equation 4.4): terms including material derivative, $\widehat{\boldsymbol{M}}_{\mathbf{f}}$, transport of fluctuating kinetic energy by pressure fluctuations $\widehat{\boldsymbol{T}}_{\mathbf{pf}}$ (●), fluctuating viscous stresses $\widehat{\boldsymbol{T}}_{\mathbf{vf}}$ (■) and second moment of velocity fluctuations $\widehat{\boldsymbol{T}}_{\mathbf{Rf}}$ (♦); small-scale viscous dissipation, $\widehat{\boldsymbol{D}}_{\mathbf{vf}}$ and shear production of fluctuation kinetic energy, $\widehat{\boldsymbol{P}}$. The measurements are acquired a *Re* = 2,000 in the absence and presence of the reed (columns a and b, respectively) for $\hat{x}$ = 18 (row 1), 36 (row 2) and 48 (row 3). 113

Figure 4.13 a) Schematic rendition of the *y*-*z* plane of the channel showing the locations of the PIV planes ($\hat{z}$ = ±**1**, ±2), and cross stream variations of the streamwise velocity $\hat{u}$ (b) and of the fluctuating kinetic energy, $\hat{k}_f$ (c) that are both measured at the streamwise center of the PIV planes. The solid and dashed lines mark $z > 0$ and $z < 0$, respectively 115

Figure 4.14 Cross stream distributions of the normalized streamwise velocity $\hat{u}$ (column a) and fluctuating kinetic energy, $\hat{k}_f$ (column b) at $\hat{x}$=18 (row 1), 36 (row 2) and 48 (row 3) for spanwise stations, $\hat{z}$=**0**, **0.5**, **1**, **1.5**, **2** (*Re* = 2,000) 117

Figure 4.15 Cross stream variations of small-scale dissipation $\hat{D}_{vf}$ of the fluctuating kinetic energy, k_f (Equation 4.4) in the presence of reed at $\hat{x}$ = 18 at $\hat{z}$ = **0**, **1** and **2** 118

Figure 4.16 Cross-stream distributions (at $z = 0$) of the normalized time-averaged streamwise velocity $\hat{u}$ at $\hat{x}$ = **18**, **30** and **42** in the absence and presence of the reed (L_s/W = 10, St_L = 0.5) at *Re* = 2,000 (a.1 and b.1), 7,000 (a.2 and b.2) and 12,000 (a.3 and b.3) 120

Figure 4.17 Cross-stream distributions (at $z = 0$) of the fluctuating kinetic energy $\hat{k}_f$ at $\hat{x}$ = **18**, **30** and **42** in the absence and presence of the reeds (cf. Figure 4.17) at *Re* = 2,000 (a.1 and b.1), 7,000 (a.2 and b.2) and 12,000 (a.3 and b.3). 124

Figure 4.18 Streamwise variation of the cross-stream integrated material rate of change of $\hat{k}_f$, $<\hat{M}_f>$ in the absence and presence of the reed (cf. figure 4.18) for *Re* = 2,000 (■, ●), 7,000 (■,●), 12,000 (■,●). The position of the reed-tip is shown by a **dashed line** 125

Figure 4.19 Streamwise variations of bulk mean fluctuation kinetic energy $\hat{k}_m$ and the cross-stream averaged $<\hat{D}_{vf}>$ (columns a and b, respectively) in the absence (■) and presence (●) of the reed for *Re* = 2,000 (■, ●), 7,000 (■, ●), 12,000 (■, ●). The position of the tip is shown using vertical **dashed lines**. The asymptotic values, $\hat{k}_m$ = 0.008 and $\hat{D}_{vf}$ = 0.02 at *Re*= 12,000 are shown using horizontal dashed lines 127

Figure 4.20 Power spectra (*PSD*) of the streamwise velocity fluctuations *u*' measured at the spanwise center of the channel ($z = 0$) at three streamwise locations downstream of the reed tip $\hat{x}$ = **20**, **30** and **40** in the absence (column a) and presence (column b) of the reed at *Re* = 2,000, 7,000 and 12,000 (rows 1,2 and ,3 respectively). The solid line marks -5/3 slope. The cross-over frequency, ϕ_c for reeds is represented by the vertical dashed line and the asymptotic *PSD* 133

levels for large scales (ϕ < 1Hz) at $\hat{x}$ = 40 in the presence of reeds is represented through the horizontal dashed lines

Figure 4.21 Streamwise variation of $\hat{k}_m$ (at $z = 0$) in the absence (■) and presence of the reed (L_s/W = 10, t_s = 127 μm) at Re = 12,000 when the tip of the reed is placed at locations $\hat{x}_{tip}$ = 16 (●) and 26 (♦). The streamwise locations of the reed tips are marked using vertical dashed lines and the asymptotic level of $\hat{k}_m$ at the downstream end of the channel ($\hat{k}_m$ = 0.008) is marked by a horizontal dashed line. The data point closest to the reed tip at $\hat{x}$ = 19 is offset by $\hat{x}$ = 10 and marked using ○ for comparison with the corresponding data for for $\hat{x}_{tip}$ = 26 134

Figure 4.22 Cross-stream distributions (at $z = 0$) of the time-averaged streamwise velocity $\hat{u}$ and fluctuating kinetic energy, $\hat{k}_f$ (columns a and b respectively) in the absence (marked by a black line) and presence of reeds (L_s/W = 10, Re = 5,000) oscillating at St_L = **0.5**, **0.7** and **0.9**, at $\hat{x}$ = 18 (a.1 and b.1), 30 (a.2 and b.2) and 42 (a.3 and b.3) 137

Figure 4.23 Streamwise variation of $\hat{k}_m$ in the absence (■) and presence of for reeds of b) length, L_s/W = 10 and thickness, t_s = 25.4 μm (●, St_L = 0.9), 38.1 μm (●, St_L = 0.7) and 50.8 μm (●, St_L = 0.5) and b) of thickness, t_s = 25.4 μm and lengths L_s/W = 2.4 (♦, St_L = 0.3), 10 (●, St_L = 0.9) and 20 (♦, St_L = 1.6) at Re = 5,000. The horizontal and black line represents $\hat{k}_m$ = 0.008. The streamwise locations of the reeds are shown through the vertical dashed lines 139

Figure 4.24 a) As in figure 4.23 (a) and (b), the streamwise variations of cross-stream averaged small-scale dissipation, $<\hat{D}_{vf}>$ in the absence and presence of reeds. The horizontal dashed line represents $<\hat{D}_{vf}>$ = 0.02 (cf. Figure 4.19) 140

Figure 4.25 Variation with St_L of the channel friction factor f for 1,000 < Re < 10,000 and reeds of length L_s/W = 10 (●), 20 (■) and 30 (♦) and thicknesses t_s = 12.7, 25.4, 38.1, 50.4 and 76.2 μm 142

Figure 4.26 Variation of St_L with reed inertia ratio M^* (a), reduced speed U^* (b) and the ratio M^*/U^* (c) for $1{,}000 < Re < 10{,}000$ and reeds of length $L_s/W = 10$ (●), 20 (■) and 30 (♦) and thicknesses $t_s = 12.7$, 25.4, 38.1, 50.4 and 76.2 μm 146

Figure 5.1 Top view of the flow path within the high aspect ratio 5 mm channel, which includes a **2-D contraction**, the **cantilevered reed**, and **thin-film heater** adhered to **aluminum plates** each instrumented with a streamwise array of **thermocouple sensors** (cf. Chapter II); b) Energy balance across an elementary segment of the channel as marked by dashed lines in (a). 148

Figure 5.2 Streamwise variation of a) $ITD(x)$, b) $Nu(x)$, and c) $C_p(\hat{x})$ in the base flow (■) and with the reed (●) in the 5 mm channel for $ITD_{max} = 60^oC$ at $Re = 2{,}000$. The data of Kakac et. al. (1987) is shown using a solid black line, and the position of the tip of the reed is marked using red dashed lines 151

Figure 5.3 Variation of the increment in $Nu(x)$ relative to base flow ΔNu with the increment in bulk mean fluctuation kinetic energy $\Delta\hat{k}_m$ (cf. Figure 4.19) at $Re = 2{,}000$. The streamwise locations of these data (at $z = 0$) are marked on the x-axis on top. 153

Figure 5.4 Streamwise variation of the local Nusselt number at $Re = $ **2,000**, **7,000** and **12,000** in the absence (■) and the presence (●) of reeds oscillating at $St_L = 0.5$ ($L_s/W = 10$, $H_s/H = 0.9$, $\hat{x}_{tip}$ is marked by a dashed line) 155

Figure 5.5 a) Variation of $Nu(x)$ with $\hat{k}_m$ in the base flow (■) and in the presence of reeds (●) at $Re = 2{,}000$ (■, ●), 7,000 (■, ●) and 12,000 (■, ●); and b) Variation of the reed-induced increments ΔNu with $\Delta\hat{k}_m$ over the corresponding base flow at $Re = 2{,}000$ (♦), 7000 (♦) and 12,000 (♦). 157

Figure 5.6 a) Streamwise variation of $Nu(x)$ in the base flow (■) and in the presence of the reed ($H_s/H = 0.9$, $L_s/W = 10$, $St_L = 0.5$) for $\hat{x}_{tip} = 16$ (♦) and 26 (●) (marked by dashed lines); and b) Variation 159

of ΔNu with $\Delta\hat{k}_m$ downstream of the reed. $ITD_{max} = 60^oC$, $Re = 12{,}000$. The data at $\hat{x} = 20.4$ for $\hat{x}_{tip} = 16$ is offset by $\hat{x} = 10$ and marked using ○ for comparison with corresponding data at $\hat{x} = 28.4$ for $\hat{x}_{tip} = 26$

Figure 5.7 The effect of Strouhal number on heat transfer enhancement at $Re = 5{,}000$ by streamwise variations of $ITD(x)$ and $Nu(x)$: in (a) and (b), respectively for $St_L = 0.5$ (●), 0.7 (●), 0.9 (●) ($L_s/W = 10$ $t_s = 25.4$, 38.1, 50.8 μm); and in (c) and (d), respectively for $St_L = 0.3$ (●), 0.9 (●), 1.6 (●) ($t_s = 25.4$ μm and $L_s/W = 2.4$, 10, and 20), and the base flow (■); and (e) Variation of reed-induced increments ΔNu with $\Delta\hat{k}_m$ (relative to the base flow) at $Re = 5{,}000$ for $St_L = 0.3$ (♦), 0.5 (♦), 0.7 (♦), 0.9 (♦) and 1.6 (♦). Least square fit to corresponding data at $Re = 7{,}000$ and 12,000 is also shown using a solid black line. The locations of the reed tip are marked using dashed lines 163

Figure 5.8 Streamwise variation of a) Channel gauge static pressure, C_p in the absence (■) and presence of a rigid (♦) and at $St_L = 0.5$ (●), 0.7 (●) and 0.9 (●) ($L_s/W = 10$ at $Re = 5{,}000$). b) Variation of pressure drop along the reed, $\Delta C_{p,reed}$ with St_L relative to the pressures in the **base flow** and in the presence of **rigid reeds** (marked by solid lines). 166

Figure 5.9 Variation of f/f_b (a.1) and Nu/Nu_b (b.1) with St_L for reeds of thicknesses, $t_s = 25.4$ μm (●), 38.1 μm (●), 50.8 μm (●). Variation of global Nu with $\hat{W}_{pp}$ (a.2) in the base flow (■) for $1{,}500 < Re < 13{,}000$ (Re increases from left to right), and in the presence of the reeds, the corresponding Nu in the base flow for $Re = 5{,}000$ is marked; b.2) Variation of thermal enhancement factor η of the reeds with $\hat{W}_{pp}$, St_L at $Re = 5{,}000$ is noted near each data point 168

Figure 5.10 Variation with $\hat{W}_{pp}$ of a) Nu in the base flow (■) for **1,500** < Re < **13,000** and in the presence of reeds (●) at Re = **1,500**, **3,000**, **5,000**, **7,000** and **9000** [Laminar and turbulent channel data of Kakac et al. (1987) and Hartnett et al (1962) are marked by solid **blue**, **red** lines, and least square fit to the present 170

reed data is marked by a **black** line) Base flow transition as assessed from the data of Hartnett et al.(1962) is marked by a **vertical dashed line**. St_L at each Re increases from left to right as marked by the arrow on top; and b) Reed thermal enhancement factor, η for the data shown in (a). Representative St_L values are noted along the plot and are color-coded based on Re and marked in (b)

Figure 5.11 Variation with Re in the base flow of the friction factor f (a), and the global Nusselt number Nu (b) based on internal measurements within the channels, and of the global Nusselt number based on $LMTD$, Nu_{LMTD} (c) for the $H/W = 10$ (■) and 5 (●) channels at $\dot{Q}_{heater}" = 1.6$ KW/m^2. The solid lines denote data for **laminar** (Kakac, 1967) and **turbulent** (Hartnett, 1962) flows. The critical Reynolds number for transition to turbulence is marked by a green dashed line based on the data of Hartnett et al. (1962) 175

Figure 5.12 Variation of St_L with Re for reeds with $L_s/W = 20$ in the $H/W = 10$ (▲) and 5 (♦) channels 177

Figure 5.13 Variation with Re of Nu/Nu_b (a), f/f_b (b), and thermal enhancement factor (c) for reeds with $L_s/W = 20$ in the $H/W = 10$ (▲) and 5 (♦) channels at $\dot{Q}_{heater}" = 1.6$ KW/m^2 178

Figure 5.14 Variation with Re of Nu/Nu_b, based on internal measurements (a) and on $LMTD$ (b) for reeds discussed in. Figure 5.13 in the $H/W = 10$ (▲) and 5 (♦) channels 178

Figure 6.1 a) Front view of the fin arrays showing the thin film heater attached from below to the base plate of the fin array and the spanwise locations of two streamwise arrays of equally-spaced (38.5 mm apart) thermocouple sensors that are attached along the top and below the 5th fin from the left ($\hat{y} = -0.5$) in notches along its top edge and within grooves in the base plate; b) Front view showing the mounting fixtures for the reeds upstream of the fin array; and c) Top view of the assembled test setup showing (from left to right) the **contraction**, the **reed mounting fixture**, **offset section**, the acrylic channel, the fin channel array and the **mixing section**. The streamwise locations of pressure ports labeled 1,2 181

and 3 (●) and the thermocouple sensors over and below the 5th fin (▲) are also shown in (c)

Figure 6.2 Variation with Re of the global Nusselt numbers calculated using internal measurements (Nu) and $LMTD$ (Nu_{LMTD}) in the absence (○, ●) and presence of reeds (◊, ♦) of length $L_s/W = 20$ in the $H/W = 5$ isolated channel 186

Figure 6.3 Streamwise variation of the fin temperatures ITD_t ($\hat{z} = 2.5$ ▲)and ITD_b ($\hat{z} = -2.5$, ●) in the base flow for $Re = 1{,}500$ (●, ▲), 3,000(●, ▲), 4,500 (●, ▲) for $H/W = 5$ and $ITD_{max} = 40^oC$ 187

Figure 6.4 Variation with Re of a) Nu_{LMTD} and Nu_T for the fin array ($ITD_{max} = 40^oC$) and Nu_{LMTD} of the isolated channel ($ITD_{max} = 60^oC$); and b) friction factor, f for the fin array and isolated channels of $H/W = 5$ 189

Figure 6.5 Variation with reed Strouhal number, St_L of Nu/Nu_b and f/f_b for the fin array (♦) and the isolated channel (●) at $Re = 1{,}500$ (a.1 and b.1), 3,000 (a.2 and b.2) and 4,500 (a.3 and b.3). Channel aspect ratio is $H/W = 5$ and ITD_{max} is the same as Figure 6.4 190

Figure 6.6 Streamwise variation of the bottom ($\hat{z} = -2.5$, solid lines) and top ($\hat{z} = 2.5$, dashed lines) fin resistances $R_{fin}(\hat{x}, \hat{z})$ in the base flow (■) and in the presence of the reed (♦) a) Reed I, $Re = 1{,}500$, $St_L = 0.8$ (cf. Figure 6.5-a.1), and b) Reed II, $Re = 4{,}500$, $St_L = 2.2$ (cf. Figure 6.5-a.3) 192

Figure 6.7 Variation with normalized flow power, $\widehat{W}_{pp}$ of a) Nu_T in the fin array and b) Nu_{LMTD} in the isolated channel in the base flow (■) and in the presence of reeds (♦, ●) at Re = **1,500**, **3,000**, **4,500**. The base flow and reed symbols are color coded based on the Reynolds number and the color bar is shown on the right 194

Figure 6.8 Variation of strouhal number, St_L with M^*/U^* for reeds of length $L_s/W = 10$, and thickness $t_s = 12.7$ μm and offset $d_{offset}/W = 1.2$ (♦) and 6 (●) and $L_s/W = 5.2$ with $d_{offset}/W = 1.2$(♦). The green curve 197

is $St_L = 0.23(M^*/U^*)^{-0.33}$based on the isolated $H/W = 5$ channel data (Figure 4.29c).

Figure 6.9 Variation with *Re* of friction factor *f* (a.1) and Nu_T (b.1); and the variation of Nu/Nu_b with f/f_b (a.2) and of Nu_T with flow power, $\hat{W}_{pp}$ (b.2) in the base flow (shown by solid black lines) and in the presence of reeds: $L_s/W = 10$, $t_s = 12.7$ μm , $d_{offset}/W = 1.2$ (♦) and 6 (●), and $L_s/W = 5.2$ and $d_{offset}/W = 1.2$ (♦) 199

Figure 6.10 Schematic rendition of an A-frame air-cooled condenser indicating various air-side losses throughout the system (Kroger, 2004). 201

Figure 6.11 The double fin array facility with a single fin array cross-section shown at upper right. 202

Figure 6.12 Streamwise variation of fin base *ITD* at $\dot{Q}_{heater}$ = 17.3 W for base flow at *Re* = 3,200 (■) and with reeds ($L_s/W = 20$) at *Re* = 2,200 (●) and 3,200 (●) and $St_L = 2$ 204

Figure 6.13 Streamwise variation of fin base *ITD* at *Re* = 3,200 for the base flow at $\dot{Q}_{heater}$ = 17.3 W (■) and in the presence of the reeds in Figure 6.12 at $\dot{Q}_{heater}$ = 17.3 W (●) and 21.5 W (●). 206

Figure B.1 Cross-stream distributions ($-0.5<\hat{y}<0$) of streamwise velocity ($\hat{\bar{u}}$) for the base-flow at $\hat{x}$ = 18 for *Re* = 2,000 obtained in high aspect ratio channel of width $W = 5$mm for $\hat{z} = 0, \pm1, \pm2$. The distributions for $\hat{z} \geq 0$ are shown with solid lines and for $\hat{z} \leq 0$ are shown with dashed lines 229

Figure B.2 Cross-stream distributions (at $z = 0$) of $\hat{\bar{u}}$ and $\hat{k}_f$ (columns a and b respectively) at *Re* = **2,000**, **5,000** and **7,000** for the base flow at $\hat{x}$ = 18, 30 and 42 (row 1, 2 and 3 respectively) 231

Figure B.3 a) schematic of the streamwise locations of the reeds ($L_s/W = 10$ and thickness, $t_s = 25.4$ μm) with $\hat{x}_{tip}$ = **16**, **26** and **48** (the channel is not to scale). b) Variation of $\hat{k}_m$ (at $z = 0$) with the (normalized) 232

distance from reed tip,$\hat{x}$-$\hat{x}_{tip}$ for reeds with $\hat{x}_{tip}$ = 16 (●), 26 (■) and 48 (♦) at *Re* = 5,000 (vertical dotted lines show reed's streamwise extent). The horizontal black and orange dotted lines show the asymptotic value $\hat{k}_m$ = 0.008 (cf. Figure 4.20) and the maximum value of $\hat{k}_m$ in the base flow at *Re* = 5,000 respectively

Figure B.4 a) Streamwise Variation of local Nusselt number, *Nu*(x) in the absence (■) and presence of reeds (H_s/H = 0.9, L_s/W = 10, St_L = 0.9) with tip locations $\hat{x}_{tip}$ = 16 (●), 26 (●), and 48 (●) for ITD_{max} = 60°C and *Re*= 5,000 in 5 mm channel; Variation of b) increment in local Nusselt number, Nu_{reed}/Nu_{base} and c) ratio of bulk mean fluctuation kinetic energy, $\hat{k}_{m,reed}/\hat{k}_{m,base}$ in the presence and absence of reeds with streamwise distance from the reed-tip, $\hat{x}$-$\hat{x}_{tip}$ for $\hat{x}_{tip}$ = 16 and 26. The tip-locations are shown through dotted lines. 234

Figure B.5 $\hat{x}$ - $\hat{y}$ distributions of the normalized fluctuating kinetic energy ($\hat{k}_f$) measured using PIV (cf. figure 4.2) in the presence of the reeds of length L_s/W = 10, thickness, t_s = 38.1 μm and span, H_s/H = **0.9** [i-(a-f)], **0.5** [ii-(a-f)] and **0.16** [iii-(a-f)]; iv) shows a schematic of the reeds in the $\hat{x}$ - $\hat{z}$ plane 236

Figure B.6 a) Streamwise Variation of the fluctuation kinetic energy ratio, $\hat{k}_m$ in the absence (■) and presence of reeds (cf. figure B.5) of span H_s/H = 0.9 (●), 0.5 (●), 0.16 (●); b) power spectra of streamwise velocity fluctuations at channel's exit for base and in the presence of reeds of span **0.9**, **0.5** and **0.16**. The solid line denotes -5/3 slope. The reed tip's streamwise location is marked using dashed line in (a). 237

Figure B.7 Spanwise variation of relative increment in bulk mean fluctuating kinetic energy, $\Delta\hat{k}_m$ at $\hat{x}$ = 18, 36 and 48 for reeds of length L_s/W = 10, thickness, t_s = 38.1 μm and span a) H_s/H = 0.9 (○, □,Δ) and 0.16 (○, □, Δ) for *Re* = 5,000. The dotted lines represent the spanwise edge of the reed-tip 238

Figure B.8 Variation with the reed-span, H_s/H of a) increment in global Nusselt number, Nu/Nu_b b) increment in friction factor, f/f_b and c) strouhal number, St_L for reeds of length L_s/W = 10, at 240

ITD_{max} = 60°C and Re = 5,000 in 5 mm channel. The base-flow at Re = 5,000 is shown for reference (●)

Figure B.9 a) Variation with St_L, of a) increment in global Nusselt number, Nu/Nu_b and b) increment in friction factor, f/f_b for "full-span" reeds or H_s/H = 0.9 (■, cf. Figure 5.10) and variable span reeds (●, cf. Figure B.8); c) Variation of Nu with flow power $f \bullet Re^3$ in the absence (♦) and presence of "full-span" and "variable-span" reeds in the 5 mm channel. The base-flow or absence of reeds is shown for reference (●) 241

Figure B.10 a) Variation of thermal enhancement factor, η with St_L, for "full-span" (■) and variable span reeds (●) as discussed in Figure B.9; The base-flow or absence of reeds is shown for reference (●). For length L_s/W = 10, and St_L = 0.5, a reed of span H_s/H = 0.64 ($Reed_1$) and a"full span" reed ($Reed_2$) are marked 242

Figure C.1 Schematic of a 2.5 X 250 mm channel with reeds of span, H_s/H = 0.9, length, L_s/W = 18.8 with tip-locations $\hat{x}_{tip}$ = 30.8,(a1, configuration I), 50.8 (b1, configuration II), 70.8 (a2, configuration III) and combinations of the configurations (b2 to a4); reed of length, L_s/W = 58.8 (configuration IV)which covers the combined channel length of the three configurations is shown in b4 243

Figure C.2 Streamwise variation of local Nu(x) in the absence (■) and presence of configuration I (●), II (●) and I&II (♦) reeds as discussed in connection with Figure 5.17 in the 2.5 mm channel at Re = 2,000 for $\dot{Q}_{heater}$" = 1.6 KW/m^2 244

Figure C.3 Variation of global Nusselt number (based on method II) and channel friction factor with Re at ITD_{max} = 40^{0}C (●) and 60^{0}C (●) in the absence of reeds (Figures a.1 and b.1) and in the presence of reeds of length, L_s/W = 10 (a.2 and b.2) in the isolated 5 mm wide channel 246

LIST OF SYMBOLS AND ABBREVIATIONS

H,W,L	Channel height, width and length
D_h	Hydraulic Diameter
Re, Re_c	Reynolds number based on the hydraulic diameter, critical Reynolds number at which the flow transitions
L_{hy}	Hydrodynamic development length
x, y, z	Channel coordinate system (streamwise, cross-streamwise and spanwise)
$\hat{x}, \hat{y}, \hat{z}$	Channel coordinate system normalized by channel width, $\hat{x} = x/W$
x^*, L_{hy}^*	Normalized channel and hydrodynamic lengths, $x^*=x/(D_h Re)$
H_s, t_s, L_s	Reed height, thickness and length
E	Young's modulus and density of reed
x_o	Streamwise location of reed's root
k_b	Flexural rigidity of reed
ρ_a, ρ_s	Densities of reed and air (taken at mean flow temperature)
U	Average Channel flow speed
$U_{critical}$	Critical Average Channel flow speed for reed flutter
$p(x)$	Static gauge pressure
p'	Fluctuations of air pressure
$C_p(x)$	Static gauge pressure coefficient, $C_p = p(x)/(\rho_a U^2)$
Δp	Channel static pressure drop
f	Darcy's friction factor (based on channel pressure drop)
$\delta p^*(x)$	Coefficient of pressure differential across reed's thickness
f_{osc}	Nominal Oscillation frequency of reed
St_L	Strouhal number based on reed length, $St_L = f_{osc} \cdot L_s/U$

M^*	Reed's mass ratio $M^* = \rho_s t_s / \rho_a L_s$
U^*	Reduced channel speed, $U^* = U \cdot \sqrt{\rho_a H_s {L_s}^3 / k_b}$
y_{ref}	Cross-stream location of reed reference
y_{bin}, α	Averaged reed reference location and phase corresponding to a bin
T_{cycle}	Nominal Time period of reed oscillation
$t_{w\text{-}1}$, $t_{w\text{-}2}$	Time instants in a nominal reed cycle when the reed tip touches the top and bottom walls
$\hat{t}$	Normalized time instant along the reed oscillation cycle, $\hat{t} = t/T_{cycle}$
$\delta KE(s, t)$	Kinetic energy of reed element of length *ds* at location *s* along the reed length and time *t*
ΔE_{cycle}	Incremental Flow pumping energy per cycle in the presence of reed
$\delta KE^*(s, t)$	$\delta KE(s, t)$ normalized by ΔE_{cycle}
$KE_s(t)$	Kinetic energy of the reed integrated along reed's length
PE	Elastic potential energy of the reed
c	Celerity of travelling waves along reed
PSD	Power spectral distribution of frequencies in a time trace
ϕ	Frequencies in power spectrum of streamwise velocity
ϕ_c	Cross-over frequency
N	Sample size of instantaneous vector fields for time-average PIV
N_{ci}	Ensemble size of instantaneous vector fields for position-averaged PIV
u,v,w	Instantaneous Streamwise, cross-streamwise and spanwise components of flow velocity
$\bar{u},\bar{v},\bar{w}$	Time-averaged streamwise, cross-streamwise and spanwise components of flow velocity
$\hat{\bar{u}}$, $\hat{\bar{v}}$, $\hat{\bar{w}}$	Normalized Time-averaged streamwise, cross-streamwise and spanwise components of flow velocity, $\hat{\bar{u}} = \bar{u}/U$

E Mean kinetic energy of flow obtained from PIV, $E = 0.5\ (\bar{u}^2+\bar{v}^2+\bar{w}^2)$

u_{ci},v_{ci} Instantaneous streamwise and cross-streamwise flow velocity locked to reed reference

$\{u_{ci}\}$, $\{v_{ci}\}$ position-averaged streamwise and cross-streamwise components of flow velocity locked to reed reference

u',v',w' r.m.s of streamwise, cross-streamwise and spanwise flow velocity fluctuations as obtained from time-average PIV

$\overline{u'u'}, \overline{v'v'}, \overline{u'v'}$ *xx*, *yy* and *xy* components of Reynold's stress

$\widehat{\overline{u'u'}}, \widehat{\overline{v'v'}}, \widehat{\overline{u'v'}}$ Normalized *xx*, *yy* and *xy* components of Reynold's stress, $\widehat{\overline{u'u'}} = \overline{u'u'}/U^2$

k_{ci}, k_f position and time averaged fluctuation kinetic energy of flow

$\hat{k}_{ci}$ Fractional position averaged fluctuation kinetic energy of flow, $\hat{k}_{ci} = k_{ci} / \sum_1^{39} k_{ci}$

$\hat{k}_f$ Normalized time averaged fluctuation kinetic energy of flow, $\hat{k}_f = k_f/U^2$

$\hat{k}_m$ Bulk-mean fluctuation kinetic energy of flow

ω_z Spanwise component of vorticity

$\hat{\omega}_z$ Normalized spanwise vorticity, $\hat{\omega}_z = \omega_z \cdot W/U$

σ_u, σ_ω Estimates of maximum PIV error in flow velocity and vorticity

k_a, $k_{acrylic}$, k_{al} Thermal conductivities of air, acrylic and aluminum

t_w,t_{sw} Thicknesses of aluminum and acrylic side walls

$\dot{m}$, $\dot{V}$ Mass flow rate and volume flow rate of air

$\tilde{C}_p$ Specific heat capacity of air at atmospheric pressure

T_w Wall temperature of isolated channel side walls in ^{0}C

$T_{a,i}$ Air temperature $10W$ upstream of the channel inlet

$T_{a,o}$ Air temperature at the channel exit

T_m Bulk mean temperature of air

ITD Wall temperature difference, $ITD(x) = T_w(x)-T_{a,i}$

ITD_t, ITD_b	Wall temperature difference at the top and bottom of fin
R_{fin}	Local thermal resistance of fin
η_{fin}	Fin efficiency
t_{fin}	Fin thickness
$LMTD$	Logarithmic mean temperature difference
$\dot{Q}_{ins}$, $\dot{Q}_{heater,}$ $\dot{Q}_{air}$	Rate of heat loss to insulations, power supply by heaters, rate of heat dissipation to air
$h(x)$	Local heat transfer coefficient
h_{ins}	Insulation heat transfer coefficient
$Nu(x)$	Local Nusselt number, $Nu(x) = h(x) \bullet D_h/k_a$ based on internal measurements
Nu	Streamwise Average of local Nusselt numbers
Nu/Nu_b, f/f_b	Ratio of Nusselt numbers and friction factors between the presence and absence of reeds at constant Re
$\dot{W}_{pp}$	Flow power, $\dot{W}_{pp} = \Delta P \cdot \dot{m}/\rho_a$
COP	Coefficient of performance, $COP = \dot{Q}_{air}/\dot{W}_{pp}$
COP_{ratio}	Ratio of COP between reed and base flow at constant Nusselt number
η	Thermal enhancement factor or ratio of Nusselt numbers between reed and base flow at constant flow power
d_{offset}	Thickness of rectangular offsets upstream of fin array
$L_{mixingsection}$	Length of the mixing section downstream of fin array
u_e, $T_{a,e}$	Air Velocity and temperatures at the exitplane of the mixing section
$T_{m,e}$	Bulk mean air temperature at the exit of fin array

SUMMARY

Forced convection heat transfer in compact, air-cooled heat exchangers with high-density, high aspect ratio fin channels is typically limited by the volume flow rate of the cooling air and consequently by the low channel Reynolds number. In addition, the heat transfer in the developing inlet flows of the fin channels is constrained by thin thermal boundary layers over the fin surfaces and by limited mixing of the heated air near the fin surfaces with the cooler flow within the center of the channel. These limitations are commonly overcome by increasing the air volume flow rate, the fin planform dimensions and density, or by deliberate, passive generation of small-scale motions (e.g., using vortex generators and dimples) resulting in significant increases in flow losses. The present dissertation builds on earlier research at Georgia Tech which revealed that heat transfer within these high aspect ratio rectangular channels can be significantly enhanced with minimal penalty in flow losses by using cantilevered thin-film aero-elastically fluttering reeds to induce the formation of small-scale vortical motions within the channels. The present investigations demonstrated that reed flutter occurs when the flow speed exceeds a critical level that depends only on and can be adjusted by the reed's mass ratio, and that the reed's oscillation frequency as measured by its Strouhal number depends on its mass ratio and its reduced critical speed. It was shown that the reed interactions with the channel's inlet flow engender a hierarchy of small-scale motions of decreasing scales which result in "turbulent-like" characteristics when the channel base flow is laminar, and accelerate the onset of turbulence when the base flow is transitional at higher Reynolds numbers. It was also shown that the reed-induced small-scale motions enhance local and

global heat transfer in the channel through modulation of the thermal wall boundary layers and cross-stream mixing between the wall-bounded and central flows. Even when the Reynolds number of the inlet base flow is sufficiently high so that the flow is nearly fully-turbulent near the channel's exit, the reed significantly enhances the overall heat transfer in the channel. For a given flow power, the reed can enhance the global Nusselt numbers by up to 1.8-fold relative to the base flow and by up to 1.44-fold relative to conventional heat augmentation techniques. An important finding of the present investigations is that because the channel's losses in the presence of the reed as measured by the friction factor, scale only with the reed's Strouhal number, the losses can be significantly lowered with minimal degradation in the enhanced heat transfer. Therefore, the channel losses in the presence of the reed can be decreased up to 3-fold by reducing the reed's Strouhal number while maintaining a nearly-invariant Nusselt number. It was also shown that the thermal performance of the reeds in isolated channels can be used to predict the thermal performance of geometrically-similar fin array channels at low Reynolds and Strouhal numbers. Finally, based on the present findings it is estimated that for a given heat dissipation in air-cooled condensers of industrial power plants, the fan power can be reduced by up to 64% by using oscillating reeds in the condensers' fin channels.

CHAPTER I

A. OVERVIEW OF INLET FLOW IN RECTANGULAR CHANNELS

The thesis focuses on mechanisms of heat transfer enhancement within high aspect ratio channels that model the fin channels of air cooled heat exchangers by using aero-elastically oscillating reeds. The characteristic of the flow evolution and heat transfer within these channels including previous approaches for heat transfer enhancement are reviewed in §1.1 - 1.4, and the dynamics of air-driven free and wall-bounded flexible and heat transfer enhancement by such reeds are reviewed in §1.5 and 1.6, respectively.

1.1 Flow Evolution within the Inlet Region of Rectangular Channels

While air cooled heat exchangers range in scale from a few centimeters (electronic hardware heat sinks) to several hundred meters (power plant condensers) their air cooled fin channels have nearly the same dimensions (e.g., Bar-Cohen et al., 2002, for electronic hardware heat sinks, and Bustamante et al., 2016, for the air cooled condensers). To maximize the heat transfer within these channels, the channel aspect ratio (the ratio of height to width H/W) is kept high ($H/W \geq 5$) and to reduce parasitic flow losses, the channel length (L) is kept low ($L/W \leq 50$) such that the flow within these rectangular channels is effectively an inlet flow. As described by Shah and London (1978), these inlet flows are typically uniform at the channel entrance and are followed by a streamwise developing flow regime of boundary layers on the channel walls due to viscous effects that is characterized by streamwise thickening of the boundary layers and streamwise acceleration of flow at the channel's center. Farther downstream, the internal boundary layers over the channel surfaces

and its corners merge and the flow becomes fully developed and ultimately streamwise-invariant. The streamwise length where the streamwise velocity at the channel center is 99% of its maximum value is defined as the hydrodynamic entrance length, L_{hy} which as noted in the numerical work of Han (1960) for laminar flows depends on the hydraulic diameter $D_h = 2W \bullet H/(W+H)$, Reynolds number, $Re = U \bullet D_h/\vartheta$ (ϑ is the kinematic viscosity of air) and the channel aspect ratio. The normalized entrance length, $L_{hy}^* = L_{hy} / (D_h Re)$ decreases from 0.07 to 0.0064 as the aspect ratio increases from 1 (square duct) to infinity (parallel plates). In inlet flow where the flow along most of the channel length is developing and the streamwise pressure gradient balances viscous shear and flow acceleration, the overall streamwise pressure decrease (ΔP) is significantly higher than in a fully developed flow in a channel of the same length where the pressure gradient balances only the viscous shear. The channel pressure drop can be normalized to obtain the Darcy's friction factor

$$f = \Delta P/(0.5 \bullet \rho_a \bullet U^2 \bullet L/D_h)$$

where ρ_a is the air density and U is average flow speed. While for a given aspect ratio, in a fully developed flow f is only a function of the channel's Re, in an inlet flow f depends on both L/W and Re.

Transition from laminar to turbulent flow modifies the channel's entrance length to fully-developed flow. Transition to turbulence in conduits of varying cross sections has been studied extensively over the years. Wygnanski and Champagne (1973) studied the transition to turbulence in a fully developed circular pipe using hot-wire anemometry in the absence and presence of inlet disturbances (by an upstream cylinder). They found that in a smooth pipe with undisturbed flow, transition occurred at a critical Reynolds number Re_c = 45,000

and between 2,000 < Re_c < 17,500 in the presence of inlet disturbances (Re_c decreased as the diameter of the upstream cylinder increased). These authors also reported that transition to turbulence was accompanied by the formation of turbulent "spots" in the wall boundary layers by amplification of inlet disturbances and merging of these spots formed turbulent "slugs" within the pipe cross section. Transition to turbulence in rectangular channels (H/W = 12) was studied using hot-wire anemometry by Zanoun et al. (2009), who found out that as the disturbance levels in the inlet flow were increased from u'/U = 0.0035 to 0.2,. the critical Reynolds number Re_c decreased from 10,000 to 2,000 and the flow became fully developed at $L = 80D_h$ at Re_c = 2,000 while at Re_c = 10,000 the development length was $L = 130D_h$. Direct numerical simulations of Sandham et al., 1992 (Re = 5,000, H/W = 3) and Takeishi et al., 2015 (650 < Re < 1,500 and 1 < H/W < 9) showed that, similar to circular pipes (Wygnanski and Champagne,m 1973), transition to turbulence in rectangular channels occurs through the evolution of localized turbulent spots whose streamwise and spanwise extent depends on the aspect ratio of the channel. These turbulent spots multiply by giving rise to new spots as they advect along the channel due to flow nonlinearities, but can also disappear due to viscous effects. When transitions to turbulence occurs above a critical Reynolds number Re_c the formation rate of the spots exceeds their dissipation rate. It was also shown that below Re_c, inlet disturbances eventually decay and the channel flow remains laminar. Hartnett et al. (1962) showed that above Re_c, the streamwise location of transition and the entrance length required for a fully turbulent flow depend on the channel's Re, whether its entrance is smooth or abrupt, the magnitude of flow fluctuations u'/U at the inlet, the aspect ratio, and the roughness of the channel's walls. In reference to the present investigations, it is noted that in the present rectangular channels H/W = 1, 5 and 10 and inlet

flow fluctuations $u'/U < 1\%$, based on the work of Hartnett et al. (1962) the respective the Re_c are expected to be 4,300, 7,000 and 4,000. It should be noted that the authors escribed the unusually high critical Reynolds number for H/W=5 channel to the relatively well polished entrance configuration. In addition, at each of these critical Reynolds numbers respective flow transitions occur at L/D_h = 60, 40 and 30 and the flows became fully turbulent at L/D_h = 245, 100 and 85.

1.2 Heat Transfer Characteristics within the Inlet Flow Domain of Rectangular Channels

As the flow evolves through the entrance of a heated rectangular channel, the flow temperature which is uniform across the entrance plane is altered by the development of a thermal boundary layers along the channel walls. The relation between the streamwise development of the momentum and thermal boundary layers is governed by the Prandtl number Pr of the fluid which as shown by Incropera et al. (2002) is Pr = 0.7. As discussed by Ligrani et al. (2003), heat transfer from the heated channel walls is affected by the thickness of the thermal boundary layers and the mixing between the warmer fluid within the thermal boundary layer and the cooler fluid outside these boundary layers within the center domain of the channel or its core flow. Near the channel entrance, the thermal boundary layers are thin which leads to significantly high levels of local heat transfer coefficients $h(x)$ and local Nusselt numbers $Nu(x) = h(x) \cdot D_h/k_a$ (k_a is the thermal conductivity of air). The local heat transfer coefficient decreases with streamwise distance and becomes streamwise invariant when the flow is fully developed due to merging of the thermal boundary layers. The numerical investigation of Kakaç et al. (1987) in inlet laminar flow of channels for which $1 < H/W < 6$ and for either a constant wall temperature

or a constant heat flux boundary condition, showed that the global Nusselt number $Nu = \int_0^L Nu(x) d(\frac{x}{L})$ in the developing flow was higher than that of the fully developed flow and the global Nusselt number depends on channel's length, aspect ratio and Reynolds number. Hartnett et al. (1962) showed that mixing between the wall bounded and core flows is affected by the energy of the velocity fluctuations in the channel which increase sharply as the channel flow undergoes transition to turbulence. A comparison between the turbulent and laminar channel flows in the simulations of Kakaç et al. (1987) and measurements of Promvonge et al. (2008) shows that the rate of increase in Nusselt number with the Reynolds number increases as the channel flow transitions from laminar to turbulent flow. In reference to the present investigations, it is noted that these measurements indicate that for a channel with $H/W = 5$ and $L/W = 50$ the respective global Nusselt numbers variations for laminar and turbulent flows are $Nu \sim Re^{0.33}$ and $Nu \sim Re^{0.8}$.

1.3 Passive Approaches to Heat Transfer Enhancement in Inlet Flows

As shown by Bar-Cohen et al. (2002) in heat sinks used in electronics cooling channel heat transfer is typically limited by the available air volume flow rate because of the limitations imposed by the available fan power to drive the air flow and therefore the channel Reynolds number is inherently low ($Re < 3{,}000$). Heat transfer limitations at these low Reynolds number are manifested in two closely-coupled stages of heat transport. The first stage is the heat transport from the channel walls to the wall bounded flow $\dot{Q}_{\text{local}} = h(x) \cdot A \cdot \Delta T_{\text{w}}$ is limited by the local heat transfer coefficient $h(x)$ and the temperature difference between the air stream and the wall ΔT_{w} (A is the surface area). The second stage is the overall heat transport by the channel flow which for a given mass flow rate $\dot{m}$ is $\dot{\text{Q}}_{\text{global}} = \dot{m} \cdot \tilde{C}_{\text{p}} \cdot \Delta T_{\text{a}}$

depends on the temperature rise of the cooling air ΔT_a ($\tilde{C}_p$ is the specific heat) and is limited by the mixing between the wall bounded and core flows. Both the local and global heat transport rates can be enhanced by increasing the air flow rate (or *Re*) and/or the fin area and fin density albeit with significant penalty in increased flow power due to losses (e.g., Incropera et al., 2002). Alternatively, for a given fin area and *Re*, the heat transfer can be enhanced by passive modifications of the channel surface such as rib turbulators, dimples, and vortex generators but at the expense of higher flow losses. For example, J. C. Han et al. (1988) reported an increase of up to 2-fold in the Nusselt number at $10{,}000 < Re < 60{,}000$ in rectangular channels of aspect ratios $1 < H/W < 4$ using rib turbulators of height $e/D_h = 0.08$ and angles of attack ranging from 30^0 to 90^0. However, this increase in *Nu* was accompanied by up to a 16-fold increase in friction factor. Spherical, hemispherical, and teardrop dimples of varying depths and diameters were used by a number of researchers (e.g., Mahmood et al., 2002, Syred et al., 2001, and Chen et al., 2001). Mahmood et al., 2002 used spherical dimples of diameters between 1 and 5*H* and 0.2*H* deep in a rectangular channel of $H/W = 5{:}1$ at $Re = 5{,}000$ and reported a 2.5-fold increase in *Nu* with increases of up to 5.5-fold in the friction factor. Vortex generator have also been investigated extensively (e.g., Tiggelbeck et al., 1994, Biswas et al., 1994 and Tanaka et al., 2003). Tiggelbeck et al. (1994) studied wing vortex generators (delta, rectangular, and winglet configurations) in rectangular channels $H/W = 5{:}1$ at $2{,}000 < Re < 8{,}000$ and reported increases in *Nu* and *f* of up to 2.2- and 4.2-fold, respectively. As reported by Ligrani et al. (2003), these passive surface modifications induce unsteady secondary vortical flows and concomitant small-scale motions that increase the turbulence level and mixing within the channel and can lead to significant local

increase in the heat transfer coefficient. For example, vortex generators can increase $h(x)$ by up to 3-fold hat are followed at their downstream end, which is followed by streamwise attenuation within a few ($8H$) channel widths (Tiggelbeck et al., 1994). The heat transfer enhancements through passive surface modifications are also accompanied by increments in flow losses due to local flow separation and the ensuing mixing and induced small scale motions which are manifested by increased flow power that limits their utility. Moreover, the application of some of these surface modifications can be limited because of fabrication difficulties.

1.4 Active Approaches to Heat Transfer Enhancement

A new approach for effecting small-scale flow motions and mixing by direct actuation of dissipative scales in free and wall-bounded shear flows at wavelengths that are typically an order of magnitude smaller than the relevant local or global length scale of the base flow was demonstrated Wiltse and Glezer (1998) in the shear layers of an air jet emanating from a square conduit using piezoelectric reeds. The formation and advection of such small scale, unsteady vortical motions engendered by a synthetic jet actuator was used by Gillespie et al. (2006) to enhance thermal transport from heated surfaces of convected heat (at constant heat flux) and mixing with the core flow at low Reynolds numbers (Re = 3,000). The effectiveness of this approach especially at low Reynolds numbers that are characteristic of air-cooling applications, was later demonstrated using synthetic jet actuators integrated with heat sinks by a number of researchers (e.g., Mahalingam and Glezer., 2004, Gerty et al., 2007 and Kota et al., 2009). Mahalingam and Glezer (2004) showed that synthetic jets can be used to increase the heat transfer coefficient within high aspect ratio heat sink channels operating at 1,000 < Re < 3,600 and constant

heat flux by up to 2.5-fold compared to conventional jets. Acikalin et al. (2009) used oscillating jet-like flows produced by piezoelectric fans to create small-scale motions for external cooling of low-power electronic packages and demonstrated up to 2-fold increase in heat transfer coefficient but with up to 1.5-fold increase in power consumption over conventional fans. Enhanced cooling by induced small-scale motions was further advanced by Gerty (2008) and later on by Hidalgo et al. (2010) who implemented active enhancement of heat transfer within high aspect ratio rectangular channels to model the flow within heat sink channels using cantilevered planar piezoelectrically-driven oscillating reeds mounted along the channel's span and driven at resonance. Hidalgo et al. (2010) showed that the presence of the active reeds led to a significant decrease in the fin-to-air heat transfer resistance (relative to the base flow) such that the reduction in the flow power $\dot{W}_{\text{pp}}$ for the same heat dissipation $\dot{Q}_{\text{air}}$ as in the base flow leads to a 2.4-fold increase in the coefficient of performance $COP = \dot{Q}_{\text{air}}/\dot{W}_{\text{pp}}$ over the base flow.

B. ENHANCED HEAT TRANSFER USING FLUTTERING REEDS

Channel heat transfer can also be augmented by exploiting the coupling between the flow and a rigid or flexible autonomous flag-like reed cantilevered at its streamwise leading edge to effect cross stream flow oscillations. Fernández and Poulter (1987) used oscillating thin copper plates for heat transfer enhancement in a fully turbulent flow in a water tube (at constant wall temperature) where the plates were 1.5D long and 0.66D high. Although the rigidity of these plates limited their oscillations to $20{,}000 < Re < 50{,}000$ the authors demonstrated up to 1.5-fold increase in global Nusselt numbers relative to the base flow with an increase of up to 1.4-fold in friction factor. These authors also demonstrated that these flag-like inserts yielded higher heat transfer enhancement at lower friction factor increments compared to non-oscillating helical and tape inserts. In a similar approach, Oyakawa et al. (1996) used miniature brass plates spanning the width of an air channel between two parallel plates as flexible vortex generators at $9{,}000 < Re < 40{,}000$ oscillating between 10-60 Hz and reported between 1.3 to 1.6-fold higher global Nusselt number with marginal flow losses such that the thermal enhancement factor was $\eta = 1.2$. It is evident that the rigidity of the metal plates used in these investigations limited their use to relatively high flow speeds and set a low bound on the useful range of Reynolds number. More recently, Hidalgo et al. (2015) demonstrated the utility of flexible, thin film reeds for enhancing heat transfer within air-cooled fin channels by aeroelastic oscillations at low Reynolds numbers. As with the actively driven reeds, thin-film self-oscillating reeds can induce the formation of small scale flow motions that would normally be present in transitional and turbulent flows and can lead to significant enhancement in heat transfer.

These thin-film reeds are attractive for air-side integration in heat sinks because of their low form factor, low operating *Re* and high durability and are can be easily fabricated using microfabrication techniques such as laser cutting.

1.5 Flow Physics of Fluttering Flags

In order to optimize the channel heat transfer enhancement by using reeds, it is important to understand their oscillation mechanism and the effects of the oscillations on the channel flow. The aero-elastic oscillations of flexible flag-like plates in a free flow have been studied both numerically (e.g., Kornecki et al., 1976, Argentina et al., 2005, Eloy et al., 2007 and Alben et al., 2014) and experimentally (Taneda et al., 1968, and Zhang et al., 2000). Kornecki et al. (1976) and Argentina et al. (2005) showed the similarity between the motion of a flag and that of a thin flexible 2-D airfoil pitching about its leading edge (or root) in an incompressible potential flow using fully unsteady aerodynamic theory on the first two dominant 2-D oscillation modes. In a later investigation, Eloy et al. (2007) considered 3-D oscillation modes due to finite reed span and demonstrated the dependence of the flags motion on its aspect ratio. Zhang et al. (2000) studied a 2D silk thread cantilevered at its root and suspended in a thin flowing soap film ($Re \sim 10^4$) and observed that the thread motion had three distinct dynamical states depending on the flow speed namely, stretched straight in which the thread does not undulate, coherent flutter which is characterized by sinuous motion of the flag and travelling waves which amplify from the flag's leading edge towards its trailing edge (tip), and irregular flapping state that is characterized by chaotic cross-stream motion of the flag and absence of a nominal time period or amplitude. During the stretched straight state, the thread is aligned (root to tip) with the flow with a narrow and well-defined wake comprising of counter rotating vortices

shed from the reed's tip similar to a von-Karman Street. The flag exhibits the stretched straight or SS state until a critical speed, $U_{critical}$ above which it transitions to the coherent flutter state where the flag's wake comprises of a train of vortices (all of the same sign and resembling Kelvin Helmholtz instability of a thin vortex layer shed from the flag's tip) which change sign per half-stroke of the flag.

Shelley et al. (2005) used a 2-D potential flow analysis to show that the reduced critical speed, $U_{critical}^* = U_{critical} \cdot \sqrt{\rho_a H_s {L_s}^3 / k_b}$ (where $k_b = E \cdot I$ is the flexural rigidity and E and $I = H_s t_s^3/12$ are Young's modulus and area moment of inertia of the reed and H_s, t_s and L_s are the height, thickness and the length of the flag) depends on the flag's Mass ratio, $M^* = \rho_s \cdot t_s/(\rho_a \cdot L_s)$ (ρ_s is the air density). As shown in the numerical study of a 2-D flag by Argentina et al. (2005), the oscillation frequency, f_{osc} of the flag in free flow as characterized by its Strouhal number, $St_L = f_{osc} \cdot L_s/U_\infty$ based on the flag length L_s and free stream speed U_∞ depends on the ratio of the reed's mass ratio M^* and the dependence scales as $St_L \sim (M^*)^{-0.5}$. In a 2-D potential flow based numerical investigation of flags, Alben et al. (2014) showed that a fundamental characteristic of flag flutter is the bi-stability between the SS and coherent flutter states i.e. there exists a range of defined flow speeds in which the flag exhibits hysteresis such that at the same flow speed, the flag can have either a stretched straight or fluttering states depending on whether the flow speed is increasing or decreasing with time.

Shelley et al. (2005) showed that the flag mode shapes at and beyond the critical speed depend upon the flag's mass-ratio and bending stiffness. The influence of a finite 3-D span of the flag in free air was studied numerically by Eloy et al. (2007) and experimentally by Watanabe et al. (2002) who independently showed that the finite span

stabilizes the flag and increases the critical speed as the spanwise average pressure differential across the flag is smaller than the 2-D approximation. Doaré et al. (2011) experimentally studied the effect of flag confinement along flag span/height on reed flutter showing a decrease in critical speed as the clearance between the confinement plate and the spanwise flag edges approach the boundary layer thickness and an asymptotical decrease to 2-D critical speeds with further decrease in clearance. This reduction in critical speed was attributed to flow acceleration at the flag's spanwise edge due to the boundary layer development. The motion of flags with spanwise and cross-streamwise confinement in a channel has been studied numerically by Shoele and Mittal (2015) and Tetlow and Lucey (2009). Shoele and Mittal (2015) showed that in a confined channel, the flag motion is governed by a balance between the damping effect of added mass, Coriolis and viscous forces and the excitation of the flag due to centrifugal forces created by its curvature. The presence of confinement has been shown by these authors to marginally increase the flag's critical speed and frequency.

1.6 Heat Transfer Enhancement using Fluttering Flags

Earlier studies of heat transfer enhancement in rectangular channels using flexible, thin film fluttering flags are discussed in the review article of Yu et al. (2019). The authors reviewed the heat transfer enhancement in a rectangular channel with focus on three flag configurations: a flag clamped at its trailing edge or "inverted" flag, flag clamped at its leading edge or "straight" flag and flags oscillating due to instabilities induced by a cylinder mounted upstream of the flag. Heat transfer enhancement in a rectangular channel using a "straight" flag was studied numerically by Shoele and Mittal. (2014) which is referred to as a "reed" by the authors and Rips et al. (2020). An "inverted" flag

configuration was studied numerically by Park et al.(2016) and experimentally by Yu et al. (2018).

As shown numerically by Shoele and Mittal (2014), the production of vortical structures by the reed disrupts the thermal boundary layer on the channel walls which leads to enhancement of local heat fluxes and heat transfer coefficients**.** The presence of reeds also leads to additional viscous and form drag which increases the flow power required to drive the flow. In this study, the thermal enhancement factor η of the reed-enhanced heat transfer as measured by the ratio of global Nusselt numbers in the presence of the reed and in the base flow at a fixed flow power is up to 1.2. As noted by Shoele and Mittal (2014), this enhancement factor can be achieved using reeds whose lengths is comparable to the width of the channel. While these numerical studies provide useful insight into the physics of reed flutter and the associated vortical structures in the channel flow, they are limited by the range of Reynolds numbers investigated which was typically below 600. Furthermore, the planform dimensions of the reeds were too small to capture changes in the flow structures due to interactions between the reed and the channel walls.

While Zhang et al. (2000) showed that the oscillations of a straight flag are caused by instabilities of the flag bound flow which arise due to perturbations of the flag's surface, Yu et al. (2018) showed that the oscillations of an inverted flag are induced by shedding of leading and trailing edge vortices. While the flow field downstream of a straight flag comprises of trains of vortices alternating their sign per half-stroke of flag, the flow downstream of the inverted flag includes a combination of pairs of opposite sense vortices and single sign vortices. In a water channel of aspect ratio 2:1 and at constant heat flux, Yu et al. (2018) showed that for $12{,}000 < Re < 23{,}000$, while an inverted flag $L/W = 4$

spanning the channel height and operating at $St_L = 0.14$ leads to an increase in the global Nusselt numbers of up to 1.3-fold relative to the base flow, this flag also results in up to a 3-fold increase in the friction factor such that η is smaller than 0.8 (Yu et al., 2018). Some numerical studies have also considered clamping the inverted flag to the channel's side wall (e.g., Park et al., 2016), this configuration is limited by the relatively high penalty in flow losses and the practical difficulty of implementing such flags in a heat exchanger.

1.7 The Goals of the Present Research

The present investigations focus on the key fluid flow and heat transfer mechanisms that are induced by flexible, thin-film reeds cantilevered at their leading edge in rectangular channels operating at low to transitional Reynolds numbers ($1{,}000 < Re < 15{,}000$).

The primary goals of the current research are:

i. Characterize the kinematics of the onset of reed flutter in a channel flow and the effect of reed's geometrical and structural parameters on its critical speed, oscillation frequencies, and mode shapes.

ii. Explore the mechanisms of the formation and evolution of small-scale vortical motions by the reed oscillations and their effects on the time-averaged flow field and its fluctuating characteristics within the channel.

iii. Identify the mechanisms by which small-scale motions in the presence of reeds enhance channel heat transfer.

iv. Identify optimal reed and flow parameters for heat transfer enhancement with minimal losses.

v. Verify the scaling of reed-driven heat transfer enhancement in fin arrays used in heat exchangers.

vi. Use the results of the fin array analysis to estimate reed-enhanced system-level performance in heat exchangers of air-cooled condensers.

Following an overview of the relevant literature in Chapter I, Chapter II describes the experimental setup that included construction and testing of low and high aspect-ratio rectangular channels along with the experimental techniques for flow and heat transfer measurements. The reed dynamics including the onset of flutter, oscillation frequency and mode shapes and frequency and its effects on the channel flow in a low aspect ratio channel are discussed and compared to a high aspect ratio channel in Chapter III. The effects of the reed on the flow in a high aspect ratio channel are discussed in detail in Chapter IV and the roles of the key flow and reed parameters which affect the flow are explored. Chapter V discusses the effects of the presence of the reed on heat transfer enhancement in the high aspect ratio heated channel including optimal flow and reed parameters. The scaling of the reed driven heat transfer enhancement between the isolated channels and a model fin array of a heat exchanger and the potential effect of the reed on system-level thermal performance in an air-cooled condenser are described in Chapter VI. The thesis includes three appendices: Appendix A includes the assumptions and equations and used to evaluate the mean and fluctuating flow fields in Chapter IV; Appendix B includes additional analysis of flow field and heat transfer when the streamwise position and aspect ratio of the reed are varied; and, Appendix C outlines the effects of varying the channel's maximum wall temperatures and the presence of multiple reeds on heat transfer in the channel. Finally, Chapter VII summarizes the main new results of and describes the key insights enabled by the present investigations.

CHAPTER II

EXPERIMENTAL SETUP

2.1 Isolated Channel Configurations

The interactions of the reeds with the channel flow and the ensuing heat transfer enhancement were investigated in both low and high aspect ratio interchangeable rectangular channels in which the flow was regulated using a miniature wind tunnel facility. Air flow in the facility is driven using the building air supply through a calibrated thermal mass flow meter/controller over the range $1.67 \times 10^{-4} < \dot{V} < 8.35 \times 10^{-3}$ m^3/s. An adapter section leads to an internally-partitioned diffuser (expansion ratio 1:25, Figure 2.1a, b) followed by a primary contraction (contraction ratio 25:1 Figures 2.1c) to ensure that low streamwise turbulent intensity at the contraction exit into the channel's test section ($u'/U < 0.5\%$, measured using particle image velocimetry, PIV). For the purpose of PIV measurements in the channel test section part of the flow upstream of the diffuser was diverted to an atomizer filled with Rosco Fog fluid to create seeding particles for PIV and and thereafter was injected back into the main stream.

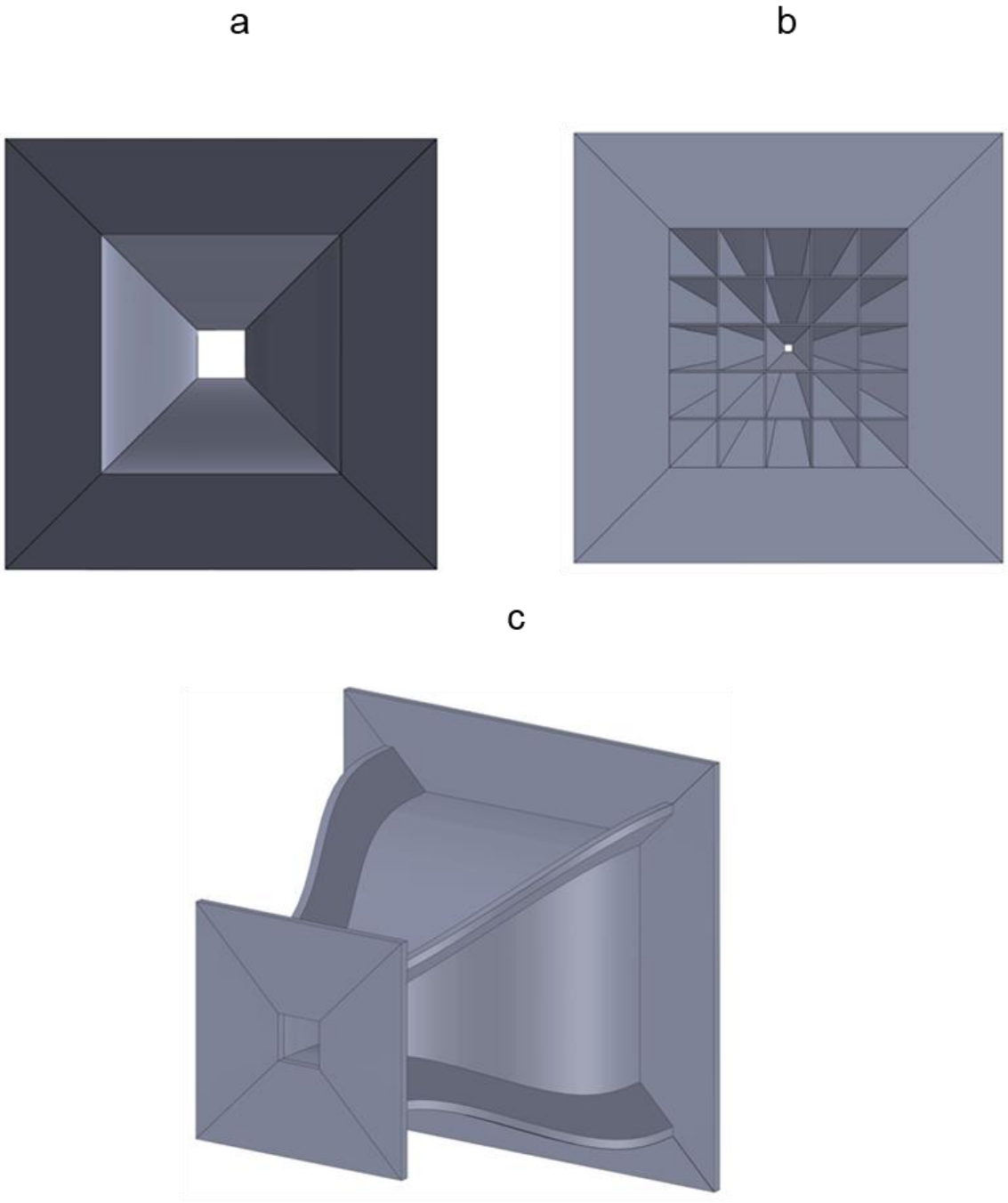

Figure 2.1 *CAD drawings of the diffuser without (a) and with installed partitions (b) and an isometric view of the contraction (c).*

2.1.1 The Low Aspect Ratio Channel

A channel section with square test section (Aspect ratio, $H/W = 1$) measuring 25 x 25 mm, and 254 mm long was connected to the primary contraction as shown in Figure 2.2 using a flange at its upstream end. Alignment between the inner surfaces of the contraction and the test section was ensured using dowel pins on the surfaces of the flange. The test section walls were fabricated from acrylic sheets (12.5 mm thick) and the inner dimension (25 x 25 mm) was within ±0.0254 mm. Thin film reeds were cantilevered vertically in between two removable stainless steel support plates (0.125mm total thickness) spanning the height of the test section and 5 mm wide. The support plate was clamped near its spanwise edges to the top and bottom outer surfaces of the test section using external fixtures as shown in Figure 2.2. The development of reeds and their mounting procedure is described in detail in §2.3.

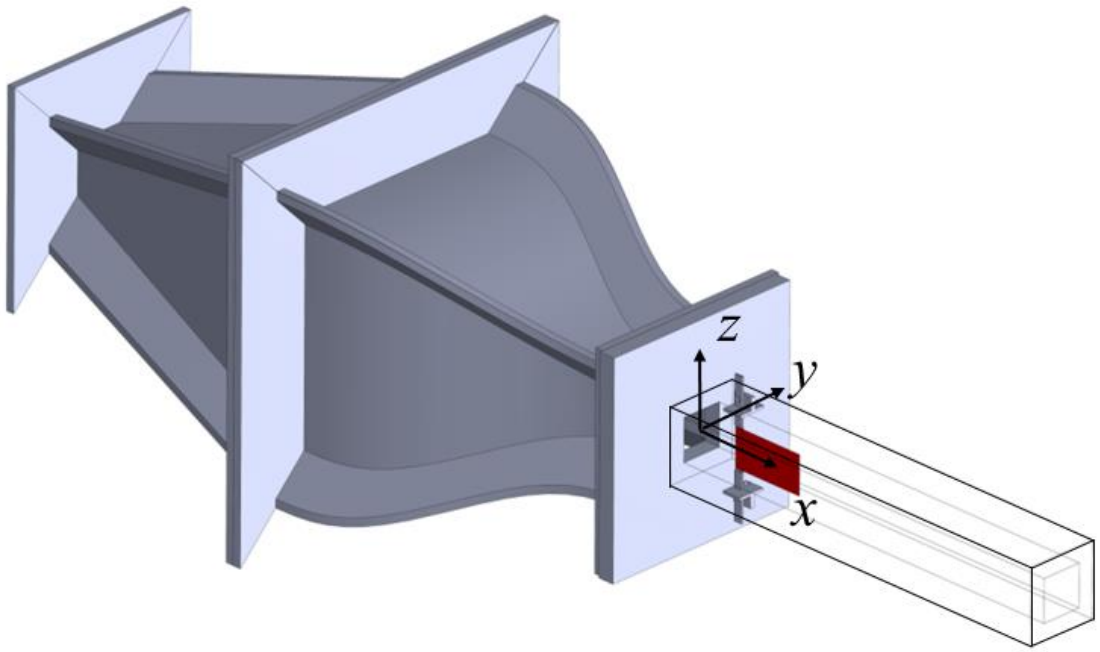

Figure 2.2 *CAD drawings of the 25 x 25 mm channel (flow from left to right) including the diffuser, contraction, and the channel test section with the spanwise-cantilevered reed (shown in red) and its mounting fixture.*

2.1.2 The High Aspect Ratio Channels

The present setup enabled testing of high aspect ratio channels (H = 25 mm, L = 250 mm) by connecting them to the primary contraction by a secondary contraction. Two channel configurations were used for separate measurements in the absence and presence of the reeds of the heat transfer and of the cross stream velocity fields (in the x-y) planes using PIV. For heat transfer measurements, the high aspect ratio cross section was formed by inserting sliding side walls into machined groove in the top and bottom walls of the primary (25 x 25 mm) channel. The side walls were fabricated out of 1.5 mm thick aluminum sheet and were instrumented with thin-film adhesive heaters and arrays of

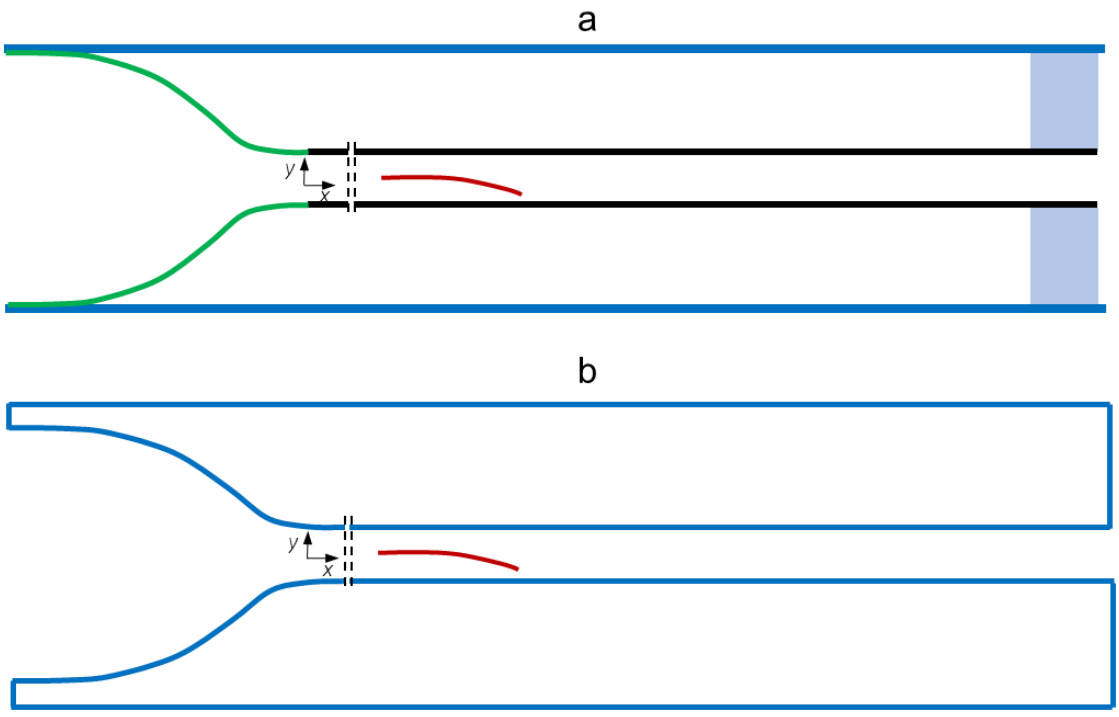

Figure 2.3. *Top views of the high aspect ratio channels (channel dimensions not to scale**)** down stream of the primary contraction: a) The heat transfer channel showing the **modular secondary contraction** and the side wall inserts, and b) The PIV channel with integrated secondary contraction elements along the side walls. The air gap between the side wall inserts and the outer side walls in (a) are sealed.*

thermocouple sensors on their back sides (cf. §2.2) and were mated to a secondary (1-D) 25 mm tall contraction fabricated using stereolithography that was attached to the primary contraction (Figure 2.3a). The air cavity between each of the outer walls and the inner wall inserts was sealed using to create a closed air-insulated gap. The majority of the heat transfer measurements were performed in a $H/W = 5$ ($W = 5$mm) channel and limited measurements were also conducted in a $H/W = 10$ ($W = 2.5$ mm) channel. The heat transfer setup is described in detail in §2.2.

For the PIV measurements (cf. §2.2) the side walls of the $H/W = 5$ channel were fabricated with an integrated secondary contraction at the upstream end (Figure 2.3b), and the top and bottom walls were replaced with smooth flat acrylic walls to enable passage of the laser sheet that was used for illumination of the flow in multiple cross stream (x-y) planes.

The flow in the heat transfer and PIV $H/W = 5$ channels was compared over the full range of flow rates using the variation with Re of the channel friction factor (Figure 2.4)

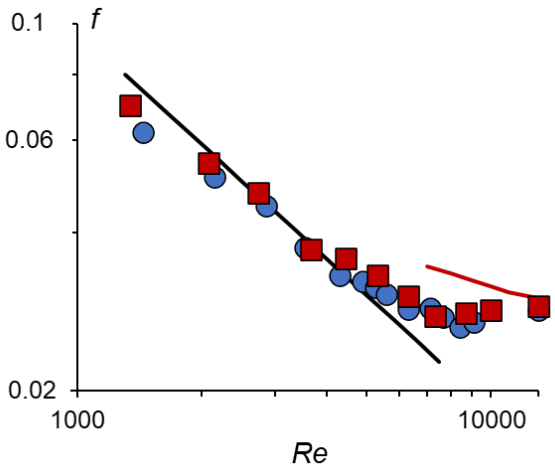

Figure 2.4. *Variation of channel friction factor, f with Re in the heat transfer* (■) *and PIV* (●) *H/W = 5 channels. Solid black and red lines represent the laminar and turbulent channel flow data of Kakac et al.,1987 and Hartnett et al., 1962 respectively for a 5 mm channel of similar aspect ratio.*

$f = \Delta P/(0.5\cdot\rho_a\cdot U^2\cdot(L/D_h)$ where ΔP is the static pressure drop along the channel, ρ_a is the air density (STP), $D_h = 4A_c/P_c$ [$A_c = W\cdot H$ and $P_c = 2\cdot(W+H)$] and $Re = U\cdot D_h/\vartheta$ (ϑ is the air kinematic viscosity at STP). The procedure for measuring the channel pressure drop is described in §2.2. The present measurements in Figure 2.4 are also compared with the numerical and experimental data for laminar (Kakaç et al., 1987) and turbulent (Hartnett et al., 1962) channel flows, respectively. These data indicate that the variations of f with Re in the two channels are similar indicating overall similar evolution of the base flows although f in the PIV channel is somewhat smaller (up to 7%).

2.2 Flow and Heat Transfer Diagnostic Techniques

2.2.1 Pressure and Mass Flow Measurements

The static gauge pressure $p(x)$ was measured at five streamwise locations in the high aspect ratio channels (H/W=5 and 10) at $\hat{x} = x/W$= 3.2, 17.2, 27.2, 36.2 and 46.2 using pressure ports mounted on the bottom channel wall (the channel pressure drop using the gauge pressure at $\hat{x}$ = 3.2). Each static pressure port was connected to a scanivalve pressure scanner and a pressure transducer (temperature compensated, resolution of 0.3 Pa). The transducer's output voltage was sampled at 10 Hz for 60 sec for each static port (the maximum fractional uncertainty of the time-averaged pressure was 0.03). The average air speed in the channel U was computed from measurements of the mass flow rate was using a thermal flow controller with maximum fractional uncertainty of 0.0075. The corresponding maximum fractional uncertainties of the channel Reynolds number and friction factor were 0.0087 and 0.0335 (e.g., .Wells, 1992).

2.2.2 Spectral Measurements using Hot Wire Sensors

Flow fluctuations in the channel were analyzed using a miniature hot-wire sensor (2 mm long, 5 μm diameter wire) aligned along the y-axis (at y =z = 0 and $\hat{x} = x/W$ = 20, 30 and 40) and a standard CTA anemometer sampled at 20 KHz. The time-averaged sensor output was scaled relative to the time-averaged streamwise velocity measured by PIV (cf. § 2.4.1) in the absence of the reeds and the scaling coefficients were used to compute the power spectral density (*PSD*) of streamwise velocity fluctuations $u' = u-\bar{u}$ with frequency resolution of 1 Hz

2.2.3 Particle Image Velocimetry

The time-averaged cross stream and streamwise velocity and velocity fluctuations in the base flow and in the and presence of reeds were measured using a standard low-speed, 2-D PIV in several cross stream *x-y* planes using a LaVision system (Kearney, 2013, and Lambert, 2016). The dual head pulsed Nd:Yag laser (532nm, maximum pulse frequency 15 Hz, pulse width 3-5 ns) was driven using a programmable timing unit at 8 – 10 Hz (aliasing with reed motion was avoided) at Δt between 1.5 to 10 μs depending on the flow speeds. The seeded flow was imaged using a CCD camera (1,200 x 1,600 pixels) whose optical axis was normal to the laser sheet. Laser sheets were generated using round and cylindrical lenses (focal length 120 and 50 mm, respectively) mounted on a traverse along with mirrors to vary the streamwise (x) and spanwise (z) positions of the laser sheet along the channel, and the nominal sheet thickness was 1 mm. The flow was seeded using 1-5 μm fog particles produced by an atomizer which was connected to the facility upstream of the channel test section.

The streamwise and spanwise locations of the PIV fields of views are noted in Chapter III and IV. In the H/W = 1 mm channel each field of view was W x 0.75W in the cross stream and streamwise directions, and data were acquired in streamwise increments of 1.4W with 16% overlap between streamwise widows from X = 1.6W to 9.7W over and and downstream of the reed as shown schematically in Figure 2.5. The methodology for stitching the data in the overlapping fields was discussed by Honohan (2003). In the H/W = 5 channel PIV data was obtained only downstream of the reed at discrete streamwise

windows whose centers are $\Delta X = 6W$ apart between X=18W and 42W in nonoverlapping windows.

These PIV data were processed using LaVision's software based on a standard double frame, FFT cross-correlation (e.g., Raffel, Willert and Kompenhans, 1998) and using the follow-on processing procedure as described by Lambert (2016). The time-averaged cross stream velocity components $\bar{u}(x,y)$ and $\bar{v}(x,y)$ were used to compute the time-averaged spanwise vorticity concentrations ω_z using the velocity components of 8 neighboring points based on the flow circulation(e.g., Brzozowski (2011).

The present PIV measurements were acquired in two modes. First, conventional time-averaged in which there is no phase relationship between the acquired data and the reed motion. For these time-averaged measurements N = 3000 realizations were acquired and ensemble-averaged at each streamwise window. For PIV grid locations (i, j) where there are a small number of instantaneous vectors missing due to the low-density particle seeding and/or rejected vectors, the averaging uses a sample size smaller than the entire sample size ($N_{i,j}$<N). The second, more intricate data acquisition mode was phase-locked to the motion of the reed (cf., §2.4.2). This was accomplished using the motion of a reference point on the reed as determined by a stationary laser-based range finder (shown

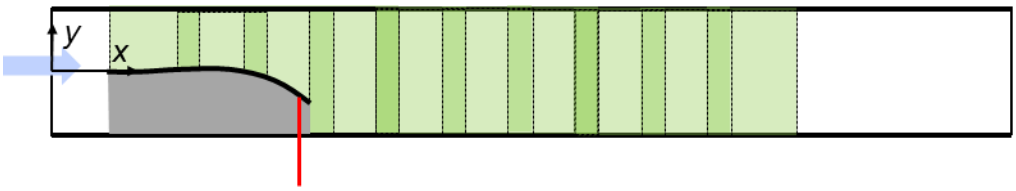

Figure 2.5. *Schematic of overlapping PIV views (at z=0) in the H/W = 1 channel (flow is from left to right). The trace of reed centerline is shown in black and its shadow is shown in gray. A reference point near the reed tip is monitored using a laser based* ***range finder*** *for determining the instantaneous position of the reed.*

schematically in Figure 2.5) and creating ensembles of image pairs for a predetermined number of reed positions or cross stream location of the reference point between the channel walls that were ensemble-to obtain a sequence of phase-averaged flow fields. In these measurements, the spatial resolution within each view in the H/W = 1 and 5 channels were 0.25 mm and 0.04 mm respectively.

As discussed by Brzozowski (2009), the errors in velocity measurements from PIV due to the precision of the PIV setup (calibration, particle position/pixel displacement and camera timing) and errors arising from calculations of the velocity vectors have a bi-normal distribution with zero mean and finite variance. These errors coupled with velocity fluctuations in the test section are reflected in variations of the measured velocity. An estimate of the RMS error in the velocity ($\sigma_{u,1}$) and vorticity ($\sigma_{\omega,1}$) using the PIV system were obtained based on the analysis of Adrian (1991) and Westerweel (2000) who showed

Table 2.1 *Error estimates of the measured velocity and vorticity distributions in the H/W=1 and 5 channels.*

Case	Vector Resolution	ΔT	Multi pass processing	# of realizations, N	$\sigma_{u,1}/\bar{u}$	$\sigma_{u,2}/\bar{u}$	$\sigma_{\omega,1}/\bar{\omega}_z$	$\sigma_{\omega,2}/\bar{\omega}_z$
H/W = 1 Phase-averaged PIV	0.25 mm	2 μs	2 passes of 64X 64 pixels 2 passes of 32 X 32 pixels	170	0.007	NA	0.023	NA
H/W=5 Position-averaged PIV	0.04 mm	1.5-10 μs	2 passes of 64X 64 pixels 2 passes of 24 X 24 pixels	60-100	0.002	NA	0.01	NA
H/W=1 Time-averaged PIV	0.25mm	2 μs	2 passes of 64X 64 pixels 2 passes of 32 X 32 pixels	3000	0.007	0.008	0.023	0.026
H/W=5 Time-averaged PIV	0.04mm	1.5-10 μs	2 passes of 64X 64 pixels 2 passes of 24 X 24 pixels	3000	0.002	0.005	0.01	0.025

that the predominant source of PIV errors is the resolution of sub-pixel displacements of the particles. The RMS errors in the velocity ($\sigma_{u,1}$) and vorticity ($\sigma_{\omega,1}$) in the present measurements were computed based on the interrogation window size, number of gray levels in the camera, number of particles within interrogation window, the standard gaussian image noise and number of sampled instantaneous vector fields following the procedure of Brzozowski (2009). Table 2.1 summarizes the PIV cases investigated in the present study in column 1, the description of the cases (PIV resolution, laser timing, DT, vector processing parameters and number of realizations, *N*) in columns 2 through 5 and estimates of the fractional RMS error in the velocity ($\sigma_{u,1}/\bar{u}$) and vorticity ($\sigma_{\omega,1}/\bar{\omega}$) in the PIV cases in column 6 and 8. In addition, an upper bound ($\sigma_{u,2}$, $\sigma_{\omega,2}$) to the PIV error is estimated using the RMS velocity fluctuations from the PIV data taken at a low Reynolds number (*Re*=2,000) at the entrance of the low and high aspect ratio channel where the natural flow fluctuations are small. Upper bounds of the fractional RMS errors in velocity, $\sigma_{u,2}/\bar{u}$ and vorticity, $\sigma_{\omega,1}/\bar{\omega}$ are the estimated and tabulated for the various PIV cases in columns 7 and 9 of Table 2.1. It should be noted that in the absence of a clear phase reference in the base flow, the upper bounds of velocity and vorticity errors $\sigma_{u,2}/\bar{u}$ and $\sigma_{\omega,1}/\bar{\omega}$ respectively, could not be obtained for phase-averaged PIV flow-field and are marked as NA in Table 2.1.

2.2.4 Range Finder Measurements of the Reed Motion

As shown in Figure 2.5, the motion of a reference point along the reed mid span 5 mm upstream of its tip (when the reed is at rest) was measured using a laser based range finder to detect the onset of reed motion and obtain a time series of the cross-stream motion

of the reference point. This time series was used for phase-locked PIV measurements (cf., §2.5). The present range finder has a resolution of 36 μm and is sampled at 20 KHz to obtain a time-series of the reed motion. These data are used to determine the primary reed frequency, f_{osc} which is then used to calculate the reed's Strouhal number, $St_L = f_{osc} \cdot L_s / U$ based on the reed length L_s and the average flow speed U with a maximum fractional uncertainty of 0.023.

2.2.5 Heat Transfer Measurements

The top and front views of the heat transfer channel test section are shown in Figures 2.6a and b (cf., §2.1.2). The back side of each of the channel's aluminum side walls is instrumented (at mid-span) with seven equally-spaced T-type thermocouple sensors (cf. Figure 2.6a) to measure the streamwise distribution of wall temperature, T_w. These thermocouple sensors are potted into grooves along the length of the wall surfaces. Each surface is then covered with an adhesive thin film heater (25.4 x 254 x 0.25 mm,) having maximum heat flux, $\dot{Q}_{\text{heater}}$" = 15.5 KW/m^2. In addition, six equally spaced thermocouple sensors are mounted along the span (z) of the right wall ($\hat{y} = y/W = -0.5$) at the channel exit to measure spanwise variation of T_w. The back of each heated side wall is

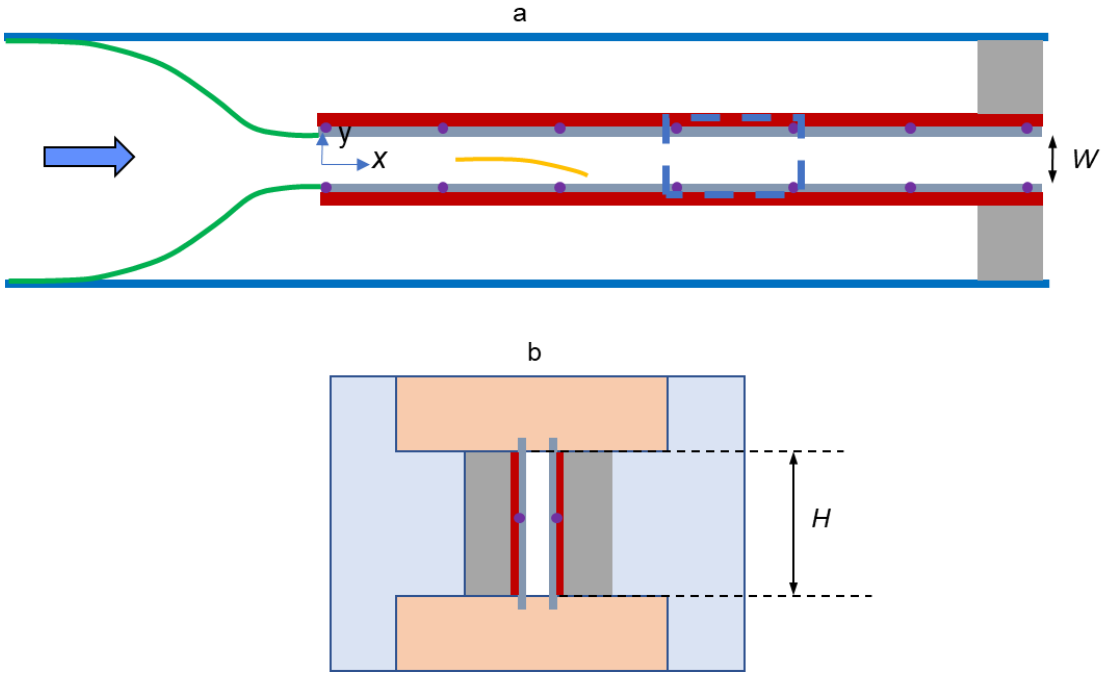

***Figure 2.6**. a) Top view of the heat transfer channel configuration, including a **2-D contraction**, **cantilevered reed**, and **thin-film heater** mounted on **aluminum surfaces** instrumented with arrays of thermocouple sensors and insulated on the sides using air gap and **styrofoam plugs** [an **elementary panel** marked between two adjacent thermocouple sensor was used for measurements of the local heat transfer (cf. §2.6 and 5.1)]; b) Front view of the channel.*

insulated using an air gap to the inner walls of the primary channel (H/W=1) and the heaters and the gap are sealed at its downstream end using a Styrofoam plug (cf. Figure 2.6a). The thin film heaters were powered using a DC power source and the voltage and current across the heater were monitored to calculate the heater power, $\dot{Q}_{\text{heater}}$ with a fractional uncertainty of 0.008. When steady state heating was achieved (20 - 25 minutes), the temperature data from the thermocouple sensors was sampled at 10 Hz for 10 sec and averaged to yield T_w. The resolution of the data acquisition module was 0.02°C with a maximum error of 0.5°C and the T-type thermocouple sensors had nominal errors of 0.5°C so that the maximum error in temperature measurements was 1.02°C or fractional uncertainty of 0.012 . Figure 2.7a and b illustrate the streamwise variations in time-average T_w measured at Re = 1,500 in the presence of a reed (planform dimensions 22 x 50 mm and thickness, t_s = 12.7 μm) for $\dot{Q}_{\text{heater}}$ = 17 Watts on the left ($\hat{y}$ = 0.5) and right ($\hat{y}$ = -0.5) aluminum side

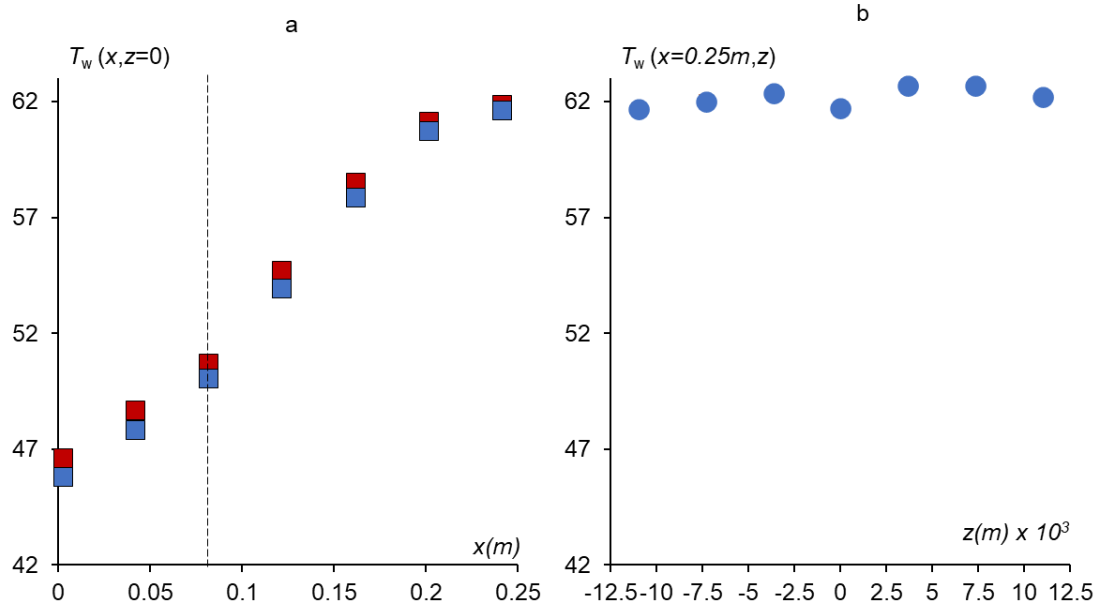

***Figure 2.7**. a) Streamwise variation of wall temperature $T_w(x)$ at Re = 1,500 in the presence of a reed (planform 22 x 50 mm and thickness, t_s = 12.7 μm) measured over the left ($\hat{y}$ = 0.5, ■) and right ($\hat{y}$ = -0.5, ■) walls as shown in in Figure 2.6, and b) spanwise variations of T_w measured at the bottom wall near the channel exit (x = 0.25 m). The reed tip location is shown using a vertical dashed line.*

walls and along the span of the bottom wall at the channel exit. These data show that the differences in streamwise variations of temperatures on the side walls is marginal (the left wall is cooler by 0.5^{o}C ostensibly due to the slight asymmetry in reed motion). The variations of T_w along the channel span do not exceed 0.7^{o}C at the channel exit (cf. Figure 2.6b) and are significantly smaller than the streamwise variations of the wall temperatures. In the heat transfer studies in chapter V, an average of the left and right wall temperatures was used to represent the streamwise variations of the wall temperature in the channel and the spanwise variations of wall temperatures were neglected in calculations of the Nusselt number. The local Nusselt numbers in the absence and presence of reeds are calculated based on an energy balance across an elementary panel between adjacent thermocouple sensors (cf. Figure 2.6a) which is discussed further in § 5.1.

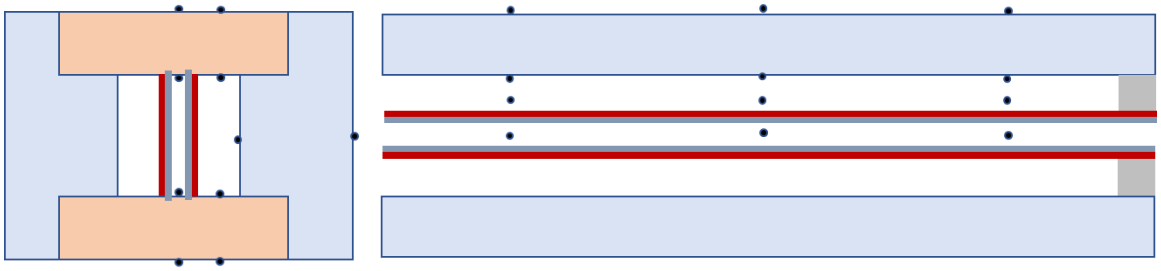

a *b*

***Figure 2.8**. a) Front view of the heat transfer test section showing the air cavities formed by the walls, the **heater** and **Styrofoam plugs** and the location of the thermocouple sensors in the cavity for measuring the heat flux losses through the cavity and walls; and b) Top view of the channel showing streamwise stations of the thermocouple sensors.*

In order to calculate the heat transfer to the air in the channel, the insulation heat flux losses were calculated and subtracted from the heater power. The heat flux losses from the *H*/*W*=5 channel through the insulated air cavity/gap were measured using an array of 24 thermocouple sensors mounted on the side, top and bottom walls of the insulation as shown in Figures 2.8a and b. The local heat flux losses, $\dot{Q}_{ins,x}{}'' = k_{acrylic}.\Delta T/t_{sw}$ were calculated using the temperature difference ΔT across the wall thickness, t_{sw} of side walls acrylic the channel, as measured at the center of three streamwise panels of length, $L_{channel}/3$ for each of the side, top and bottom walls of the insulation. The variation of channel average heat flux loss

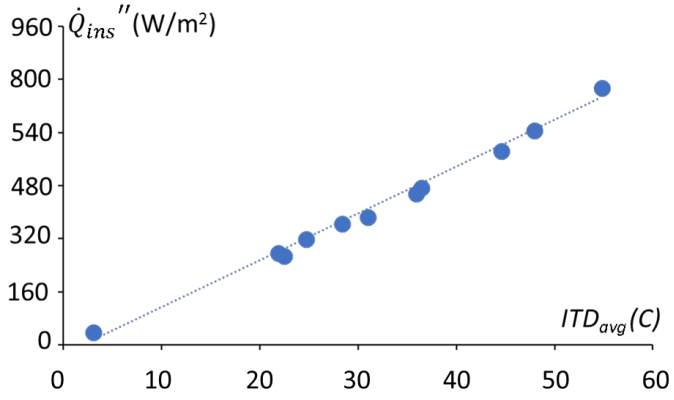

***Figure 2.9**. Variation of the total heat flux losses $\dot{Q}_{ins}{}''$ from the H/W=5 channel with average channel wall temperature ITD_{avg}, whose slope yields the insulation heat transfer coefficient.*

$\dot{Q}_{ins}'' = \sum \dot{Q}_{ins,x}'' A_p/(2LH)$ (where $A_p = L_{channel}/3 \cdot H_p$, A_p and $H_p = H$ are the panel area and height respectively) based on the total heater surface area ($2LH$) in the $H/W = 5$ channel with $ITD_{avg} = T_{w,avg} - T_{a,i}$, (where $T_{w,avg}$ is the average channel wall temperature) is shown in Figure 2.9. The slope of this nearly linear variation yields the insulation heat transfer coefficient $h_{ins} = 11$ Watts/m^2K. This analysis was checked with good agreement by sealing the channel at its downstream end and comparing the insulation losses in the absence of flow with the power supplied to the heater at steady state. The total heat dissipation rate to air, flowing inside the channel $\dot{Q}_{air}$ was calculated by subtracting the total heat losses to the insulation (integrated across all the panels) from the heater power and on average, $\dot{Q}_{air} = 0.8\dot{Q}_{heater}$. The maximum fractional errors in the measured heater power and the heat dissipated to air are 0.008 and 0.0125 respectively.

The heat transfer coefficients in H/W=5 and 10 channels are calculated using two methods. In the first method the *local* heat transfer coefficient $h(x)$ and Nusselt number, $Nu(x) = h(x) \cdot D_h/k_a$, ($k_a$ is the thermal conductivity of the air) were obtained from an energy balance on an elementary panel formed between adjacent thermocouple sensors (shown in Figure 2.6a). These local heat transfer coefficients were then averaged over the channel length to yield the global heat transfer coefficient h_m and global Nusselt number Nu. The details of these calculations are discussed in §5.1. The maximum fractional error in local and global Nusselt numbers (accounting for error in the heat dissipated to air and the differences in wall and air temperatures) is 0.05. The second method is based on a technique that is widely used in studies of heat sinks and relies on assessment of the logarithmic mean temperature differences between the fin and the air at the inlet and exit of the fins which is referred to as

LMTD and used in the fin array studies in Chapter VI. The LMTD yields the global Nusselt number, Nu_{LMTD} with a maximum fractional error of 0.063.

2.3 The Self-Oscillating Reeds

2.3.1 Reed Development

In the present investigations, reeds of varying thickness (12.7 μm < t_s< 200 μm), length (12 mm < L_s < 150 mm), and span 4 mm < H_s < 22 mm (H_s was 22 mm in most of the investigations) were fabricated from polyester and mylar thin film materials having nominal Young modulus E = 5 GPa and density ρ_s = 1,370 kg/m. The thin film sheets were laser cut to the required dimensions using a variable power CO_2 Laser cutter. Although the laser was set at its minimum power of 20 Watts, the thermal stresses resulted in slightly asymmetric reed motion as discussed in §2.4.2.

During measurements in the H/W = 1 channel (Chapter III), the reeds were cantilevered vertically within the center plane (y = 0) of the channel using a mounting fixture that clamps it along its height along a 5 mm strip at the upstream edge between two stainless steel plates 0.1 and 0.025 mm thick to minimize blockage losses. The assembly is shown in streamwise and top views in Figures 2.10a. and b respectively and a side view of the assembled fixture with the reed in the channel is shown in Figure 2.10c (the reed was glued in place using cyanoacrylate glue). The cantilever fixture was mounted within

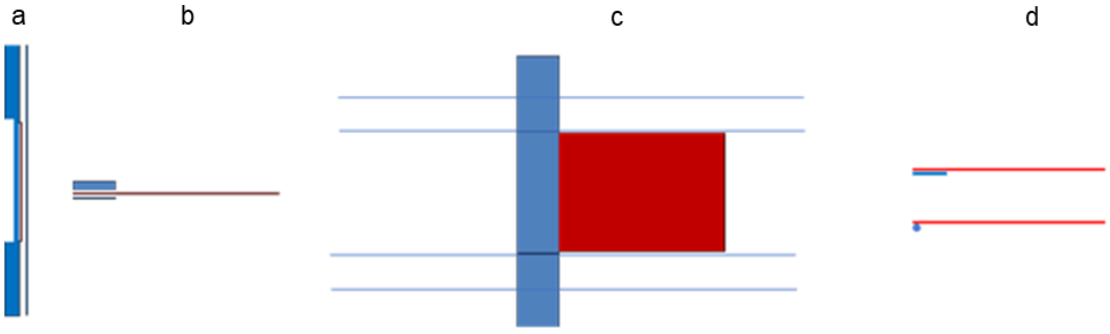

Figure 2.10 *Front (streamwise, a) and top (b) views of the reed clamping assembly and side view (c) of the assembled reed fixture in the channel. The spanwise recess of the left clamp in (a) spans the height of the channel to minimize blockage. Single-sided reed mounting fixtures using a plat plate and a cylinder are shown in (d).*

the test section through two access holes within the opposite (top and bottom) walls (cf. Figure 2.1). The tension of the cantilever assembly was adjusted using a torque wrench to ensure mounting repeatability. During the investigations in the high aspect ratio channels two alternative asymmetric mounting fixtures were considered using a single stainless 0.025 mm thick and 5 mm wide stainless steel plate and a 0.25 mm diameter stainless steel cylinder shown in top views in Figure 2.9d) to which the reed was affixed along it upstream edge using cyanoacrylate glue. Although the asymmetric mounting resulted in slight flow asymmetry downstream of the reed, the differences in reed oscillation frequency, channel pressure drop and heat transfer were negligible between the three reed mounts while the critical speeds for the asymmetric mounts were between 3 and 5% lower than for the clamping plate. Therefore, the cylinder mount was selected for the investigations in the isolated $H/W = 5$ and 10 channels in Chapters IV and V. Due to practical considerations of bulk manufacturing and mounting location the plate mount was used in the fin array experiments of Chapter VI and in the corresponding isolated channels for comparison with the fin array.

The reed's critical speed at which it begins to oscillate was determined by gradual computer-controlled increase of an initial channel speed at which the reed was stationary at increments of 0.3 m/s while monitoring the laser range finder output (cf. §2.2) until the oscillation threshold was crossed. Thereafter the speed was decreased at the same rate to the initial speed while observing the termination of the oscillations. The channel speed at each increment was maintained for 10 seconds and time series of the range finder and flow controller signals were sampled at 20 KHz. The critical speed was determined by the onset of oscillations in the range finder signal (cf. Figure 3.5 in §3.2).

2.3.2 Position-Locked Reed Motion Analysis

In the H/W = 1 and 5 channels the reed motion was characterized by imaging a trace along its mid-span between its upstream and downstream edges (cf., Figure 2.5) that was illuminated using a pulsed Nd:Yag laser sheet normal to the channel's center plane (y = 0). The scattered light from the intersection of the laser sheet and the reed was imaged using a CCD camera (1,600 x 1,200 pixels) that was mounted vertically above the channel's test section such that its optical axis was along the channel's center plane (y = 0), and parallel to the reed's leading edge (the field of view was similar to the PIV setup Figure 2.5). The range finder output was used as a phase reference for triggering the laser and CCD camera when the intersection of the range finder laser and the reed was located at 39 equally-spaced cross stream positions along the width of the channel (i.e., along the y coordinate) using a comparator. At each of the 39 positions, 170 traces of the reed surface were obtained and digitized with a resolution of 30 μm/pixel. Since the reed's motion along its length varied

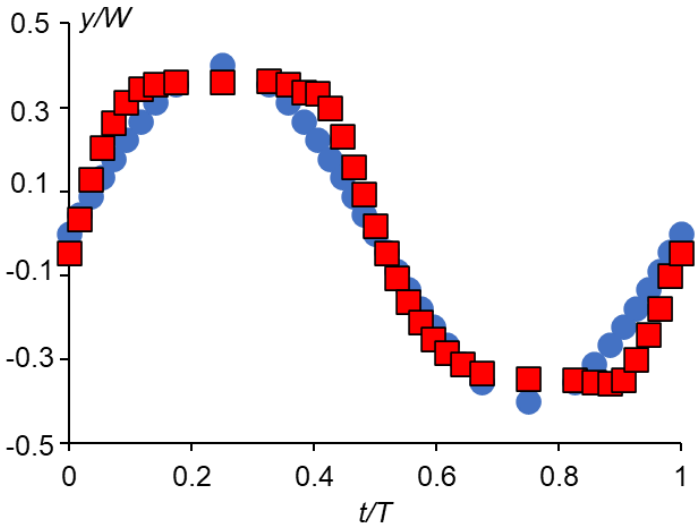

Figure 2.11. *Conditionally-averaged and normalized oscillation cycle* ***($\hat{y}$-$\hat{t}$)*** *of a reference point at the spanwise center of the reed and 5 mm upstream of its tip (at rest) based the range finder measurements* (●) *and the digitized centerline images* (■)

somewhat from cycle to cycle as moved across the channel, these digitized traces were conditionally averaged by first extracting the y-location of the digitized reed tip and then selecting the digitized traces where the tip's y location were within one standard deviation of the average tip location. These selected digitized traces were then averaged to yield the most probable *x*-*y* coordinates of the reed's centerline at each of the set cross stream reed reference positions. The average time stamp of the cross stream positions of the reed reference were obtained by organizing the time-traces of the range finder data into successive cycles and ensemble averaging the instantaneous time stamps corresponding to each cross stream elevation. The conditionally averaged cross stream locations of the reference point on the reed (cf. Figure 2.5) were compared based on the range finder and the digitized reed trace data and are shown in Figure 2.11. While the locations based on two measurement sources (range finder and digitized reed traces) appear to be in reasonable agreement close to the channel center ($y = 0$), some differences are evident close to the channel walls (up to 0.27 mm or 0.06 L_s at $y/L = -0.3$ and $t/T=0.9$). It is conjectured that the reed undergoes some spanwise bending and hence the shadow of the reed's spanwise edge on the image plane leads to a projection of the reed centerline trace to the camera that marginally differs from the true trace at the reference location as measured by the range finder. The *x*-*y* data corresponding to the reed centerline traces are used to characterize the evolution of the reed's kinetic energy as discussed further in Chapter III.

2.4 Processing of PIV Data

2.4.1 Time-Averaged Velocity Measurements

Each time-averaged velocity and vorticity fields in the H/W = 1 and 5 channels was computed using particle image velocimetry data consisting of 3,000 image pairs (cf., §2.2) acquired at frame rates between 8-10 Hz in the base flow and in the presence of the reeds (in the presence of reeds the acquisition frame rate frequency was adjusted to prevent aliasing with the reed motion). Although it was demonstrated that the time-averaged data did not change beyond about 800 instantaneous fields, a significantly larger sample size was used to reduce random PIV error in the second moment of velocity fluctuations (e.g., Trip et al., 2012). The instantaneous velocity fields were obtained using the standard PIV (DaVis 8.2) software.

The time-averaged streamwise and cross stream velocity components $\bar{u}$ and $\bar{v}$, respectively and the corresponding second moments of the velocity fluctuations $\overline{u'u'}$, $\overline{v'v'}$, and $\overline{u'v'}$ were computed as follows:

$$\overline{u'u'} = \frac{\sum_{i=1}^{N}(u_i - \bar{u})^2}{N}$$

$$\overline{v'v'} = \frac{\sum_{i=1}^{N}(v_i - \bar{v})^2}{N}$$

$$\overline{u'v'} = \frac{\sum_{i=1}^{N}(u_i - \bar{u})(v_i - \bar{v})}{N}$$

While these second order moments are clearly similar to the Reynolds Stresses in turbulent flows, it is refrained from referring to them using this terminology since the present channel inlet flows range from laminar to transitional and may not become fully-turbulent at the highest Reynolds numbers investigated. Furthermore, although some of the present data were acquired position-locked to the reed's motion, since the oscillation frequency and phase of the reed's motion vary cycle to cycle owing to its interactions with the cross flow and the shedding of vorticity concentrations, triple decomposition analysis (e.g., Hussain et al., 1972) was not attempted.

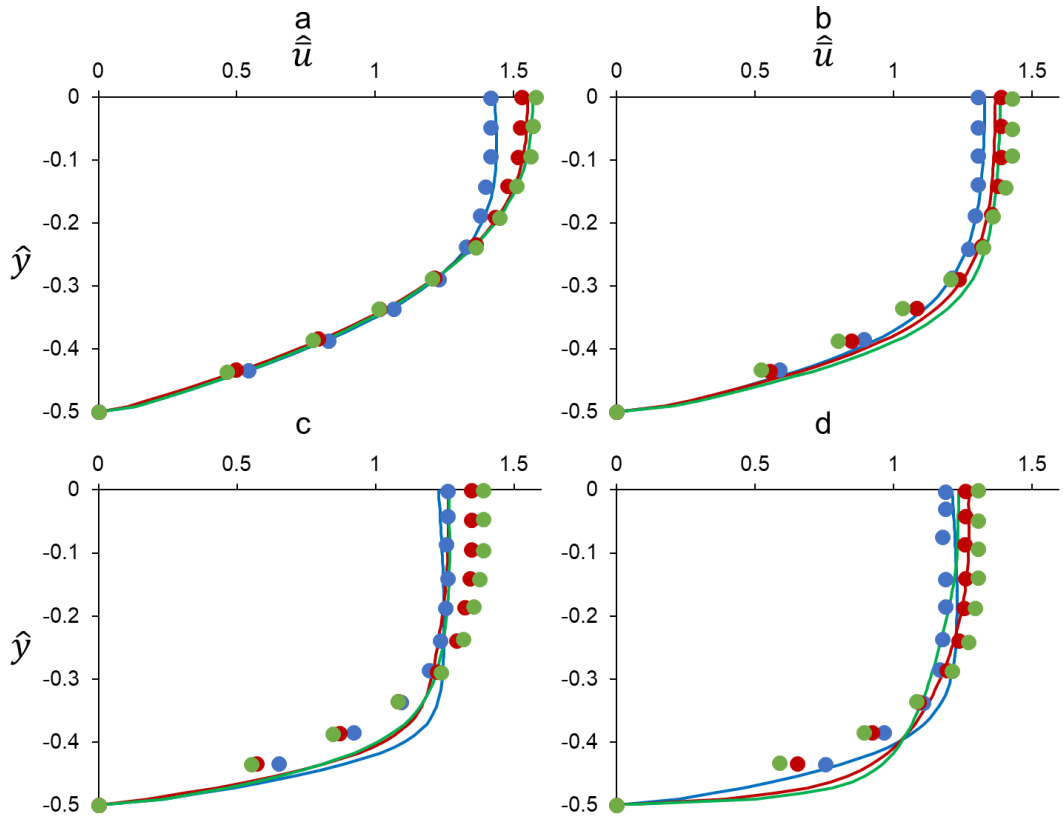

Figure 2.12 *Cross-stream distributions of the normalized time-averaged streamwise velocity $\hat{\bar{u}}$ (at z = 0, -0.5<$\hat{y}$<0) for the base-flow in the H/W=5 channel at $\hat{x}$ = 18 (●), 36 (●) and 48 (●) for Re = 2,000 (a), 5,000 (b), 7,000 (c) and 12,000 (d) The solid lines are a comparison with the data of Sparrow et al.(1967).*

Cross-stream distributions of the normalized time-averaged streamwise velocity $\hat{\bar{u}}(y)= \bar{u}(y)/U$ in the base flow of the H/W=5 channel were extracted at the streamwise center of the PIV fields at spanwise center of the channel (z = 0) centered at $\hat{x}= x/W$ = 18, 36 and 48 at Re = 2,000 (Figures 2.12). These data are compared with corresponding data in a similar channel (H/W=5) by Sparrow et al. (measured using pitot tube, 1967) at 1,000 < Re < 5,000 (at Re = 2,000 the base flow is laminar). At Re = 2,000, the present experimental data shows excellent agreement with the data of Sparrow et al. (1967) where the differences in $\hat{\bar{u}}(y)$ do not exceed 2% at all streamwise locations. Although the data of Sparrow et al. (1967) was limited to $Re \leq$ 5,000, they showed that the laminar cross-stream velocity distributions depend on $x^* = x/(Re \cdot D_h)$ and therefore their data were extrapolated for comparison with the present data at Re = 7,000 and 12,000 (cf. Figures 2.11b, c and d respectively). These comparisons show significant differences at higher Re as the base flow transitions to turbulence.

2.4.2 Velocity Measurements Position-Locked to the Reed Motion

Using the procedure described in §2.3.2 for obtaining traces along the midspan of the reed that are locked to the reed motion, velocity (and vorticity) fields along and downstream of the reed were measured in the H/W = 1 channel (§3.3) by using the range finder output to trigger the PIV camera to acquire 170 image pairs at each of 39 equi-spaced cross-stream positions of the reed reference (the trace of the reed centerline was acquired simultaneously). The reed traces were then conditionally selected (using the procedure described in §2.4.2) and the corresponding PIV image pairs for the selected reed traces were extracted, processed and averaged to obtain the conditionally-averaged velocity distributions at a given cross-stream position of the reed (cf., Chapter III).

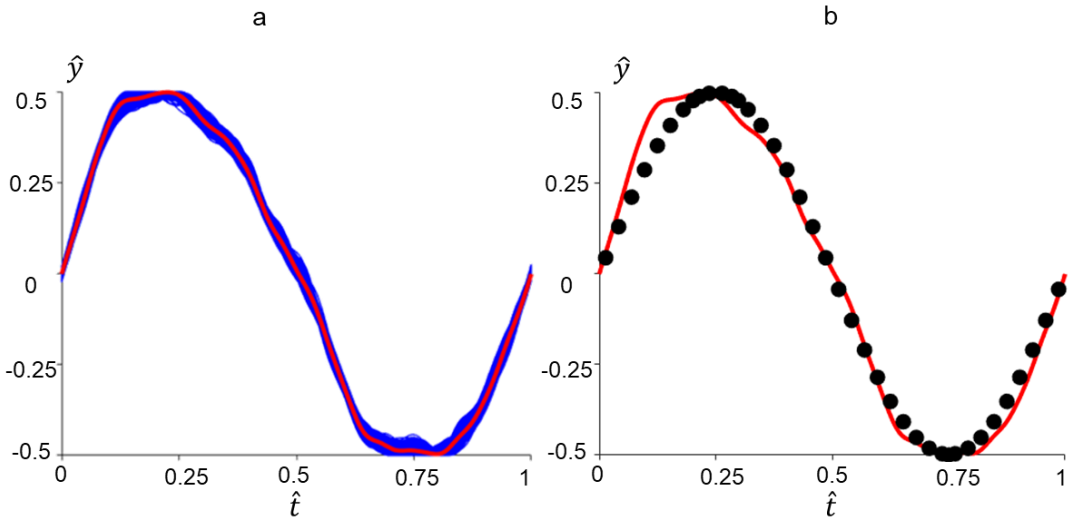

Figure 2.13 *a) Superimposed 3000* ***instantaneous cycles of the reed position*** *inferred from the range finder measurements and the* ***time-averaged cycle****, and b) the cross stream center* (●) *of each data bin based on a sine function that is fitted to the* ***time-averaged cycle****.*

The position based averaging procedure proved to be too long for the higher aspect ratio channel leading to degradation of the image quality owing to accumulation of fog particles on the channel walls. Therefore, a revised version of the locked data was devised based on bin-averaging technique in which a continuous stream of the PIV image pairs are sorted into bins that are characterized by a fixed phase relative to the reed motion *during post processing*. The cross-stream positions of the reed across the channel width are identified by the range finder data during the continuous acquisition of 3,000 PIV image pairs (the position of the range finder's reference point moves marginally along the reed during the oscillation cycle). The time-traces of the reed's cross stream position $\hat{y}_{ref}(t) = y_{ref}(t)/W$ were identified by successive zero-crossings (Mendonca et al., 2014), and each cycle normalized by its *own* period T_{inst} $\hat{t} = t/T_{inst,}$ (Figure 2.13a). A time-averaged cycle is calculated from the mean of the instantaneous cycles. These data showed that the standard deviation of the periods of the instantaneous cycles is about 2% of the period of

the time-averaged averaged cycle. The time-averaged cycle shows that the reed motion between the channel center ($\hat{y}$ = 0) and the top and bottom wall ($\hat{y}$ = ±0.5) are slightly different due to the asymmetry in the attachment of the reed's root to the support post (cf., § 2.3). A sine function with amplitude and frequency that match the average cycle was discretized into 38 bins whose centers are equally spaced in time ($\hat{t}$) along the average reed cycle (cf., Figure 2.13b). The time-based phases at the bin-centers were $\alpha_{bin} = 2\pi\hat{t} = (2k - 1)(\pi/38)$ and the reed reference's cross-stream elevation in the channel corresponding to the timing of the bin centers were $\hat{y}_{bin} = \sin(\alpha)$ for $k = 1, 2, 3, \ldots 38$. While the phase based width of each bin was $\Delta\alpha_{bin} = 2\pi/38$, the cross-stream width of the individual bins varies during the oscillation cycle as $\Delta\hat{y} = \pi/38 \bullet \cos(2\pi\hat{t})$ and has minima near the top and bottom walls ($\hat{t}$ = 0.25 and 0.75 respectively) and maxima near the channel center ($\hat{t}$ = 0 and 0.5). The PIV images that are captured along with the reed reference's time-trace were then sorted into the individual bins based on the phase of the reed reference

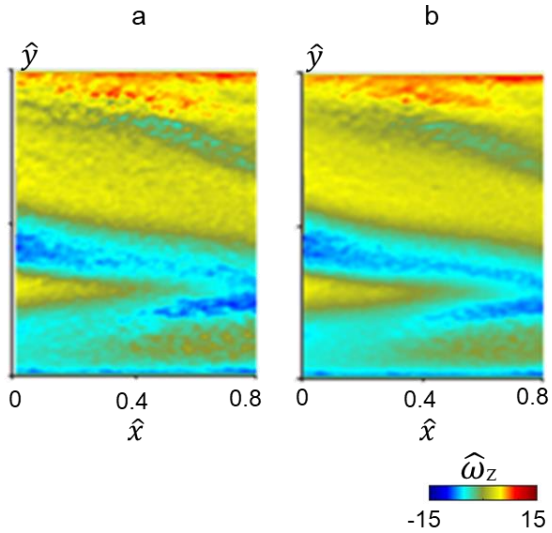

Figure 2.14 *Example of sorted PIV data acquired for a reed (L_s/W = 10, H_s/H = 0.9) oscillating at 65Hz at Re=2,000 at $\hat{y}$ = 18, $\hat{z}$ = 0: Cross stream distributions of instantaneous spanwise vorticity, $\widehat{\omega}_z$ corresponding to sorted PIV image (a) and bin-average (b)*

during the PIV acquisition. The flow fields obtained from the sorted PIV images within each bin were averaged to obtain the bin-averaged flow fields. While the average number of PIV image pairs within the bins was 78, the number of image pairs varied between the bins with a maximum of 100 images for $\alpha = \pi/2$ and minimum of 60 images for $\alpha = \pi/38$. An example of the sorted data is shown in figure 2.14 for $\alpha_{bin} = 3\pi/38$ and the PIV view of a reed with $L_s/W = 10$ and $H_s/H = 0.9$ oscillating at 65 Hz captured at $\hat{x} = 18$, $\hat{z} = 0$. Figure 2.14b and c show an instantaneous sorted spanwise vorticity field ($\hat{\omega}_z = \omega_z \cdot W/U$) and the bin-averaged vorticity field respectively. A key drawback of this technique is that even though good resolution of the phase-based variations can be obtained far away from the walls, the phase-based variations degrade near the walls due to insufficient time resolution.

CHAPTER III

DYNAMICS OF REED FLUTTER IN A RECTANGULAR CHANNEL FLOW

Overview

This chapter focuses on the characterization of reed flutter in rectangular channels, including the reed dynamics at the onset of flutter and the interactions between the reed and the flow that lead to the formation and advection of a hierarchy of small-scale vortical structures. The reed's dynamics are captured by imaging a streamwise trace through its mid-span and analyzed by using proper orthogonal decomposition (POD) and assessment of its mechanical energy. The vortical motions induced by the reed motion are investigated using particle image velocimetry (PIV) and hot wire anemometry.

3.1 Review of Mechanisms of Reed Flutter

As noted in Chapter I, the flutter mechanism of cantilevered thin flags (or flexible reeds) in uniform cross flows and within flow ducts has been studied extensively. Shelley and Zhang (2011) noted the existence of a critical cross flow speed, U_{critical}, below which the reed is stable and above which surface perturbations can amplify into coherent fluttering. The motion of the surface of a rectangular reed having planform length and span dimensions L_s, and H_s, respectively, and thickness, t_s in a uniform cross flow with velocity $U > U_{\text{critical}}$ is characterized along its centerline $y = y(x, t)$, as shown schematically in Figure 3.1. The dynamics of reed motion in the perturbed state in Figure 3.1 is obtained using Euler-Bernoulli theory for bending beams (Shelley et al., 2005) through a force balance

between the structural and fluid dynamic forces on a reed element while neglecting the viscous shear stresses on the reed.

$$M^* \frac{\partial^2 y*}{\partial t^{*2}} = -\frac{1}{U^{*2}} \frac{\partial^4 y*}{\partial x^{*4}} + \delta p^* \tag{3.1}$$

where $y^* = y\,(x, t)/L_s$, $x^* = x/L_s$, $t^* = t \cdot U/L_s$. The reed inertia ratio M^* (or the ratio of the reed's mass (per unit area) and the mass of the air with which it interacts) is $M^* = \rho_s \cdot t_s/(\rho_a \cdot L_s)$ in which ρ_s and ρ_a are the reed and air densities, respectively. The reduced flow speed of the reed U^* is the ratio of the flow kinetic energy and the reed's elastic potential energy is given by $U^* = U \cdot \sqrt{\rho_a H_s {L_s}^3 / k_b}$ where $k_b = E \cdot I$ is the flexural rigidity and E and $I = H_s t_s^3/12$ are Young's modulus and area moment of inertia of the reed,

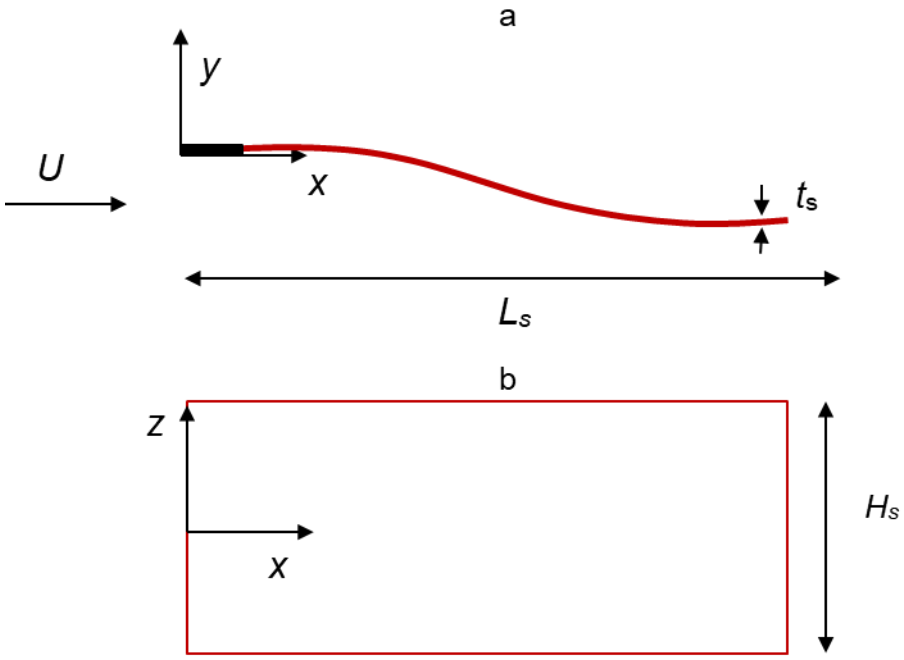

Figure 3.1. *a) The centerline of the reed's planform surface y(x, t) z = 0 of a reed measuring L_s X H_s X t_s and oscillating in a uniform cross flow with speed U; and b) The projection of the reed in x-z plane.*

respectively. Finally, the normalized pressure difference across the reed at some position x^* due to perturbations from its stable state is $\delta p^* = \delta p(x^*) / (\rho_a \cdot U^2)$.

The right-hand side of this equation includes two competing forces which govern the motion of a reed element: a stabilizing elastic force ($1/U^{*2} \cdot \partial^4 y^*/\partial x^{*4}$) corresponding to the bending stiffness of the reed and a destabilizing pressure force ($C_p$due to the flow over the perturbed state of the reed). Figure 3.2 depicts the instantaneous flow along and downstream of a reed suspended in a soap film during its motion downward (Zhang et al., 2000), in which the instantaneous streamlines around the reed are visualized using interference fringes created by reflection from a monochromatic light source. This image shows the formation of a train of clockwise (CW) vortices downstream of the reed. The streamlines in flow below the bottom surface of the reed are closer to each other near the trailing edge compared to the leading edge, indicating a streamwise increase in velocity and lower pressure along the bottom surface. On the top surface of the reed, the streamlines diverge away from the reed as the flow expands leading to a streamwise adverse pressure gradient. Therefore, the reed curvature during its motion is accompanied by a pressure

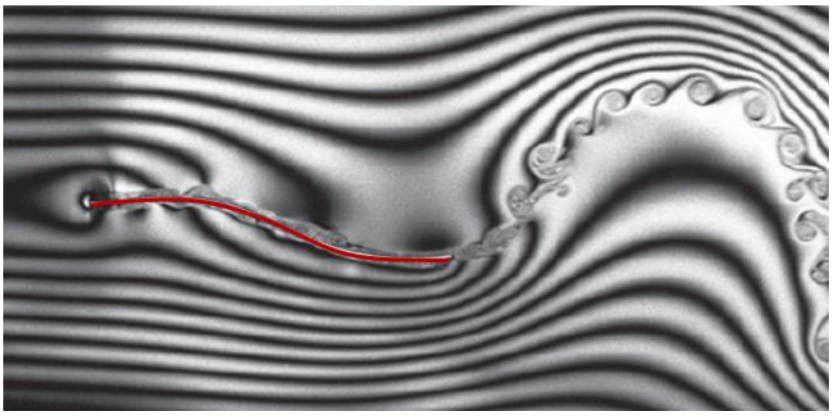

Figure 3.2. *Soap film flow visualization (the flow is from left to right) around an undulating silk reed by Zhang et. al. (2000). The interference fringes were produced using monochromatic light to represent instantaneous streamlines.*

difference between the two surfaces. The temporal rate of change of the lift force on the reed can be evaluated by calculating the vorticity flux at the tip of the reed based on a vorticity balance equation as described by Shih et al. (1994). When the flow-driven lift force can overcome the reed's elastic restoring forces, it transitions to an oscillatory motion with a frequency which depends upon the balance between the two opposing forces (Argentina et al., 2005).

Shelley et al. (2005) performed a stability analysis of a 2-D cantilevered reed in free flow using equation 3.1 and a potential flow model to derive a stability boundary M^*-U^* above which the reed oscillates and below which the reed is in a stable stationary state, as reproduced in Figure 3.3. These data show that along this boundary the reduced critical speed of the reed, U^* decreases with increasing M^* and that the reduced velocity, $U_{critical}^*$ is nearly invariant for heavier reeds ($M^*>1$), indicating that at fixed flow density and reed mechanical properties (E and ρ_s) for such reeds, $U_{critical}$ increases as $(t_s/L_s)^{1.5}$. While this

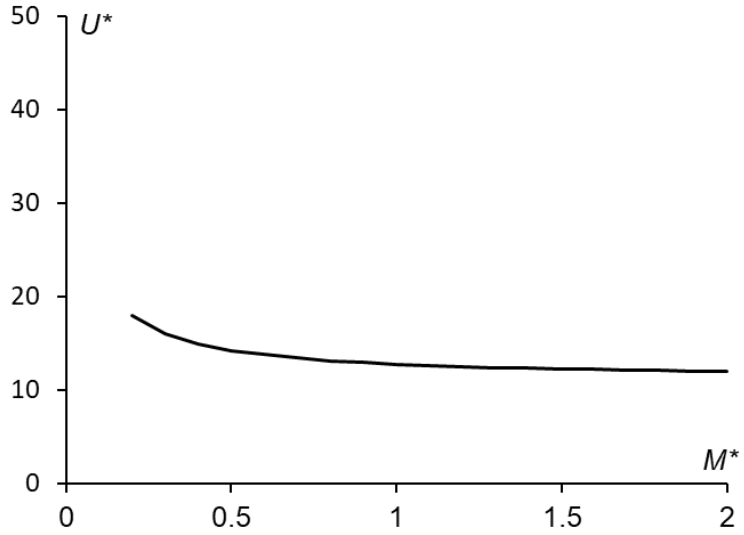

Figure 3.3. *The stability boundary of a reed cantilevered at the root in a uniform cross flow derived from the potential flow model of Shelley et al (2005). For reed of given mass ratio M*, the domains below and above the curve correspond to flow speeds U* for which the reed is stable or unstable to flutter, respectively.*

analysis provides the parameters influencing the onset of reed motion (M^* and U^*), it doesn't account for viscous losses on the reed, and when the reed is immersed in a channel, the analysis doesn't account for the proximity of the channel walls which is a central element of the present investigations.

3.2 Reed Fluttering in Channel Flow

The present investigations focus on fluttering reeds in low and high aspect ratio rectangular channels. The motion of a cantilevered reed was first investigated in a channel having a square (25 x 25 mm) cross section and 250 mm long (cf. Chapter II), and a schematic rendition of the reed mounting in a rectangular channel is shown in Figure 3.4a. In the present investigations, the reed was cantilevered across the span (H) of the channel and was fabricated using a thin film including polyester (E = 5GPa, ρ_s = 1,390 kg/m^3), and mylar (E = 4.5GPa, ρ_s = 1,370 kg/m^3) reeds. The reed planform dimensions were varied over a broad range (12 mm < L_s < 150 mm, 4 mm < H_s < 22mm), as was the thickness (12.7 μm < t_s < 200 μm). The motion of the reed is monitored on its centerline (intersection with the plane z = 0), nominally 5 mm upstream of its tip using a laser-based range finder as shown schematically in Figure 3.4b.

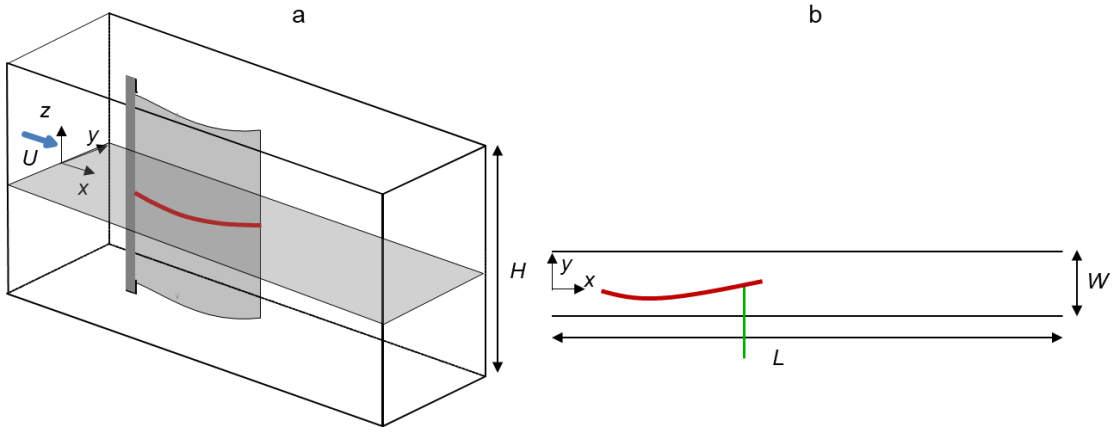

Figure 3.4*. a) Schematic of a section of a channel showing the placement of a thin-film reed cantilevered on a thin (5 mm) stainless-steel plate mounted between the top and bottom wall of the channel at downstream of the channel's entrance; and b) A cross section of the reed in the x-y plane z = 0. The motion of the reed is monitored along its centerline using a laser range-finder* ***(marked by a green line segment)****.*

The critical speed of the reed motion and the onset of its oscillations were determined by gradually increasing the average air speed in the channel while monitoring reed motion. An example of the characterization of the critical speed in the present channel is discussed below using a polyester reed measuring 45 x 22 mm and 38.1 μm thick. The flow speed was increased at a low rate from some reference speed below U_{critical} (16 cm/sec/sec) using a flow controller in the air supply (cf., Chapter II)

The temporal variation of the reed motion (5 mm upstream of its tip) is shown in Figure 3.5a in terms of the oscillation amplitude $A_{\text{tip}}/W = (y_{\text{tip}}-\overline{y_{tip}})/W$, where $\overline{y_{tip}}$ is the time-averaged position of the reed's tip (the rest position of the tip is not necessarily at the cross-stream center of the channel, $y = 0$, in the present example, the tip of the reed is the offset relative to cross-stream center by about $0.01W$) as the average air speed in the channel is varied between 4.72 (at $t = 0$) and 4.88 m/sec ($t = 1$ sec). When the flow speed is just below the onset of oscillations (500 msec < t < 600 msec), the reed exhibits a mild flutter with a nominal amplitude $A_{\text{tip}} < 0.05W$. The oscillation amplitude increases with air speed to $0.26W$ for $t > 500$ msec, and the critical speed (defined when the oscillation

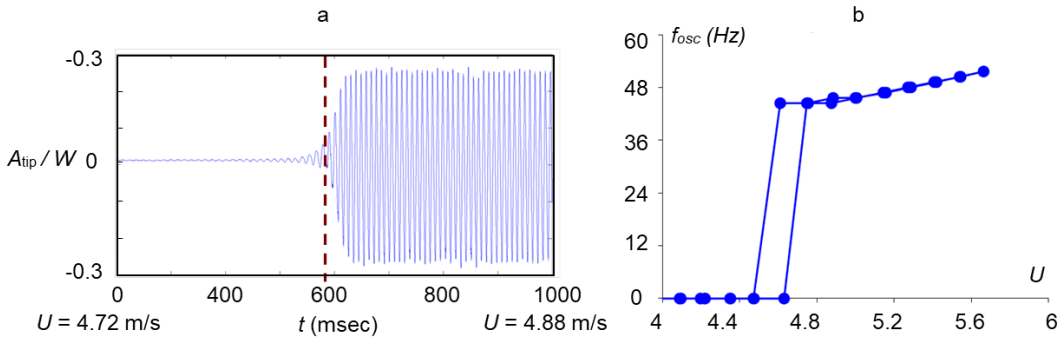

Figure 3.5. *a) The variation with time of reed's oscillation as the channel speed increases between 4.72 and 4.88 m/sec (the reed offset at t = 0 from the channel center is about 0.01W); and b) The variation of reed oscillation frequency with increasing/decreasing air speed in the channel.*

amplitude exceeds $0.05W$) is $U_{critical} = 4.8$ m/sec (the oscillation frequency, f_{osc} is approximately 47 Hz or the strouhal number $St_L = f_{osc} \cdot L_s/U = 0.42$). The oscillation amplitude reaches a quasi-steady magnitude of $0.26W$ within 6 oscillation cycles, and the oscillation frequency increases to 48 Hz when the air speed reaches $U = 4.88$ m/sec. Figure 3.5b shows the variation of oscillation frequency of the reed as the speed of the air flow in the channel is increased from 4 m/s to 5.7 m/s and then decreased back to 4 m/s at increments/decrements of 0.3 m/s. Each speed is maintained for 10 seconds and the time series of the rangefinder signal is sampled at 20 KHz for computing a power spectrum. Within the range of the present investigations, it was found that following the onset of the critical speed the reed frequency increases as $U^{1.3}$. It can also be observed that the when the channel speed is decreased, the reed continues to oscillate until a lower critical speed (4.5 m/s), thereby displaying hysteresis (as described by Watanabe et al., 2002 for reeds in uniform flow). For the current work, unless otherwise noted, critical speed is defined as the flow speed above which the reed starts oscillating when the flow speed is gradually increased in the channel.

Using the procedure described in connection with Figure 3.5, the critical speed was characterized for two reed lengths $L_s = 30$ and 45 mm and a range of reed thicknesses $t_s = 13$, 25, and 38, and 50 μm. Figure 3.6 shows the variation of the reduced critical speed, $U_{critical}$* with the reed inertia ratio, M*. In these experiments, independent measurements of the critical speed were repeated (four times) for each reed configuration and the variances are marked by the error bars. The stability boundary of a reed in a uniform flow shown in Figure 3.3 is also included for reference. These data show that $U_{critical}$* decreases with increasing inertia ratio (as the reed becomes heavier compared to air) and asymptotes

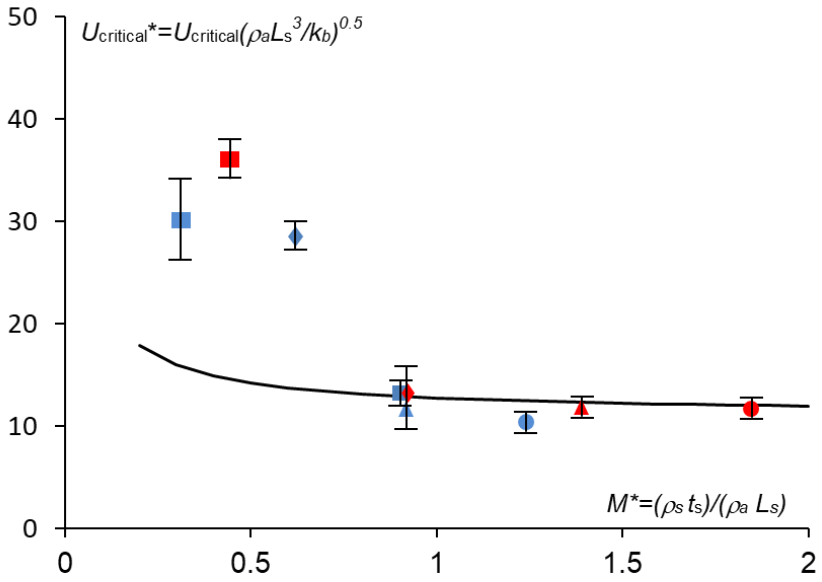

Figure 3.6*. a) Variation of the critical flow speed $U_{critical}$* with the reed mass ratio M*: t_s = 13 μm (■), 25 μm (◆), 38 μm (▲), 50 μm (●) and for L_s = 45 and 30 mm. The solid black line is the critical speed of a 2-D reed in uniform stream based on the potential flow model of Shelley et al. (2005) (cf. Figure 3.3). The variance of the measured critical speed are shown by a bar for each reed.*

to $U^* \approx 12$ for $M^* > 1.5$ indicating that for a given reed length the (dimensional) critical speed $U_{critical}$ of the heavier reeds increases with thickness as $t_s^{1.5}$. It is noteworthy that for $M^* > 0.8$, the measurements agree well with the uniform flow model indicating that the proximity of the channel walls, viscous effects, and 3-D modes of the reed motion become less important as the mass of the reed is increased. The increasing deviation between the model and the measured critical speed when M^* is lower indicates that these effects are more important, and it might be argued that reed-wall interactions over a longer reed length for the thinner reeds due to their low bending rigidity. The variations of critical speeds, $U_{critical}^*$ with M^* were also measured in higher aspect ratio channels with H/W = 5 and 10 for the same reeds as in H/W = 1 channel and, since these variations collapse on M^*-$U_{critical}^*$ curve of the H/W = 1 channel, they are not discussed further.

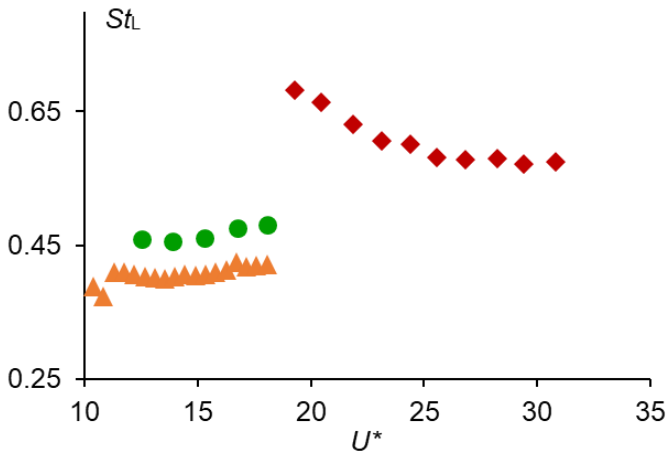

Figure 3.7*. Variation of the reed Strouhal Number St_L (L_s = 45mm) with the reduced velocity U^* for t = 25 μm (◆), 38 μm(●), and 50 μm(▲).*

The motion of the reed is also characterized in terms of its oscillation frequency that was assessed from time traces of reed motion near its tip (cf. Figure 3.5). Figure 3.7 shows the variation of the reed oscillation frequency (represented by the Strouhal number, St_L) with the reduced speed U^*. It is noted that for these data sets, the channel Reynolds number, $Re = U{\cdot}D_h / \vartheta$ (D_h is the hydraulic diameter) varies within the range $1{,}000 < Re < 18{,}000$ and the reed thickness is increased incrementally: t_s = 25, 38, and 50 μm for reeds of length, L_s=50 mm. For thicker reeds (t_s = 38.1 and 50 μm), St_L is nearly invariant with the reduced speed, U^* ($St_L \approx 0.45$ and 0.4 respectively) but for a thin reed (t_s = 25 μm), St_L decreases from 0.68 to 0.57 for $19 < U^* < 31$. These variations indicate "mode-switching" for the thin reed as has also been observed by Alben (2015) through an inviscid flow model for reeds (or flags) in channels.

The interactions of the reed with the channel flow also leads to form drag due to channel blockage created by the reed and viscous drag on the reed and channel surfaces. These reed-channel interactions are manifested in the form of increased pressure drop

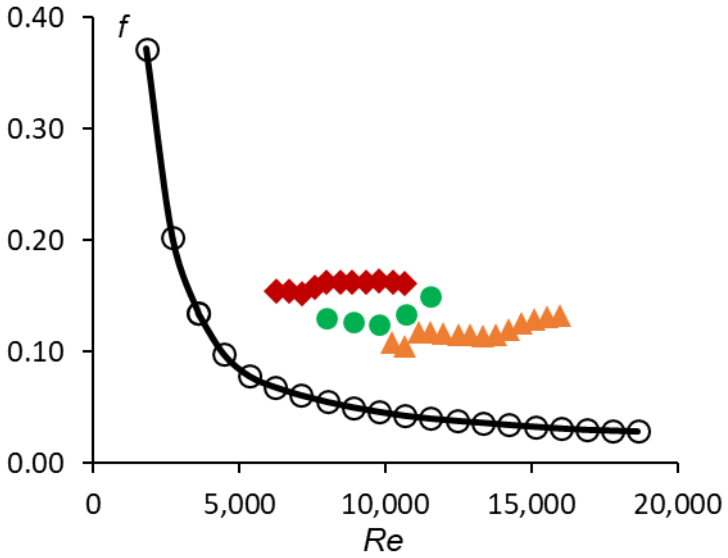

Figure 3.8. *Variation of the channel friction factor, f with the Re in the absence (○) and presence of reeds: t_s = 25 μm(◆), 38 μm(●), and 50 μm(▲).*

within the channel measured using Darcy friction factor, $f = \Delta P/(0.5 \cdot \rho_a \cdot U^2 \cdot L/D_h$, where ΔP is the static pressure drop across the channel (cf. Chapter II). Figure 3.8 shows the variation with *Re* of friction factor in the absence and presence of the reed (L_s=50 mm and t_s = 25, 38 and 50 μm). In the absence of the reeds, the friction factor decreases with *Re* ($f \sim 400Re^{-1}$). The high levels of *f* in the base-flow compared to fully-developed flow ($f = 64Re^{-1}$) show that because the channel is short (L/D_h = 10), the channel entrance effects are significant and the channel pressure drop has to balance both the wall shear stresses and increase in flow momentum. In the presence of reeds, there is an increase in *f* at all *Re* and for each thickness. Since the critical *Re* above which the reed oscillates increases as the reed thickness increases (as described in connection with Figure 3.6), the curves of *f* vs. *Re* shift towards the right as the thickness increases. There is an increase in *f* of about 115% at *Re* = 6,200 (t_s = 25 μm), 132% at *Re* = 8,000 (t_s = 38 μm) and 157% at *Re* = 10,000 (t_s = 50 μm). It should be noted that for an invariant *Re*, the increase in *f*

decreases with increase in reed thickness (e.g., at Re = 10,000, the increments in f are 283, 216 and 157% for t_s = 25 38, and 50 μm respectively). The decrease in f can be attributed to the decrease in the reed oscillation frequency as its thickness increases. For example, at Re = 10,000, St_L decreases from 0.7 to 0.4 as t_s increases from 50 to 25 μm. The dependence of the friction factor on the oscillation frequency is discussed further in § 4.5.

3.3 Flow Dynamics in the Presence of Reed in Low Aspect Ratio Channels

The effects of the reed on the flow within a low-aspect ratio channel are investigated in a channel having a cross section of 25 x 25 mm (cf. Chapter II) where the channel walls are farther apart and effect mild interactions with the reed motion. The motion of a reed (22 x 45, 38 μm thick, critical speed 4.8 m/s) in this channel is captured by imaging the centerline of the reed using a video camera (1,600 x 1,200 pixels) that is triggered by the motion of a reference point (as obtained from the range finder at the mid-span of the reed and $0.1L_s$ upstream of its tip when the reed is at rest, cf. Figure 3.4b). Digitized images of the reed's centerline (in the cross-stream plane, $z = 0$, cf. Figure 3.4a) are captured for 39 equally-spaced cross-stream positions of the reference point, y_{ref}, across the channel width and the conditionally-averaged centerlines (cf. chapter II) are shown in Figures 3.9. As shown in Chapter II, the difference between the positions of the reference point based on the centerline position and the range finder does not exceed $0.06L_s$. The data in figure 3.9 shows that the reed comes in contact with channels' left ($\hat{y} = 0.5$, $y/L_s = 0.27$) and right

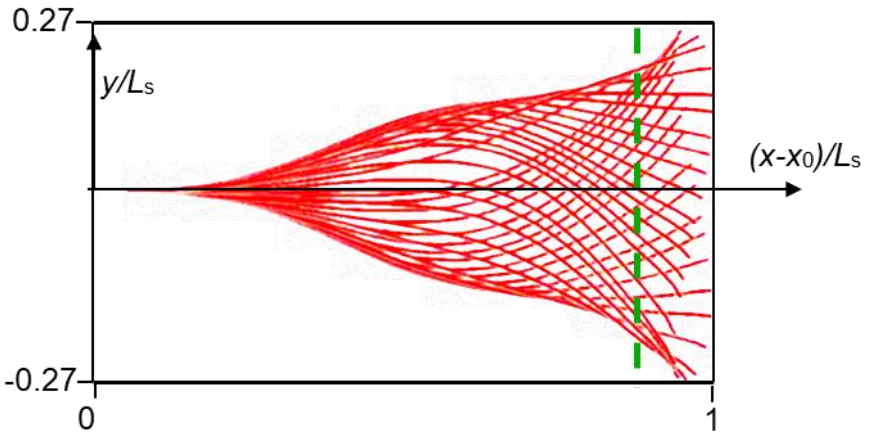

Figure 3.9. *Overlaid traces of the centerline of a reed measuring* 22 x 45 (*38 μm thick*) in a *25 mm channel at 39 equally spaced positions of a* ***reference point*** y_{ref} *near its tip (cf. Figure 3.4b) for U = 4.8 m/sec. The centerlines are conditionally averaged from ensembles that are acquired position-locked to the motion of the reference point.*

($\hat{y}$ = -0.5, y/L_s = - 0.27) walls only near its tip. That the critical speed of the reed is close to the speed of a similar reed in a uniform flow (c.f., figure 3.6) shows that the effects of its interactions with the walls on its critical speed are insignificant. The data in Figure 3.9 also show slight asymmetry between the reed's motions towards the left and right walls during the oscillation cycle. The asymmetry stems from pre-stressing during the laser fabrication process.

The kinetic energy of the reed is calculated using the motion of its (conditionally averaged) centerline across the channel width (neglecting spanwise variations). In these calculations, the reed length was divided into elements of length $ds = L_s/100$ or 0.45 mm (15 times the imaging resolution, cf. chapter II) and the x-y coordinates at the center of each element, s, are computed for each of the 39 centerlines during the oscillation cycle. The times corresponding to each position of the reference point, y_{ref}, are extracted from the average reed oscillation cycle (cf. chapter II) to yield the time-stamp of each centerline, $t_{ref}(i)$. The streamwise (V_x) and cross-streamwise (V_y) reed velocities were obtained at 38

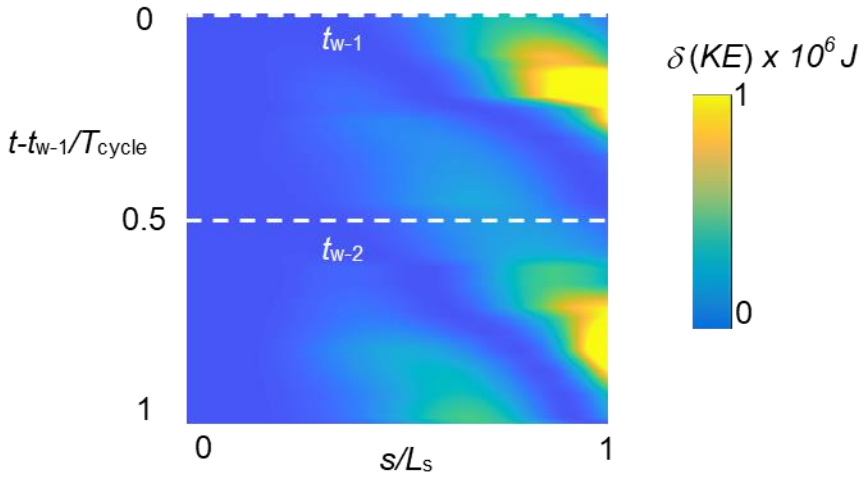

Figure 3.10. *Color raster plot of the variation of the reed kinetic energy in the 25 mm channel along its centerline s during the nominal oscillation period T_{cycle} = 0.02 sec (L_s = 45 mm, t_s = 38 μm). At t_{w-1} and t_{w-2} (marked by dotted lines) the reed tip touches the channel left (1) and right (2) walls, respectively.*

instants $\tau = [t_{ref}\ (i)\ +\ t_{ref}\ (i+1)]/2$ along the average cycle and are defined as $V_x(s,\tau) = (\Delta x(s) / \Delta t_{ref})$ and $V_y(s,\tau) = (\Delta y(s) / \Delta t_{ref})$ where Δ refers to differences between $t_{ref}\ (i+1)$ and $t_{ref}\ (i)$. The reed velocity magnitudes, $V(s,\tau) = (V_x^2+V_y^2)^{0.5}$ were used to calculate the elemental kinetic energy of the reed, $\delta\,(KE)\ (s,\tau) = 0.5\rho_s\, V_s^2 t_s W_s(ds)$, and the total kinetic energy of the reed $KE(\tau) = \int_{s=0}^{s=L_s} \delta(KE)(s,\tau)$. The present investigations demonstrated that the reed's total kinetic energy $KE \approx$ O ($10^{-6} J$) is typically four orders of magnitude higher than its elastic potential energy $PE = \int_{s=0}^{s=L_s} (1/24) \cdot E t_s{}^3 \left(\frac{\partial^2 y}{\partial x^2}\right)^2 dx(s)$ (Williams, 2009). The variation of the reed's kinetic energy (at its nominal critical speed) along its length during the oscillation cycle, $\delta\,(KE)\ (s/L_s,\ \tau/T_{cycle},)$, where the nominal oscillation period T_{cycle} is 0.02 sec is shown using color raster plot in Figure 3.10. It should be noted that the cycle begins when the reed is at the left wall ($t_{w\text{-}1} = 0$, $\hat{y} = 0.5$) moving towards the right wall ($t_{w\text{-}2} = 0.5 \cdot T_{cycle}$, $\hat{y} = -0.5$) and ends back at the left wall. These data show the presence of multiple travelling waves of celerity, $(ds/dt)/U = 0.5$, from the root to the tip of the reed per oscillation cycle that intensify along the reed length. These travelling waves lead to periodic peaking and release of the kinetic energy near the tip ($0.84 < s/L_s < 1$). These peaks occur when the tip is at the cross-stream center of the channel ($\tau/T_{cycle} = 0.25$ and 0.75) and indicate the acceleration and deceleration of the reed towards the channel walls (the arrival times at the walls are marked by the dotted lines).

The flow structures induced by the interactions between the reed and the channel flow are assessed from PIV measurements that are acquired locked to the cross stream position of the reed (as in Figure 3.9, cf. Chapter II). These data are acquired within the cross stream (x-y) plane $z = 0$ over the reed's surface and downstream of its trailing edge. As described in connection with Figure 3.9, these data are taken at 39 equally-spaced cross-stream positions of a reference point on the reed, y_{ref}, such that 170 images are included and averaged at each position to yield the position-averaged flow field. The field of view at each of the reed's position is comprised of four partially overlapping (16%) streamwise fields each spanning the width, W, of the channel and $\Delta x = 0.75W$ long (the entire field of view is $1.6 < \hat{x} < 4.2$). A separate CCD camera is triggered to simultaneously acquire images of the reed's centerline synchronized with the PIV images. It is instructive to first consider the flux of spanwise vorticity ($u \cdot \omega_z$) across the width of the channel at $0.05L_s$

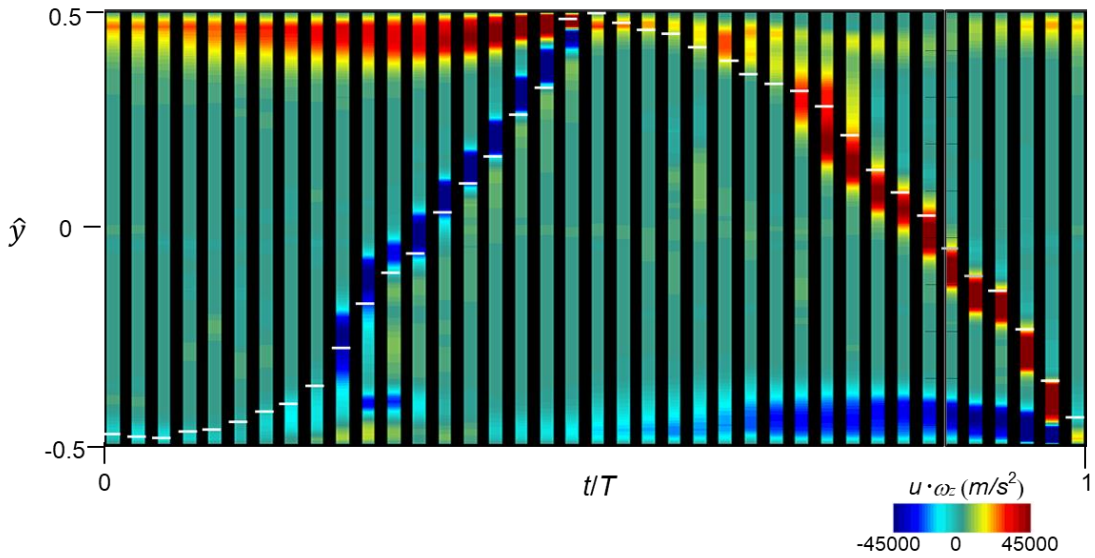

Figure 3.11. *Color raster strips of the spanwise vorticity flux, $u \cdot \omega_z$ across the width of the channel during the reed oscillation cycle. Each strip is plotted at sequential time steps as a reference point near the reed-tip passes through 39 positions across the width of the channel (the cross-stream position of the reed tip is indicated by white line segments).*

downstream of the reed tip. The cross stream variation of the flux is plotted using color raster plots (Figure 3.11) in unit strips that span the width of the channel [to the channel's left ($\hat{y}$ = 0.5) and right ($\hat{y}$ = -0.5) walls] at each of the 39 cross stream positions of the reed during the oscillation cycle. A white line segment marks the elevation of the reed-tip at each flux strip as the reed moves from the right to the left wall and back. At the beginning of the cycle ($\hat{y}$ = -0.45), the reed tip is near the right wall ($\hat{y}$ = -0.5) and as it moves towards the left wall ($\hat{y}$ = 0.5), a flux of CW vorticity is shed from the reed's left surface which moves leftwards with the reed. Concurrently, the CCW vorticity flux on the channel's left wall associated with the wall-boundary layer (just downstream of the reed) diffuses towards the channel center until the reed-tip touches the left wall. At this instant, the interactions between the CW and CCW vortical structures on the reed and the left-wall modulate the left-wall boundary layer. As the reed-tip moves towards the right wall, a CCW vorticity flux sheds from the right surface of the reed and interactions between this CCW vorticity and CW vorticity on the right wall modulates the boundary layer on the right wall near the end of the reed cycle. The modulation along the right wall appears to occur at the reed oscillation frequency: it is suppressed during the first half of the reed cycle ($t/T < 0.5$), increases during the second half ($t/T > 0.5$) , and is suppressed again when the reed-tip touches the right wall. As shown in Figure 3.16a, the shedding of CW and CCW vorticity from the left and right reed surfaces each cycle lead to the dominant peaks at twice the reed-frequency in velocity spectra acquired near the channel's centerline while the periodic modulation of the wall-boundary layer leads to a dominant peak at the reed oscillation frequency in spectra acquired near the channel wall (Figure 3.16b).

Figure 3.12 shows 18 color raster plots of position-averaged spanwise vorticity concentrations ω_z superposed with velocity vectors over and downstream of the reed (cf. Figure 3.9 and Figure 3.11) at *Re* = 7,200 (the reed centerline is colored in red). *It should be noted that a portion of the flow field on the right of the reed was in the reed's shadow where the velocity data could not be obtained and has been shown in gray in Figure 3.12. Even though the reed's motion is slightly asymmetric (cf. Figure 3.9), the vorticity fluxes shed from the reed's right and left surfaces are antisymmetric (as evident in Figure 3.11) indicating that the flow on the right of the reed (in the shadowed region) evolves nearly identical to the flow on its left*. Each image is characterized by the cross-stream distance ($-0.5 < \hat{y}_{tip} < 0.5$) of the reed-tip to the channel's center ($\hat{y} = 0$). The sequence covers a full cycle of the reed motion in the channel; the cycle begins when the tip is near the channel's right wall ($\hat{y} = -0.5$), Figures 3.12-a.1 ($\hat{y}_{tip} = -0.42$) to c.2 ($\hat{y}_{tip} = 0.45$) show the reed motion from the right wall towards the left wall ($\hat{y} = 0.5$)and Figures 3.12-d.2 ($\hat{y}_{tip} = 0.37$) to f.3 ($\hat{y}_{tip} = -0.45$) show the reed motion from left towards the right wall. The reed's shape and motion clearly affect the flow on both of its sides. In Figure 3.12-a.1, the concave reed shape produces an adverse pressure gradient along the reed's left surface leading to formation of CW surface vorticity which merges with CW vorticity on the channel's right wall causing the shedding of CW vortex near the right wall as the reed moves leftwards (Figure 3.12-b.1). As the reed-tip reaches the channel center (Figure 3.12-e.1, $\hat{y}_{tip} = -0.05$), the reed shape changes such that the vorticity concentrations accumulate at the tip (while diminishing near the root) and are shed downstream. As the reed-tip approaches the left-wall (Figure 3.12-b.2, $\hat{y}_{tip} = 0.35$), the reed constricts the flow between its left surface and the left wall suppressing the vorticity along both surfaces (due to

favorable pressure gradients). The constriction causes a jet-like flow near the reed-tip leading to full detachment (from the reed) and downstream advection (past the streamwise

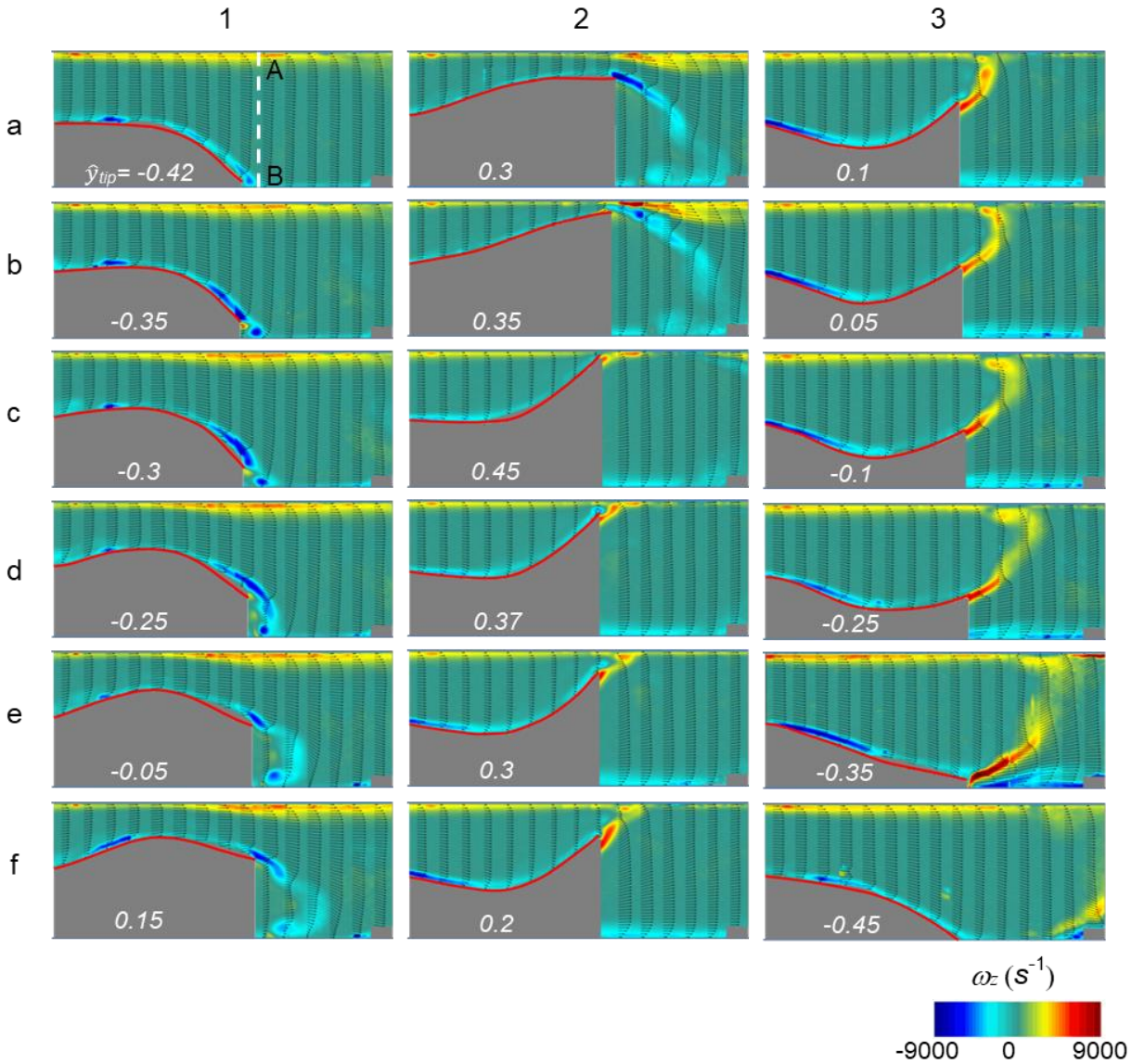

Figure 3.12. *Color raster plots showing distributions of position-averaged spanwise vorticity concentrations superposed with cross-stream velocity vectors in the cross-stream x-y plane z = 0 left of the surface of the reed in Figure 3.9 and in its near wake. The trace of the reed's centerline is shown for reference (the velocity field under the reed which is not illuminated by the PIV laser sheet is marked in gray). These images are locked to 39 equally-spaced positions of the reed reference point y_{ref} (cf. Figure 3.9) near the reed tip ($\hat{y}_{tip}$ marked at the bottom of each image). The spanwise vorticity flux in Figure 3.11 is extracted at AB and shown for reference.*

edge of the image) of the CW vorticity concentrations that nearly span the channel width. When the reed is in contact with left wall (Figure3.12-c.2, $\hat{y}$ = 0.45), the flow between the reed's left surface and the channel's left wall is blocked and the reed sheds CCW vorticity concentrations from its right surface. As a result of the blocked flow above the left surface of the reed, the reed bends towards its right surface upstream of its tip and begins to move towards the right wall of the channel (Figure 3.12-d.2, $\hat{y}$ = 0.37). As the reed continues its sweeping motion towards the right wall, the layer of CCW vorticity begins to roll up and interact with the CCW vorticity layer on the channels' left wall**.** This interaction severs the wall vorticity layer **(**e.g., Figure 3.12-e.2, $\hat{y}$ = 0.3**)** resulting in shedding of a CCW vortex (similar to CW vortex observed in Figure 3.12-b.1). As the reed detaches from the left wall (Figure 3.12-e.2), the reed sheds concentrations of CCW and CW vorticity near its tip from its right and left surfaces respectively. However, while the left reed surface experiences favorable pressure gradient (whose magnitude increases as the reed curvature increases along the reed length), the right surface experiences adverse pressure gradient leading to strengthening of CCW vorticity on the right surface and suppression of CW vorticity on the left surface. Figures 3.12-d.2 to e.3 show the accumulation and shedding along the right reed surface of this CCW vorticity concentration during the motion of the reed between the channel's left and right walls before it is advected downstream past the edge of the image (Figure 3.12-f.3) (Similar to the evolution of the CW vorticity concentrations between Figures 3.12-a.1 to c.2).

The dynamics and influence of the vortical structures shed from the reed surfaces on the channel flow are studied through 39 position-averaged (cf. Figure 3.9) flow-fields downstream of the reed ($3.1 < \hat{x} < 9.7$, $\hat{x}_{tip} = 3$) at the cross-stream (x-y) plane, z = 0. These

data were acquired using five, partially overlapping fields of view (downstream of reed) across the width of the channel, each $1.5W$ long with streamwise overlap of 16%. Selected color raster plots of position-averaged spanwise vorticity along with the reed centerlines are shown which illustrate the advection and diffusion of vorticity concentrations downstream of the reed as it moves from the channel's right to the left wall when its tip is at $\hat{y}_{tip}$ = - 0.45, - 0.25, -0.05. 0.3, and 0.45 (Figures 3.13a-e, respectively). It should be noted that the streamwise locations of the root and tip of a straight reed ($\hat{x}$ = 1.2 and 3) are

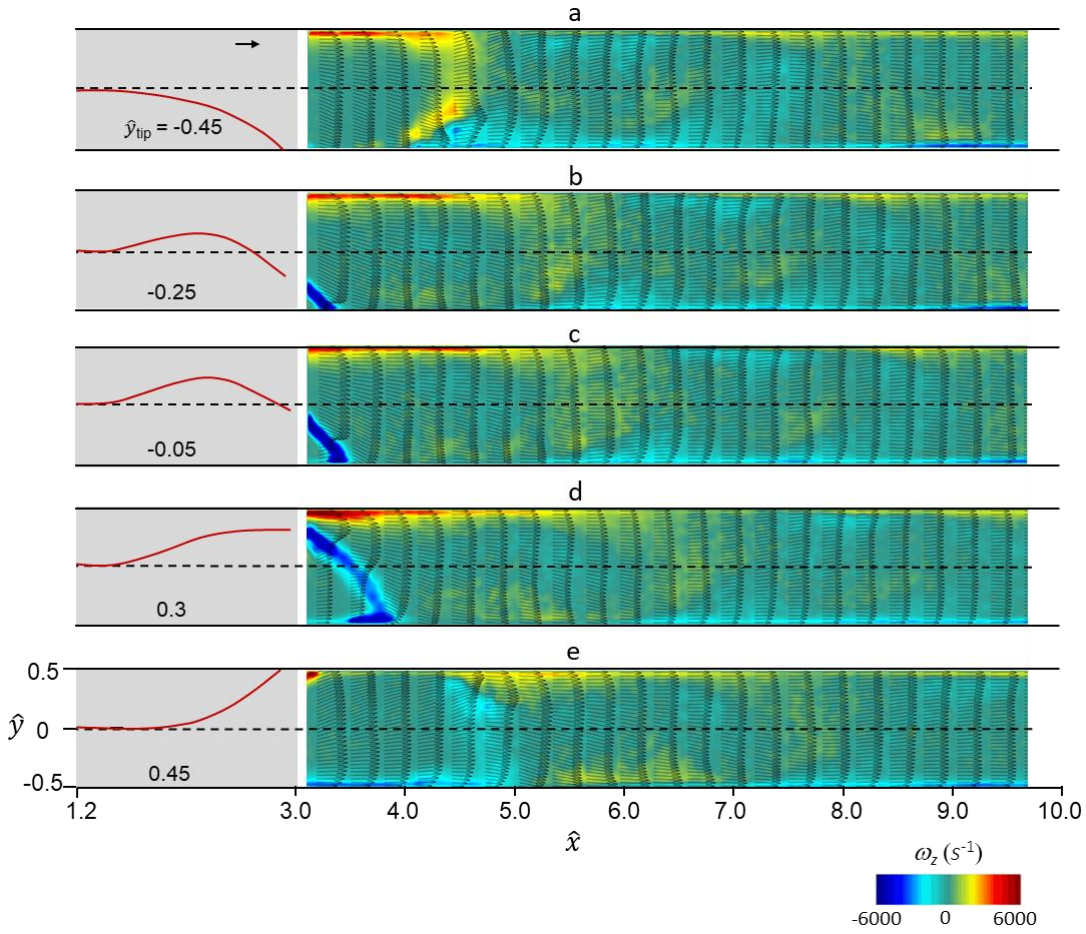

Figure 3.13. *Color raster plots of the position-averaged spanwise vorticity, ω_z in the x-y plane (z = 0) downstream of the reed (3.1 < $\hat{x}$ < 9.7) as the reed (cf. Figure 3.12) moves from the right to left wall (a-e). The* ***reed centerlines*** *and its tip location $\hat{y}_{tip}$ are shown for reference. Velocity vector of magnitude 5m/s is shown for reference in (a).*

shown for reference and the scale of the colorbar (as compared to Figure 3.12) has been reduced to elucidate the vortical structures downstream of the reed. The channel flow downstream of the reed shows the time-evolution of vortical structures shed from the reed-tip. When the reed is at the right wall (Figures 3.13a, cf. Figure 3.12-f.3), a CCW vorticity concentration (spanning the channel width) can be observed for $4 < \hat{x} < 4.7$ which was shed from the right reed surface during its motion from the left to the right wall (cf. Figures 3.12-d.2 to f.3). This vorticity concentration creates a velocity profile near the right wall ($4.3 < \hat{x} < 4.4$) which resembles a wall jet and increases the momentum near the wall. Further downstream, $8.6 < \hat{x} < 9.7$, the jet created during the prior reed oscillation cycle (at similar tip-position) can be observed near the right wall albeit the increase in momentum near the wall is smaller ostensibly due to diffusion. As the reed moves from the right to the left wall, (Figure 3.13b-e), a CW vorticity concentration is shed from the reed's left-surface and a wall-jet can be observed near the channel's left-wall (Figure 3.13e).

The effect of the advected vortical structures on the flow downstream of the reed is also characterized using the kinetic energy of the velocity fluctuations. Following the methodology adopted by Hussain et al. (1972), two approaches to calculating the fluctuating kinetic energy are considered: a) position-averaged $k_{ci}(x, y, t_{ref})$ where t_{ref} is the timing (during the cycle) corresponding to each position of the reed-reference, y_{ref} and b) time-averaged $k_f(x, y)$ where

$$k_{ci}(x, y, t_{ref}) = 1/N_{ci} \cdot \left(\sum_{N_{ci}} (u_{ci} - \{u_{ci}\})^2 + (v_{ci} - \{v_{ci}\})^2 \right) \quad 1.1$$

$$k_f(x, y) = 1/N \cdot \left(\sum_{N} (u - \bar{u})^2 + (v - \bar{v})^2 \right) \quad 1.2$$

a total of N_{ci} ensembles of the streamwise and cross stream velocity components fields u_{ci} and v_{ci} (locked to each of the 39 reed positions) are averaged to yield the position-averaged fields $\{u_{ci}\}(x, y, t_{ref})$ and $\{v\}(x, y, t_{ref})$ and the time-averaged fields $\bar{u}$ and $\bar{v}$.

Figure 3.14 shows the distributions of fractional position-averaged fluctuation kinetic energy, $\hat{k}_{ci} = k_{ci} / \sum_1^{39} k_{ci}$ downstream of the reed (in cross stream plane $z = 0$) for the tip positions and the streamwise domain of Figure 3.13 ($\sum_1^{39} k_{ci}$ is the sum of the position-averaged fluctuation kinetic energies). A comparison between these data and the

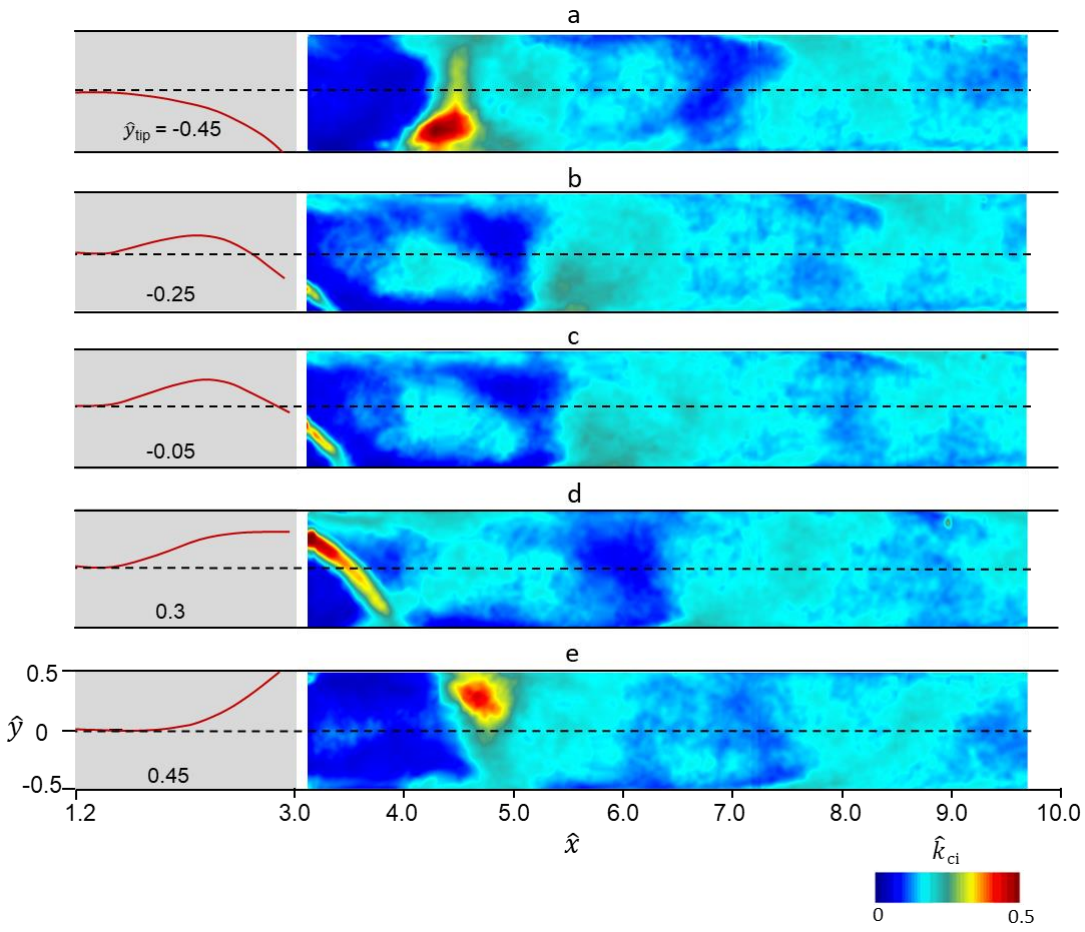

Figure 3.14. *Color raster plots of the position-averaged fractional fluctuation kinetic energy , $\hat{k}_{ci}$ in the $\hat{x} - \hat{y}$ plane ($z = 0$) downstream of the reed ($3.1 < \hat{x} < 9.7$) as the reed (cf. Figure 3.13) moves from the channel's right to left wall (a-e). The* ***reed centerlines*** *and tip-locations $\hat{y}_{tip}$ are shown for reference.*

corresponding position locked vorticity fields (cf. Figure 3.13) shows that in the proximity of the reed-tip, the velocity fluctuations are associated with the shed vortical structures but farther downstream ($\hat{x} > 5.5$) these fluctuations expand their domain of influence as the vortical concentrations spread.

The time-average energy of the velocity fluctuations in the absence and presence of the reed are characterized using the distributions of (normalized) fluctuating kinetic energy of the flow $\hat{k}_f(x,y) = k_f/U^2$ (cf. Equation 1.2; U is the average channel speed) as shown in Figure 3.15a and b. Even though the flow in the absence of the reed is transitional (Re = 7,200), the fluctuation kinetic energy (cf. Figure 3.14a) is low throughout the center domain of the channel [$\hat{k}_f\ (\hat{x}\ ,\ \hat{y} = 0) < 0.006U^2$] and is slightly elevated near the walls at the channel exit [$\hat{k}_f\ (\hat{x} = 9.7, \hat{y} = \pm 0.4) \approx 0.02U^2$]. In the presence of the reed, the fluctuating kinetic energy levels near the tip are up to 20 times higher than in the base flow.

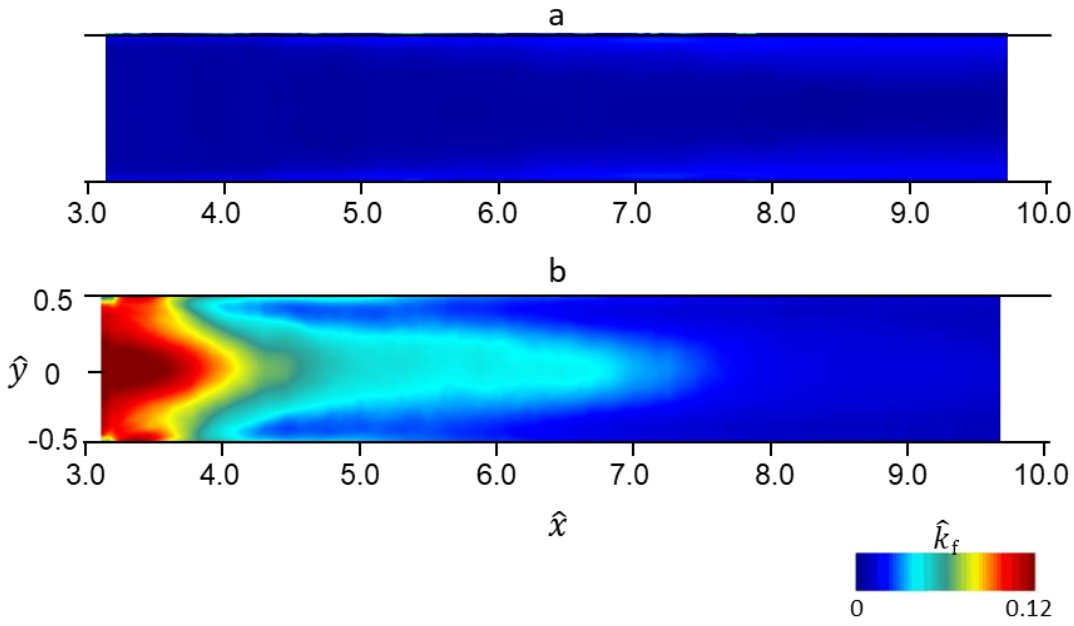

Figure 3.15*. Color raster plots of the fluctuating kinetic energy $\hat{k}_f$ (Re = 7,200) in the $\hat{x} - \hat{y}$ plane (3.1 < $\hat{x}$ < 9.7, z = 0) in the absence (a) and presence of the reed (b, cf. Figure 3.12).*

However, it is remarkable that these levels decrease monotonically with streamwise distance and are nearly the same as the levels of the base flow at the channel's exit. It is also noteworthy that the streamwise rate of decrease $\hat{k}_f$ is higher near the channel's side walls than at the center domain of the channel ostensibly owing to viscous effects. As shown by Wiltse et al.(1998), the small-scale dissipation increases significantly in a shear layer that is forced at high frequencies. It appears that similar mechanisms may also cause the observed reduction in $\hat{k}_f$ downstream of the reed which is oscillating at 50 Hz ($St_L = 0.42$). The streamwise evolution of the kinetic energy associated with the reed-induced flow fluctuations is discussed in more detail in connection with the reed oscillations in high aspect ratio channels in § 4.3 and 4.4.

The characteristic frequencies of the velocity fluctuations induced by the reed (Re = 7,200) are assessed from velocity power spectra obtained by Dr. P. Hidalgo (private communication). The spectra were measured using an uncalibrated hot wire sensor sampled at 20 KHz downstream of the reed at $\hat{x}$ = 3.08, 5.08 and 7.08 (0.08W, 2.08W, and 4.08W relative to the tip of the reed), and Figures 3.16a and b show measurements along the channel's centerline and 0.08W leftwards from its right wall or at $\hat{y}$ = -0.42,

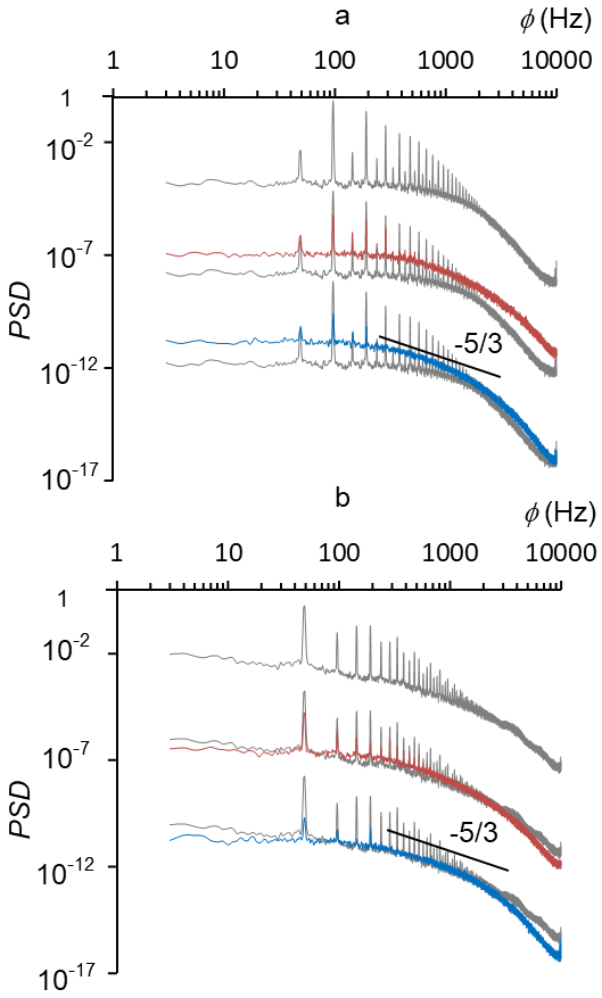

Figure 3.16. *Power spectra of the streamwise velocity measured along: the channel's centerline (a) and 0.08W leftwards from the right wall (b) at the streamwise stations:* $\hat{x}$ = *3.08*, ***5.08***, *and* ***7.08***. *The spectra at* $\hat{x}$ = ***5.08*** *and* ***7.08*** *are shifted down by four and eight decades, respectively and the spectrum at* $\hat{x}$ = *3.08 is repeated (in gray) for reference. The solid black line depicts -5/3 slope.*

respectively. In these plots, the spectra measured at $\hat{x}$ = 5.08 and 7.08 are displaced vertically downward by four and eight decades, respectively and the spectrum near the reed at $\hat{x}$ = 3.08 is repeated for reference (in gray).

The spectrum on the channel's centerline at $\hat{x}$ = 3.08 (Figure 3.16a) exhibits spectral peaks at the reed's oscillation frequency (50 Hz) and its higher harmonics suggesting the presence of multiple oscillation modes. The dominant spectral peak occurs at twice the reed oscillation frequency due to alternate shedding of CW and CCW vortical structures from its left and right surfaces during the motion towards each of the channel walls as shown in Figure 3.12. In contrast, the corresponding spectral measurements $0.08W$ left from the channel's right surface in Figure 3.16b shows a dominant spectral peak at the reed's oscillation frequency corresponding to the shedding of a CW vortex once per cycle due to the interaction between the reed and the wall (cf. Figure 3.12). The centerline spectral distributions at $\hat{x}$ = 3.08 and 7.08 (Figure 3.16a) demonstrate that as the vortical concentrations are advected downstream, the spectral peaks at the reed harmonics diminish but there is a broadband increase in spectral content of the embedding channel flow for all other frequencies below 5,000 *Hz***.** In fact, at $\hat{x}$ = 7.08 there is an increase of nearly a decade in the magnitude of the spectral content of the low-frequency end of the flow (below 50 Hz) but the spectral peaks decrease by up to three decades with no discernible peaks beyond the fourth harmonic of the reed-frequency. These observations suggest that the interaction of the reed with the flow leads to energy transfer to lower frequencies or *down* the energy cascade. The spectrum at $\hat{x}$ = 7.08 exhibits a brief inertial subrange (depicted by a line segment with a -5/3 slope) indicating the presence of energy cascade to small-scale motions in turbulent shear flows (Pope, 2000b). However, as noted in connection

with the streamwise decrease in fluctuating kinetic energy near the wall in Figure 3.15, the spectra near the channel wall at $\hat{x}$ = 3.08 and 7.08 (Figure 3.16b) demonstrate a streamwise decrease in spectral content by up to three decades at the reed harmonics and by one decade at the low end of the spectrum.

These data indicate that the time-periodic alternate shedding of vortical concentrations from the reed increases the energy of a broad range of small-scales in the channel's center cross stream domain and establishes an inertial sub-range which leads to increased mixing. In addition, these vortical structures disrupt the vorticity layers along the channel walls and thereby can help reduce the thickness of the thermal boundary layer. As shown in Chapter V, the combined effects of thinner thermal boundary layer and increased small-scale mixing of the channel can lead to significant enhancement in heat transfer in the presence of the reed.

3.4 Some Aspects of Reeds Flow Dynamics in High Aspect Ratio Channels

As discussed in Chapter I, the flow interactions of reeds with channel flows owe much of their importance to their application for heat transfer enhancement in higher aspect ratio channels that are characteristic of the fin channels in a broad range of heat exchangers (e.g., Bar-Cohen et al., 2002). Therefore, following the investigations of the interactions between the reed and the flow within a low aspect ratio channel where the wall effects are muted, the focus of the present investigation is shifted to reed-flow interactions in higher aspect ratio channels as a prelude to their effects on heat transfer enhancement. The bulk of these investigations focus on a channel of aspect ratio $H/W = 5$ ($W = 5$ mm) as described in Chapter II. This section provides a comparison of the reed dynamics and the ensuing small-scale vortical motions between high and low aspect ratio channels ($W = 25$ and 5 mm, $H = 25$ mm, $L = 250$ mm).

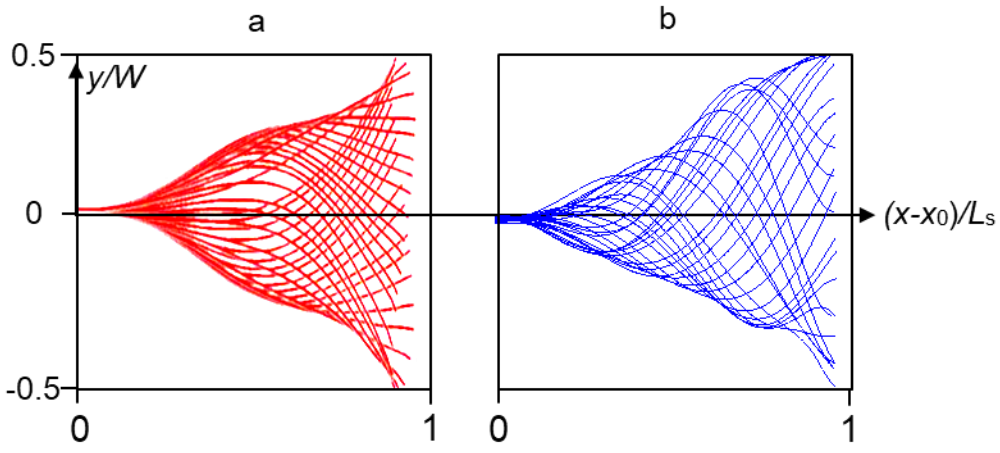

Figure 3.17. *Overlaid traces of centerlines of 38 μm thick reeds in 25 (a) and 5 mm (b) high channels in which the respective reed lengths are 45 and 50 mm and the air flow is set at each reed's critical speeds. Each set of data are scaled with the corresponding channel width and reed length. The streamwise location of the reed root is* x_o.

The dynamics of reed motion in the 25 and 5 mm channels are compared using two reeds having the same thickness (38.1 μm), respective lengths of 45 and 50 mm, inertia ratios M^* = 0.9 and 0.95, $U_{critical}$ = 4.8 and 5 m/s, and oscillation frequencies of f_{osc} = 50 and 65 Hz. It should be noted that even though the reed lengths are nearly identical, L_s/W = 1.8 and 10 in the low- and high-aspect ratio channels H/W = 1 and 5, respectively. The critical speeds and oscillation frequencies indicate that the proximity of the channel side walls has only a marginal effect on the reeds' motions. Multiple traces of the conditionally averaged reed centerlines (described in connection with Figure 3.9) were obtained for each of the reeds as shown in Figures 3.17a and b in which the centerlines' x and y coordinates are scaled with the corresponding reed lengths L_s and channel widths W, respectively. As expected, these data show that the reeds' cross stream motion scales with the channel width and, more importantly, that their interactions with the channel side walls occur only at the tip in the 25 mm channel and along the vicinity of the tip [$0.9 < (x\text{-}x_0)/L_s < 1$, x_o is the streamwise location of the root of the reed] in the 5 mm channel. A comparison between the traces of the reed centerlines in the two channels show that the reed motion in the 5 mm channel develops higher order modes compared to the 25 mm channel. The reeds modes appear to manifest as travelling waves along the reed's length with shorter wavelength in the 5 mm channel. The motion of these waves can be further inferred from x-t diagrams of distributions of the reeds' kinetic energy in Figure 3.19.

The reed motion in the 5 and 25 mm channels are decomposed using POD analysis of its centerline traces (cf. Figure 3.17) similar to the technique used by Han et al. (2003) into 38 orthogonal bending modes. The first two POD modes of each reed's motion capture

approximately 95% of the total modal energy in each channel. The reed centerline traces are then reconstructed based on the first and second modes only and these reconstructed traces are shown for the 5 (Figures 3.18-a.1 and a.2) and 25 mm channels (Figures 3.18-a.2 and b.2). *The reed envelopes were also constructed by a combination of modes I and II and these reconstructed envelopes nearly covered the full excursions of the reed motion as expected*. It should be noted that while the reed motion based on Mode 1 and Mode 2 in the 25 mm channel is nearly symmetric about $y = 0$, the reed traces based on Mode 1 in the 5 mm channel are asymmetric about the channel center ($y = 0$) and tilted towards the top wall. It is conjectured that this asymmetry (which is also evident in actual reed traces in Figure 3.17b) could be because the reed root is slightly offset from $y = 0$ (cf. Chapter II). When the channels walls are farther apart (Figure 3.18-a.1), the Mode 1 exhibits simple bending with single-sign slope and no inflection point during the entire oscillation cycle. However, Mode1 in the 5 mm channel is significantly different and exhibits reduced cross-

stream motions up to the node at $x/L_s = 0.5$, and some flattening near the channel wall for $x/L_s > 0.88$ (although the full traces in Figure 3.17 do not show this). These data indicate that the effective oscillating segment of the reed is shorter in the 5 mm channel compared to the 25 mm channel and that the oscillations are "hinged" around the node at $0.56L_s$ and ostensibly related to the marginally higher oscillation frequency. This observation is consistent with the frequency measurements in §4.5 which show that the reed frequency increases with decreasing reed length. It is remarkable that the features of Mode 2 of the reed that captures less than 20% of the modal energy are similar in the two channels (Figures 3.18-a.2 and b.2), indicating the proximity of the walls does not significantly change the dynamics of the reed motion and may be thought of as primarily shortening its oscillating segment.

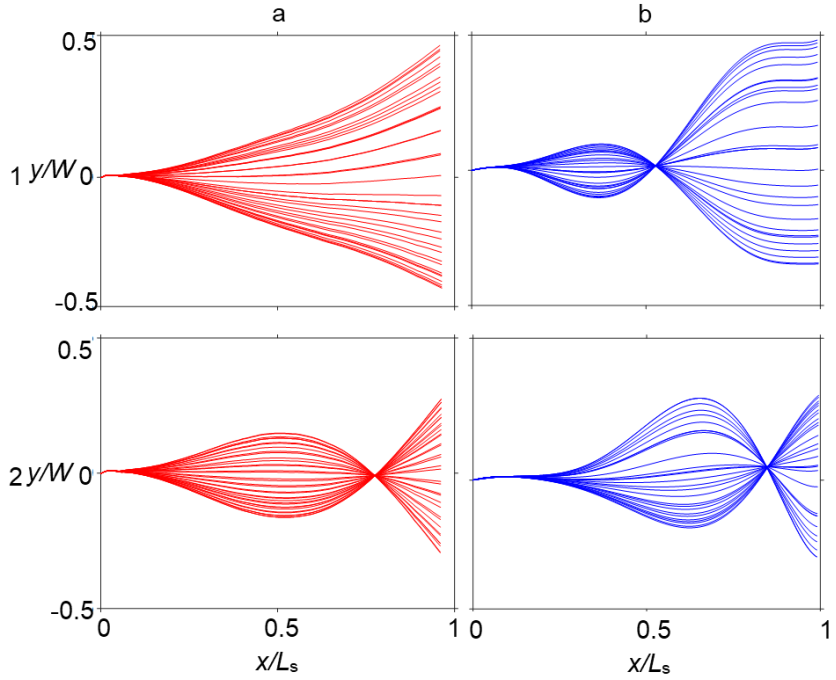

Figure 3.18. *Reconstructions of reed traces based on first and second POD modes of the reed's centerline motion in the 25 (a.1, a.2) and 5 mm (b1, b2) channels (cf. figure 3.17).*

The distribution of the kinetic energy along the reed $\delta(KE)(s, t)$ during the oscillation cycle is calculated through the motion of its centerline (cf. figure 3.17). These distributions are scaled with the increment of fluid pumping energy required in the presence of the reed during its oscillation period above the base flow: $\Delta E_{cycle} = (\Delta P_s \cdot \dot{m}/\rho_a) T_{cycle}$ where ΔP_s is the increment in pressure drop across the channel due to the reed and $\dot{m}$ is the mass flow rate through the channel ($\Delta E_{cycle} = 12 \cdot 10^{-4}$ and $2 \cdot 10^{-4}$ Joule in the 25 mm and 5 mm channels). The normalized kinetic energy distributions, $\delta(KE)^*(s, t) = \delta(KE)(s, t)/\Delta E_{cycle}$ for the reeds in 25 and 5 mm channels (cf. Figure 3.17) are shown in Figure 3.19a and b. The times when the tip of the reed first touches the left and right walls during its excursions are marked by dashed lines. These *s-t* distributions demonstrate the temporal propagation of travelling waves along the reed length during the cycle (as shown by the diagonal bands in Figures 3.19a and b). The wave propagation speeds or celerity $c = ds/dt$ are estimated from the slope of the bands and are 2.4 and 2.3

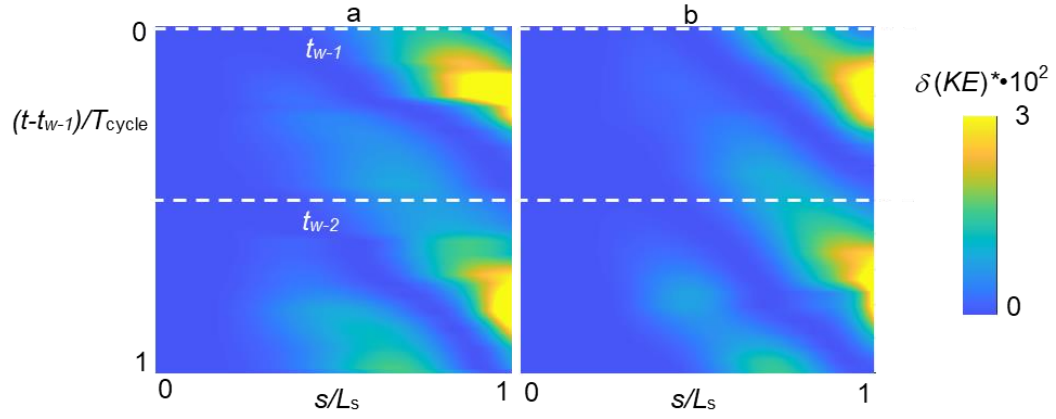

Figure 3.19. *Color raster plots of the variation of the reed's kinetic energy along its length s during the nominal oscillation period T_{cycle} in the 25 (a) and 5 (b) mm channels (cf. figure 3.17). The times t_{w-1} and t_{w-2} correspond to the times at which the reed tip first touches the channel's left (1) and right (2) walls.*

m/sec for the 25 and 5 mm channels, respectively. The reed kinetic energy intensifies as it propagates along each reed and reaches its maximum at the tip when the tip is at the center of the channel ($t - t_{w-1} = 0.25\ T_{cycle}$). As the tip approaches the right wall, it decelerates and loses it *KE* and the cycle resumes upstream of the tip until the tip reaches the center again ($t - t_{w-1} = 0.75\ T_{cycle}$). In the 5 mm channel, the *KE* propagates along a shorter domain along the reed with a similar speed (c = 2.3 m/s) to the 25 mm channel—consistent with the "hinge" effect that is shown in the POD modes (Figure 3.18b1). The total kinetic energy of the reed (integrated along its centerline), $KE_s^*(t) = \int_0^{L_s} \delta(KE_s)^*(s, t)d(s)$, was also calculated and its variation along the oscillation cycle is shown for the 25 mm and 5 mm channel in Figure 3.20. These data are plotted so that the cycle begins at the time that the tip touches the left wall (t_{w-1}) and it begins to move towards the right wall (t_{w-2}) similar to the discussions of Figures 3.19a and b. Even though the tip of the reed is at rest on the walls, the (total) normalized kinetic energy is nonzero since the bulk of the reed is

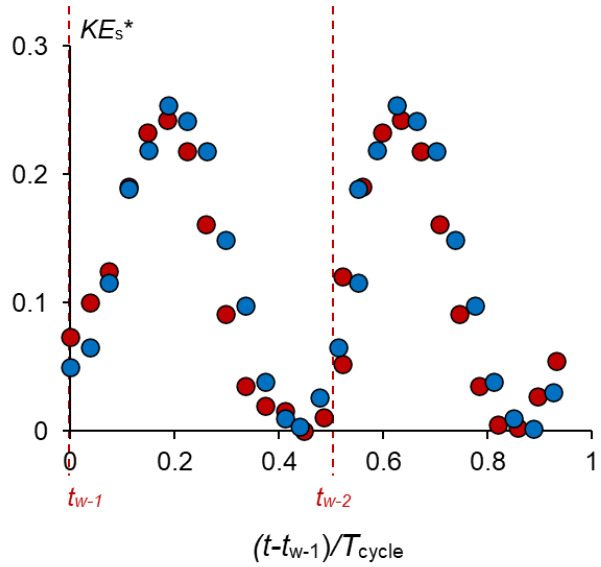

Figure 3.20. *Variation of the normalized kinetic energy during a nominal oscillation cycle of the reeds in the 25 mm (●) and 5 mm (●) channels. The cycle shown starts at the time at which the reed tip first touches the channel left wall (t_{w-1}) and the time it touches the right wall (t_{w-2}) is marked by a dashed line.*

still moving**.** Furthermore, the frequency of the reed's kinetic energy variations is twice its oscillation frequency as the reed-tip crosses the channel center twice per cycle when its *KE* peaks. It is remarkable that these normalized distributions for the two channels nearly collapse on top of each other which means that the integrated kinetic energy of the reed scales with the incremental pumping energy, ΔE_{cycle} of the channel flow. These data show that the reed kinetic energy at any instant in the cycle is up to six times smaller in the 5 mm channel which is not surprising since the reed amplitude is five times smaller and reed frequency only increases by 20%.

The influence of the reed on the small scale motions downstream of it tip which have been characterized for the high aspect ratio channel in § 4.3 and 4.4 indicate that its streamwise evolution can be characterized using a cross-stream integral measure: the (normalized) bulk mean fluctuation kinetic energy, $\hat{k}_m(x) = 1/U^3 \int_{-0.5}^{0.5} \bar{u} \bullet (\overline{u'^2} + \overline{v'^2}) d(\hat{y})$, where $\overline{u'^2}$ and $\overline{v'^2}$ are the variances of streamwise and cross- streamwise velocity fluctuations measured using PIV. The streamwise variation of $\hat{k}_m$ downstream of the tip is compared for the reeds in the 25 and 5 mm channels in Figure 3.21. These data indicate that $\hat{k}_m$ at the tip of the reeds is six times smaller in the 5 mm channel (commensurate with the lower reed kinetic energy, cf. Figure 3.20) and decreases in the streamwise direction albeit at significantly higher rates in the 25 mm channel such that $\hat{k}_m$ is identical in the two channels near the channel exit (which is at x-x_{tip} = 7W and 36W in the 25 and 5 mm channel). It is conjectured that since the turbulence production in the base flow is low (as evident by low levels of fluctuation

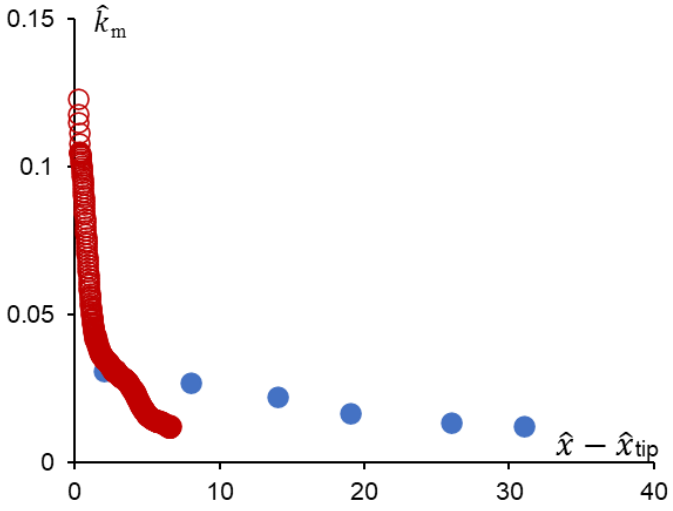

Figure 3.21. *Streamwise variation of the normalized bulk mean fluctuation kinetic energy* $\hat{k}_m$ *measured in the x-y plane z = 0 downstream of the reed tip* x_{tip} *in the 25* (○) *and 5* (●) *mm channels for the reeds discussed in connection with Figure 3.20.*

kinetic energy, cf. Figure 3.15b), the energy of the small scales (as measured by $\hat{k}_m$) decreases downstream by small-scale dissipation. The work of Wiltse et al. (1998) on high-frequency forcing of a square jet shear layer showed that the maximum small-scale dissipation occurs at the actuation frequency. It is therefore conjectured that the decrease in $\hat{k}_m$ downstream of the reed is associated with similar increased dissipation at the reed oscillation harmonics. The scale of this dissipation is estimated as $D_{vf} = \hat{k}_m^{3/2} / L_f$ (Sreenivasan, 1984) ($L_f = W$ is the length scale of the largest eddies) and it is up to three times higher in the 25 mm channel leading to precipitous decrease in fluctuation kinetic energy in the 25 mm channel. While it might be argued that lower levels of fluctuation kinetic energy in the 5 mm channel may lead to low heat transfer enhancement, it should be noted that *Re* is also lower in the 5 mm channel since *U* is nearly identical (*Re* = 7,200 and 2,000 in the 25 and 5 mm channels, respectively). As will be shown in chapter V, the reed induced heat transfer enhancement can be increased in the 5 mm channel by increasing *Re*.

CHAPTER IV

CHARACTERISTICS OF REED DRIVEN SMALL-SCALE MOTIONS IN HIGH ASPECT RATIO CHANNELS

Overview

This chapter focuses on characterization of reed driven small-scale motions in high aspect ratio channels by analyzing the streamwise and spanwise changes in the global flow field, and the distributions of the kinetic energy associated with the flow fluctuations in the presence and absence of reeds. The effect of reed parameters (including its thickness, length and span) and channel parameters (including flow Reynolds number and the location of the reed in the channel) on the small-scale motions are studied through time-averaged and phase-averaged PIV and hotwire in a $H/W = 5$ or $W = 5$ mm wide channel.

4.1 Introduction

Chapter III demonstrates the salient characteristics of the interactions between a self-oscillating reed and the channel flow in a low aspect ratio channel [$H/W \approx 1$, $L_s/W = O(1)$; H and W are the channel span and width and L_s is the reed length] and highlights the effects of the increase in the channel's aspect ratio, or the proximity of its side walls to the oscillating reed. The present chapter builds on the findings presented in Chapter III and expands the investigations of the effects of the interactions between the reed and the flow within channels whose widths are significantly shorter than the length of the reed [$L_s/W = O(2)$]. These investigations owe part of their importance to practical applications in the fin channels of air-cooled heat exchangers that are designed to yield high heat

transfer surface area (e.g., Bar-Cohen et al., 2002). In these channels, the heat transfer characteristics are measured by Nusselt number (*Nu)* and their efficiency depends on the channel's friction factor (*f*). Each of these parameters depends on multiple dimensionless ratios as listed in Equation 4.1 and 4.2 **(**excluding the roughness, ε/H and Prandtl number, *Pr***)**.

$$f = \Pi_1(L/W, H/W, Re, L_s/W, H_s/W, St_L\, x_0/W) \tag{4.1}$$

$$Nu = \Pi_2\,(L/W, H/W, Re, St_L, L_s/W, H_s/W, x_0/W) \tag{4.2}$$

In the current investigations, the effects of the reed on the channel flow were explored over a range of Reynold numbers and reed planform shapes (L_s/W, H_s/W) and thicknesses that varied their operating frequencies measured by the Strouhal number (St_L), and for a few reed locations (x_0/W).

Similar to the analysis described in Chapter III, the flow structure induced by the reed oscillations was characterized by acquiring PIV data measured locked to the motion of the reed, and the reed-induced changes in the global flow fields were characterized using time-averaged flow fields, while the flow's spectral characteristics were assessed using hot-wire anemometry. The effect of the reed on the channel flow is assessed from streamwise and spanwise changes in the velocity fields and concentrations of the spanwise vorticity and of the fluctuation kinetic energy.

4.2 Phase-Locked Measurements of the Reed-Induced Flow Field

The flow field downstream of the reed is investigated using PIV snapshots that are captured in conjunction with measurements of the cross stream position of the reed. The reed's position is characterized by the intersection of its surface centerline with the laser beam of a range finder that is normal to the channel's left ($\hat{y}$ = 0.5) and right ($\hat{y}$ = -0.5) walls (cf. Chapter II) and intersects the reed's centerline at $0.1L_s$ upstream of its trailing edge when the reed is at rest in the absence of cross flow (the position of the range finder beam relative to the tip varies somewhat during the oscillation cycle). The PIV images are acquired at 8.52 Hz during the cross stream motion of the reed and the acquisition frequency is selected to prevent aliasing with the motion (which is nominally at 65 Hz). The corresponding cross stream position of the reed's surface is recorded at the time that the PIV images are acquired and time series of the reed motion and of the PIV images are sampled simultaneously by the data acquisition system. The time series of the reed's

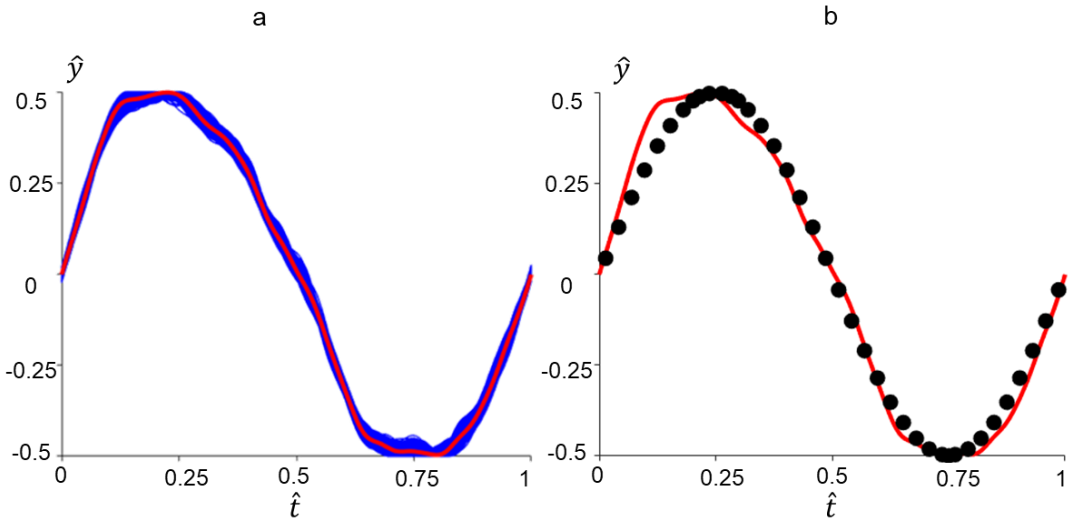

Figure 4.1 *a) Superimposed 3000* ***instantaneous cycles of the reed position*** *inferred from the range finder measurements along with the* ***ensemble-averaged cycle****, and b) the cross stream center* (●) *of each data bin based on a sine function that is fitted to the* ***ensemble-averaged cycle****.*

motion is organized in successive cycles that are ensemble-averaged (shown in Figure 4.1a), and the ensemble-averaged cycle is fitted to a sine function $0.5 \cdot \sin(2\pi\hat{t})$ where $\hat{t} = t/T_{cycle}$, T_{cycle} is the period of the time-averaged cycle. The PIV images are grouped in 38 "bins" that are characterized by isochronous ($\Delta\hat{t} = 1/38$) increments during the reed's motion across the channel width whose cross stream centers and timing within the cycle ($\hat{y}_{bin}$ and $\hat{t}_{bin}$) are marked in Figure 4.1b. The width of the individual bins varies during the oscillation cycle as $\Delta\hat{y} = \pi/38 \bullet \cos(2\pi\hat{t})$ and has minima near the top and bottom walls ($\hat{t} = 0.25$ and 0.75 respectively) and maxima near the channel center ($\hat{t} = 0$ and 0.5). The PIV images that are captured along with the reed's position are then sorted into these bins (cf. Chapter II). Note that owing to cross-stream asymmetry in the attachment of reed to its upstream post, the reed motions between the channel's center ($\hat{y} = 0$) and its left and right walls ($\hat{y} = 0.5$ and -0.5 respectively) are slightly different ($|\hat{y}_m| = 0.37$ and 0.32, respectively, where $\hat{y}_m = \int_0^{\hat{t}} \hat{y}\ (d\hat{t})$ is the time-averaged tip-elevation between the channel center to the walls). The flow fields of the sorted PIV images within each "bin" are averaged to obtain the phase (or bin) -averaged flow field while the reed is at that given position ($\hat{y}_{bin}$) within the channel. In what follows, each "bin" is referred to by the specific phase ($\alpha = 2\pi\hat{t}$) of its center cross-stream location ($\hat{y}_{bin}$) where α varies in equal increments of $2\pi/38$ within $\pi/38 \leq \alpha \leq 2\pi\text{-}\pi/38$. The average number of images within the bins (centered about each discretized phase) was 78, and the actual number of images varied from a maximum of 100 at $\alpha = \pi/2$ to a minimum of 60 at $\alpha = \pi/38$.

The phase-averaged flow fields at Re = 2,000 downstream of a reed for which L_s/W = 10, H_s/H = 0.9, and St_L=0.5 (f_{osc} = 65 Hz) and whose tip is located at $\hat{x}_{tip}$ = 16 are first analyzed using cross-stream distributions of phase-averaged (normalized) streamwise flux of spanwise vorticity ($u \bullet \omega_z W/U^2$) extracted at the channel's mid-span (z = 0) at $\hat{x}$ = 17.7. These distributions are obtained for each of the 38 isochronous bin phases ($\Delta\alpha = 2\pi/38$) through the average reed cycle ($\pi/38 \leq \alpha \leq 2\pi - \pi/38$) and are shown as color raster strips in Figure 4.2. Since these distributions are obtained 1.7W *downstream* of the reed-tip, there is a phase delay between the cross stream position of the reed tip and the distributions of the vorticity flux. The phase delay is estimated from the convection time 1.7W / U of the vorticity between the tip of the reed and the measurement station and the

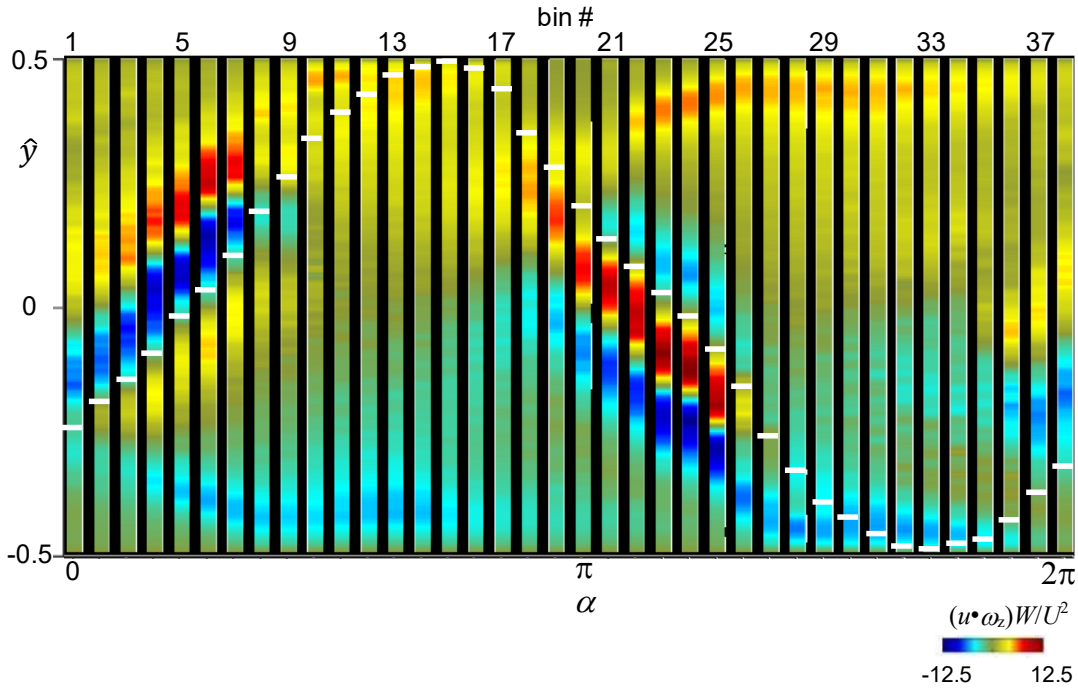

Figure 4.2. *Color raster strips of the spanwise vorticity flux across the width of the channel during the reed oscillation cycle. The strips are plotted at sequential, equal phase steps as the reed tip passes through the 38 increments across the width of the channel (the cross stream positions of the reed tip offset for the convection time delay are indicated by white line segments across each strip). The bin numbers are marked for reference along the top of the figure.*

position of the reed tip offset by the phase delay and corresponding to each bin in Figure 4.1b is marked using a white line segment in Figure 4.2. The cycle begins when the (offset) reed tip is on the right of the channel's center ($\hat{y}_{tip}$ = -0.25) and moving leftwards towards the channel's left wall ($\hat{y}$ = 0.5) (bins 1 to 14), followed by motion from the left to right walls ($\hat{y}$ = -0.5) (bins 15 to 33) and then from the right wall towards the channel center (bins 34 to 38). These data indicate that the bin-averaging may not be as effective when the reed tip is in the vicinity of the left and right channel walls for $|\hat{y}_{tip}| > 0.3$ where the phase-based variations in the flow appear to be washed out ostensibly owing to insufficient time resolution. When the reed-tip is on the right of the channel center ($\hat{y}_{tip}$ = -0.25, bin 1), the boundary layers near the channel walls exhibit reduced vorticity fluxes, ostensibly due to interactions between reed's undulations and the flow on each of its sides upstream of its tip. A thin band of flux of CW (blue) vorticity to the left of the reed's left surface marks this surface boundary layer while the vorticity flux on its right surface appears to be diminished ostensibly as a result of changes in the pressure gradient along the reed that are coupled with its undulating curvature (as also evident for the low aspect ratio 25 mm channel in Figures 3.12b to f). As the reed moves towards the left wall (bins 3 to 7), a CCW (red) vorticity band appears to the left of the reed's CW vorticity band. It is conjectured that this band is associated with interactions of the reed's left surface with the left wall upstream of the tip and local separation of the wall (CCW) vorticity layer. Simultaneously, a CCW band is observed on the right surface of the reed in bins 3 - 7 which is indicative of the evolution of the boundary layer on the reed's right surface due to changes in reed curvature during its motion towards left wall. As the reed approaches the left wall (bins 8 to 14), the vorticity flux on the left wall increases owing to the contraction

of the channel flow by the reed and the increased flow momentum near the left wall. It is also apparent that as the reed moves towards the left wall there is an intermittent concentration of CW vorticity near the right wall as a result of earlier interaction with the reed's tip. This concentration indicates time-periodic modulation that can contribute significantly to cross-stream mixing and enhancement of heat transfer. As the reed approaches the left wall, the appearance of bands of CCW and CW vorticity fluxes to the right of its right surface (bins 19 to 25) are antisymmetric to the appearance of the corresponding bands to the left of its left surface during its leftwards motion (bins 1 to 7). Owing to the interactions between the reed surface and the flow at and upstream of its tip, the wall-bound vorticity flux is modulated at *twice the frequency of the reed*. This is remarkable since in the 25 mm channel, the wall vorticity is modulated at the frequency of the reed (cf. Figure 3.11) due to interactions of reed-bound and wall-bound vorticity fluxes at its tip and there are no reed-wall interactions upstream of the tip. The interactions of reed surfaces and flow upstream of tip in the 5 mm channel evidently lead to the formation of additional bands of fluxes of CW and CCW vorticity close to the tip. Such interactions are clearly absent in the lower aspect ratio channel in which $L_s/W = 1.8$ compared to $L_s/W = 10$ in the high aspect ratio channel.

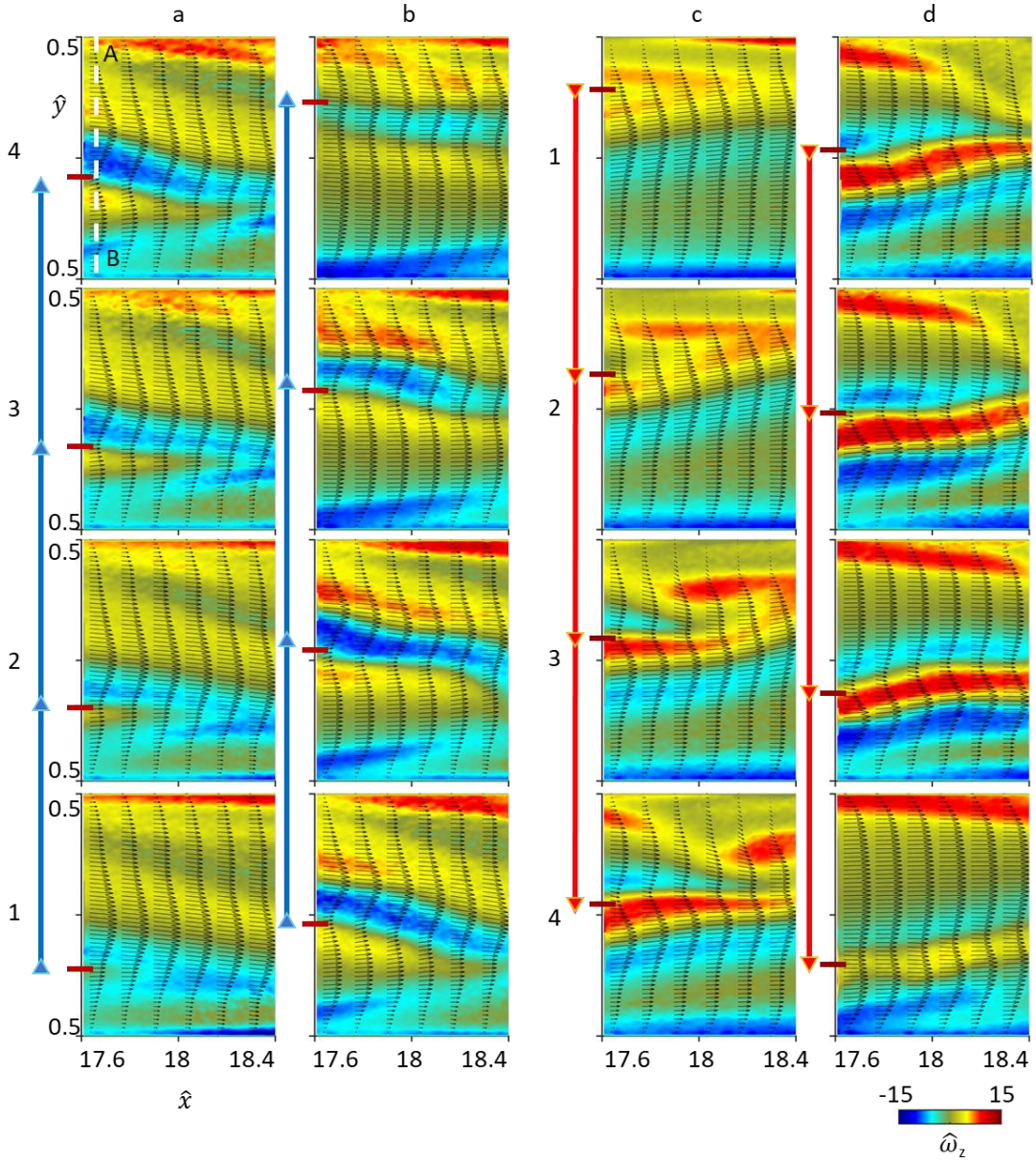

Figure 4.3 *Color raster plots of distributions of bin-averaged spanwise vorticity, $\hat{\omega}_z$ (superposed with the velocity vectors) downstream of the reed tip, ($\hat{x}_{tip} = 16$) for* $17.6 < \hat{x} < 18.4$ *at the channel's mid-span z = 0. Selected cross-stream locations of the tip* $-0.3 < \hat{y}_{tip} < 0.3$ *are shown when the tip is moving towards channel's left wall ($\hat{y} = 0.5$) from bins 1 to 8 (a1 to b4, $\pi/38 < \alpha < 15\pi/38$, cf. Figure 4.2) and towards right wall ($\hat{y} = -0.5$) from bins 19 to 26 (c.1 to d.4, $37\pi/38 < \alpha < 51\pi/38$). The location of the reed tip (corrected for the convection delay of the flow) is shown upstream of each image. The dashed line segment AB is the location where the vorticity fluxes in Figure 4.2 are extracted.*

The "phase-averaged" vorticity fields during the motion of the reed (cf. Figure 4.2) at *Re* = 2,000 are calculated across the channel width within the field of view $-0.5 < \hat{y} < 0.5$ and $17.6 < \hat{x} < 18.4$ at the channel's mid-span $z = 0$ (six such streamwise fields were measured downstream of the reed such that their streamwise centers, $\hat{x}_c$ are equally spaced between $\hat{x}_c = 18$ and 48). Cross-stream bin-averaged concentrations of the spanwise vorticity distributions are shown in Figure 4.3. These data were selected to elucidate the interactions of the reed with the flow about the center of the channel within the range $-0.3 < \hat{y}_{tip} < 0.3$ where the bin-averaging is more robust. These data are organized in two groups of left and right column pairs (Figures 4.3-a.1 through b.4 and 4.22-c.1 through d.4) that each shows a sequence of the reed motion leftwards (from channel's right to left wall) and rightwards, respectively (bins 1 – 8 and 19 - 26 in Figure 4.2). As discussed in connection with Figure 4.2 the corresponding positions of the reed tip accounting for the convection delay are shown upstream of each image. Clearly, the reed partitions the flow within the channel into two streams (left and right of the reed) and the interactions of the flow within these partitions with the reed's undulating surface are reflected in the phase-averaged fields downstream of the tip. When the reed-tip is moving leftwards and away from the right wall ($\hat{y}_{tip} = -0.25$, Figure 4.3-a.1) the flow speed within the right channel partition is low due to reed blockage and there is a concentration of CW (blue) vorticity in midstream that probably peeled off the right wall ($\hat{y} = -0.5$), the flow in the left partition expands along the reed's concave surface which leads to the formation of a CW vorticity layer on the reed's left surface and shows some velocity deficit in its near wake (Figures 4.3-a.2 through a.4, $-0.2 < \hat{y}_{tip} < -0.1$). The CW vorticity layers from the right wall and the reed's left surface are advected across the streamwise extent of the

window. At the same time, the CCW (red) vorticity layer on the right surface of the reed intensifies as the flow speeds up and is inserted between the two CW vorticity layers. As the reed tip continues to move leftwards, the CW vorticity layer from the right wall moves towards the channel's centerline (Figure 4.3-b.1 through b.3), and similar internal separation that occurs within the left partition leads to the formation of a layer of CCW vorticity layer to the left of the CW vorticity on reed's left surface that is advected into the left stream. Meanwhile, the CCW vorticity on the left surface exhibits clear upstream modulation while the CW vorticity along the right layer intensifies and recovers from the earlier separation.

The evolution and advection of the vorticity concentrations during the rightward motion of the reed (columns c and d in Figure 4.3) are similar to and antisymmetric with respect to the corresponding opposite concentrations during the leftward motion. As an example, a comparison between Figures 4.3-a.1 and c.1 shows the antisymmetry in vorticity concentrations about the channel's center.

To assess the variations in the flow that originate at different positions along the reed's span, phase-averaged vorticity fields (similar to Figure 4.2) are computed for five equally spaced PIV stations between the channel's mid-span ($\hat{z}$ = 0) and top wall ($\hat{z}$ = 2.5) $\hat{z}$ = 0, 0.5, 1, 1.5 and 2 (Figures 4.4-a.1, a.2, a.3, b.1 and b.2 respectively) at $\hat{x}_c$ = 18 (as shown in §4.3, the time-average flow fields are symmetric about midspan, $\hat{z}$ = 0). The vorticity flux distributions in the planes $\hat{z}$ = 0 and 0.5 (Figure 4.4-a.1 and a.2) are similar although the CW and CCW vorticity bands to the left of the reed surfaces at $\alpha = \pi/38$ migrate slightly towards the right wall at $\hat{z}$=0.5 ostensibly due to spanwise bending of the

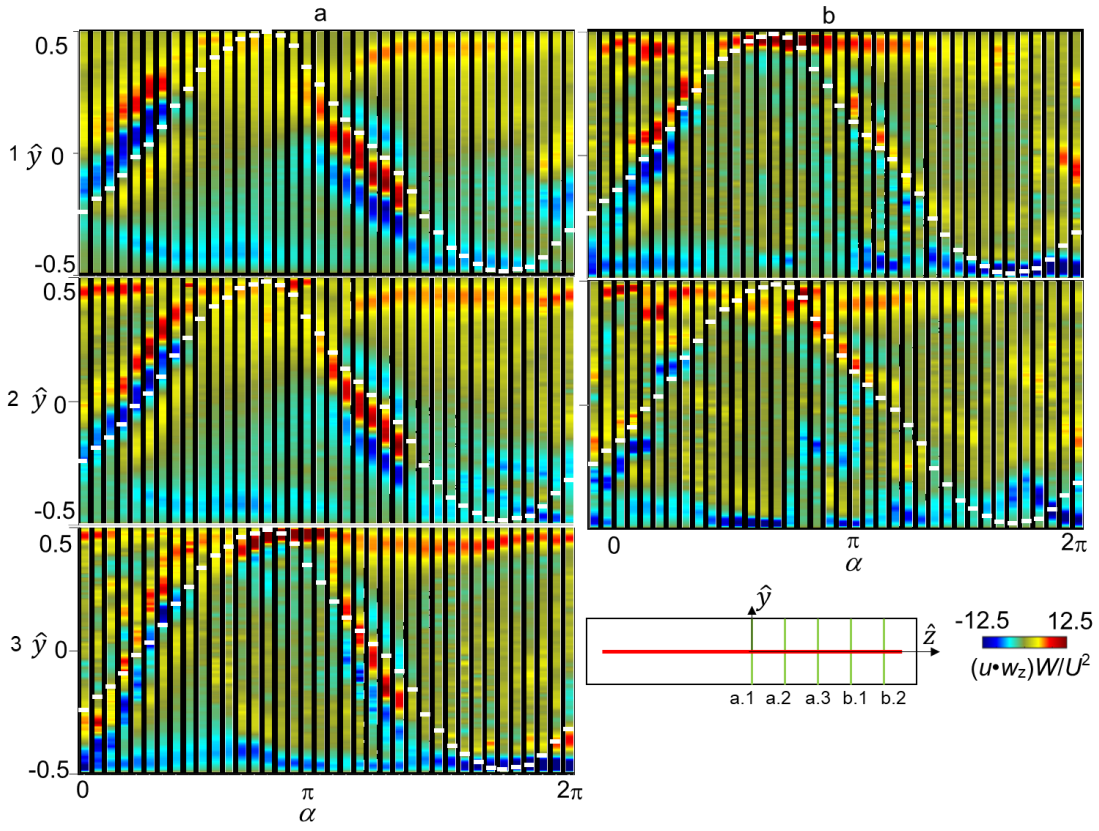

Figure 4.4*. Similar to Figure 4.2, spanwise variations of cross-stream, phase-averaged distributions of phase-averaged vorticity flux during the reed oscillation cycle (the cross-stream position of the reed tip offset for the advection time delay is indicated by white line segments) at the spanwise locations $\hat{z}$ = 0 (a.1), 0.5 (a.2), 1 (a.3), 1.5 (b.1), 2 (b.2) (as shown schematically below 4.4-b.2).*

reed. These bands of vorticity flux deflect even further towards the right wall at $\hat{z}$ = 1.5 and appear to be fragmented close to the channel's top wall. These data indicate that the vortical structures associated with these bands are modulated intermittently during the reed motion due to interactions with the top wall. At $\hat{z}$ = 2, the CW and CCW vorticity concentrations across the channel width (not locked to reed motion) are ostensibly due to interactions between the reed and the corner flows (bound by the left, right and top walls).

The variations in the cross-stream distributions of vorticity fluxes are also computed farther downstream of the reed at the channel's mid span and compared with the corresponding time-averaged data in the presence and absence of the reed to assess the effect of reed on the time-averaged flow in the channel. Measurements similar to Figure 4.2 taken at $\hat{x}$ = 23.7, 35.7 and 47.7 are shown in Figures 4.5-a.1, b.1 and c.1 respectively. The phase variations of vorticity flux distribution in Figures 4.5-a.1, b.1 and c.1 exhibit time-periodic modulations of the vorticity layers along the left and right walls in which the degree of modulation diminishes with streamwise distance and is absent at $\hat{x}$ = 47.7. Remarkably, the bulk flow near the center of the channel shows little phase-dependent variations. The absence of phase dependent variations indicates that effects of the reed are either no longer locked to its cross-stream motion, or that these effects decay by $\hat{x}$ = 35.7. It is noted that the hot-wire velocity spectra near the channel exit (§4.4) exhibit a wide range of spectral components at the reed frequency and its higher harmonics indicating that the effects of the reed are sustained far beyond the phase coherence relative to its motion (the reed's streamwise domain of influence is also discussed in some detail in §4.3). The corresponding time-average distributions of vorticity flux in the absence and presence of the reed in columns 2 and 3 respectively of Figure 4.5 show clear concentrations of

spanwise vorticity in the wall layers that intensify with streamwise distance while the corresponding time-averaged data in the absence of the reed show that the vorticity flux is distributed and more diffused across the channel without clear streamwise intensification. These data indicate that in the presence of the reed the momentum flux near the side walls increases and the peak vorticity fluxes (at $\hat{y} = \pm 0.45$) are about 35% higher in the presence of the reed. The higher momentum and vorticity flux near the wall in the presence of the reed are discussed further in connection with the kinetic energy budget of the time averaged flow in § 4.3.

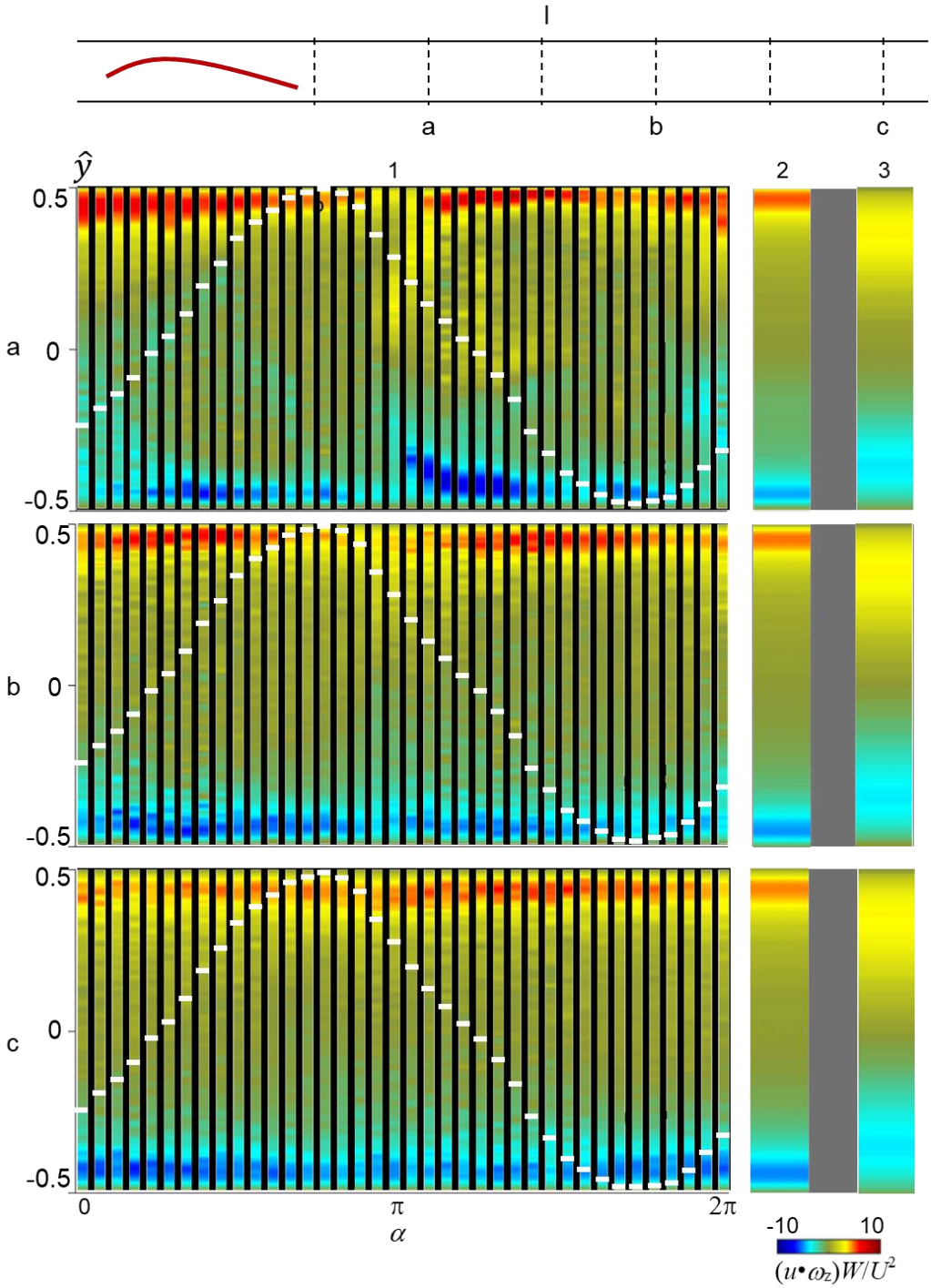

Figure 4.5. *Streamwise variations (Re = 2,000) of phase-averaged cross-stream distributions of vorticity flux as in Figure 4.2 (column 1) and the corresponding time-averaged vorticity flux in the presence* (*column 2*) *and absence* (*column 3*) *of the reed at* $\hat{x}$ *= 23.7* (*a*), *35.7* (*b*), and *47.7* (*c*) *shown schematically above Figure 4.5a*.

4.3 The Time-Averaged Reed-Flow Interactions (*Re* = 2,000)

Following the analysis of the oscillation-locked interactions between the reed and the flow in the high aspect ratio channel, attention is shifted to characterization of the time-averaged effects of the reed on the flow. For a given mass flow rate, the reed motion and the associated channel losses are driven by an increase in pressure (over the base flow) throughout the channel length. The streamwise variations of the static gauge pressure coefficient along the channel $C_p(\hat{x}) = p(\hat{x})/(0.5 \cdot \rho \cdot U^2)$ [$p(\hat{x})$ is the gauge static pressure] in the absence and presence of reed at *Re* = 2,000 are shown in Figure 4.6 ($\hat{x}_{tip}$ is the position of the tip of the reed at rest). In the absence of the reed, the channel pressure gradient downstream of the reed, $dC_p/d\hat{x} \approx -0.025$ is nearly constant in the domain $17.2 < \hat{x} < 46.2$ indicating a nearly fully-developed flow. It is noted that while the current measurements do not include the pressure variations associated with the channel entrance (e.g., Sparrow et al., 1967), in the domain that would be covered by the reed ($3.2 < \hat{x} < 17.2$), $dC_p/d\hat{x} = -0.043$. In the presence of reed, the pressure levels along the channel are higher

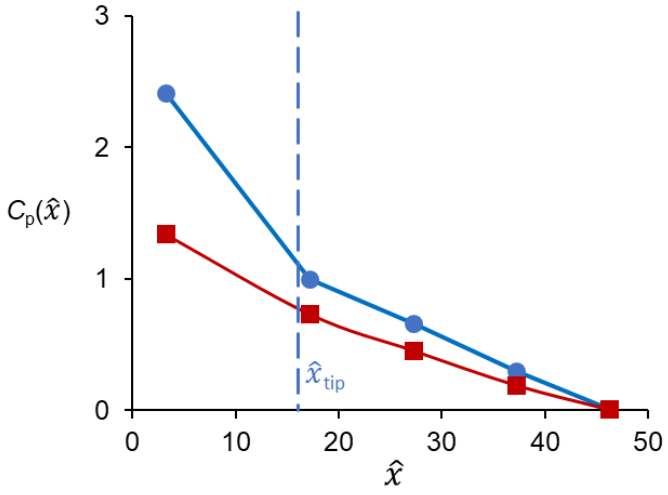

Figure 4.6 *Streamwise variation of the channel static gauge pressure coefficient, $C_p(\hat{x})$ in the absence (■) and presence of the reed (●) at Re = 2,000.*

than in the base-flow and the streamwise pressure gradient is significantly higher along the reed ($dC_p/d\hat{x}$ = - 0.1 for 3.2 < $\hat{x}$ < 17.2) than downstream of the reed ($dC_p/d\hat{x}$= - 0.035 for 17.2 < $\hat{x}$ < 46.2). While the higher pressure drop along the reed is associated with the energy required to sustain the the reed motion, the marginally higher pressure drop downstream of the reed compared to the base flow is associated with the advection of the vortical structures which are produced near its tip (cf. § 4.2).

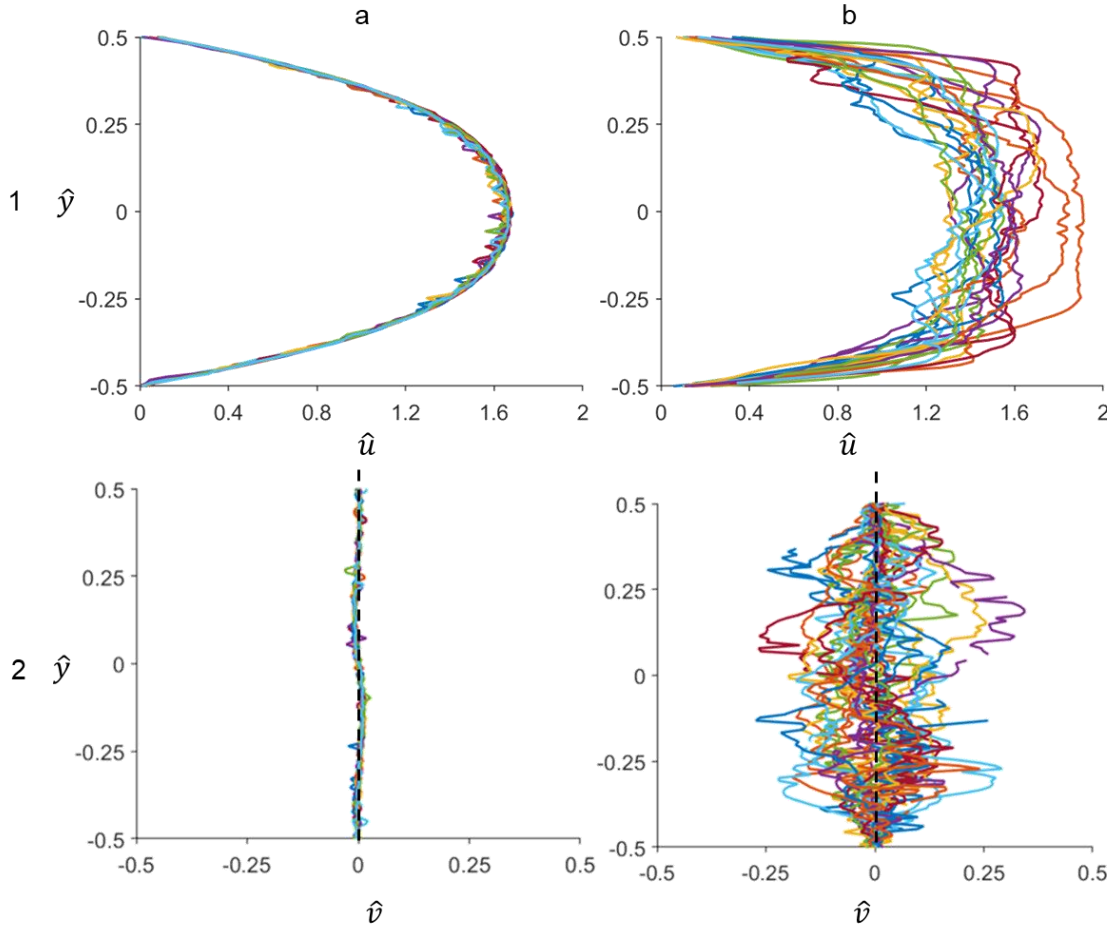

Figure 4.7 *Instantaneous cross stream distributions* ($\hat{x}$ *= 36,* $\hat{z}$ *= 0) of streamwise and cross stream velocity components* ($\hat{u}$ in *a.1 and b.1* and $\hat{v}$ in *a.2 and b.2, respectively) in the absence and presence of the reed (columns a and b, respectively) at Re = 2,000 in the 5 mm channel. The scale of* $\hat{v}$ *is enlarged (the black dotted line is* $\hat{v}$ *= 0).*

The time-averaged streamwise evolution of the flow is assessed from PIV measurements in the cross stream (x - y) plane z = 0 (the field of view of each measuring 0.8W X W) at six equally-spaced streamwise locations between the reed tip ($\hat{x}_{tip}$ = 16) and the channel exit ($\hat{x}$ = 50). The data at each streamwise position comprises an ensemble of 3,000 images acquired at 8.52 Hz. In the current analysis, cross stream profiles are extracted at the streamwise center of each of these windows. The differences between the flows in the absence and presence of the reed are demonstrated by considering instantaneous cross stream distributions of the streamwise ($\hat{u} = u/U$) and cross stream ($\hat{v} = v/U$) velocity components as shown in Figure 4.7 (20 cross stream profiles) acquired at $\hat{x}$ = 36. While in the absence of the reed the instantaneous velocity profiles are nearly invariant (with time), significant fluctuations are visible throughout the channel width in the presence of the reed, even though the measurements are acquired at 20W downstream of its tip. These fluctuations are caused by the advection of the induced vortical structures and are directly related to changes in the time-averaged flow field in the presence of the reed. Asymmetry between the cross stream velocity distributions near the channels' left ($\hat{y}$ = 0.5) and right wall ($\hat{y}$ = 0.5) that is evident in Figure 4.7-b.2 is ostensibly due the slight asymmetry in the reed motion (cf. Figure 4.1, §4.2). As shown in Figures 4.8 and 4.9, these effects are small and can only be detected in the cross stream distributions of average cross stream velocity component $\hat{\bar{v}}$ and $\widehat{\overline{u'v'}}$.

The instantaneous realizations are time-averaged to obtain the mean and fluctuating flow fields for the PIV windows downstream of the reed. The evolution of the time-averaged flow fields are explored using cross stream distributions of streamwise and cross stream velocity components, spanwise vorticity, and energy budgets of the mean and

fluctuating kinetic energies that are computed at the streamwise center of each field in the absence and presence of the reed. Figures 4.8 show the cross stream distributions of the time-averaged streamwise and cross stream velocity components ($\hat{\bar{u}}$ in Figures 4.8-a.1 and b.1, and $\hat{\bar{v}}$ in Figures 4.8-a.2 and b2) and of the magnitude of the spanwise vorticity ($|\hat{\bar{\omega}}_z|$, $\hat{\bar{\omega}}_z = \bar{\omega}_z \cdot W/U$ in Figures 4.8-a.3 and b.3) and the differences between the distributions in the absence and presence of the reed ($\Delta\hat{\bar{u}}$, $\Delta\hat{\bar{v}}$, $\Delta|\hat{\bar{\omega}}_z|$) are shown in Figures 4.8-c.1 through c.3. In the absence of the reed, the cross stream distributions of $\hat{\bar{u}}$ are nearly identical for $18 < \hat{x} < 48$ and $|\hat{y}| > 0.25$ and exhibit some marginal streamwise increase by spreading towards the channel center ($|\hat{y}| < 0.25$) as the flow becomes more fully developed (as also evident in the pressure distributions of Figure 4.6). The velocity distribution downstream of the reed in the presence of the reed ($\hat{x} = 18$) is remarkably nearly parabolic and is larger than the corresponding velocity in the base channel even though the two flows have the same volume flow rate. This indicates that the spanwise effects of the reed lead to increased blockage near the top and bottom walls (Figure 4.8-b.1) which is also evident in corresponding cross stream distributions of $\Delta\hat{\bar{u}}$ (Figure 4.8 - c.1) in vicinity of reed tip. Farther downstream of the reed ($24 < \hat{x} < 30$, Figure 4.8-b.1) the streamwise velocity flattens near the center of the channel and increases near the walls ($|\hat{y}| = 0.4$) where it is significantly higher than in the base-flow ($\Delta\hat{\bar{u}} \approx 0.5$). For $\hat{x} > 30$, $\hat{\bar{u}}$ in the presence of the

reed decreases somewhat for $|\hat{y}| > 0.25$ or $\Delta\hat{\bar{u}} \sim 0.3$ near the walls at the channel exit ($\hat{x} = 48$). The cross-stream distributions of $\hat{\bar{v}}$ in the absence and presence of reed (Figures 4.8-a.2 and b.2) show that it is significantly smaller than the corresponding streamwise

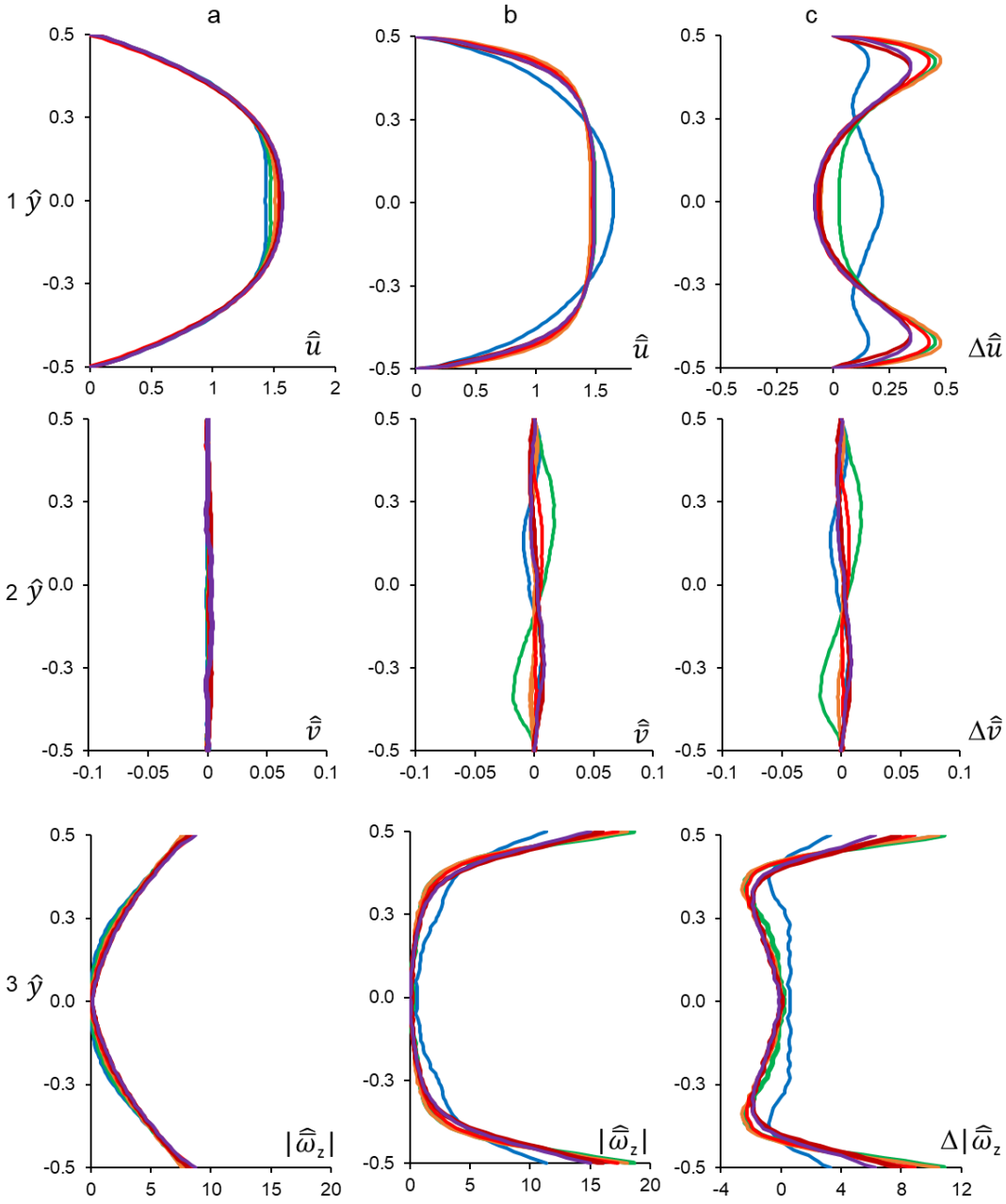

Figure 4.8 *Cross stream distributions (at z = 0) of the time-averaged streamwise and cross streamwise velocity components* ($\hat{\bar{u}}$ *in row 1* and $\hat{\bar{v}}$ in *row 2, respectively*) *and of the magnitude of spanwise vorticity* ($\hat{\bar{\omega}}$ in *row 3*) *in the absence and presence of reed (columns a and b, respectively) at* $\hat{x}$ = ***18***, ***24***, ***30***,***34***, ***42***,***48*** *for Re = 2,000. Column c shows the differences between the presence and absence of the reed.*

velocity. The time-averaged cross stream velocities during the reed's motion towards and away from each of the walls should be antisymmetric about the channel's centerline. The present data shows that the motion is nearly symmetric and that the symmetry reverses between the streamwise stations $\hat{x}$ = 24 and 48. As discussed in connection to Figure 4.7 - b.2, the instantaneous realizations of $\hat{v}$ show slight asymmetry about the centerline which is also evident in Figure 4.8 – b.2. The distributions of the mean spanwise vorticity $|\widehat{\omega}_z|$ (Figure 4.8-a.3 and b.3) show that in the absence of the reed, $|\widehat{\omega}_z|$ is streamwise-invariant (as expected from the velocity profiles in Figure 4.8-a.1 and a.2). However, in the presence of the reed (Figure 4.8-b.3), there is a significant increase in the vorticity magnitude near the wall in accord with the higher streamwise velocity. Figure 4.8-c.3 shows that for $\hat{x}$ = 18, $\Delta|\widehat{\omega}_z|$ = 3.3 at the wall ($\hat{y}$ = ±0.5) and increases to 10.5 at $\hat{x}$ = 24. It should be noted that for $|\hat{y}|$<0.3, the vorticity magnitude decreases in the presence of the reed as the velocity profiles become flat about the centerline (cf. Figure 4.8-b.1). Even though the channel exit is 34W downstream of the reed there are still significant increments in wall bound vorticity in the presence of the reed indicating its potential influence on thermal transport from the walls.

The effects of the reed oscillations on the flow fluctuations within the channel are assessed through the *x*-*y* components of second moments of streamwise and cross stream velocity fluctuations, $u' = u-\bar{u}$ and $v' = v-\bar{v}$ at the PIV stations discussed in connection with Figure 4.8. Cross stream distributions at the streamwise center of these windows in the absence and presence of the reed are analyzed for $\widehat{u'u'}$, $\widehat{v'v'}$ and $\widehat{u'v'}$. In the absence of the reed, $\widehat{u'u'}$, $\widehat{v'v'}$ and $\widehat{u'v'}$ are vanishingly small throughout the channel ($\widehat{u'u'}$, $\widehat{v'v'}$ and $\widehat{u'v'}$ are smaller than $2\cdot10^{-4}$) and therefore are not discussed further. Figures 4.9a through c show the cross stream distributions of $\widehat{u'u'}$, $\widehat{v'v'}$ and $\widehat{u'v'}$respectively in the presence of the reed. To begin with, $\widehat{u'u'}$ (Figure 4.9a) is an order of magnitude larger than $\widehat{v'v'}$ and $\widehat{u'v'}$ (Figures 4.9b and c) and therefore they are plotted on different scales. In the presence of the reed and near its tip ($\hat{x}$ = 18, Figure 4.9a) the cross stream variations of $\widehat{u'u'}$ symmetric about the channel center and show a tri-lobed profile with local maxima at $\hat{y}$ = 0, ±0.35 and minima at $\hat{y}$ = ±0.2. A comparison with the vorticity flux at this station (cf. Figure 4.2, §4.2) shows that while the lobes at $\hat{y}$ = ±0.35 are associated with the periodic disruptions of wall-

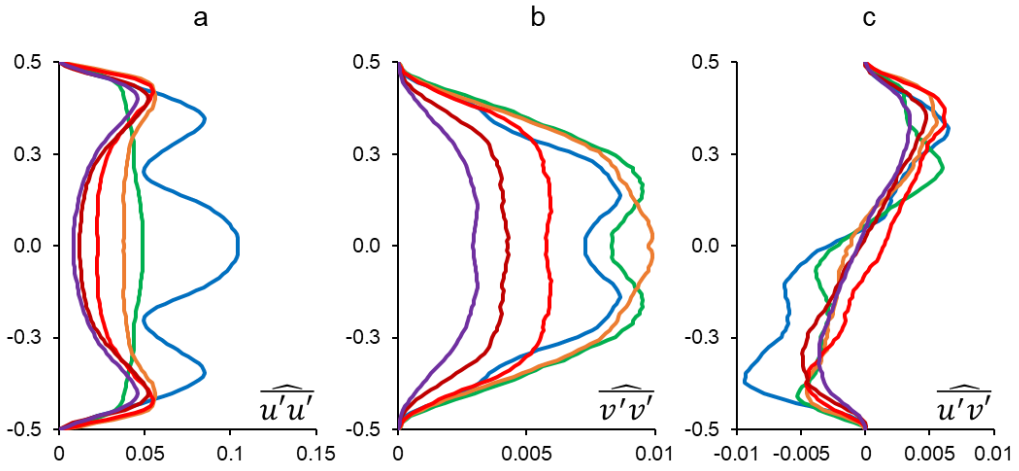

Figure 4.9 *Cross stream distributions at z = 0 of* $\widehat{u'u'}$ (a), $\widehat{v'v'}$ (*b*) *and* $\widehat{u'v'}$ (*c*) *in the presence of the reed at* $\hat{x}$ = ***18***, ***24***, ***30***, ***34***, ***42***, ***48*** *for Re = 2,000.*

boundary layer due to reed-tip blockage, the lobe at the channel center is associated with the passage of triple bands of vorticity which arise due to reed interactions with the channel flow upstream of its tip. At $\hat{x} = 24$, the tri-lobed fluctuations vanish, and $\widehat{\overline{u'u'}} \sim 0.04$ for $|\hat{y}| < 0.3$. This decrease is associated with elevated levels of small-scale dissipation of the fluctuations which are discussed in connection with the energy budget of the fluctuations in Figure 4.12. For $\hat{x} > 24$, while $\widehat{\overline{u'u'}}$ decreases in the channel core ($|\hat{y}| < 0.3$), it actually increases for $0.3 < |\hat{y}| < 0.45$ for $24 < \hat{x} < 30$ followed by a decrease for $\hat{x} > 30$ (which is smaller than the corresponding decrease in the channel core). As a result, near the channel exit, $\widehat{\overline{u'u'}}$ is higher near the walls than at the channel center ($\widehat{\overline{u'u'}} = 0.045$ at $\hat{y} = \pm 0.4$ and $\widehat{\overline{u'u'}} = 0.008$ at the channel center ($\hat{y} = 0$)). Figure 4.9b shows the cross stream distributions of $\widehat{\overline{v'v'}}$ which are an order of magnitude smaller than the $\widehat{\overline{u'u'}}$ with modified scale of the *x* axis to resolve the lower levels. The cross stream distributions of $\widehat{\overline{v'v'}}$ are symmetric about the channel center (similar to $\widehat{\overline{u'u'}}$) and exhibit a maxima at the channel center, $\widehat{\overline{v'v'}} = 0.01$ at $\hat{x} = 30$ and for $\hat{x} > 30$, with a decrease throughout the channel width such that at the channel center $\widehat{\overline{v'v'}} = 0.0025$ at $\hat{x} = 48$. It is conjectured that since the reed velocities are five times smaller than the average channel speed, the cross stream fluctuations are smaller than the streamwise fluctuations (as also evident in the instantaneous realizations in Figure 4.7-b.1 and b.2). The cross stream variations of $\widehat{\overline{u'v'}}$ (Figure 4.9c) show that their magnitudes are of the same order as $\widehat{\overline{v'v'}}$, although $\widehat{\overline{u'v'}} > 0$ for $\hat{y} > 0$ and $\widehat{\overline{u'v'}} < 0$ for $\hat{y} < 0$. As the reed approaches each of the walls, while the increase in *u* (due to contraction of flow stream between the reed and channel, cf. Figure 4.3) is nearly symmetric, the increase in *v* is antisymmetric about the channel centerline ($y = 0$)

which leads to anti symmetry in $\widehat{\overline{u'v'}}$. At $\hat{x}$ = 18, $\widehat{\overline{u'v'}}$ distributions show a local minima ($\widehat{\overline{u'v'}}$ = - 0.008) at $\hat{y}$ = -0.37.and maxima ($\widehat{\overline{u'v'}}$ = 0.0065) at $\hat{y}$ = 0.32 with the different magnitudes ostensibly being due to the asymmetry in reed motion between the top and bottom wall (as discussed in § 4.2). Further downstream the magnitude of $\widehat{\overline{u'v'}}$ decreases as the effect of reed dampens and for $\hat{x}$ > 30 the cross stream distributions are nearly identical (cf. Figure 4.9b3). These data show that the second moment of velocity fluctuations near the reed tip are dominated by the streamwise component ($\widehat{\overline{u'u'}}$) near the tip which decrease at larger rates near the channel center and sustain to significantly higher values near the channel walls.

The evolution of channel's flow field is further investigated using an energy balance of the time-averaged and fluctuating components of its kinetic energy in the absence and presence of the reed. Equation 4.3 shows the traditional budget of the mean kinetic energy (per unit mass) $E = 0.5\,(\bar{u}^2 + \bar{v}^2 + \bar{w}^2)$ (Pope, 2000a), in terms of its substantial derivative or material rate of change of the mean kinetic energy

$$\frac{DE}{Dt} = \frac{\partial}{\partial x_j}\left(-\frac{p\bar{u}_j}{\rho_a} + 2\vartheta\bar{u}_i S_{ij} - \overline{u_i' u_j'}\bar{u}_i\right) - 2\vartheta S_{ij}S_{ij} + \overline{u_i' u_j'}S_{ij} \tag{4.3}$$

where $u_1 = u$, $u_2 = v$, and $u_3 = w$, S_{ij} is the symmetric part of the mean strain rate, and changes in gravitational potential energy are neglected (cf. Appendix A). As noted in Appendix A, it is assumed that $\bar{w} = 0$ and $\partial/\partial z = 0$ at $z = 0$ (due to spanwise symmetry), ρ_a and the streamwise pressure gradient $\partial p/\partial x$ = constant (based on the pressure distributions in Figure 4.6), and $\partial p/\partial y << \partial p/\partial x$ (changes in cross stream momentum and viscous stresses are smaller than the streamwise components as $\bar{v} << \bar{u}$ in the region downstream of the reed tip, cf. Figure 4.8) and hence $\partial p/\partial y$ is neglected.

The material rate of change of the mean kinetic energy ($M = \frac{DE}{Dt}$)is affected by the transport of mean kinetic energy due to the mean pressure $T_p = \frac{\partial}{\partial x_j}\left(-\frac{p\bar{u}_j}{\rho_a}\right) = -\frac{\bar{u}_j}{\rho_a}\frac{\partial p}{\partial x_j}$ (using continuity, $\frac{\partial \bar{u}_j}{\partial x_j} = 0$), mean viscous stresses $T_v = \frac{\partial}{\partial x_j}\left(2\vartheta\bar{u}_i S_{ij}\right)$ and second moments of velocity fluctuations $T_R = \frac{\partial}{\partial x_j}\left(-\overline{u_i' u_j'}\bar{u}_i\right)$; the dissipation of the mean kinetic energy (by the mean viscous stresses) is $D_v = -2\vartheta S_{ij}S_{ij}$, and the shear production of fluctuation kinetic energy $k_f = 0.5(\overline{u'^2} + \overline{v'^2} + \overline{w'^2})$ by the second

moments of velocity fluctuations is $P = \overline{u_i' u_j'} S_{ij}$ (which increases the fluctuating kinetic energy in the channel).

Each term in the mean kinetic energy budget (Equation 4.3) is normalized by U^3/W [the notation "^" is used to denote each normalized term, e.g., $\hat{T}_p = T_p / (\frac{U^3}{W})$]. The normalized mean kinetic energy budget in the absence and presence of the reed at Re = 2,000 at $\hat{x}$ = 18, $\hat{z}$ = 0 is illustrated in Figure 4.10-a.1 and b.1. For clarity, the line plots of the transport terms $\hat{T}_p$ $\hat{T}_v$, and $\hat{T}_R$ are marked in red, while the dissipation $\hat{D}_v$ and shear production of fluctuation kinetic energy $\hat{P}$ are marked in blue and green, respectively. In the absence of the reed (Figures 4.10-a.1 and b.1), turbulent transport and production ($\hat{T}_R$, and $\hat{P}$) are negligible as can be expected considering the low-levels of second moments of velocity fluctuations in the base flow and the material rate of change of the energy is therefore influenced primarily by the balance between the mean viscous and pressure transport terms $\hat{T}_v$ and $\hat{T}_p$, and the mean viscous dissipation $\hat{D}_v$. While $\hat{M}$ and $\hat{T}_p$ vanish at channel walls since $\bar{u}$(y) = 0, $\hat{T}_v$ and $\hat{D}_v$ are clearly non-zero and balance each other ($\hat{T}_v$ = 0.03). Away from the walls, $\hat{D}_v$ decreases and it nearly vanishes for $|\hat{y}|$ = 0.25 as the viscous shear stresses diminish (as is also evident in near zero levels of vorticity in Figure 4.8-a.3), $\hat{T}_v$ changes sign at $|\hat{y}|$ = 0.4 such that $\hat{T}_v \leq 0$ for $|\hat{y}| < 0.4$ and $\hat{T}_p$ increases as the speed of the mean flow increases. The balance between $\hat{D}_v$, $\hat{T}_v$ and $\hat{T}_p$ results in near-zero $\hat{M}$ for $|\hat{y}| > 0.25$, and for $|\hat{y}| < 0.25$, $\hat{M}$ increases due to streamwise acceleration of flow (cf. Figure 4.8-a.1) caused by $\hat{T}_p$.

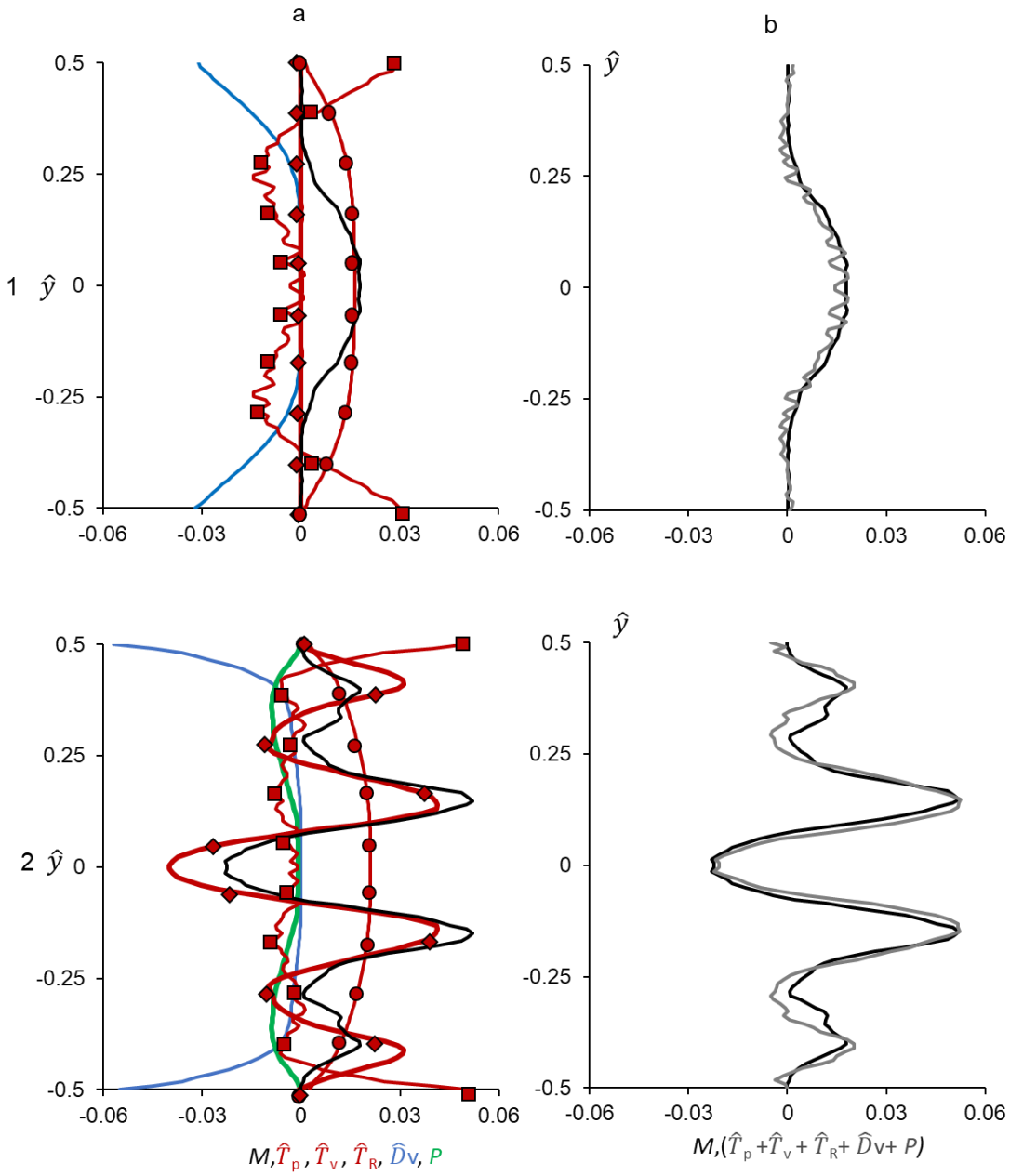

Figure 4.10 *Line plots of cross stream distributions of the terms in the dimensionless mean kinetic energy budget (Equation 4.3) terms including the material derivative,* $\widehat{\boldsymbol{M}}$*, transport of mean kinetic energy by mean pressure* $\widehat{\boldsymbol{T}}_{\boldsymbol{p}}$ *(●), mean viscous stress* $\widehat{\boldsymbol{T}}_{\boldsymbol{v}}$ *(■), and second moment of velocity fluctuations,* $\widehat{\boldsymbol{T}}_{\boldsymbol{R}}$ *(♦), mean viscous dissipation,* $\widehat{\boldsymbol{D}}_{\boldsymbol{v}}$ *and shear production of fluctuation kinetic energy,* $\widehat{\boldsymbol{P}}$*. The measurements are acquired at* $\hat{x} = 18$ *for Re = 2,000 in the absence (a.1) and presence of the reed (a.2). Column b shows the sum of the terms on the right hand side of Equation 4.3 (gray line) along with* $\widehat{\boldsymbol{M}}$ *in the absence (b.1) and presence (b.2 of the reed).*

All the terms of the energy budget change in the presence of the reed (Figure 4.10 - a.2). The most significant changes occur in the transport $\hat{T}_R$ and shear production $\hat{P}$ due to the elevated levels of the second moments of velocity fluctuations. Similar to the base flow, near the walls $\hat{T}_v$ is balanced by $\hat{D}_v$, which is significantly higher in the presence of the reed (0.06 vs. 0.03). The higher levels of $\hat{D}_v$ at the wall are due to increased levels of viscous shear stresses in the presence of reed as is evident in the increased vorticity levels in Figures 4.8-a.3 and b.3. Away from the walls, $\hat{D}_v$ decreases towards the channel center due to reduction in viscous shear stresses ($\hat{D}_v \approx 0$ at $\hat{y} = \pm 0.3$) and $\hat{T}_p$ increases in the presence of the reed albeit at higher cross stream rates than the base flow due to larger $\bar{u}(y)$ (cf. Figure 4.8-b.1). It is to be noted that in the presence of the reeds, shear production ($\hat{P}$) is evident between the channel walls and the center (a negative value signifies positive transfer of energy from the mean flow field to the fluctuations) and has local extrema at $\hat{y} = \pm 0.4$. The second moments of velocity fluctuations are also associated with transport of the mean kinetic energy through $\hat{T}_R$ whose magnitudes are significantly higher than $\hat{P}$ and a balance between $\hat{T}_R$ and $\hat{T}_p$ leads to cross stream changes in $\hat{M}$ farther away from the wall ($|\hat{y}| < 0.25$). While at the channel center, $\hat{T}_R < 0$ leading to a reduction in $\hat{M}$, at $\hat{y} = \pm 0.15$, $\hat{T}_R > 0$, leading to an increase in $\hat{M}$. In proximity to the wall ($\hat{y} = \pm 0.4$), both $\hat{T}_P$ and $\hat{T}_R$ lead to an increase in $\hat{M}$. In summary, these data show that the elevated levels of pressure gradients near the reed tip increase the mean kinetic energy in the channel that is transported from the channel center towards the wall by elevated second moment of velocity fluctuations in the presence of the reeds (relative to the base flow). While a small fraction of this energy is lost to the production of fluctuating kinetic energy in close

proximity to the wall, the balance (which is significantly higher than in the base flow) is transported and dissipated at the wall by mean viscous stresses.

The validity of the assumptions that were used in the present adaptation of the energy budget equation (4.3) are assessed by comparing the sum of the computed terms on its right hand side with the calculation of the material derivative that is on its left hand side in the absence and presence of the reed as shown in Figures 4.10-b.1 and b.2 respectively. The reasonable agreement in the cross stream profiles of the sum of the right hand side terms with the corresponding material derivative lends credence to these assumptions.

Following the data in Figure 4.10, the streamwise evolution of the energy budget of the mean kinetic energy (at $z = 0$) is considered using measurements at two additional streamwise stations farther downstream ($\hat{x}$ = 36 and 48) and the corresponding line plots to Figures 4.10-a.1 and a.2 are shown Figure 4.11 (the data at $\hat{x}$ = 18 are reproduced for reference). In the absence of the reed (Figures 4.11-a.1 through a.3), the streamwise variations of $\hat{T}_p$, $\hat{T}_v$, $\hat{T}_R$, $\hat{D}_{\mathrm{v}}$, and $\hat{P}$ are small and therefore $\hat{M}$ exhibits a small streamwise decrease about the centerline (from 0.018 at $\hat{x}$ = 18 to 0.014 at $\hat{x}$ = 48 $\hat{y}$ = 0). By comparison, in the presence of the reed (Figures 4.11-b.1 through b.3) the most significant changes between $\hat{x}$ = 18 and 48 are in $\hat{T}_{\mathrm{R}}$ within $|\hat{y}| < 0.25$ and in $\hat{T}_{\mathrm{v}}$ and $\hat{D}_{\mathrm{v}}$ near the wall while $\hat{T}_{\mathrm{P}}$ and $\hat{P}$ decrease monotonically towards the channel's exit plane ($\hat{x}$ = 48). It is also noted that the $\hat{T}_{\mathrm{v}}$ (which balances $\hat{D}_{\mathrm{v}}$ near the wall) increases in the streamwise direction and is significantly higher than in the base flow due to the higher level of viscous shear stress at the wall in the presence of the reed. It is conjectured that the higher streamwise momentum and vorticity near the wall farther downstream of the reed (cf. Figure 4.8-b.2

and b.3) lead to sustained levels of second moment of velocity fluctuations and mean strain rates which support the elevated levels of $\hat{T}_{\mathrm{R}}$ near the wall. Remarkably, while compared to the base flow the cross stream distribution of $\hat{M}$ is obviously significantly different near the reed, it asymptotes to the levels of the base flow near the center of the channel at the channel's exit plane (Figure 4.11-a.3 and b.3). However, the effects of the reed are still apparent and pronounced near the walls with important consequences for increased heat transfer.

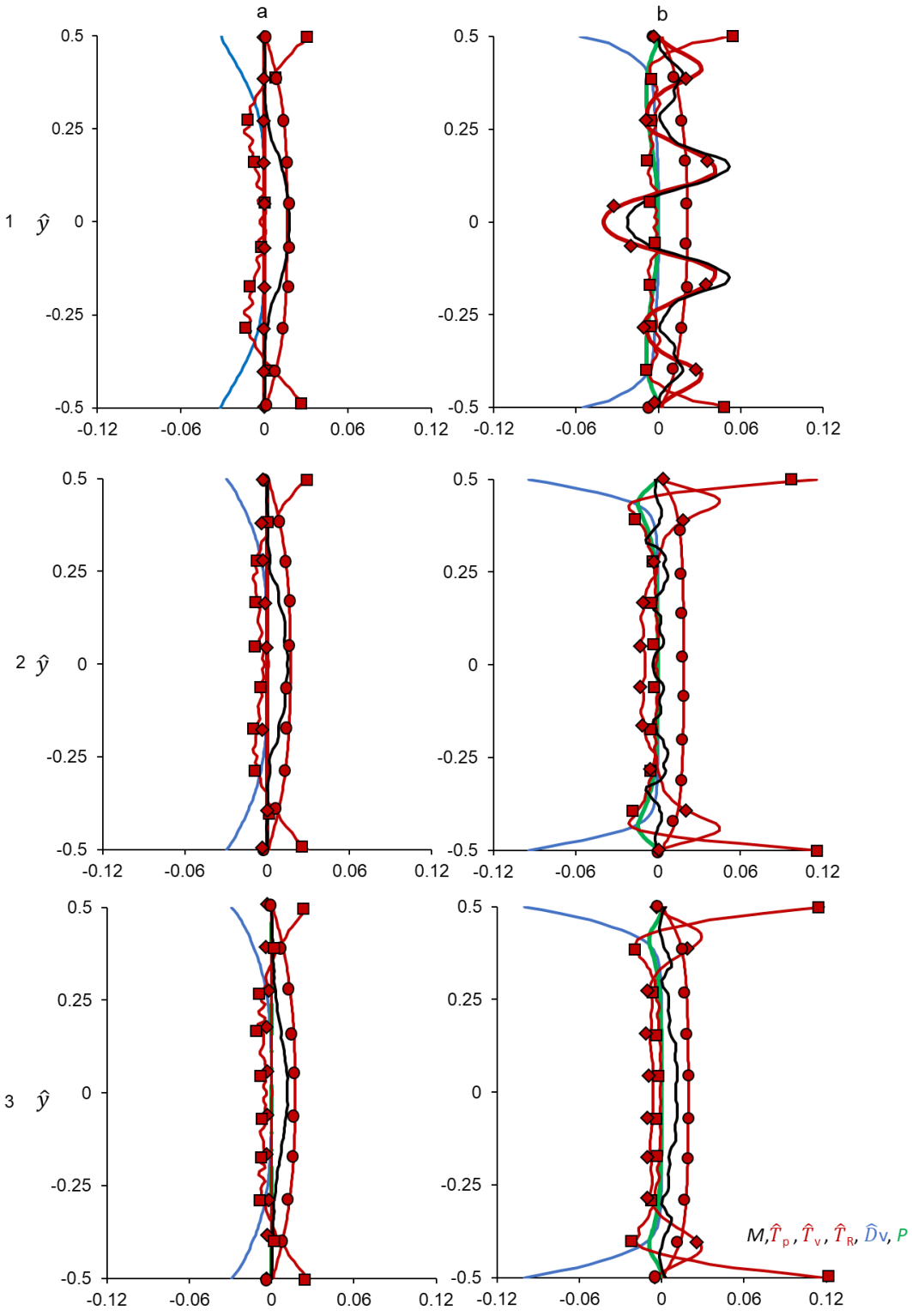

Figure 4.11 *As in Figures 4.10-a.1 and a.2 in the absence and presence of the reed (columns a and b, respectively) for $\hat{x}$ = 18 (row 1), 36 (row 2) and 48 (row 3).*

While Equation 4.3 describes the budget of the mean kinetic energy of the flow, the changes in fluctuating kinetic energy [$k_f = 0.5\,(\overline{u'^2} + \overline{v'^2} + \overline{w'^2})$] are described in Equation 4.4:

$$\frac{\mathrm{D}k_f}{\mathrm{D}t} = -\frac{\partial}{\partial x_j}\left(\frac{\overline{p'u_j'}}{\rho_a} - 2\vartheta\overline{u_\iota' e_{\iota J}} + 0.5\cdot\overline{u_\iota'^2 u_j'}\right) - 2\vartheta\overline{e_{\iota J}e_{\iota J}} - \overline{u_\iota u_J}S_{ij} \tag{4.4}$$

where e_{ij} is the symmetric part of the fluctuating strain rate (cf. Appendix A). In addition to the assumptions made in connection with Equation 4.3, it is assumed that $w' \approx v'$ and that $e_{12} = e_{23} = e_{31}$ based on statistically isotropic cross stream and spanwise velocity fluctuations (Delafosse et al., 2011). Equation 4.4 shows that the material rate of change of the fluctuating kinetic energy is affected by the transport of fluctuating kinetic energy k_f by the pressure fluctuations p' given by $T_{pf} = \frac{\partial}{\partial x_j}\left(-\frac{\overline{p'u_j'}}{\rho_a}\right)$, fluctuating viscous stresses $T_{vf} = \frac{\partial}{\partial x_j}\left(2\vartheta\overline{u_\iota' e_{ij}}\right)$, and by second moment of velocity fluctuations, $T_{Rf} = 0.5\cdot\frac{\partial}{\partial x_j}\left(-\overline{u_i'^2 u_J'}\right)$, the dissipation of the fluctuating kinetic energy by the fluctuating viscous stresses is $D_{vf} = -2\vartheta\overline{e_{ij}e_{ij}}$, and the shear production of fluctuation kinetic energy by the second moment of velocity fluctuations working against the mean flow is $P = \overline{u_i' u_j'}S_{ij}$. The dissipation of the fluctuating kinetic energy D_{vf} represents the loss of fluctuating kinetic energy to heat by small-scale dissipation while D_v (Equation 4.1) represents large scale dissipation due mean strain rates. It is noted that P is the same as in Equation 4.1 but with opposite sign, denoting the transfer of energy from mean flow to the fluctuations. In addition, the pressure transport term, T_{pf} was calculated from the balance of Equation 4.4

as $Tpf = M_f - (T_{vf} + T_{Rf} + D_{vf} + P)$. As with the mean kinetic energy budget, each term in the fluctuating kinetic energy budget (Equation 4.4) is normalized by U^3/W.

Similar to the discussion of the mean energy budget in Figures 4.10 and 4.11, the fluctuating kinetic energy budget k_f is analyzed in the absence and presence of the reed using data at $\hat{x}$ = 18, 36 and 48 and shown in Figure 4.12. As in Figure 4.11, in Figure 4.12 the line plots of the transport terms $\hat{T}_{pf}$ $\hat{T}_{vf}$, and $\hat{T}_{Rf}$ are marked in red, and the dissipation $\hat{D}_{vf}$ and shear production of fluctuation kinetic energy $\hat{P}$ are marked in blue and green, respectively. Since in the absence of the reed (Figures 4.12-a.1 through a.3) the flow is laminar, the magnitudes of the velocity fluctuations along the channel are small (cf. Figure 4.9-a.1 through a.3) and result in negligible changes in the material derivative $\hat{M}_f$. In the presence of reeds (Figures 4.12-b.1 through b.3), the material rate of change of the fluctuating energy $\hat{M}_f$ immediately downstream of the reed is smaller in magnitude compared to $\hat{M}$ (~50% on the centerline, cf. Figure 4.12-b.1 and 4.11-b.1) and nearly vanishes farther downstream at $\hat{x}$ = 36 and 48. It is noteworthy that the contribution of the viscous dissipation $\hat{D}_{vf}$ is large and therefore $\hat{M}_f$ must be balanced by the pressure fluctuation $\hat{T}_{pf}$ which is not computed directly from the measurements, but is estimated from the overall balance. The data in Figure 4.12-b.1 shows that near the reed ($\hat{x}$ = 18) the transport of k_f by Reynold's stresses, $\hat{T}_{Rf}$ has a local maximum at $\hat{y}$ = 0 and two local minima at $\hat{y}$ = ±0.1 with vanishingly small levels for $|\hat{y}| > 0.1$. That $\hat{M}_f$ = -0.01 at the channel center indicates that k_f decreases due to the streamwise decrease in velocity fluctuations and the speed of the mean flow downstream of the tip of the reed (cf. Figure 4.8 and 4.9). The magnitude of the viscous dissipation $\hat{D}_{vf}$, is larger than 0.06 throughout the channel width (cf. Figure 4.12-b.1) and peaks at the

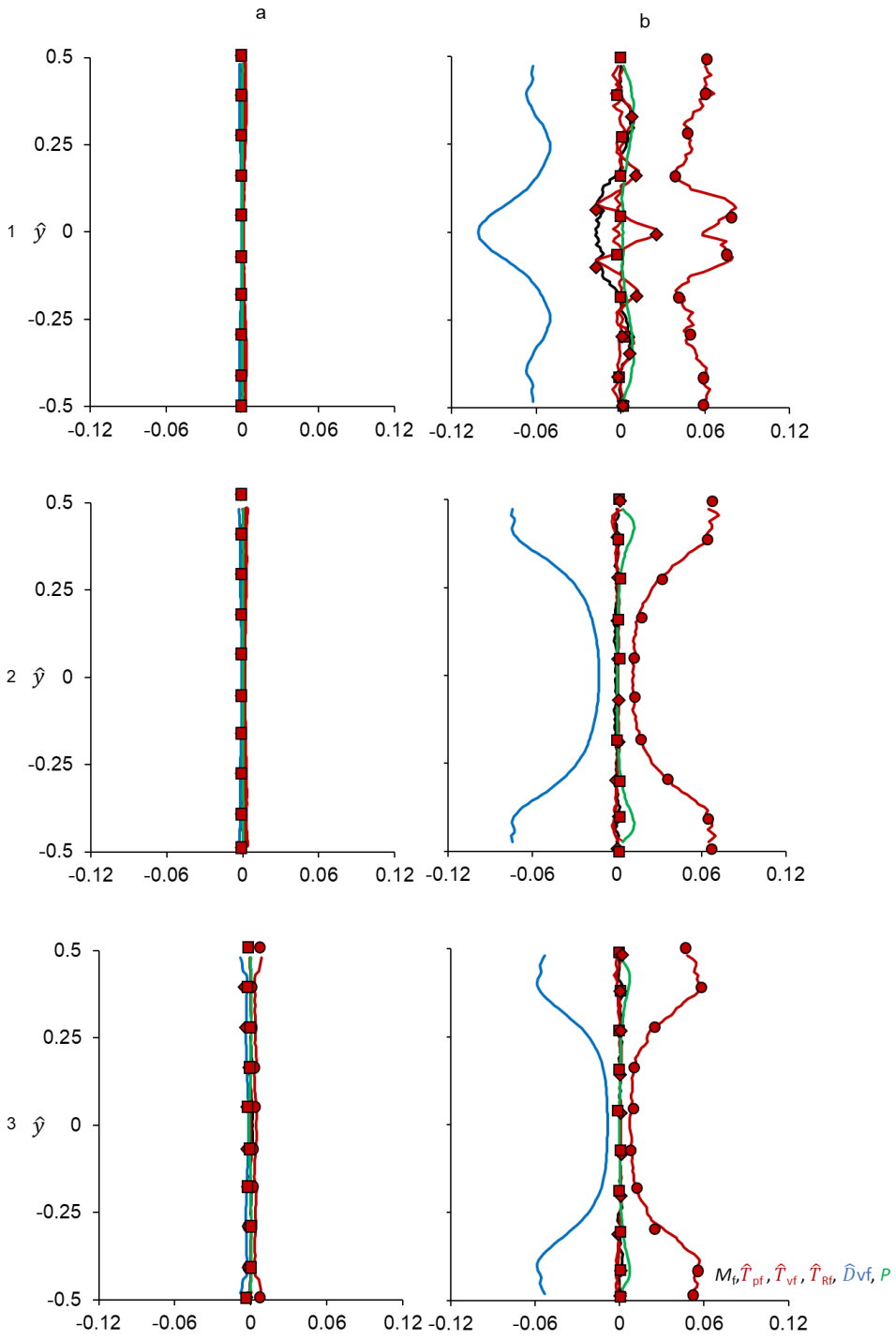

Figure 4.12 *Line plots of cross stream distributions of the terms in the dimensionless fluctuating kinetic energy budget (Equation 4.4): terms including material derivative,* $\widehat{\boldsymbol{M}}_{\mathbf{f}}$*, transport of fluctuating kinetic energy by pressure fluctuations* $\widehat{\boldsymbol{T}}_{\mathbf{pf}}$ (●)*, fluctuating viscous stresses* $\widehat{\boldsymbol{T}}_{\mathbf{vf}}$ (■) *and second moment of velocity fluctuations* $\widehat{\boldsymbol{T}}_{\mathbf{Rf}}$ (♦)*; small-scale viscous dissipation,* $\widehat{\boldsymbol{D}}_{\mathbf{vf}}$ *and shear production of fluctuation kinetic energy,* $\widehat{\boldsymbol{P}}$*. The measurements are acquired at Re = 2,000 in the absence and presence of the reed (columns a and b, respectively) for* $\hat{x}$ *= 18 (row 1), 36 (row 2) and 48 (row 3).*

channel center which can be associated with the high levels of shear in the vortical structures that are advected across the center of the channel as the reed is oscillating (cf. Figure 4.2). As the strength and phase coherence of the vortical structures appears to dissipate and diminish farther downstream from the reed ($\hat{x}$ = 36 and 48), $\widehat{D}_{\mathrm{vf}}$ decreases somewhat compared to its levels at $\hat{x}$ = 18 (Figures 4.12-b.2 and b.3) but it is remarkable that the levels of $\widehat{D}_{\mathrm{vf}}$ are still quite high near the channel's walls due to the increased levels of shear at the wall with the stronger gradient of the streamwise velocity compared to the base flow as is also evident from the distributions of the spanwise vorticity in Figure 4.8-b.3. As discussed above, the fluctuating energy budget along the channel which is primarily is affected by $\widehat{D}_{\mathrm{vf}}$ is balanced by the by pressure fluctuation transport, $\widehat{T}_{\mathrm{pf}}$. These data indicate that although the vortical structures that are induced by the oscillations of the reed severely diminish in magnitude, the mean flow remains significantly different from the base flow (especially near the walls) owing to sustained levels of transport by second moment of velocity fluctuations and elevated levels of viscous transport. *The fluctuating kinetic energy budget also shows that these stresses are sustained by pressure transport which indicate that the flow along the channel is subjected to pressure pulsations that are associated with the oscillations of the reed* (similar to pulsating flow, (Trip et al., 2012)).

The spanwise variations in the mean and fluctuating flow fields were also assessed using PIV measurements (as in Figures 4.8 and 4.9) in several equally-spaced spanwise cross sections of the channel within $-2 < \hat{z} < 2$ (the channel top and bottom walls are at $\hat{z} = \pm 2.5$) at $\hat{x}=18$ in the absence and presence of reed. The (small) spanwise variations in the absence of reed are discussed in Appendix B.1. The flow symmetry (mean and fluctuating) about the spanwise center of the channel ($\hat{z} = 0$) in the presence of reed is demonstrated in Figure 4.13 at $\hat{z} = \pm 1$ and ± 2 using cross stream variations of streamwise velocity, $\hat{u}$ (Figure 4.13b) and of the fluctuating kinetic energy $\hat{k}_f$ (Figure 4.13c). These

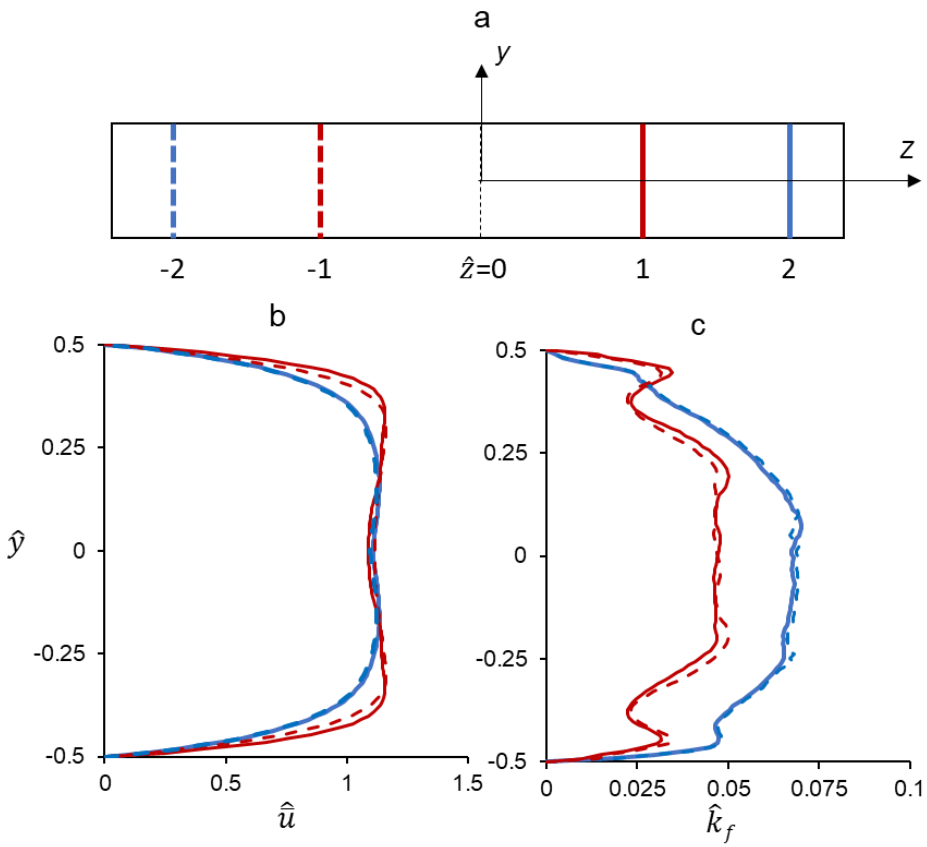

Figure 4.13 *a) Schematic rendition of the y-z plane of the channel showing the locations of the PIV planes ($\hat{z} = \pm 1, \pm 2$), and cross stream variations of the streamwise velocity $\hat{u}$ (b) and of the fluctuating kinetic energy, $\hat{k}_f$ (c) that are both measured at the streamwise center of the PIV planes. The solid and dashed lines mark $z > 0$ and $z < 0$, respectively.*

data indicate that while there are significant spanwise variations in $\hat{\bar{u}}$ and $\hat{k}_f$ the presence of the reed, these variations are nearly symmetric about $\hat{z} = 0$. It is noted that there is marginal cross-stream asymmetry in $\hat{k}_f$ at $\hat{z} = \pm 2$, where $\hat{k}_f\,(\hat{y} > 0) < \hat{k}_f\,(\hat{y} < 0)$ which is a result of some asymmetry in the reed motion that is associated with the attachment of reed to its upstream post (as discussed in § 4.2).

Considering the spanwise symmetry of the flow about the reed centerline, the spanwise variations in cross stream distributions of $\hat{\bar{u}}$ and $\hat{k}_f$ along the channel ($\hat{x}$ = 18, 36 and 48) are addressed for the segment $\hat{z} > 0$ and shown in Figure 4.14. At $\hat{x}$ = 18 and in the channel center ($|\hat{y}| < 0.25$), the streamwise velocity, $\hat{\bar{u}}$ (Figure 4.14-a.1), decreases in the spanwise direction for $0 < \hat{z} < 1$ and, for $\hat{z} > 1$ becomes nearly spanwise-invariant in the channel's center while it increases slowly closer to the channel's side walls. These data indicate that the effects of the reed are clearly not spanwise uniform and that the induced spanwise vorticity concentrations are significantly bent near the wall and potentially lead to the formation of streamwise vortices of alternating sense as the reed oscillates towards and away from the side wall surfaces. While the present PIV planes do not capture these structures because of their *x-y* orientation, the presence of streamwise tip vortices downstream of the reed is evident in the 3-D numerical study on similar reeds by Rips et al. (2020). The cross stream distributions of $\hat{k}_f$ at $\hat{x}$ = 18 (Figure 4.14-b.1) intensify significantly near the top wall ($\hat{z}$ = 2) owing to the interaction with the reed but diminish rapidly at $\hat{x}$ = 36 and 48 and are primarily confined to the channel's side walls with little spanwise variation (Figures 4.14-b.2 and b.3).

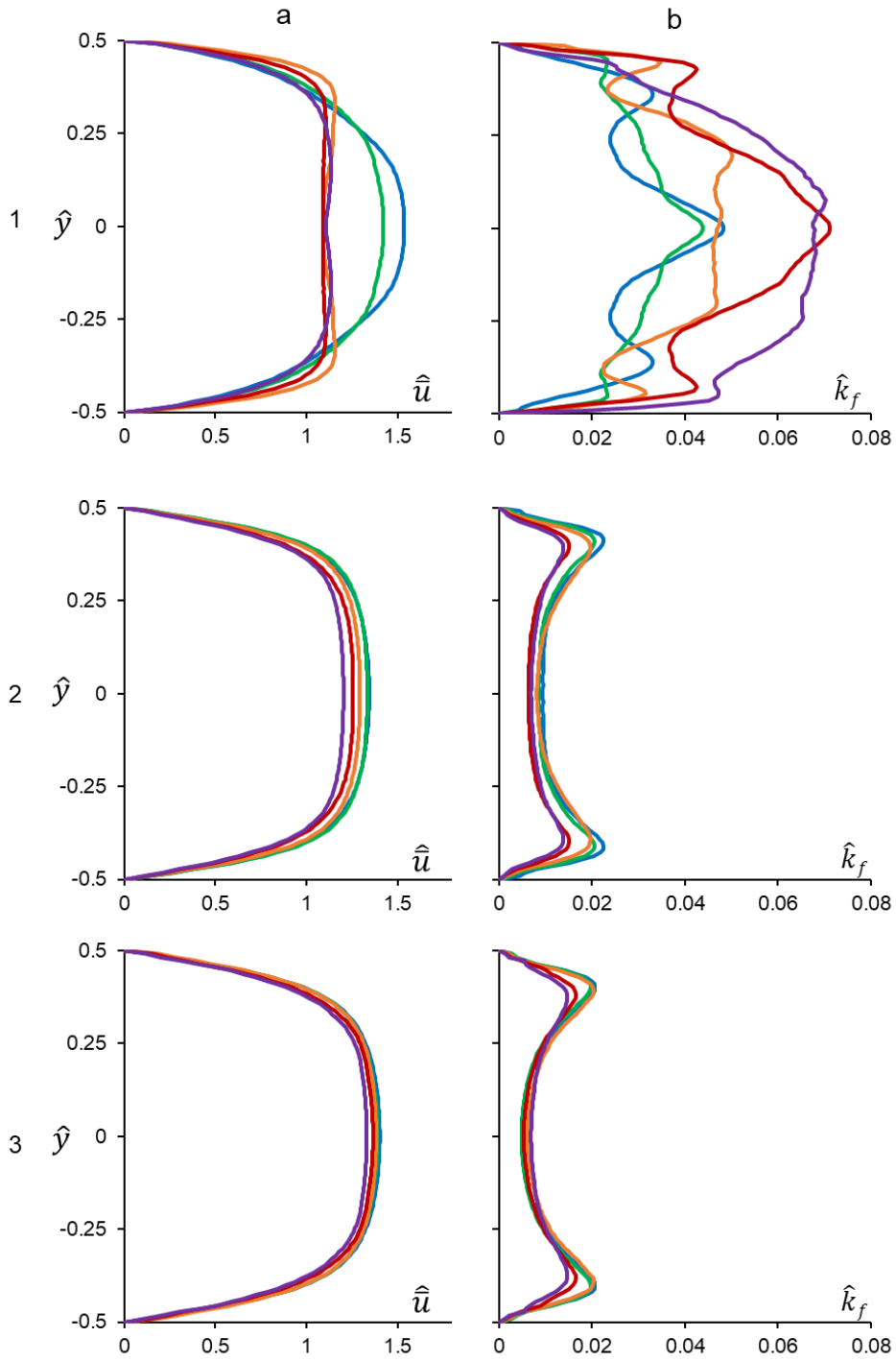

Figure 4.14. *Cross stream distributions of the normalized streamwise velocity $\hat{\bar{u}}$ (column a) and fluctuating kinetic energy, $\hat{k}_f$ (column b) at $\hat{x}$=18 (row 1), 36 (row 2) and 48 (row 3) for spanwise stations, $\hat{z}$=**0**, **0.5**, **1**, **1.5**, **2** (Re = 2,000).*

The spanwise variations of small-scale dissipation $\widehat{D}_{\mathrm{vf}}$, a dominant term in the energy budget of $\hat{k}_{\mathrm{f}}$ (cf. Figure 4.12) which is clearly connected with the decrease in $\hat{k}_{\mathrm{f}}$ downstream of the reed is compared in Figure 4.15 between $\hat{z}$ = 0, 1 and 2 at $\hat{x}$ = 18. These data show that $\widehat{D}_{\mathrm{vf}}$ increases in magnitude between $\hat{z}$ = 0 and 1 across the entire channel width but there is a stronger increase near the channel's center in proximity to the top wall indicating again the effects of the interactions between the spanwise edge of the reed and the top wall. This increase in $\widehat{D}_{\mathrm{vf}}$ near the channel's center is consistent with the higher levels of second moment of velocity fluctuations, (as evident from higher levels of $\hat{k}_{\mathrm{f}}$ at the center in Figure 4.14b.1) downstream of the reed.

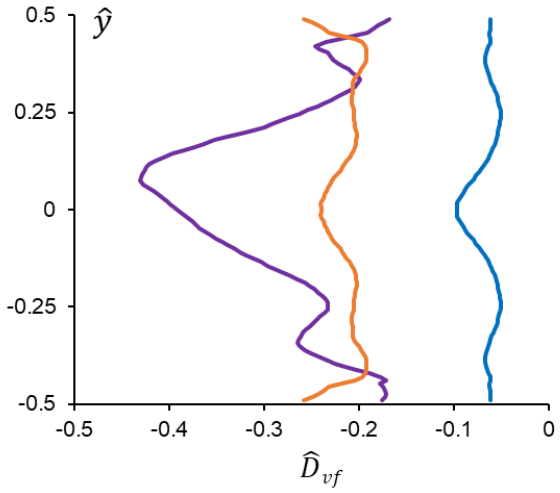

Figure 4.15 *Cross stream variations of small-scale dissipation $\widehat{D}_{\mathrm{vf}}$ of the fluctuating kinetic energy, k_f (Equation 4.4) in the presence of reed at $\hat{x}$ = 18 at $\hat{z}$ =* ***0****,* ***1*** *and* ***2.***

4.4 The Role of the Reynolds Number

The discussion of the reed effects on the flow within high aspect ratio channels in Section 4.3 focused on a laminar base flow. This section addresses the effect of the channel Reynolds number on the interactions with the reed as the base flow undergoes natural transition to turbulence at elevated flow speeds and the impact of the transition on the evolutions of reed-induced perturbations at Re = 2,000, 7,000 and 12,000, for which the reed's Strouhal number is $St_L = 0.5$ ($L_s/W = 10$, $H_s/H = 0.9$). The respective average channel flow speeds U, reed frequencies f_{osc}, and thicknesses t_s are U = 5, 17.5 and 30 m/s and f_{osc} = 65, 220 and 380 Hz and t_s = 38.1, 76.2 and 127 μm. As in§ 4.3, the flow is characterized using time-averaged PIV obtained at six equidistant streamwise locations in the channel's spanwise center plane ($z = 0$).

The mean flow fields in the absence and presence of reeds are analyzed using cross-stream distributions of mean streamwise velocity $\hat{\bar{u}}$ (each normalized by the respective average channel speed). As discussed in §4.3, the time-averaged cross-stream velocity in the channel is significantly smaller than the streamwise velocity, and therefore its discussion is omitted here. Figure 4.16 illustrates the streamwise variations in cross stream distributions of $\hat{\bar{u}}$ at $\hat{x}$ = 18, 30, and 42 in the absence and presence of reeds (columns a and b) at Re = 2,000 (Figures 4.16 – a.1 and b.1), 7,000 (Figures 4.16 - a.2 and b.2) and 12,000 (Figures 4.16 - a.3 and b.3). As already discussed in connection with

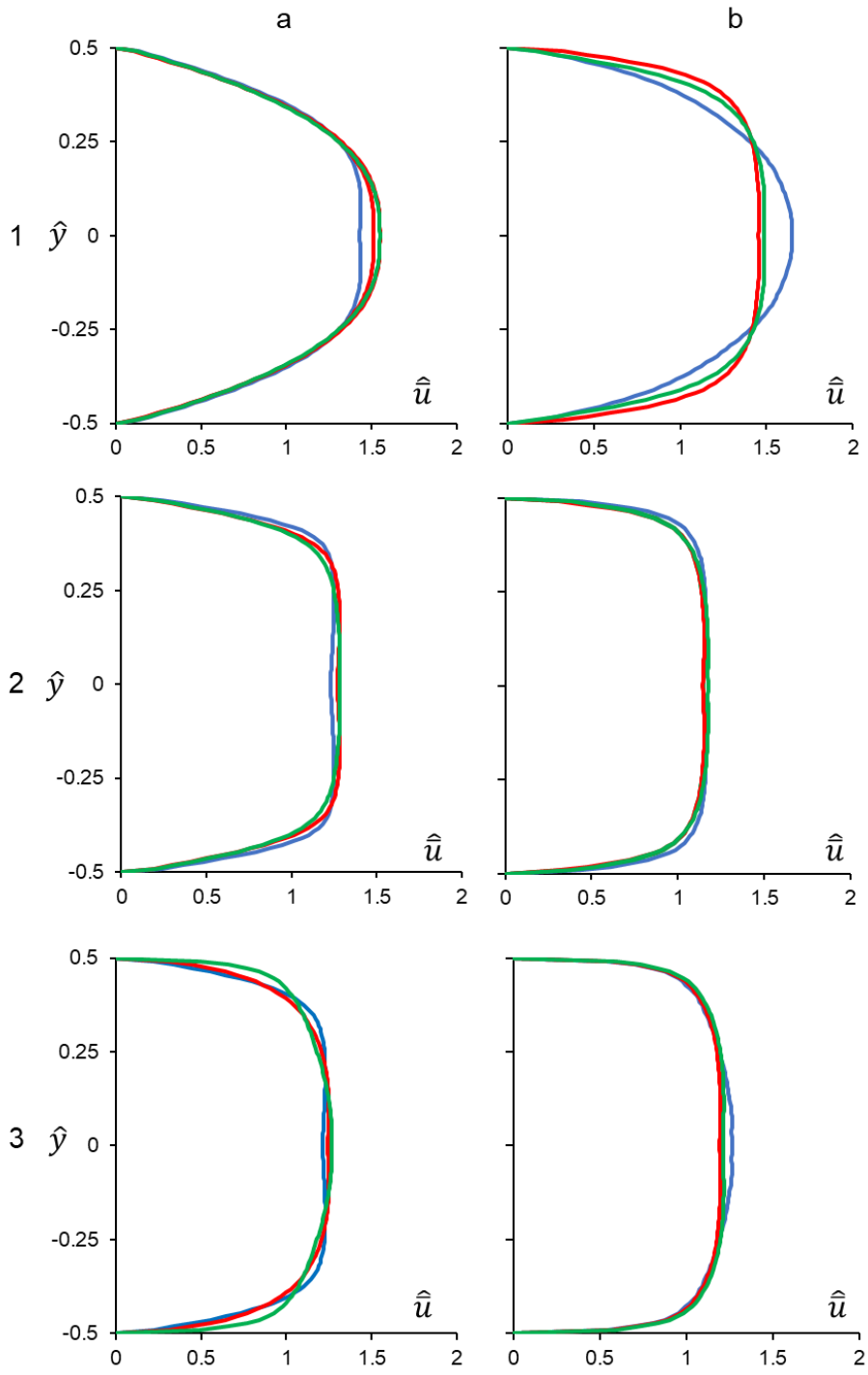

Figure 4.16 *Cross-stream distributions (at $z = 0$) of the normalized time-averaged streamwise velocity $\hat{\bar{u}}$ at $\hat{x}$ = **18**, **30** and **42** in the absence and presence of the reed ($L_s/W = 10$, $St_L = 0.5$) at Re = 2,000 (a.1 and b.1), 7,000 (a.2 and b.2) and 12,000 (a.3 and b.3).*

Figure 4.8 (repeated here for reference), at *Re* = 2,000, near the reed, $\hat{\bar{u}}(\hat{y})$ is higher than in the base flow throughout the width as a result of blockage near the spanwise edges of the reed (cf. the discussion in connection with Figure 4.14), and, farther downstream ($\hat{x}$ = 30 and 42) $\hat{\bar{u}}$ decreases near the channel center ($\hat{y}$ = 0) and increases near the channel side walls ($\hat{y}$ = ±0.45) due to transport of mean kinetic energy by second moment of velocity fluctuations. Although the blockage induced by the spanwise edges of the reed is smaller at *Re* = 7,000, $\hat{\bar{u}}$ near the side walls in the presence of the reed is still higher than in the base flow with a marginal decrease at the channel center (Figures 4.16-a.2 and b.2), e.g., at $\hat{x}$ = 18, $\Delta\hat{\bar{u}}$ = 0.2 and -0.08 at $\hat{y}$ = ±0.45 and 0. Similarly, at *Re* = 12,000 (Figures 4.16-a.3 and b.3), the differences between $\hat{\bar{u}}(\hat{y})$ in the base flow and near the tip of the reed ($\hat{x}$ = 18) are characterized by higher $\hat{\bar{u}}$ near the side walls ($\Delta\hat{\bar{u}}$ = 0.26 at $\hat{y}$ = ±0.45), but farther downstream ($\hat{x}$ = 42), $\hat{\bar{u}}(\hat{y})$ is identical in the absence and presence of reed. In fact, at *Re* = 7,000 and 12,000 $\hat{\bar{u}}(\hat{y})$ at $\hat{x}$ = 30 and 42 in the presence of reed is also nearly identical. These data indicate that the interactions between the perturbations induced by the reed and natural instabilities of the transitional base flow (*Re* = 7,000) accelerate the transition to turbulence and that even at *Re* = 7,000 the mean flow in the presence of the reed is similar to the base flow at *Re* = 12,000, where the base flow is nearly fully turbulent (this is discussed further in connection with Figure 4.17).

The differences the time-averaged fluctuating flow field are also analyzed in the absence and presence of reeds using the corresponding cross-stream distributions of the kinetic energy, $\hat{k}_f$ at $\hat{x}$ = 18, 30 and 42 as shown in Figure 4,17 for *Re* = 2,000 (Figures 4.17-a.1 and b.1), 7,000 (Figures 4.17-a.2 and b.2) and 12,000 (Figures 4.17-a.3 and b.3). The distributions of $\hat{k}_f$ at *Re* = 2,000 are discussed in § 4.3 (Figure 4.14) and are repeated here for reference. Compared to the presence of the reed at *Re* = 2,000 (Figure 4.17-b.1), the velocity fluctuations in the base flow are negligible. The reed leads to a tri-lobed distribution of $\hat{k}_f$ near its tip, that decreases farther downstream due to small-scale dissipation. At *Re* = 7,000 and 12,000, the base flow exhibits some streamwise increase in $\hat{k}_f$ due to transition to turbulence which is higher for *Re* = 12,000 (Figures 4.17-a.3) and is manifested primarily by larger streamwise increases near the side walls of the channel, and a local minimum at its center. The nearly four-fold increase in $\hat{k}_f$ at *Re* = 7,000 (Figure 4.17-a.2) between $\hat{x}$ = 30 and 42 near the side walls ($\hat{y}$ = ±0.45) indicates that the transition begins close to the wall near the channel exit while at *Re* = 12,000 transition occurs farther upstream. Near the walls at $\hat{x}$ = 18, $\hat{k}_f$ is an order of magnitude higher at *Re* = 12,000 than at *Re* = 7,000 and continues to increase streamwise near the wall until $\hat{k}_f$ ($\hat{y}$ = ±0.45) ≈ 0.018 through $\hat{x}$ = 42 albeit at a lower rate. In the presence of reed (Figures 4.17-b.2 and b.3), $\hat{k}_f(y)$ is significantly higher than in the base flow near the tip ($\hat{x}$ = 18) throughout the channel height. There is a local peak at the channel center at *Re* = 7,000 that flattens out at *Re* = 12,000 with peaks near the side walls (recall that each distribution of $k_f(\hat{y})$ is normalized by its own averaged channel speed). However, the dimensional levels of the peak, $k_f(\hat{y} = 0, \hat{x} = 18)$, show a nearly 10-fold increase between *Re* = 2,000 and 7,000 (from 1.37 to 14.39 m^2/s^2, respectively) showing that the reed-induced

fluctuations amplify with *Re* in the transitional base flow. The distributions of $\hat{k}_f$ in Figure 4.17-b.2 and b.3 also show that the fluctuations induced by the reed encounter increased dissipation (as discussed in connection with Figure 4.19) that is manifested by a significant streamwise decrease in $\hat{k}_f$. For example, the decreases in $\hat{k}_f(\hat{y} = 0)$ at *Re* =7,000 are 87% and 41% between $\hat{x}$ = 18 & 30 and 30 & 42 respectively and at *Re* =12,000 are 66% and 54% between $\hat{x}$ = 18 & 30 and 30 & 42 (compared to 58% and 60% at *Re* = 2,000, respectively). It may be concluded that since the base flow near the tip of the reed is already transitional at *Re* = 12,000 small-scale dissipation is higher compared to *Re* = 7,000 which leads to lower $\hat{k}_f$ at $\hat{x}$ = 18 (2*H* downstream of tip). An important observation is that at both *Re* = 7,000 and 12,000, the levels of $\hat{k}_f$(y) across the channel width in the presence of reed near the exit plane of the channel ($\hat{x}$ = 42) become nearly identical to the levels in the base flow at *Re* = 12,000 indicating, as expected, that the presence of the reed accelerates the transition process (similar to pulsating channel flows, e.g., Trip et al., 2012).

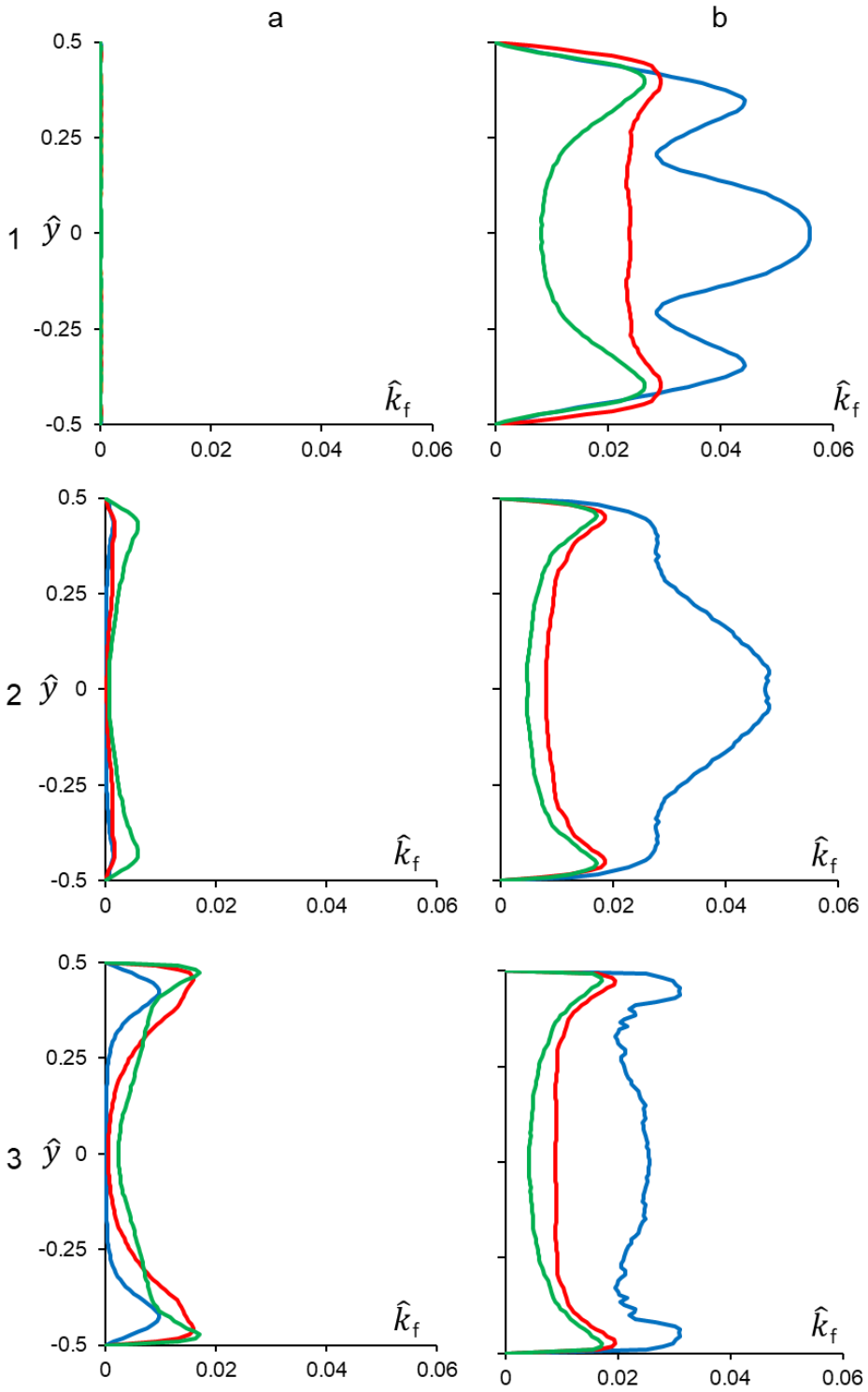

Figure 4.17 *Cross-stream distributions (at $z = 0$) of the fluctuating kinetic energ $\hat{k}_f$ at $\hat{x} =$ **18**, **30** and **42** in the absence and presence of the reeds (cf. Figure 4.17) at Re = 2,000 (a.1 and b.1), 7,000 (a.2 and b.2) and 12,000 (a.3 and b.3).*

The details of the streamwise evolution of the small-scale motions in the flow are captured using cross-stream integral of Equation 4.4 and considering the dominant terms which are $\widehat{M}_f$, $\widehat{D}_{vf}$ and $\widehat{T}_{pf}$ at the streamwise centers of PIV planes (similar to §4.3). Neglecting the smaller terms, the cross-stream integrated Equation 4.4 is: $<\widehat{M}_f> = <\widehat{D}_{vf}>+<\widehat{T}_{pf}>$, where $<\widehat{D}_{vf}>$ represents a loss due to small-scale dissipation ($<\widehat{D}_{vf}> < 0$). Following the assumptions associated with Equation 4.4, $<\widehat{M}_f> = \frac{d\hat{k}_m}{d\hat{x}}$, where $\hat{k}_m$ is the (normalized) bulk mean fluctuation kinetic energy $\hat{k}_m = \int_{-0.5}^{0.5} \hat{\bar{u}}(\hat{y})\, \hat{k}_f(\hat{y}) d(\hat{y})$. The streamwise variations of $<\widehat{M}_f>$ in the absence and presence of reed for *Re* = 2,000, 7,000 and 12,000 are shown in Figure 4.18. In the absence of the reed, $<\widehat{M}_f> > 0$ for *Re* = 7,000 and 12,000 indicating that $\hat{k}_m$ increases in the streamwise direction as the base flow transitions to turbulence and the peaks ($\hat{x}$ = 30 and 20 at *Re* = 7,000 and 12,000) indicate the streamwise location where the transition occurs. That $<\widehat{M}_f> \sim 0$ near the channel exit ($\hat{x}$ = 48) shows that the flow has fully developed and $\hat{k}_m$ is streamwise

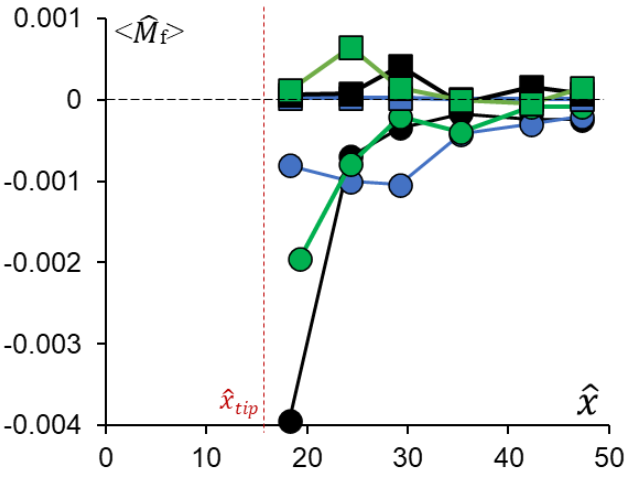

Figure 4.18 *Streamwise variation of the cross-stream integrated material rate of change of* $\hat{k}_f$, $<\widehat{M}_f>$ *in the absence and presence of the reed (cf. figure 4.18) for Re = 2,000 (■, ●), 7,000 (■,●), 12,000 (■,●). The position of the reed-tip is shown by a* ***dashed line****.*

invariant. In the presence of reeds, $<\widehat{M}_f> < 0$ for all *Re* which simply indicates that $\hat{k}_m$ decreases in the streamwise direction and based on the cross-stream averaged budget of $\hat{k}_f$, this means that the (cross-stream) averaged small-scale dissipation $<\widehat{D}_{vf}>$ is higher than the transport of $\hat{k}_f$ by pressure fluctuations $<\hat{T}_{pf}>$. It should be noted that in Figure 4.18, the magnitude of $<\widehat{M}_f>$ near the reed tip is significantly higher than that of the base flow. In addition, for $\hat{x} > 40$, $<\widehat{M}_f> \sim -10^{-4}$ indicating that in the presence of reeds $\hat{k}_m$ is nearly streamwise-invariant at all *Re* near the channel exit. At *Re* = 2,000, while $<\widehat{M}_f> \sim -10^{-3}$ for $\hat{x} < 30$ indicating a nearly constant rate decrease of $\hat{k}_m$, it diminishes to near zero level at the channel exit. At *Re* = 7,000 and 12,000, while the magnitudes of $<\widehat{M}_f>$ near the tip ($\hat{x} = 18$) are 2- and 4-fold higher than at *Re* = 2,000, they also diminish faster and reach $<\widehat{M}_f> \sim -10^{-4}$ for $\hat{x} \geq 30$ indicating that $<\widehat{D}_{vf}>$ is nearly balanced by $<\hat{T}_{pf}>$. These data show that near the channel exit ($\hat{x} > 40$), $\hat{k}_m$ reaches the same asymptotic level at all the Reynolds numbers considered here.

The evolution of asymptotic levels of $\hat{k}_m$ that are comparable upstream of the channel's exit in the presence of the reed are further explored and compared with the base flow by considering the streamwise variations of $\hat{k}_m$ and $<\widehat{D}_{vf}>$ as shown in Figures 4.19 in the absence and presence of reed at *Re* = 2,000 (Figures 4.19-a.1 and b.1), 7,000 (Figures 4.19-a.2 and b.2) and 12,000 (Figures 4.19-a.3 and b.3). Each of the figures includes a dashed line that marks for reference the corresponding streamwise-asymptotic levels of $\hat{k}_m$ and $<\widehat{D}_{vf}>$ at *Re* = 12,000 (0.008 and 0.02, respectively). The present data show that $|<\widehat{M}_f>| < 0.029|<\widehat{D}_{vf}>|$ or $0.03|<\hat{T}_{pf}>|$ and since $|<\widehat{D}_{vf}>| \approx |<\hat{T}_{pf}>|$ only $<\widehat{D}_{vf}>$ is discussed here. At *Re* = 2,000, $\hat{k}_m$ and $<\widehat{D}_{vf}>$ (Figures 4.19-a.1 and b.1) are negligible in the base

flow, but in the presence of reed, $\hat{k}_m$ decreases downstream of the reed from 0.03 at $\hat{x}$ = 18 to 0.0125 at the channel exit ($\hat{x}$ = 47). Evidently, the small-scale dissipation, $<\hat{D}_{vf}>$ (Figures 4.19-b.1) which drives the decrease in $\hat{k}_m$ also exhibits a streamwise decrease from 0.09 at $\hat{x}$ = 18 to 0.03 at $\hat{x}$ = 47 indicating that within the current channel both quantities are still significantly larger than in the base flow and would remain well above

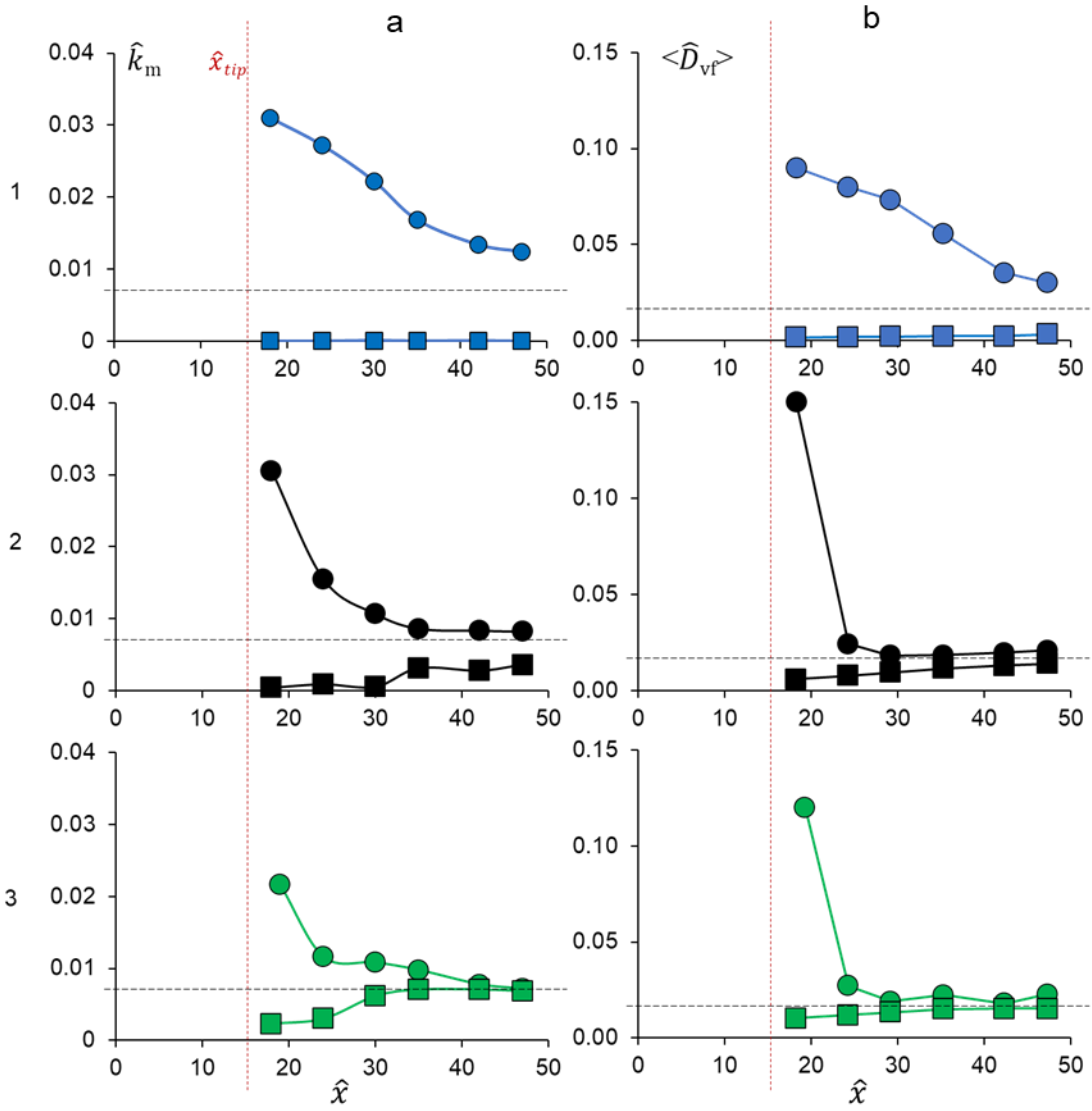

Figure 4.19 *Streamwise variations of bulk mean fluctuation kinetic energy $\hat{k}_m$ and the cross-stream averaged $<\hat{D}_{vf}>$ (columns a and b, respectively) in the absence (■) and presence (●) of the reed for Re = 2,000 (■, ●), 7,000 (■, ●), 12,000 (■, ●). The position of the tip is shown using vertical* ***dashed lines****. The asymptotic values, $\hat{k}_m$ = 0.008 and $\hat{D}_{vf}$ = 0.02 at Re= 12,000 are shown using horizontal dashed lines.*

the base flow levels in a longer channel. At *Re* = 7,000, while an increase in $\hat{k}_m$ for the base flow (Figure 4.19-a.2) is evident at $\hat{x}$ = 30 due to transition, for $\hat{x} \geq 36$, $\hat{k}_m$ asymptotes to ~ 0.003 which is still well below the corresponding level at *Re* = 12,000 (in Figure 4.19-a.3). In the presence of reed (Figure 4.19-a.2), $\hat{k}_m$ is higher than the base flow throughout the channel and the rate of its streamwise decrease is higher than at *Re* = 2,000. However, for $\hat{x} \geq 36$, $\hat{k}_m$ = 0.0082 which is just slightly above the level of the asymptote at *Re* = 12,000 (0.008). The corresponding small-scale dissipation, $<\hat{D}_{vf}>$ (Figure 4.19-b.2) in base flow increases monotonically until $<\hat{D}_{vf}>$ ~ 0.02 and in the presence of reed, $<\hat{D}_{vf}>$ decreases rapidly from 0.15 near the tip ($\hat{x}$ = 18) to $<\hat{D}_{vf}>$ ~ 0.02 for $\hat{x} \geq 30$ and nearly matches the corresponding level in the base flow and the asymptote at *Re* = 12,000 near the channel exit ($\hat{x}$ = 47). It is noted that in the presence of reed $<\hat{D}_{vf}>$ near the tip ($\hat{x}$ = 18) at *Re* = 7,000 is 66% higher than the corresponding $<\hat{D}_{vf}>$ at *Re* = 2,000 which leads to a higher streamwise decrease in $\hat{k}_m$ near the tip at *Re* = 7,000. The smaller levels of $<\hat{D}_{vf}>$ farther downstream ($\hat{x} \geq 30$) at *Re* = 7,000 are associated with lower streamwise decrease of $\hat{k}_m$. The streamwise trends of $\hat{k}_m$ and $<\hat{D}_{vf}>$ in the absence and presence of reed are similar at *Re* = 7,000 (Figures 4.19-a.2 and b.2) and 12,000 (Figures 4.19-a.3 and b.3). It is noteworthy that both in the absence and presence of reed at *Re* = 12,000 $\hat{k}_m$ asymptotes to $\hat{k}_m$ ~ 0.008 for $\hat{x} \geq 40$ which is also its asymptotic level at *Re* = 7,000 in the presence of reed while $<\hat{D}_{vf}>$ at *Re* = 7,000 and 12,000 asymptotes to $<\hat{D}_{vf}>$ ~ 0.02 for $\hat{x} \geq 40$. These data further lend credence to the observation that the reed-induced perturbations accelerate the transition to turbulence in the predominantly developing inlet channel flow at *Re* = 7,000. This acceleration of the transition to turbulence of the (laminar) inlet flow is further hastened at higher Reynolds numbers, and is accompanied by accentuated

dissipation of the reed-induced flow fluctuations and the decay of $\hat{k}_{\mathrm{m}}$ to the levels that are associated with the natural transition to fully-developed turbulent channel flow at the prevailing Reynolds number. That the reed induced fluctuations upstream of the channel's exit are still higher than in the base flow, can lead to enhanced heat transfer within the channel (as discussed in Chapter V).

As alluded to by Figures 4.16 and 4.17, the evolution of reed-induced perturbations is affected by interactions with the small-scale motions in the transitioning base flow. The streamwise evolution of the spectral content of the flow is shown in Figure 4.20 using power spectral density (*PSD*) of the streamwise velocity fluctuations, *u*', at the spanwise center ($z = 0$) of the channel. These measurements are obtained using a hot wire sensor which having a cross-stream width of 2 mm ($|\hat{y}| < 0.2$, centered about $y = 0$). The spectral measurements are obtained at three equally spaced streamwise positions downstream of the reed ($\hat{x}$ = 20, 30 and 40) for *Re* = 2,000, 7,000 and 12,000 in the absence (Figures 4.20-a.1 through a.3) and presence of reeds (Figures 4.20-b.1 through b.3). In the absence of the reeds at *Re* = 2,000 (Figure 4.20-a.1), the spectra exhibit low *PSD* ($PSD < 10^{-5}$) at all streamwise positions. The presence of the reed (Figure 4.20-b.1) leads to a remarkable 2-decade increase in the flow's spectral energy to $PSD \sim 10^{-4}$ for $\phi < 1{,}000$ Hz, with spectral peaks at the reed's fundamental frequency (65 Hz) and its higher harmonics and spectral decay for $\phi > 1{,}000$ Hz (all spectral components are higher than the base flow spectral components). Farther downstream ($\hat{x}$ = 30, 40), the spectral peaks at the reed harmonics diminish by 1-2 orders of magnitude and the *PSD* at the large scales ($\phi < 50$ Hz) increases by up to an order in magnitude. It is remarkable that the reed oscillations lead to a spectrum that is reminiscent of turbulent spectra at considerably higher Reynold numbers with a brief -5/3 slope.

As the Reynold number is increased to 7,000, the spectral content of the base flow (Figure 4.20-a.2) increases significantly at all streamwise stations with a peak at 380 Hz and several of its harmonics that are probably associated with transitional instabilities of the flow, and a pronounced spectral decay (higher than -5/3) past 1000 Hz. Similar spectral

trends are observed farther downstream with an increase in the energy of the large-scale motions between $\hat{x}$ = 20 and 30. That the *PSD* become nearly invariant for $30 < \hat{x} < 40$ indicates that the flow becomes nearly fully developed. In the presence of the reed ($\hat{x}$ = 20, Figure 4.20-b.2) the levels of the spectral content of the *PSD* at *Re* = 7,000 increase significantly compared to the base flow by up to 2 decades at about 1,000 Hz, and up to 3 decades for $\phi >$ 1,000 Hz with a well-defined inertial subrange. Farther downstream ($\hat{x}$ = 30 and 40), the spectral levels decrease due to small-scale dissipation (as discussed in connection with Figure 4.21) albeit the spectra at the reed harmonics show higher decrease (the spectral peak at the third reed harmonics decreases by two decades, whereas the spectra for $\phi <$ 100 Hz and $\phi >$ 1000Hz decreases by less than a decade between $\hat{x}$ = 20 and 40). A comparison between the reed spectra at $\hat{x}$ = 40 between *Re* = 2,000 and 7,000 (shown in green in Figures 4.20-b.1 and b.2) shows the presence of a cross-over frequency, $\phi_c \approx$ 1000 Hz (marked by a vertical dashed line in column b), below which the spectral levels are higher at *Re* = 2,000 by up to 6 times and above which the spectral levels are higher for *Re* = 7,000 by up to 2 decades. This indicates that even for the same Strouhal number the interactions between reed induced scales and the transitional flow (*Re* = 7,000) lead to formation of smaller scales which, as shown in Chapter V, lead to higher heat transfer enhancement. When the Reynolds number is increased to 12,000, the amplitude of spectral components in the base flow (Figure 4.20-a.3) at $\hat{x}$ = 20 at $\phi >$ 2 KHz increases significantly compared to the base flow at *Re* = 7,000 (including the dissipation range). As the transition process continues farther downstream ($\hat{x}$ = 30 and 40), the upward offset of the spectra with increasing streamwise distance diminishes until the flow becomes nearly fully developed (at $\hat{x}$ = 40). It is noted that while the spectral peaks that are associated with

the transitional flow are no longer present, the spectra exhibit a lower, wider peak around 260 Hz. The spectral changes that are brought about by the presence of the reed (Figure 4.20-b.3) at $\hat{x}$ = 20 include spectral peaks at the reeds oscillation frequency (380 Hz) and its harmonics. Similar to the spectra at *Re* = 7,000, the spectral components at the reed harmonics are offset downward by a factor of 1 and 2 decades at $\hat{x}$ = 30 and 40 respectively. In accordance with the accelerated dissipation in the presence of the reed, the spectral components at $\hat{x}$ = 30 and 40 within the range ϕ < 300 Hz are actually marginally *lower* in the presence of the reed than the corresponding spectra of the base flow. In addition, compared to the reed spectra at $\hat{x}$ = 40 for *Re* = 7,000 (cf. Figure 4.20-b.2), while the spectral levels below the cross-over frequency ϕ_c are nearly invariant (for $\phi < \phi_c$, $PSD \sim 10^{-4}$), the spectra above ϕ_c increase at *Re* = 12,000 by up to 3 times indicating that the interactions with the fully turbulent base flow further increases the energy of smaller scales.

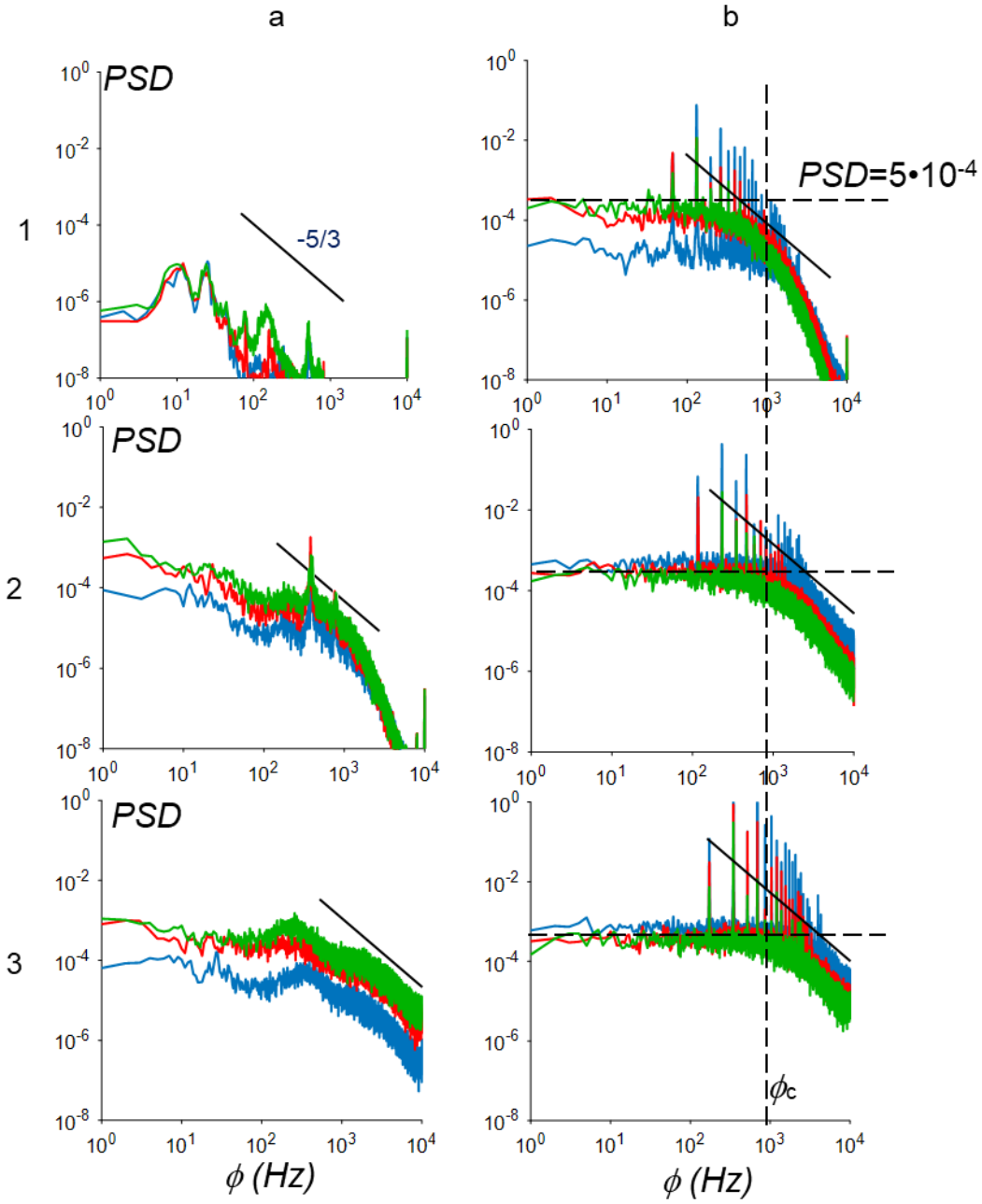

Figure 4.20 *Power spectra (PSD) of the streamwise velocity fluctuations u' measured at the spanwise center of the channel (z = 0) at three streamwise locations downstream of the reed tip $\hat{x}$ = 20, 30 and 40 in the absence (column a) and presence (column b) of the reed at Re = 2,000, 7,000 and 12,000 (rows 1,2 and ,3 respectively). The solid line marks -5/3 slope. The cross-over frequency, ϕ_c for reeds is represented by the vertical dashed line and the asymptotic PSD levels for large scales (ϕ<1Hz) at $\hat{x}$ = 40 in the presence of reeds is represented through the horizontal dashed lines.*

Considering the streamwise changes in the base flow, especially during transition, it is instructive to examine the effects of the streamwise position of the reed relative to the base flow. These effects are compared for an invariant reed length (L_s/W=10) in Figure 4.21 between tip streamwise placements at $\hat{x}_{tip}$ = 16 and 26 at Re = 12,000 using the streamwise variation of $\hat{k}_m$ (at z = 0). The variation of $\hat{k}_m$ for $\hat{x}_{tip}$ = 16 was discussed in connection with Figure 4.19-b.3 (L_s/W = 10, t_s = 127 μm, f_{osc} = 380 Hz and St_L = 0.5), and is repeated here for reference. These data show similar increase in intensity of small-scales even when the tip of the reed is placed where the turbulence level in the base flow is already relatively high. In fact, $\hat{k}_{m,\,base}$ = 0.0023 and 0.0041 at $\hat{x}_{tip}$ = 16 and 26, respectively (the asymptotic level is $\hat{k}_m$ = 0.008), and the level of the reed-induced $\hat{k}_m$ at $\hat{x}$ = 29 for $\hat{x}_{tip}$ = 26 is only about 18% lower than at the same distance from the tip for $\hat{x}_{tip}$ = 16 ($\hat{x}$ =19) despite the significant increase in the background turbulence level in the channel. Furthermore,

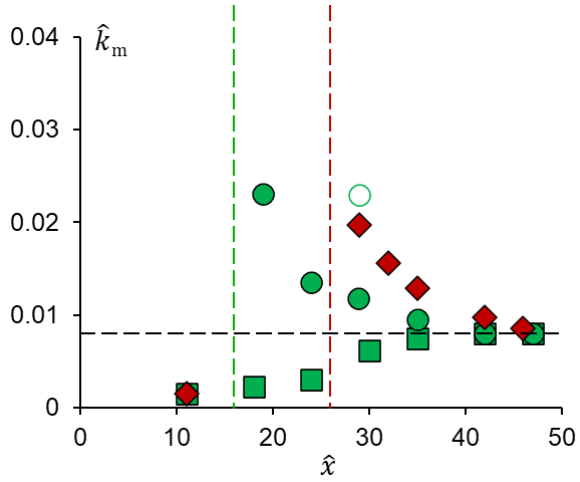

Figure 4.21 *Streamwise variation of $\hat{k}_m$ (at z = 0) in the absence (■) and presence of the reed (L_s/W = 10, t_s = 127 μm) at Re = 12,000 when the tip of the reed is placed at locations $\hat{x}_{tip}$ = 16 (●) and 26 (♦). The streamwise locations of the reed tips are marked using vertical dashed lines and the asymptotic level of $\hat{k}_m$ at the downstream end of the channel ($\hat{k}_m$ = 0.008) is marked by a horizontal dashed line. The data point closest to the reed tip at $\hat{x}$ = 19 is offset by $\hat{x}$ = 10 and marked using ○ for comparison with the corresponding data for $\hat{x}_{tip}$ = 26.*

downstream of the tip $\hat{x}_{tip}$ = 26, the exponential rate of streamwise decay of $\hat{k}_m$ is 1.4 times *higher* than for $\hat{x}_{tip}$ = 16 and it asymptotes to nearly the same level of $\hat{k}_m$ = 0.008 as in the base flow near the channel's exit. These data show that despite the higher levels of turbulence intensity in the base flow, the reed is still able to effect significantly higher levels of $\hat{k}_m$ (5 times the base level) although its rate of decay is higher than when the reed is placed farther upstream where the inlet base flow is still transitional. *The present data indicate that when the tip of the reed is placed at streamwise position where the base flow is already asymptotically turbulent for this Reynold number, the streamwise decay of the reed-induced oscillations would be higher and therefore its streamwise domain of influence would be shorter with significant ramifications for enhancement of heat transfer over the base flow downstream of the tip of the reed.*

4.5 The Role of the Reed Oscillation Strouhal Number

The role of the reed's oscillation frequency on the evolution of the flow in the channel is captured by varying its Strouhal number at a given intermediate transitional Reynolds number (Re = 5,000) of the channel flow (the evolution of the channel's time-averaged base flow is described in Appendix B). This Reynolds number is selected because the flow response is somewhat more muted over a range of reed frequencies than at Re = 7,000 (characterized in §4.4), but the channel speed is above the critical speed of a range of reeds covering nearly the entire channel span H_s/H = 0.9 that are designed with several lengths and thicknesses to achieve Strouhal numbers between 0.3 and 1.6.

The effect of reed Strouhal numbers on the mean and fluctuating flow fields are first assessed using reeds of L_s/W = 10 and t_s = 25.4, 38.1 and 50.8 μm for which St_L = 0.9, 0.7 and 0.5 (f_{osc} = 180 Hz, 140 and 95 Hz), respectively. Similar to §4.4, the mean and fluctuating flow fields are assessed using cross-stream distributions of the streamwise velocity $\hat{\bar{u}}$ and fluctuating kinetic energy $\hat{k}_f$ at z = 0 at $\hat{x}$ = 18 (Figures 4.22-a.1 and b.1), 30 (Figures 4.22-a.2 and b.2) and 42 (Figures 4.24-a.3 and b.3). As noted in connection with Figure 4.16, compared to the base flow, the oscillations lead to increases in the streamwise velocity near the walls and its flattening near the center of the channel downstream of the reed. Furthermore, as shown in Figures 4.22-a.1, a.2, and a.3, these changes are nearly the same at all Strouhal numbers, nearly streamwise invariant, and resemble the distributions of $\hat{\bar{u}}$(y) in the base flow at higher Reynolds numbers (Re = 12,000, Figure 4.16). Figure 4.22-b.1 shows that while the effects of the reed Strouhal number on $\hat{\bar{u}}$(y) are marginal near

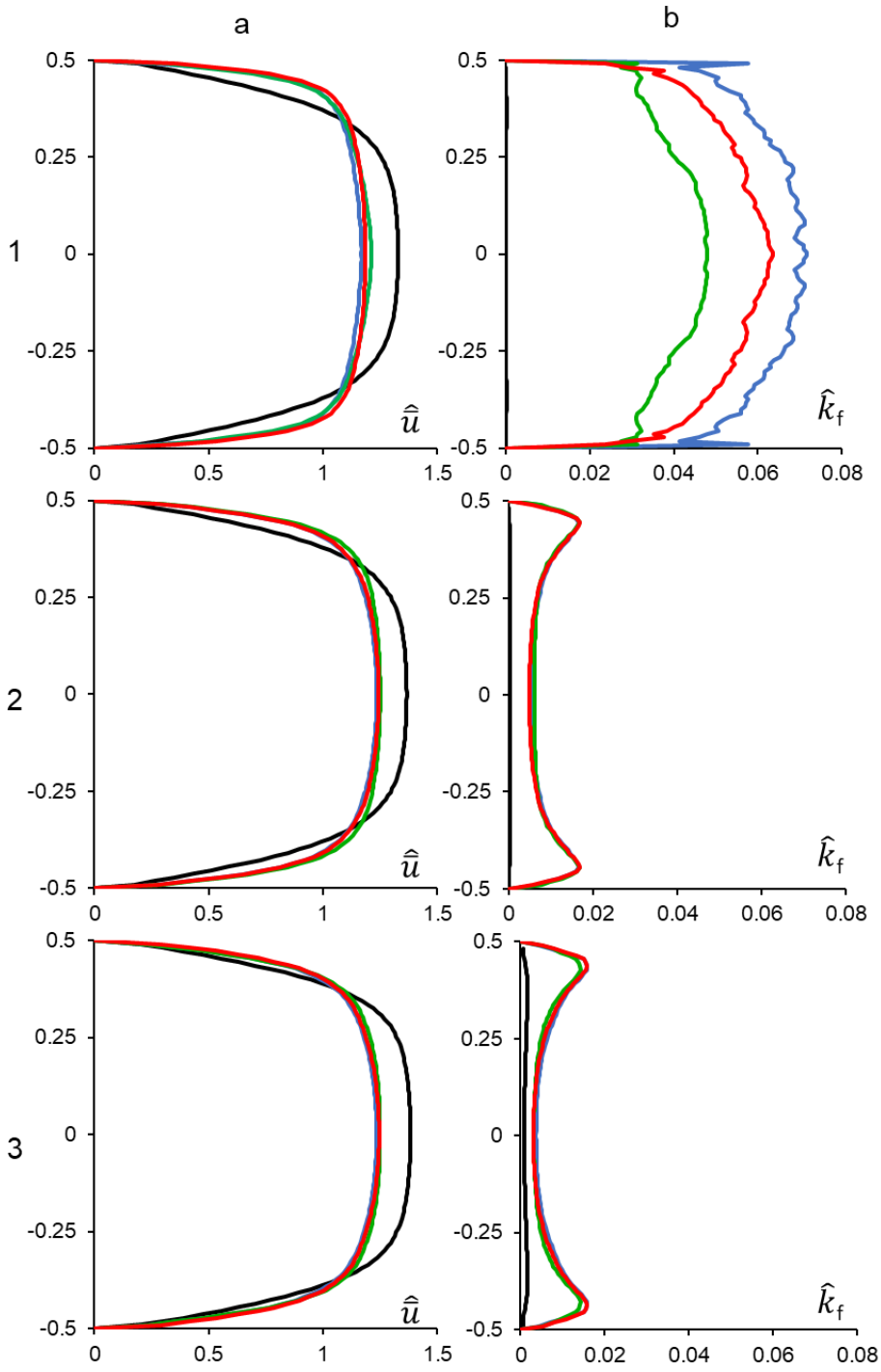

Figure 4.22*. Cross-stream distributions (at z = 0) of the time-averaged streamwise velocity* $\hat{\bar{u}}$ *and fluctuating kinetic energy,* $\hat{k}_f$ *(columns a and b respectively) in the absence (marked by a black line) and presence of reeds (*$L_s/W = 10$*, Re = 5,000) oscillating at* St_L *= **0.5**, **0.7** and **0.9**, at* $\hat{x} = 18$ *(a.1 and b.1), 30 (a.2 and b.2) and 42 (a.3 and b.3).*

its tip and nearly indistinguishable farther downstream, the cross stream distributions of $\hat{k}_f$ (y) near the reed's tip increase (across the channel width) with St_L and are significantly higher than in the base flow $\hat{k}_f$ (y). These distributions are clearly associated with the changes in the kinetic energy of the reed motion which increases as the square of the oscillation frequency (cf. §3.4). For example, at the channel center ($y = 0$), $\hat{k}_f$ for $St_L = 0.5$, 0.7 and 0.9 are 0.045. 0.062 and 0.072, respectively compared to 0.0004 in the base flow. However, similar to the corresponding data in Figure 4.17, the induced increases in $\hat{k}_f$ diminish rapidly farther downstream, become nearly streamwise-invariant, and the variations between oscillations at the different Strouhal numbers become indistinguishable at $\hat{x} = 30$ and 42 (Figures 4.22-b.2 and b.3). That the differences in $\hat{k}_f$ due to the reed St_L in Figure 4.22-b.1 nearly vanish downstream, indicates that higher induced velocity fluctuations are also accompanied by increased dissipation.

The changes in streamwise evolution of the small-scale motions downstream of the reed due to the variation in St_L are captured using the bulk mean fluctuating kinetic energy $\hat{k}_m$ (similar to the analysis in §4.4). The range of St_L in Figure 4.22 was expanded in Figure 4.23. In addition to St_L (f_{osc}, Hz) = 0.9 (180), 0.7 (140), and 0.5 (95) using $L_s/W = 10$ (Figure 4.23a), a broader range of Strouhal numbers was achieved using reeds that are t_s = 25.4 μm thick and variable lengths L_s/W = 2.4, 10, 20 yielding St_L (f_{osc}, Hz) = 0.3 (250), 0.9 (180), and 1.6 (160) (Figure 4.23b). As shown in Figures 4.23a and b, the streamwise variations of $\hat{k}_m$ in the absence of reeds are much smaller ($\hat{k}_m < 0.001$) than in its presence. As expected based on Figure 4.22-b.1, for reeds of length, $L_s/W = 10$ (St_L = 0.5, 0.7 and 0.9, Figure 4.23a), downstream of the tip ($\hat{x}$ = 17.5) $\hat{k}_m$ increases with St_L ($\hat{k}_m$ = 0.042, 0.05 and 0.065 for St_L = 0.5, 0.7 and 0.9 respectively). Farther downstream, $\hat{k}_m$ decreases exponentially but near the tip its streamwise diminution rate

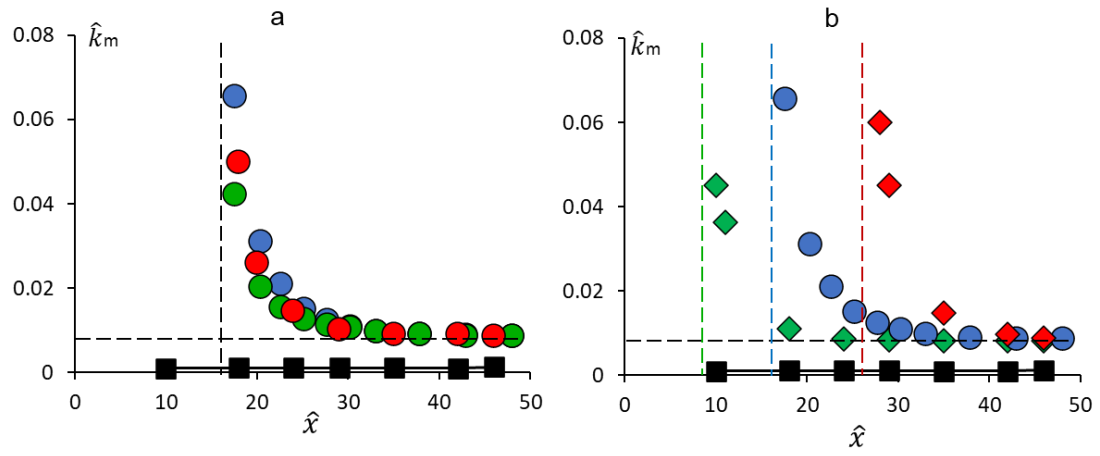

Figure 4.23 *Streamwise variation of $\hat{k}_m$ in the absence (■) and presence of for reeds of b) length, L_s/W = 10 and thickness, t_s = 25.4 μm (●, St_L= 0.9), 38.1 μm (●, St_L = 0.7) and 50.8 μm (●, St_L = 0.5) and b) of thickness, t_s = 25.4 μm and lengths L_s/W = 2.4 (♦, St_L = 0.3), 10 (●, St_L = 0.9) and 20 (♦, St_L = 1.6) at Re = 5,000. The horizontal and black line represents $\hat{k}_m$ = 0.008. The streamwise locations of the reeds are shown through the vertical dashed lines*

increases with St_L where $\Delta\hat{k}_m/\Delta\hat{x}$ are -0.007, -0.008 and - 0.012 for St_L = 0.5, 0.7 and 0.9. As a result of the enhanced dissipation at higher St_L, farther downstream the decay rates of $\hat{k}_m$ equalize and become independent of St_L (at $\hat{x}$ = 24 $\hat{k}_m$ ~0.014, and for $\hat{x}$ > 24 $\hat{k}_m$ = 0.008). As noted above, the variation of $\hat{k}_m$ with St_L for increasing reed length (Figure 4.23b) also yields some insight into the effects of the streamwise position of the reed tip (marked by vertical dashed lines) in the developing channel flow. These data show that while as expected, $\hat{k}_m$ increases with the Strouhal number (from 0.045 to 0.065 between L_s/W = 2.4 and 10), it decreases slightly as St_L is increased further (to 0.06 at L_s/W = 20) exhibiting some saturation ostensibly due to increased small-scale dissipation (as discussed in Figure 4.24). Similar to the observations in connection with Figure 4.23a, the streamwise rate of decrease of $\hat{k}_m$ in Figure 4.23b increases with St_L ($\hat{k}_m$ asymptotes to 0.008 near the channel exit).

The streamwise variations of dissipation of small scales $<\hat{D}_{vf}>$ are assessed in Figures 4.24a and b in the absence and presence of reeds respectively. As expected based on Figure

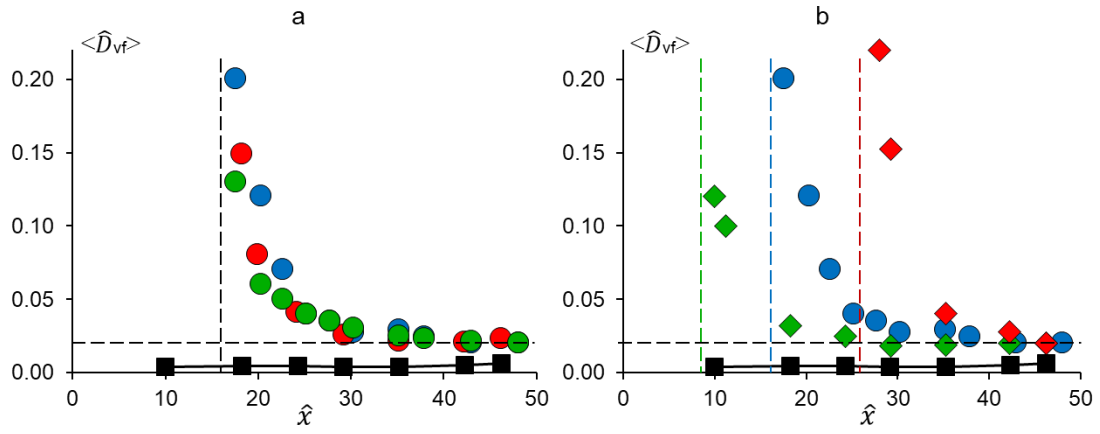

Figure 4.24 *a) As in figure 4.23 (a) and (b), the streamwise variations of cross-stream averaged small-scale dissipation,* $<\hat{D}_{vf}>$ *in the absence and presence of reeds. The horizontal dashed line represents* $<\hat{D}_{vf}>$ *= 0.02 (cf. Figure 4.19)*

4.23, small-scale dissipation which in the base flow is lower than with the reeds ($<\widehat{D}_{vf}>_{base} < 6 \cdot 10^{-3}$), increases significantly with St_L near the tip, and ultimately decays farther downstream and is nearly identical for all St_L near the channel exit ($<\widehat{D}_{vf}> = 0.02$, which is the level of the base flow at Re = 12,000 near the channel exit, cf. Figure 4.19). As discussed in Chapter V, enhanced local heat transfer at higher St_L decreases farther downstream of the tip and therefore St_L can be tuned for optimizing the reed's thermal performance.

The present investigations have demonstrated that increasing the reed Strouhal number results in increased global flow losses within the channel. These losses arise because the power for the motion of the reed is extracted from the embedding channel flow (cf. §3.1), and the formation and dissipation of the reed-induced vortical motions (cf. Figures 3.12 and 4.3) contribute to additional losses in the mean and fluctuating kinetic energy budgets (c.f. Equation 4.3 and 4.4) that must be compensated for by the air supply (cf. Figure 4.6). That the intensity of the reed-induced small-scale vortical motions and their dissipation *increase* with St_L (cf. Figures 4.23 and 4.24) indicates that channel pressure losses also increase with St_L.

The flow losses in the channel are assessed using the channel's friction factor $f = \Delta P/(0.5 \cdot \rho_a \cdot U^2 \cdot L/D_h$, (e.g., Çengel et al., 2006) over a range of Strouhal numbers of several reeds (span $H_s/H = 0.9$) as shown in Figure 4.25 The Strouhal numbers were varied

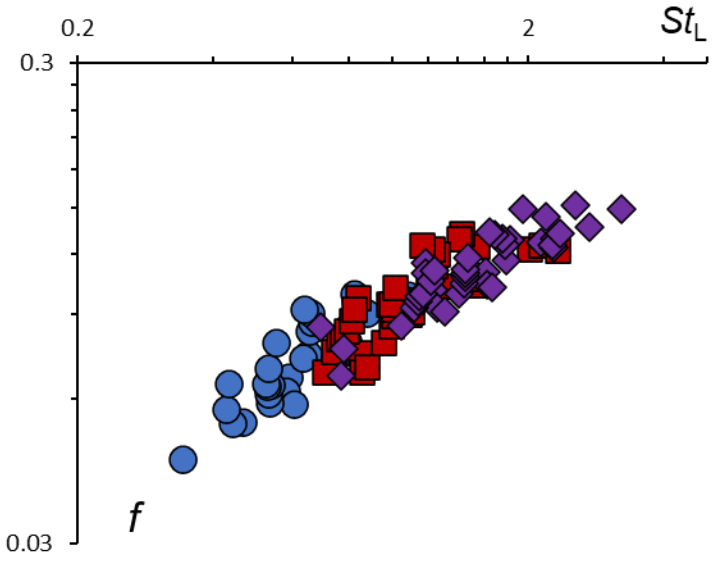

***Figure 4.25**. Variation with St_L of the channel friction factor f for 1,000 < Re < 10,000 and reeds of length $L_s/W = 10$ (●), 20 (■) and 30 (♦) and thicknesses t_s = 12.7, 25.4, 38.1, 50.4 and 76.2 μm.*

over a range of channel Reynolds numbers (1,000 < *Re* < 10,000) using multiple reeds of different lengths (L_s/W = 10, 20, 30, L_s = 50, 100 and 150 mm) and thicknesses (t_s = 12.7, 25.4, 38.1, 50.4 and 76.2 μm). These data show that the channel friction factor, *f*, increases with St_L by over a factor of 3 as St_L increases from 0.46 to3.22. Using a least-squares fit, the variations of *f* with St_L are shown in Equation 4.5

$$f = 0.1 \bullet (St_L)^{0.5} \qquad 4.5$$

Figure 4.25 shows that the friction factors induced at all Strouhal numbers by all the tested reeds (different lengths and thicknesses) collapse on a *single curve* regardless of the channel's Reynolds number. *This finding indicates that, at least within the range of the present measurements, the flow losses in the presence of the reeds primarily scale with* St_L.

Since the flow losses within the channel depend primarily on the reed Strouhal number, it is desirable to understand how for a given flow speed in the channel the reed parameters can be selected to yield a desired Strouhal number. As shown in other studies on oscillating reed dynamics (e.g., Argentina et al., 2005, Eloy et al., 2007, and Shoele et al., 2015), the reed motion is governed primarily by two dimensionless numbers: its inertia ratio $M^* = \rho_s t_s / (\rho_a L_s)$ and reduced velocity, $U^* = U \bullet \sqrt{\rho_a H_s {L_s}^3 / k_b}$, which are determined by the reed's mechanical properties (density ρ_s, and flexural rigidity k_b) and geometric dimensions (L_s x H_s x t_s) and the average flow speed and density (U and ρ_a). In the present investigations, the dependence of St_L on M^* and U^* is determined using data for all the reeds discussed in connection with Figure 4.25 (L_s/W = 10, 20 and 30 and t_s = 12.7, 25.4, 38.1, 50.4 and 76.2 μm) as shown in Figures 4.26a and b. Figure 4.26a

shows that St_L nominally decreases with M^* but for a given M^* some scatter in St_L is evident as the flow speed and hence U^* change. Similarly, Figure 4.26b shows that St_L nominally increases with U^* but with significant scatter. However, if M^* and U^* are combined to form the ratio M^*/U^*, it is shown in Figure 4.26c that the entire set of data collapses on a single curve for all the tested reeds and flow speeds (or *Re*). Since M^*/U^* varies as $U^{-1}(t_s/L_s)^{5/2}$, it is more sensitive to variations in reed's planform shape (length and thickness) than to the flow speed**.** Using a least-squares fit,

$$St_L = 0.23 \left(\frac{M^*}{U^*}\right)^{-0.33} \qquad 4.6$$

The data in Figure 4.26c show that St_L decreases rapidly with increasing M^*/U^* for $M^*/U^* < 0.05$, and for $M^*/U^* > 0.05$, St_L is nearly invariant (decreases from 0.52 to 0.46 as M^*/U^* changes from 0.05 to 0.15). This means that for a given reed length and thickness the frequency increases with flow speed as $U^{1.33}$, and for a given flow speed, the frequency decreases with reed thickness and length as $t^{-0.75}$ and $L^{-0.25}$. By comparison, the natural frequency of the reed in vacuum and away from walls varies as t and L^{-2} (G. A. Tetlow and A. D. Lucey, 2009) showing that the reed motion in proximity to the walls of the channel is significantly different. The variations of St_L with M^*/U^* were also computed for the low aspect ratio channel with $H/W = 1$ and the higher aspect ratio channel with $H/W = 10$. While the variations of St_L with M^*/U^* in $H/W = 5$ and 10 channels collapse on top of each other, reed Strouhal number is marginally smaller in the low aspect ratio channel (for a given M^*/U^*) such that $St_L = 0.24\,(M^*/U^*)^{-0.25}$ which is consistent with the observations in connection with reed centerlines in § 3.4.

An important finding of the present investigations is that the losses that are associated with the reed's motion are directly related to and decrease precipitously with its strouhal number, St_L as derived from the reed's oscillation frequency. It was found that the reed frequency decreases with increase in reed's length and thickness (for a fixed flow speed) and increases with increase in flow speed for a given reed planform shape (length and thickness) such that the reed strouhal number, St_L primarily scales with M^*/U^***.** The small-scale and the channel loss analysis suggest that by reducing the reed St_L the channel losses can be significantly decreased, while the intensity of small-scale motions as measured by $\hat{k}_m$, sustain downstream of the reed. The reed driven small-scales persist near the channel side walls and the reed makes a laminar base-flow look "turbulent" which, as seen in chapter V, leads to significant heat transfer enhancement. Even at fully turbulent *Re*, there exist a finite channel length where the reed enhances small-scale motions as compared to the base leading to heat transfer enhancement.

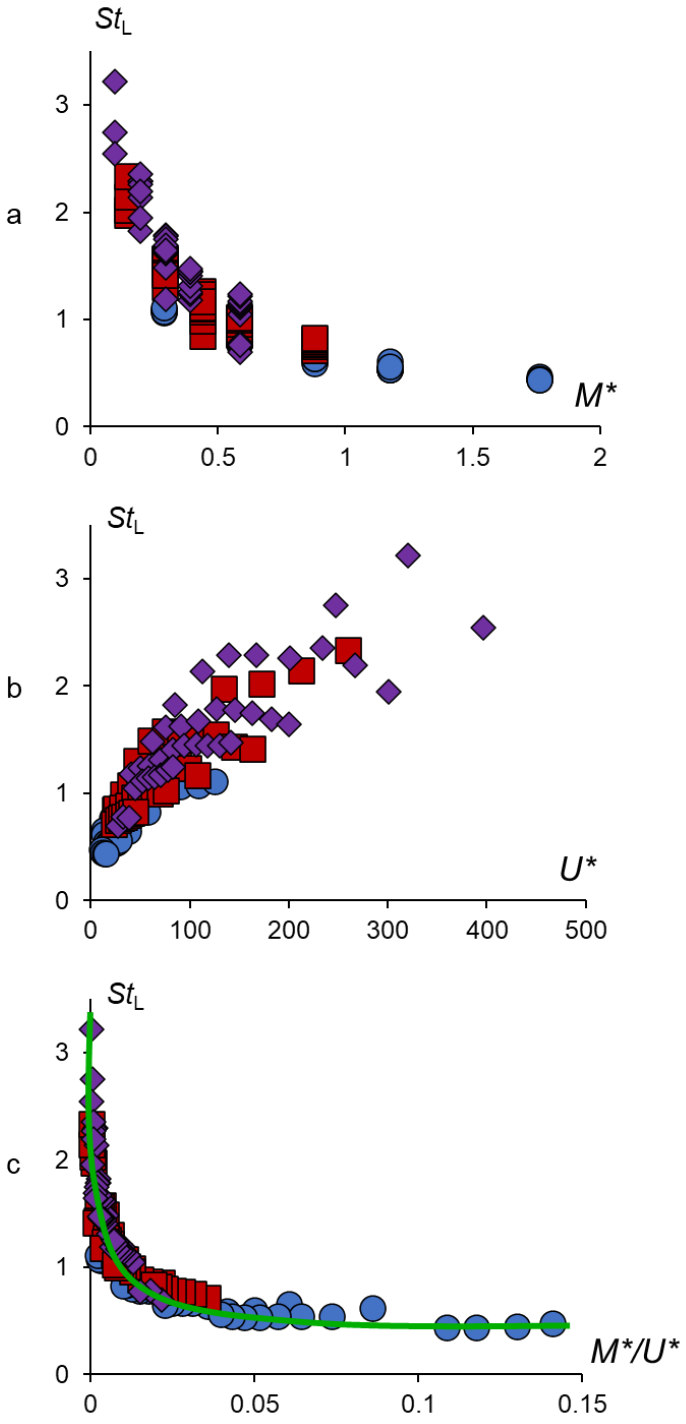

Figure 4.26. *Variation of St_L with reed inertia ratio M* (a), reduced speed U* (b) and the ratio M*/U* (c) for 1,000 < Re < 10,000 and reeds of length L_s/W = 10 (●), 20 (■) and 30 (♦) and thicknesses t_s = 12.7, 25.4, 38.1, 50.4 and 76.2 μm.*

CHAPTER V

HEAT TRANSFER ENHANCEMENT USING SELF-OSCILLATING REEDS

Overview

This chapter focuses on characterization of heat transfer enhancement effected by small-scale motions that are induced by the oscillations of reeds (cf. Chapters III and IV) mounted across the span of a high aspect ratio, heated channel (H/W = 5 or 5-mm wide channel). The effects of dominant parameters including the reed Strouhal number and the flow Reynolds number on the heat transfer enhancement are discussed in conjunction with the kinetic energy of the flow's small-scale motions. Limited investigations conducted in another higher aspect ratio channel (H/W = 10) illustrate the scaling of reed driven heat transfer enhancement.

5.1 Heat Transfer Analysis in the High Aspect Ratio Channel

To begin with, a description of "internal measurements" (cf. chapter II) which is used to assess the heat transfer characteristics in the high aspect ratio channels is given. This methodology utilizes the wall temperature measurements and the heat flux to the air from the heater to calculate the local and global Nusselt numbers.

The present heat transfer measurements were conducted in the high-aspect ratio HT channel that is described in detail in Chapter II (and is used in Chapters III and IV). In this

channel the wider (top and bottom) walls were constructed of aluminum plates covered (on the outside) with thin-film heaters and instrumented with a streamwise array of T-type thermocouple sensors along their mid spans ($z = 0$) as shown schematically in Figure 5.1a

In the present investigations, the power to the heaters is adjusted so that their power $\dot{Q}_{\text{heater}}$ is varied to achieve a desired difference between the wall temperature $T_{\text{w}}(x)$ and the air temperature $T_{\text{a,i}}$ measured $10W$ upstream of the channel inlet:

$$ITD(x) = T_{\text{w}}(x) - T_{\text{a,i}}$$

In the present experiments, $ITD_{\text{max}} = 60^{\text{o}}\text{C}$ in both the base flow and in the flow with reed.

The thermal enhancement is characterized using the local and global variations in heat transfer coefficient and is compared with the corresponding flow losses. The variation

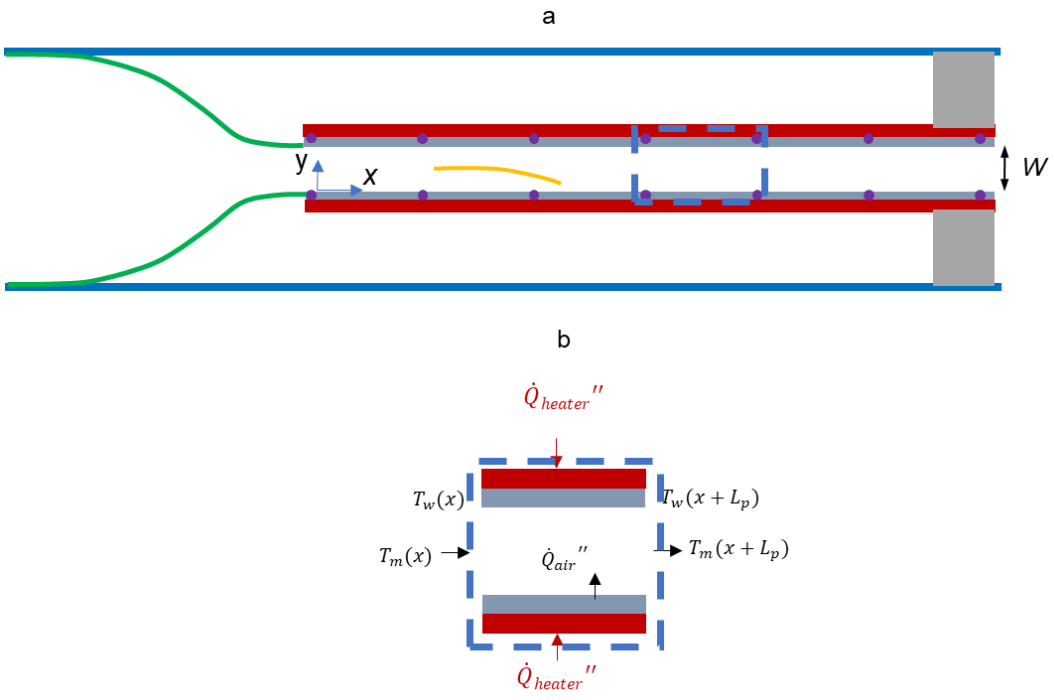

Figure 5.1 *a) Top view of the flow path within the high aspect ratio 5 mm channel, which includes a **2-D contraction**, the **cantilevered reed**, and **thin-film heater** adhered to **aluminum plates** each instrumented with a streamwise array of **thermocouple sensors** (cf. Chapter II); b) Energy balance across an elementary segment of the channel as marked by dashed lines in (a).*

of the local heat transfer coefficient along the channel is assessed by discretizing each of the aluminum plates into seven elementary panels, each $L_p = L/7$ long (between adjacent thermocouple sensors, cf. Figure 5.1) and spanning the channel height. The discretized local heat transfer coefficient, $h(x)$, is computed at the streamwise and spanwise center of each panel. The effective heat flux rate supplied by the heater to the i-th panel is

$$\dot{Q}_i'' = \dot{Q}_{heater}'' - h_{ins}(T_i - T_{a,o})$$

where $\dot{Q}_{heater}''$ is the heat flux supplied by the heater, h_{ins} is the heat transfer coefficient of the insulation (which is computed by assessing the insulation losses as discussed in Chapter II), T_i is the average panel temperature computed as $T_i = 0.5 \cdot [T_w(x) + T_w(x+L_p)]$ (cf. Figure 5.1b), and $T_{a,o}$ is the ambient air temperature. The streamwise conduction within the aluminum plates is also accounted for and modifies the heat flux to the air within the channel

$$\dot{Q}_{i,air}'' = \dot{Q}_i'' + k_{al}\left(\frac{t_w}{L}\right)\left(\frac{dT_w}{dx}(x + L_p) - \frac{dT_w}{dx}(x)\right)$$

where k_{al} is the thermal conductivity of the aluminum plates and t_w is the plate thickness. An energy balance is carried out across a control volume spanning the elementary panel (as shown by dashed lines in Figure 5.1b) which relates the heat flux supplied to the air to the increase in thermal energy of the incoming flow as follows:

$$\dot{Q}_{i,air}'' \cdot A_{panel} = \dot{m} \cdot \tilde{C}_p \cdot T_{m,i} = 0.5\, \dot{m} \cdot \tilde{C}_p \cdot [T_m(x+L_p) + T_m(x)].$$

where $\dot{m}$ is the mass flow rate in the channel, $\tilde{C}_p$ is the specific heat of the air, $T_m(x)$ is the local bulk mean flow temperature defined as $T_m(x) = \int_{-W/2}^{W/2} (u/U) T(y) dy$ (Incropera et al., 2002) and $T_{m,i} = 0.5 \cdot [T_m(x+L_p) + T_m(x)]$ is the average bulk mean flow temperature at the center of a control volume spanning the elementary panel. The local heat transfer coefficient at the streamwise and spanwise center of each panel is then computed using Newton's law

$$h(x) = \frac{\dot{Q}_{i,air}''}{T_i - T_{m,i}}$$

It is noted that some heat is lost at the channel inlet through conduction at the interface between the channel walls and the facility upstream which ultimately heats up the channel air upstream of its inlet and cannot be neglected. The air temperature at the channel inlet $T_{m,0}$ is therefore calculated by an energy balance on a control volume between the plane $x = -10W$ (where $T_{a,i}$ is measured) and $x = 0$ which is the channel inlet

$$T_{m,0} = T_{a,i} + k_{al} \cdot t_w \cdot W \cdot (dT_w/dx)_{x=0} / (\dot{m}\tilde{C}_p).$$

In addition, the boundary condition for wall temperature at the channel exit is assumed as $dT_w/dx = 0$, which is used in implementing the energy balance on the last elementary panel upstream of the channel exit. The discretized local heat transfer coefficient at the center of each panel, x_p is normalized using the hydraulic diameter of the channel, D_h, and the thermal conductivity of the air, k_a, to obtain the local Nusselt number for each panel

$$Nu(x) = h(x) \cdot D_h/k_a$$

The global Nusselt number Nu is defined as

$$Nu = \int_0^L Nu(x) d(\frac{x}{L})$$

The integral is discretized to obtain an estimated of the global Nusselt number which is:

$$Nu = 1/L(\sum_{p=1}^{7} Nu_p \, L_p)$$

where Nu_p is the local Nusselt number $Nu(x = x_p)$ at the center of each panel.

5.2 Characteristics of Reed-Driven Heat Transfer enhancement at *Re* = 2,000

The effects of the reeds on heat transfer in the heated channel was first measured at a relatively low Reynolds number (Re = 2,000) that is characteristic of high-performance

heat exchangers (the flow at this Reynolds number is discussed in §4.2 and 4.3) using a reed for which H_s = 22 mm, L_s = 50 mm, t_s = 38.1 μm and which is operating at St_L = 0.5 (f_{osc} = 65 Hz). The streamwise variation of wall temperature, $ITD\,(x)$, and of the local Nusselt number, $Nu(x)$, calculated as outlined in §5.1 are shown in Figures 5.2a and b. These data show that at a given heater power the reed oscillations lead to a reduction in wall temperatures and hence the heater power, $\dot{Q}_{\text{heater}}$ is increased from 23 Watts in the base flow to 29 Watts in the presence of the reed to maintain the same maximum wall temperature ITD_{max} = 60°C. In the absence of the reed, $ITD\,(x)$ increases monotonically and reaches ITD_{max} at $\hat{x} \approx 40$. As evident in Figure 5.2a, although the wall temperatures are nearly the same in the absence and presence of reed near the entry ($\hat{x}$ = 0.5) and exit of the channel ($\hat{x}$ = 49.5), the wall temperatures when the reed is installed are lower within the channel ($8.3 \leq \hat{x} \leq 32.3$), even when the heater power is increased to maintain the same ITD_{max}. Figure 5.2b demonstrates that, as expected, in the base flow $Nu(x)$ decreases monotonically (as $\hat{x}^{-0.2}$) through the channel [from $Nu(\hat{x} = 4.4) = 12.3$ to

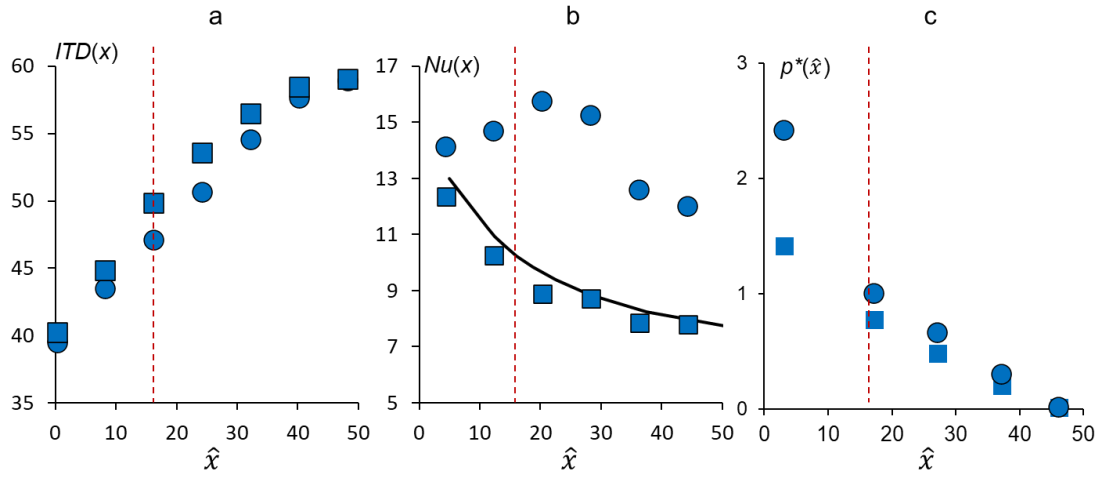

Figure 5.2. *Streamwise variation of a) ITD(x), b) Nu(x), and c) $C_p(\hat{x})$ in the base flow (■) and with the reed (●) in the 5 mm wide channel for ITD_{max} = 60°C at Re = 2,000. The data of Kakac et. al. (1987) is shown using a solid black line, and the position of the tip of the reed is marked using red dashed lines.*

$Nu(\hat{x} = 44.4) = 7.8$] due to the development of thermal boundary layer along the channel side walls. This streamwise variation of $Nu(x)$ closely matches the corresponding variation in developing laminar flows in-rectangular channels of similar aspect ratio and *Re* (e.g., the data of Kakaç et al., 1987 for $H/W = 4$ is shown using a black solid line in Figure 5.2b). It is noted that the heat dissipated to the air ($\dot{Q}_{air} = \dot{Q}_{heater} - \dot{Q}_{ins}$) in the presence of the reed increases from 16 Watts in the base flow to 21 Watts. The combination of a higher heat dissipation and lower wall temperatures effected by the reed leads to streamwise increments in the local Nusselt number $Nu(x)$ relative to the base flow throughout the measurement domain. The Nusselt number increases monotonically along the reed length from $Nu(\hat{x} = 4.4) = 14.2$ to $Nu(\hat{x} = 20.4) = 15.8$ and thereafter decreases downstream of the reed to $Nu(\hat{x} = 44.4) = 12$. The percentage increase in $Nu(x)$ in the presence of the reed varies from 15% to 80% between the upstream and downstream edges of the reed and thereafter decreases to 53% near the channel exit (the global percentage increase in Nusselt number in the presence of the reed is 58%).

As discussed in §4.3, the oscillations of the reed result in an increase in flow losses along its length and downstream of its tip. These losses are manifested by streamwise changes in the static gauge pressure along the channel that are captured by the local pressure coefficient $C_p(\hat{x}) = p(\hat{x})/0.5\rho U^2$ in the base flow and in the presence of reed as shown in Figure 5.2c. These data show that in the presence of the reed the pressure drop along the channel ($3 < \hat{x} < 46$) increases by 70%. Furthermore, the local increase in pressure due to the reed, i.e., $\Delta C_p(\hat{x}) = C_{p,reed} - C_{p,base}$, decreases monotonically along the channel length ($\Delta C_p = 1$, 0.22 and 0 at $\hat{x} = 3.2$, 17.2 and 46.2 respectively). It is noteworthy that while the pressure drop across the reed ($3.2 < \hat{x} < 17.2$, or $1.4L_s$) increases

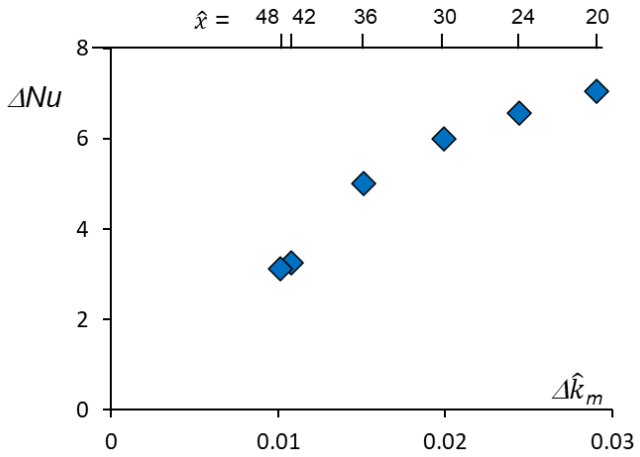

Figure 5.3 *Variation of the increment in Nu(x) relative to base flow ΔNu with the increment in bulk mean fluctuation kinetic energy* $\Delta\hat{k}_m$ *(cf. Figure 4.19) at Re* = 2,000. *The streamwise locations of these data (at z = 0) are marked on the x-axis on top.*

by 120% above the same channel length in the base flow, the pressure drop downstream of the reed ($17.2 < \hat{x} < 46.2$, or $2.9L_s$) increases by 20% only and the corresponding increments in the Nusselt number along and downstream of the reed are 50% and 65%, respectively.

The increment in $Nu(x)$ along the reed is clearly coupled to the pressure losses and result from the oscillatory undulations of the reed and its interactions with the top and bottom walls that lead to modulation of the momentum and thermal boundary layers (as evident from the vortical concentrations near its tip, cf. §4.2 and Figure 4.2). These modulations coupled with cross stream mixing enhance the local heat transfer from the wall surfaces along the reed. As discussed in §4.3, downstream of the reed, the convected flow perturbations induced by the reed increase the levels of fluctuating kinetic energy in the flow. The reed-induced increments relative to the base flow of the Nusselt number, ΔNu, and of the bulk mean fluctuation kinetic energy, $\Delta\hat{k}_m$, are shown in Figure 5.3 which also shows the streamwise location of these measurements. These data show that ΔNu increases with $\Delta\hat{k}_m$ but that the rate of change of ΔNu decreases as $\Delta\hat{k}_m$ increases. In fact,

close the tip of the reed ($20<\hat{x}<24$) where $\hat{k}_m$ levels are high, $\Delta Nu/\Delta\hat{k}_m \sim 106$, but near the channel exit ($36<\hat{x}<48$), $\Delta Nu/\Delta\hat{k}_m \sim 348$. Although downstream of the reed ΔNu decreases with $\Delta\hat{k}_m$, because the small scale motions induced by the reed at this low Reynolds number dissipate (cf. Figure 4.19, the Nusselt number in the presence of the reed is higher than in the base flow even near the channel exit ($28W$ downstream of the tip).

5.3 The Role of the Reynolds Number in the Reed-Enhanced Heat Transfer

The effects of the transition to turbulence in the base flow on reed-enhanced heat transfer are considered by varying the channel's Reynolds number. Corresponding to the investigations in §4.4, heat transfer measurements are carried out in the base flow and in the presence of the reeds measuring $L_s/W = 10$ and $H_s/H = 0.9$ and operating at $St_L = 0.5$ at $Re = 2{,}000$, 7,000 and 12,000, with $ITD_{max} = 60^oC$. Figure 5.4 shows the streamwise variation of $Nu(x)$ in the absence and the presence of reeds (tip location shown through dashed line) where the data for $Re = 2{,}000$ (cf. Figure 5.2b) is repeated for reference. At $Re = 2{,}000$, $Nu(x)$ in the base flow ($\dot{Q}_{heater} = 23$ Watts) undergoes a mild streamwise decrease with the development of thermal boundary layers. However, in the presence of the reed ($\dot{Q}_{heater} = 29$ Watts) there is an increase in $Nu(x)$ for $4.4 < \hat{x} < 20.4$ up to a local

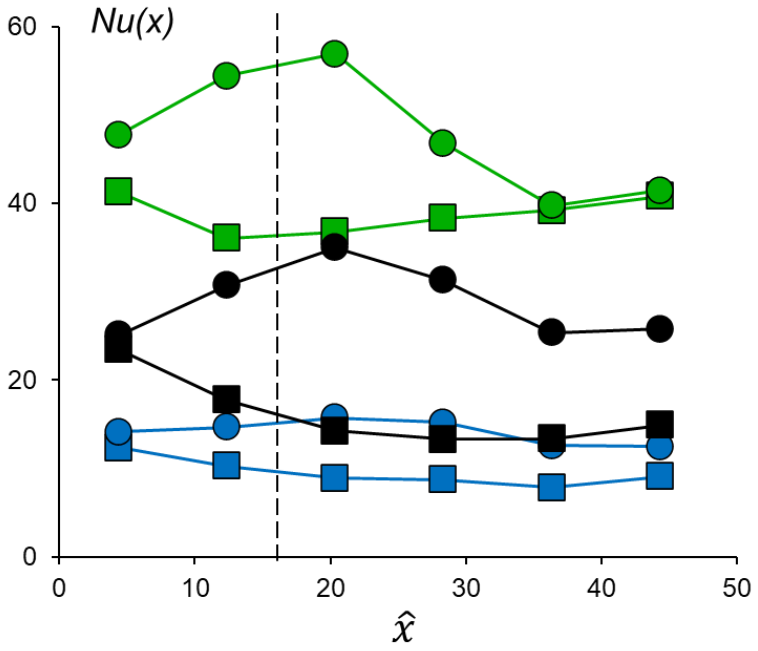

Figure 5.4. *Streamwise variation of the local Nusselt number at Re = **2,000**, **7,000** and **12,000** in the absence (■) and the presence (●) of reeds oscillating at $St_L = 0.5$ ($L_s/W = 10$, $H_s/H = 0.9$, $\hat{x}_{tip}$ is marked by a dashed line).*

maximum near the tip at $\hat{x}$ = 20.4 which is about 1.8-fold larger than in the base flow followed by monotonic decrease through the channel's exit plane. It is noted that streamwise variation of *Nu*(*x*) downstream of the reed tip is associated with a similar variation of $\hat{k}_{\mathrm{m}}$ which (at *Re* = 2,000) decreases monotonically from 0.03 at $\hat{x}$ = 18 to 0.012 at the channel's exit (the variation of *Nu*(*x*) with $\hat{k}_{\mathrm{m}}$ is discussed further in connection with Figure 5.5). The streamwise variation of *Nu*(*x*) at *Re* = 7,000 ($\dot{Q}_{\mathrm{heater}}$ = 40 Watts) in the base flow reaches a local minimum at $\hat{x}$ = 30 and then begins to increase through the end of the channel with the transition to turbulence (note that the levels of *Nu*(*x*) for $\hat{x}$ > 20 are similar to the levels in the presence of the reed at *Re* = 2,000). In the presence of the reed at *Re* = 7,000 ($\dot{Q}_{\mathrm{heater}}$ = 55 Watts), *Nu*(*x*) has a local maximum at $\hat{x}$ = 20.4 near its tip which is 2.45-fold higher than in the base flow before it monotonically diminishes and appears to reach a plateau at $\hat{x}$ = 44.4 through the end of the channel. Similar to *Re* = 7,000, when the Reynolds number is increased further to 12,000 ($\dot{Q}_{\mathrm{heater}}$ = 82 Watts), *Nu*(*x*) in the base flow has a local minimum at $\hat{x}$ = 12.4 beyond which it increases to a plateau (*Nu*(*x*) = 39) near the channel exit ($\hat{x}$ = 44.4) as the base flow becomes asymptotically turbulent. In the presence of the reed ($\dot{Q}_{\mathrm{heater}}$ = 87 Watts), *Nu*(*x*) reaches a maximum near its tip which is 1.4-fold higher than in the base flow before it decreases monotonically to a plateau (*Nu*(x) = 39.1) near the channel exit ($\hat{x}$ = 44.4). It is noteworthy that at this Reynolds number, the plateauing levels of *Nu*(*x*) near the exit of the channel in the base flow and in the presence of the reed are similar indicating that for these operating conditions higher heat transfer can be achieved when using a reed in a shorter channel (and lower pressure losses).

As discussed in chapter I, the local Nusselt number is primarily affected by the thickness of thermal boundary layers near the channel walls and the cross-stream mixing within the channel. As evident in § 4.2, (cf. Figure 4.2), the reed induced small scale vortical motions modulate the wall boundary layer and increase velocity fluctuations throughout the channel height which could lead to higher cross-stream mixing. The variations in $Nu(x)$ with the intensity of small scale motions as measured by $\hat{k}_m$ is therefore assessed and compared between the base flow and in the presence of reeds at Re = 2,000, 7,000 and 12,000 (Figure 5.5a). It should be noted that in Figure 5.5a, $\hat{x}$ increases from left to right for the base flow data and from right to left in the presence of the reeds. In the base flow at Re = 2,000, $\hat{k}_m \sim 0$ and the decrease in $Nu(x)$ is primarily due to streamwise thickening of a laminar thermal boundary layer (cf. Figure 5.2b). As the Reynolds number of the base flow is increased to 7,000 and 12,000, $Nu(x)$ increases due to the thinner thermal boundary layers even for $\hat{k}_m < 0.001$. As is evident in Figure 5.5a, $Nu(x)$ in the base flow increases with $\hat{k}_m$ with transition to turbulence at these Reynolds numbers. In the presence

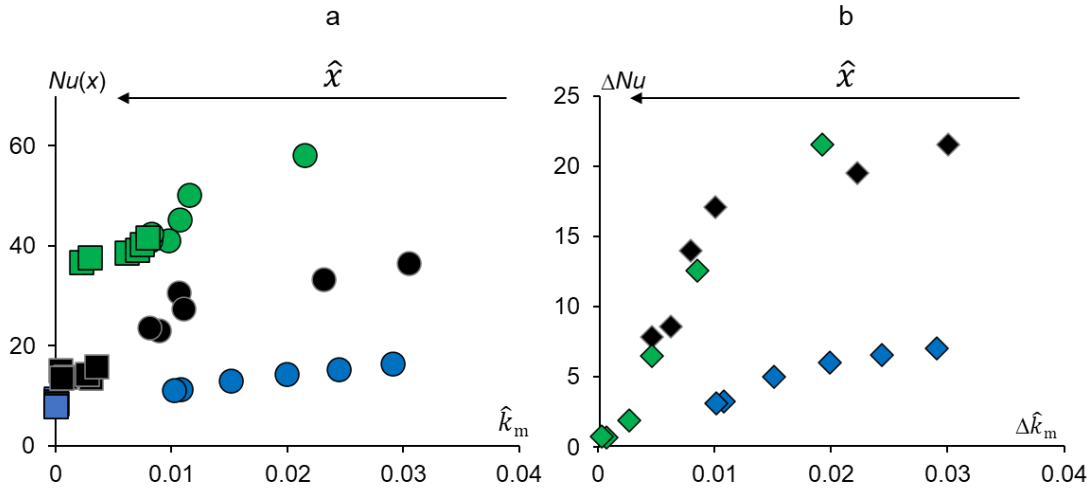

Figure 5.5 *a) Variation of $Nu(x)$ with $\hat{k}_m$ in the base flow (■) and in the presence of reeds (●) at Re = 2,000 (■, ●), 7,000 (■, ●) and 12,000 (■, ●); and b) Variation of the reed-induced increments ΔNu with $\Delta\hat{k}_m$ over the corresponding base flow at Re = 2,000 (♦), 7000 (♦) and 12,000 (♦).*

of the reed, $\hat{k}_m$ is significantly higher than in the base flow at *Re* = 2,000 throughout the channel which leads to a corresponding increase in *Nu*(*x*) by the induced fluctuations within the wall boundary layers and mixing with the flow near the center of the channel. A similar trend is also seen at *Re* = 7,000 and 12,000 albeit with rates which increase with *Re* (e.g., at $\hat{k}_m = 0.01$, $d(Nu)/d(\hat{k}_m) = 283$, 530 and 1263 at *Re* = 2,000, 7,000 and 12,000) due to interactions between the reed induced velocity fluctuations and the natural small scale motions in the transitioning flow.

The relation between the increment in *Nu*(*x*) over the base flow due to actuation by the reed, ΔNu, and the corresponding increment in $\hat{k}_m$, $\Delta\hat{k}_m$, is shown in Figure 5.5b. While these curves nearly collapse at *Re* = 7,000 and 12,000, ΔNu for a given $\Delta\hat{k}_m$ is significantly lower at *Re* = 2,000 in the absence of transition in the base flow (e.g, for $\Delta\hat{k}_m = 0.01$ and 0.02 ΔNu = 3 and 6 at *Re* = 2,000 compared to $\Delta Nu \sim 12$ and 20 at *Re* = 7,000 and 12,000). This difference indicates that the smaller scales in the flow that are connected with the interactions between the reed and the transitional base flow (at *Re* = 7,000 and 12,000, see also the corresponding discussion of the velocity spectra in Figure 4.20) play a significant role in heat transfer enhancement. The collapse of the curves of $\Delta Nu[\Delta\hat{k}_m]$ indicates that the effect of the perturbations induced by the reed on transition is nearly the same at each Reynolds number (7,000 and 12,000) and, as a result, the heat transfer enhancement by the ensuing small-scale motions is also similar even though the Reynolds numbers and the (absolute) levels of $\hat{k}_m$ are different. The effect of transition is further manifested by the observation that while at *Re* = 2,000 and 7,000, ΔNu and $\Delta\hat{k}_m > 0$ throughout the channel, at *Re* = 12,000 near the channel exit, ΔNu and $\Delta\hat{k}_m$ nearly vanish. However, even at

Re = 12,000 the reed increases $Nu(x)$ over the base flow over a significant length of the channel ($\hat{x} < 36$, cf. Figure 5.4) where the inlet base flow is undergoing transition (cf. Figure 4.19) and hence increases the global Nusselt number.

Following the investigation of the effects of the streamwise placement of the tip of the reed on small scale motions in the channel in §4.4 for Re = 12,000 (for which the base flow evolves from a nominally-laminar entrance flow to developed turbulent flow), the corresponding streamwise changes in $Nu(x)$ and variation in ΔNu with $\Delta\hat{k}_m$ are shown in Figure 5.6 for $\hat{x}_{tip} = 16$ and 26. The streamwise variations in $Nu(x)$ for $\hat{x}_{tip} = 16$ are discussed in Figure 5.4 ($L_s/W = 10$, $H_s/H = 0.9$, $St_L = 0.5$ and $f_{osc} = 380$ Hz) and are repeated here for reference . When the reed is placed such that $\hat{x}_{tip} = 26$, the base flow is already asymptotically turbulent near the tip (cf. Figure 5.6a) and $Nu(\hat{x} = 28) = 37$ and is

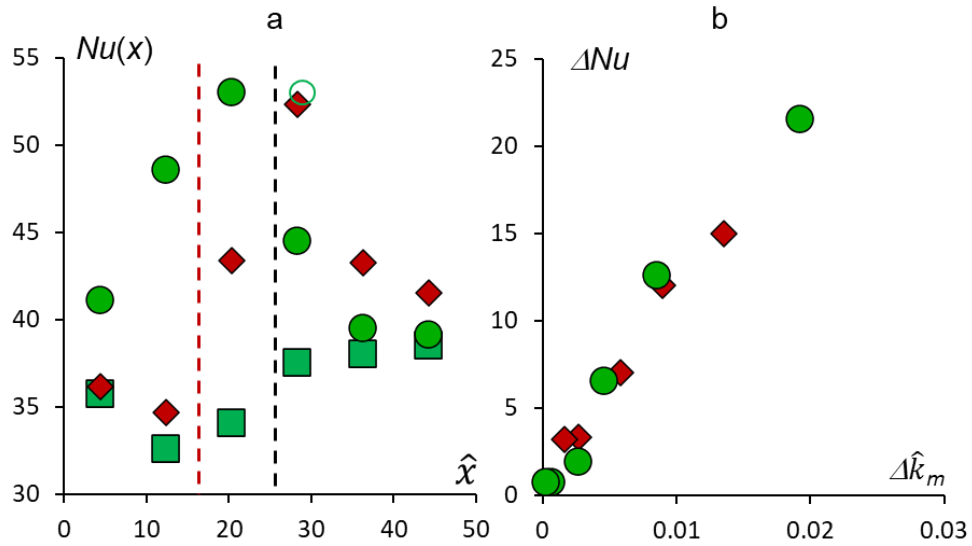

Figure 5.6 *a) Streamwise variation of $Nu(x)$ in the base flow (■) and in the presence of the reed ($H_s/H = 0.9$, $L_s/W = 10$, $St_L = 0.5$) for $\hat{x}_{tip} = 16$ (♦) and 26 (●) (marked by dashed lines); and b) Variation of ΔNu with $\Delta\hat{k}_m$ downstream of the reed. $ITD_{max} = 60^oC$, Re = 12,000. The data at $\hat{x}$ = 20.4 for $\hat{x}_{tip}$ = 16 is offset by $\hat{x}$ = 10 and marked using ○ for comparison with corresponding data at $\hat{x}$ = 28.4 for $\hat{x}_{tip}$ = 26.*

nearly streamwise-invariant farther downstream. However, in the presence of reed, $Nu(x)$ near the reed tip for $\hat{x}_{tip} = 26$ is nearly identical to the corresponding $Nu(x)$ that is effected for $\hat{x}_{tip} = 16$. As noted in Figure 4.22, even though the velocity fluctuations within the base flow increase between the streamwise positions of the tip of the reed at $\hat{x}_{tip} = 16$ and 26, the levels of $\hat{k}_m$ induced at the same reed Strouhal number are nearly the same near its tip resulting in similar $Nu(x)$. Similar to the trends for $\hat{k}_m$ in Figure 4.22, the streamwise rate of decay of $Nu(x)$ from the peak is significantly faster for $\hat{x}_{tip} = 26$ (the exponential decay rate is 1.28 times higher than at $\hat{x}_{tip} = 16$). However, as shown in Figures 5.6 a and b, the increment in $Nu(x)$ over base flow at $\hat{x}_{tip} = 26$ is lower than at $\hat{x}_{tip} = 16$ leading to lower levels of ΔNu with lower $\Delta\hat{k}_m$ while the rates of decrease of ΔNu with $\Delta\hat{k}_m$ for these two streamwise locations are nearly identical.

The reed-driven heat transfer enhancement is coupled with its mechanical oscillations and the induced small-scale motions downstream of its tip. This coupling clearly results in an increase in pressure drop within the channel or in the friction factor f which must be taken into account when assessing the efficiency of the heat transfer enhancement. To this end, it is instructive to compare the ratio of global Nusselt numbers in the presence and absence of reeds Nu/Nu_b (as a representative of the heat transfer enhancement) with the ratio of the friction factor, f/f_b which can be considered as the cost of achieving the heat transfer enhancement. For the reeds discussed in connection with Figure 5.5 which oscillate at $St_L = 0.5$ and $Re = 2{,}000$, 7,000 and 12,000, these ratios are: $Nu/Nu_b = 1.58$, 1.85, and 1.28 and $f/f_b = 1.7$, 3.1 and 2.8, respectively. It should be noted that in these discussions the friction factor with the reed is nearly invariant since it only depends on the reed's Strouhal number ($f = 0.1 \bullet (St_L)^{0.5}$, cf. § 4.5) but the base flow friction

factor first decreases from $f_b = 0.048$ at $Re = 2{,}000$ to $f_b = 0.026$ at Re=7,000 before increasing to $f_b = 0.029$ at $Re = 12{,}000$ where the base flow is naturally transitioning to turbulence, thereby resulting in the evident trends in f/f_b.

In addition, in connection with Figure 5.6 it is noted that moving the reed tip ($L_s/W = 10$) between $\hat{x}_{tip} = 16$ and 26, Nu/Nu_b decreases by 6% (1.28 to 1.21) while f/f_b decreases by 1% (from 2.8 to 2.77). Therefore, placing the reed upstream in the channel yields an overall better heat transfer enhancement while keeping the channel losses nearly invariant. For this reason, the effect of reed Strouhal number discussed in §5.4 was investigated upstream.

It is noted that the effect of streamwise position of the reed was also explored using a different reed [$L_s/W = 10$, $H_s/H = 0.9$, $St_L(f_{osc},\text{Hz}) = 0.9(180)$] at $Re = 5{,}000$ when the base flow is transitional and yielded similar results to what is shown in Figure 5.6. These measurements have been described along with an additional streamwise position of the reed ($\hat{x}_{tip} = 48$) in Appendix B.

While in the present measurements the Strouhal number was invariant, based on the findings of §4.5 the channel losses associated with the oscillations of the reed can be reduced by reducing its Strouhal number. The impact of reed operation at reduced St_L on heat transfer enhancement is explored in §5.4.

5.4 The Role of the Reed Strouhal Number in the Balance Between Heat Transfer Enhancement and Flow Losses

Following the discussions in §5.3 which showed that heat transfer enhancement by the reed is accompanied by increased channel losses, the present section focuses on identifying means for reducing the channel losses while maintaining the heat transfer enhancement. The approach is based on the earlier findings that the flow losses in the presence of reed can be significantly reduced by reducing its oscillating frequency or Strouhal number (cf. §4.5).

The effects of the reed Strouhal on the channel's local and global heat transfer as measured by the Nusselt number and the bulk mean fluctuating kinetic energy, $\hat{k}_m$, are first assessed for a transitional Reynolds number $Re = 5{,}000$ where, as discussed in §4.5 $0.3 < St_L < 1.6$ is achieved using reeds with $H_s/H = 0.9$ and varying their thicknesses and lengths: $L_s/W = 10$ with $t_s = 25.4$, 38.1, 50 μm, and $L_s/W = 2.4$, 10, 20 with $t_s = 25.4$ μm, where ITD_{max} is kept unchanged by increasing heater power relative to the base flow (32 Watts). Similar to the discussions of Figures 5.2a and b, Figures 5.7a and c and 5.7b and d show the streamwise variation of wall temperatures, $ITD(x)$ and $Nu(x)$, respectively, for the different reed oscillation frequencies. In Figures 5.7a and b, $L_s/W = 10$ and $St_L = 0.5$, 0.7, and 0.9, (the heater power is increased with St_L to 45.7, 46.2 and 47 W). In Figures 5.7c and d, $t_s = 25.4$ μm and $St_L = 0.3$, 0.9, and 1.6 (the heater powers are increased with St_L to 46, 47 and 48 Watts). The streamwise variations of ITD (Figures 5.7a and c) show that even at the same ITD_{max} and increased heater power with St_L, $ITD(x)$ decreases throughout the channel relative to the base flow except at $St_L = 1.6$ for $L_s/W = 20$. As illustrated by

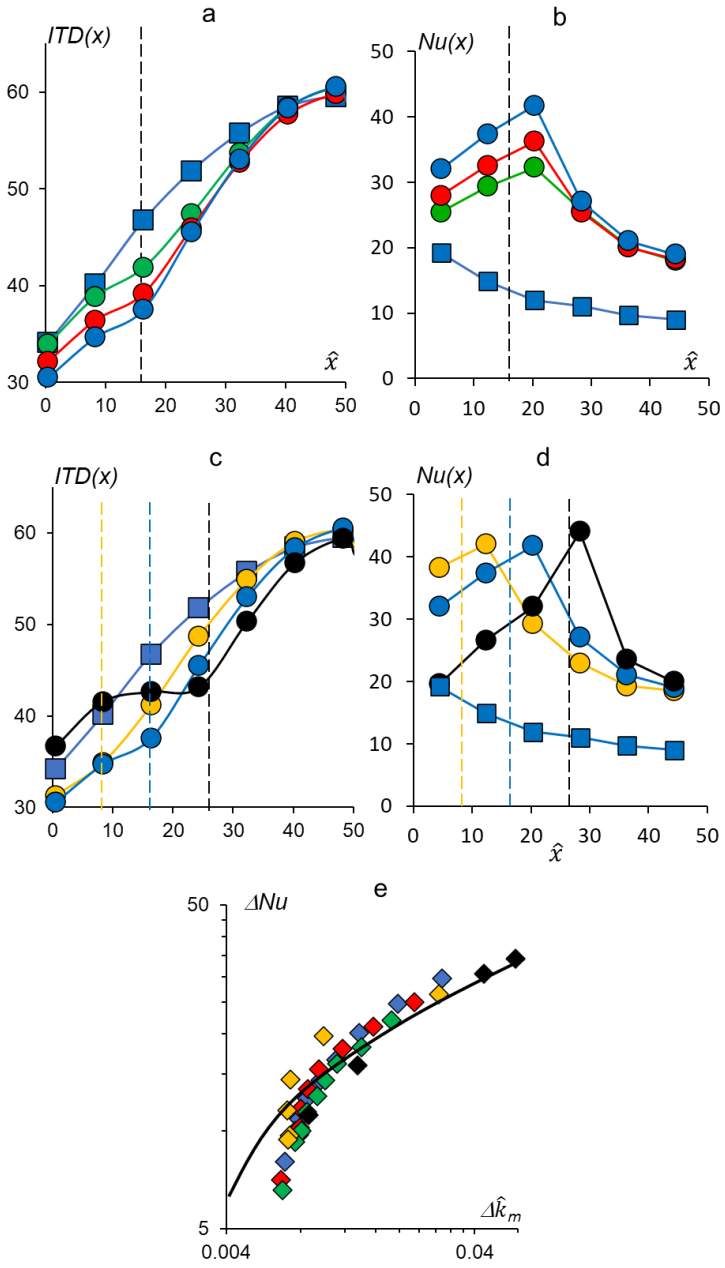

Figure 5.7 *The effect of Strouhal number on heat transfer enhancement at Re = 5,000 by streamwise variations of ITD(x) and Nu(x): in (a) and (b), respectively for* St_L *= 0.5 (●), 0.7 (●), 0.9 (●) (*L_s/W *= 10,* t_s *= 25.4, 38.1, 50.8 μm); and in (c) and (d), respectively for* St_L *= 0.3 (●), 0.9 (●), 1.6 (●) (*t_s *= 25.4 μm and* L_s/W *= 2.4, 10, and 20), and the base flow (■); and (e) Variation of reed-induced increments ΔNu with* $\Delta\hat{k}_m$ *(relative to the base flow) at Re = 5,000 for* St_L = 0.3 (♦), 0.5 (♦), 0.7 (♦), 0.9 (♦) *and* 1.6 (♦). *Least square fit to corresponding data at Re = 7,000 and 12,000 is also shown using a solid black line. The locations of the reed tip are marked using dashed lines.*

Carruthers et al. (2005) long reeds (dubbed "streamers" by the authors) in free air exhibit diminished cross stream motion along 30% of their length downstream from their support, and it is conjectured that the diminished reed motion leads to reduction in heat transfer at the wall and elevated temperatures for $0 < \hat{x} < 10$ as evident in Figure 5.7c. The magnitude of the decrement in $ITD(x)$ relative to the base flow increases along the reed and reaches a maximum at its tip and then gradually diminishes and vanishes at the channel exit (cf. Figures 5.7a and c). As evident in Figure 5.7a for reeds of length $L_s/W = 10$, while the decrement in *ITD* along the reed and a small region (~10W) downstream of the reed tip increases with St_L, farther downstream *ITD* becomes nearly invariant St_L. For example, for $St_L = 0.5$, 0.7 and 0.9 the decrements in *ITD* are 5.7, 7.5 and 8.7°C, respectively near the reed tip ($\hat{x} = 16.4$) and about 5°C for all St_L at $\hat{x} = 24.4$ respectively.

The combined effect of higher heater power and lower wall *ITD*'s due to the reeds is also evident in higher local Nusselt numbers, $Nu(x)$, in the presence of reeds. The streamwise variations in of $Nu(x)$ (cf. §5.1) are shown in Figures 5.7b and d respectively. While for the base flow at $Re = 5{,}000$, $Nu(x)$ decreases streamwise due to thickening of thermal boundary layer (similar to Figure 5.2b at $Re = 2{,}000$), in the presence of reeds $Nu(x)$ at all St_L increases up to the tip and then decreases exponentially downstream. The Nusselt number at all St_L is higher than in the base flow throughout the measurement domain except for $L_s/W = 20$ (cf. Figure 5.7d) just upstream of the reed at $\hat{x} = 4.4$. Although the increment in $Nu(x)$ over the base flow, $\Delta Nu(x) = Nu_{reed}\text{-}Nu_{base}$ increases with St_L along the reed, the rate of exponential decrease of $Nu(x)$ downstream of the tip increases with St_L such that the increment in $Nu(x)$ becomes nearly identical just 10W from the tip. For example, as shown in Figure 5.7b for $L_s/W = 10$ near the tip $\Delta Nu(\hat{x} = 20.4) = 20$, 26

and 30 for St_L = 0.5, 0.7 and 0.9, respectively and farther downstream $\Delta Nu(\hat{x} = 28.4) \sim 16$. The streamwise variations of the increments (relative to the base flow) ΔNu with $\Delta\hat{k}_m$ as discussed in connection with Figures 4.25a and b (cf. §4.5) are shown in Figure 5.7e ($\Delta\hat{k}_m$ has similar trends to ΔNu). That the data for all reed Strouhal numbers at Re = 5,000 collapse on nearly a single curve indicates that at a fixed Reynolds number the increment $Nu(x)$ depends primarily on the increase in the fluctuation kinetic energy. Using the corresponding data for Re = 7,000 and 12,000 (represented by a least squares fit), Figure 5.7e shows that for $\Delta\hat{k}_m > 0.01$, the data for ΔNu and $\Delta\hat{k}_m$ at Re = 5,000 7,000 and 12,000 collapse on a single curve on which $\Delta Nu \sim (\Delta\hat{k}_m)^{0.8}$. This collapse indicates that for $Re \geq 5{,}000$ the small scales induced by the reed oscillation become similar as the reed accelerates transition to turbulence.

Following the characterization of the effect of St_L on heat transfer enhancement, attention is shifted to its effect on flow losses in the channel as measured by the streamwise pressure drop coefficient $C_p(\hat{x})$ along and downstream of the reed. The changes in $C_p(\hat{x})$ of the base flow and in presence of a rigid reed (stainless-steel, L_s/W = 10, t_s = 76.2 μm) that are induced by increasing reed St_L (cf. Figures 5.7a and c) is shown in Figure 5.8a. These data show that the pressure drop along the reed ($3.2 < \hat{x} < 17.2$), $\Delta C_{p,\text{reed}}$, increases with St_L ($\Delta C_{p,\text{reed}}$ = 0.8, 1.3, 2.1 for St_L= 0.5, 0.7, and 0.9, respectively) since the power required to sustain the flow losses associated with the reed motion also increases with St_L. The corresponding pressure drop along the rest of the channel (downstream of the reed, $17.2 < \hat{x} < 46.2$) $\Delta C_{p,\text{reed}}$ is nearly invariant with St_L and lower than $\Delta C_{p,\text{reed}}$ for all St_L

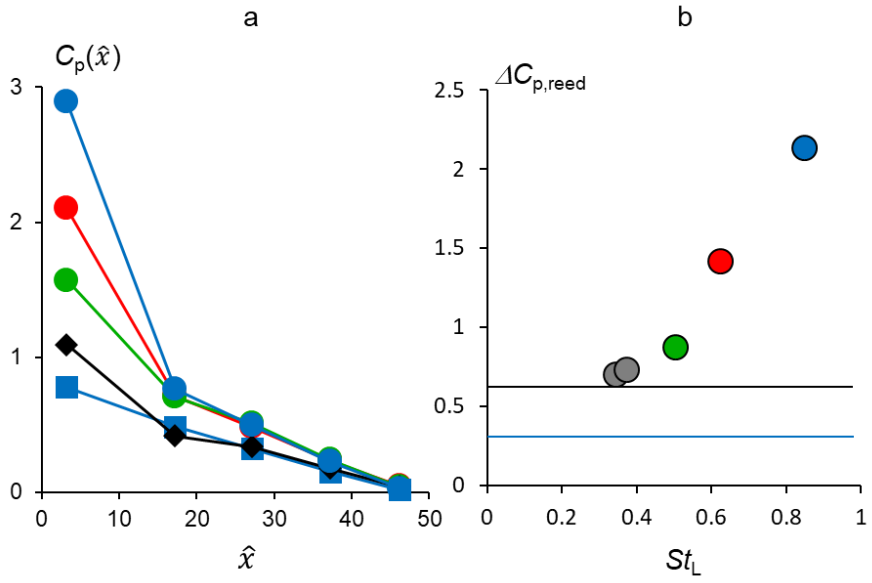

Figure 5.8. *Streamwise variation of a) Channel gauge static pressure, C_p in the absence (■) and presence of a rigid (♦) and at St_L = 0.5 (●), 0.7 (●) and 0.9 (●) (L_s/W = 10 at Re = 5,000). b) Variation of pressure drop along the reed, $\Delta C_{p,reed}$ with St_L* relative to the pressures in *the **base flow** and in the presence of **rigid reeds** (marked by solid lines).*

($\Delta C_{p,reed}$ / $\Delta C_{p,ch}$ = 1.33, 2.16, and 3.5 for St_L= 0.5, 0.7, and 0.9, respectively). This clearly indicates that most of the losses (at higher St_L) occur along the reed and the effects of the reed-induced flow fluctuations on the pressure drop (relative to the base flow) are virtually independent of St_L. It is instructive to compare the pressure drop associated with the oscillating reed with the corresponding pressure drop when a rigid (non-oscillating) reed is placed in the channel (Figure 5.8a). These data show that $\Delta C_{p,reed}$ in the absence of oscillations is significantly lower and appear to be associated with the viscous losses along the reed. The pressure drop downstream of the rigid reed is nearly the same as in the base flow. The variation of pressure drop along the reed, $\Delta C_{p,reed}$ with St_L is shown in figure 5.8b and is used to assess the pressure drop due to oscillations of the reed by subtracting the contributions due to the base flow and the nominal viscous losses due to the rigid reed ($\Delta C_{p,reed}$ = 0.25 and 0.35, respectively as marked by solid lines in Figure 5.8b). These data

show that the pressure drop due to the oscillations of the reed can be reduced by up to 84% by reducing St_L by only 45% from 0.9 to 0.3. These data show that the main contribution to the reduction in overall channel losses with St_L comes from the reductions in the losses along the reed. This finding indicates that by externally mounting the reed upstream of the channel inlet these losses can be further reduced (external reed mounting is investigated in Chapter 6).

Similar to the discussion in §5.3, the changes in global heat transfer and channel losses with Strouhal number are captured using the ratios (relative to the base flow) of the global Nusselt numbers, Nu/Nu_b, and of the friction factors, f/f_b, at a constant Reynolds number. In addition, the efficiency of reeds in enhancing channel heat transfer is measured by calculating the thermal enhancement factor, η, which is used to compare heat augmentation techniques (e.g., Ligrani et al., 2003, Promvonge et al., 2008, Yu et al., 2019, and Rips et al., 2020). Based on Promvonge et al. (2008), the thermal enhancement factor for the reed is defined as the ratio of the reed-effected Nusselt number relative to the base flow at a constant flow power.

$$\dot{W}_{pp} = \Delta P \cdot \dot{m}/\rho_a$$

$$\eta = (Nu/Nu_b)|_{\dot{W}_{pp} = \text{const.}}$$

As shown by Promvonge et al. (2008), the flow power can be normalized as

$$\hat{W}_{pp} = \frac{\Delta P \cdot \dot{m}}{0.5 \cdot (\frac{\vartheta}{D_h})^3 (\frac{L}{D_h})(\rho_a{}^2 WH)}$$

The variations with St_L in f/f_b and Nu/Nu_b and at Re = 5,000 are shown in Figures 5.9-a.1 and b.1 for the reeds in Figure 5.7, and in addition, reeds that oscillate at St_L = 0.25, 0.4 and 2.3 are also included. In accord with the trends in §4.5, while reduction in St_L by nearly

an order of magnitude (from 2.3 to 0.25) decreases f/f_b by 65% (Figure 5.9-a.1) the corresponding reduction in Nu/Nu_b is only 16% (Figure 5.9-b.1) indicating a marginal reduction with Strouhal number. The efficiency of the reeds in enhancing heat transfer is assessed by first comparing the variations in global Nusselt number with $\hat{W}_{pp}$ in the

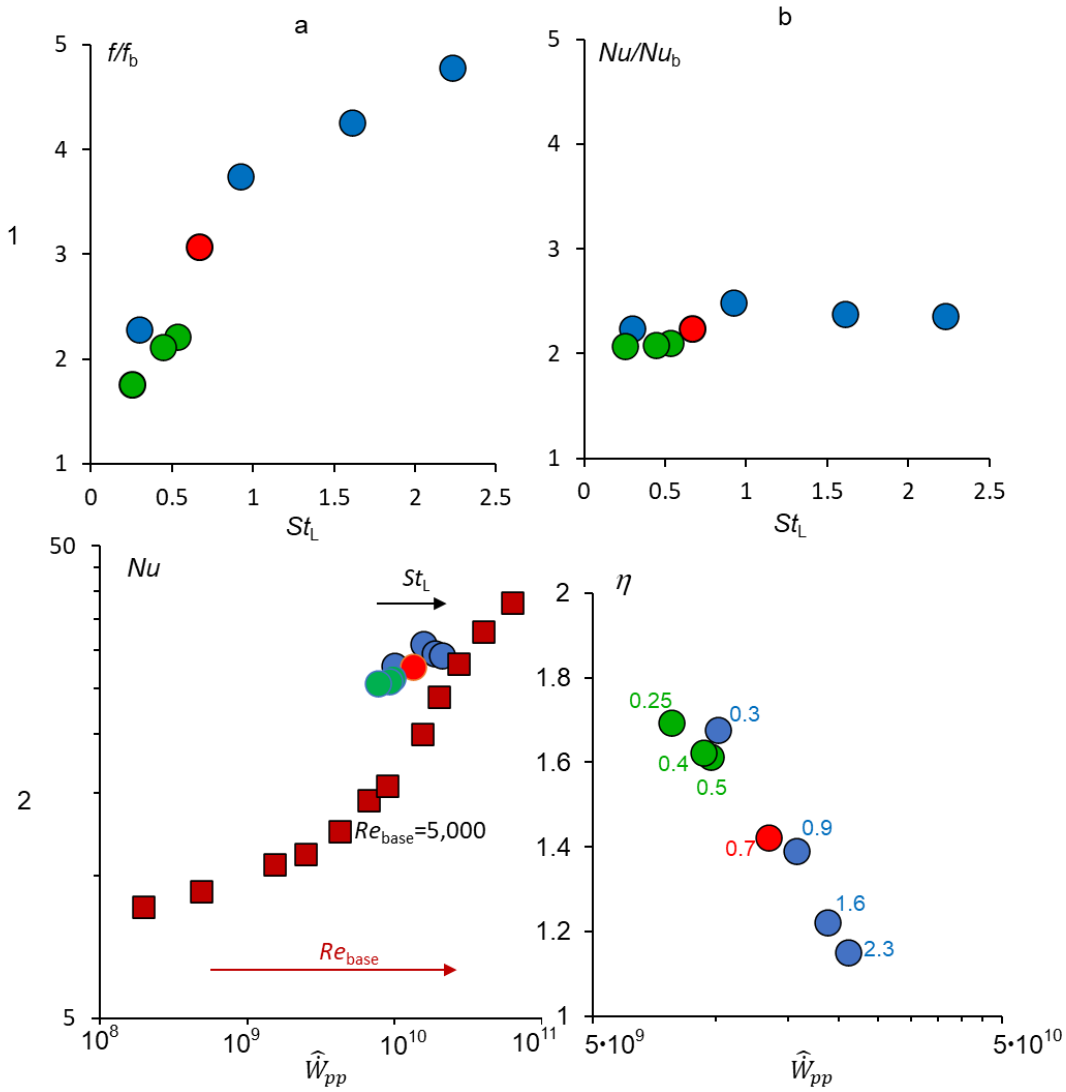

Figure 5.9. *Variation of f/f_b (a.1) and Nu/Nu_b (b.1) with St_L for reeds of thicknesses, t_s = 25.4 μm (●), 38.1 μm (●), 50.8 μm (●). Variation of global Nu with $\hat{W}_{pp}$ (a.2) in the base flow (■) for 1,500 < Re < 13,000 (Re increases from left to right), and in the presence of the reeds, the corresponding Nu in the base flow for Re = 5,000 is marked; b.2) Variation of thermal enhancement factor η of the reeds with $\hat{W}_{pp}$, St_L at Re = 5,000 is noted near each data point.*

presence and absence of reeds (Figure 5.9-a.2) and then the variations of the reed thermal enhancement factor, η with $\hat{W}_{pp}$(Figure 5.9-b.2). In the base flow, *Nu* increases monotonically with $\hat{W}_{pp}$ as discussed further in connection with Figure 5.10a. In the presence of reeds (Figure 5.9-a.2), $\hat{W}_{pp}$ increases with St_L (from left to right in Figure 5.10-a.2) and *Nu* at the same $\hat{W}_{pp}$ is higher than the base flow at all Strouhal numbers. In addition, the increment in *Nu* relative to the base-flow (at a fixed level of $\hat{W}_{pp}$) increases as St_L decreases [For e.g., $\Delta Nu|_{W_{pp}=\text{const}}$ = 5.4 and 10.1 at $St_L(W_{pp})$ = 2.3 ($2\bullet10^{10}$) and 0.25 ($0.66\bullet10^{10}$) respectively]. Figure 5.9-b.2 shows that η increases with decreasing $\hat{W}_{pp}$ and St_L from η = 1.14 at St_L = 2.3 to η = 1.7 at St_L = 0.25, indicating that the efficiency of the reeds increases as their Strouhal number decreases until its oscillation amplitude becomes much smaller (<0.1*H*) and η drops below 1, or the reeds stops oscillating.

By comparison, the use of conventional dimpled/protrusion surfaces in channels of the same aspect ratio (*H*/*W*) and nearly similar *L/W* at *Re* = 5,000 (Mahmood et al., 2002, and Elyyan et al., 2008) yielded a maximum increase in η of up to 1.22. Longitudinal rows of vortex generators used by Fiebig et al. (1991) at *Re* = 5,000 increased η by up to 1.4. The present data show that the reeds yield up to 41% and 22 % higher thermal performance enhancement (as measured by η) than the dimples and vortex generators, respectively. The efficiency of the reeds can also be assessed by comparing the ratio of their coefficient of performance $COP = \dot{Q}_{air}/\dot{W}_{pp}$ relative to the *COP* of the base flow for the same *Nu*. Similar to the trends observed in Figure 5.9-b.2, *COP* increases as St_L decreases (by over two-fold from 1.02 at St_L = 2.3 to 2.15 at St_L = 0.25). At St_L = 0.25, the global Nusselt number increases by 1.7-fold relative to the base flow for the same $\hat{W}_{pp}$.

In addition to the measurements at Re = 5,000 in Figure 5.9, the variation of the efficiency of the reed-enhanced heat transfer with St_L is also studied over a range of Reynolds numbers Re = 1,500, 3,000, 7,000 and 9,000 using reeds of L_s/W = 10, 20 and 30 and thicknesses which are 12.7 μm < t_s < 127μm. At each Reynolds number there are two Strouhal number limits: a lower bound, $St_{L,min}$ (the critical Strouhal number, cf. §3.1), and an upper bound, $St_{L,max}$, above which the interactions with the wall can damage the reeds. These bounds are noted in parenthesis for each Reynolds number: Re = 1,500 (0.6, 2.6), 3,000 (0.5, 2.5), 5,000 (0.3, 2.3), 7,000 (0.42, 1.8) and 9,000 (0.37, 1.2). Similar to Figure 5.9-a.2 and b.2, the assessment of reed efficiency at these Reynolds numbers is performed by comparing the variations of the global Nusselt number with $\hat{W}_{pp}$ in the absence and

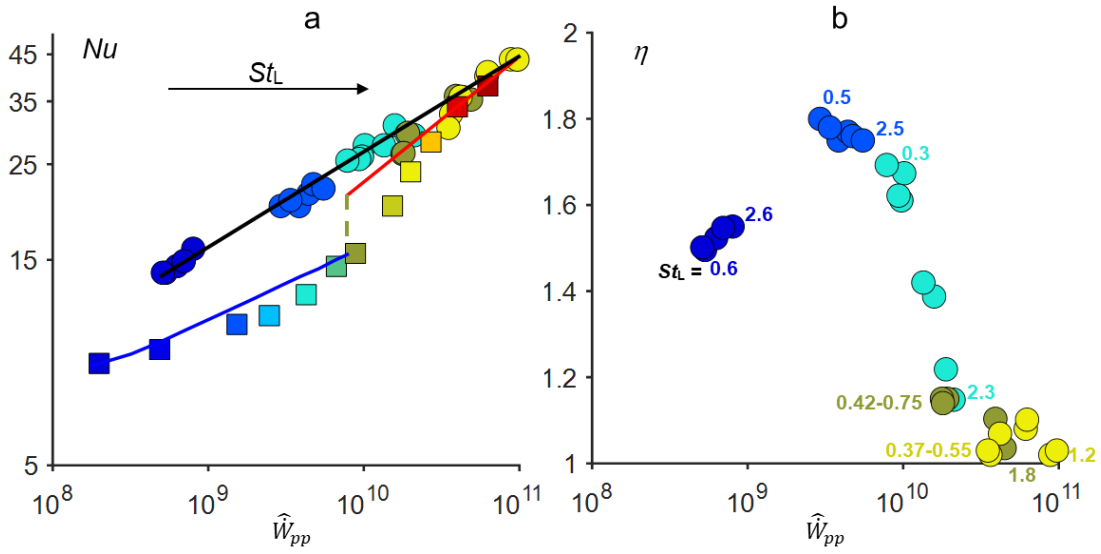

Figure 5.10. *Variation with $\hat{W}_{pp}$ of a) Nu in the base flow (■) for **1,500** < Re < **13,000** and in the presence of reeds (●) at Re = **1,500**, **3,000**, **5,000**, **7,000** and **9000** [Laminar and turbulent channel data of Kakac et al. (1987) and Hartnett et al (1962) are marked by solid **blue**, **red** lines, and least square fit to the present reed data is marked by a **black** line) Base flow transition as assessed from the data of Hartnett et al.(1962) is marked by a **vertical dashed line**. St_L at each Re increases from left to right as marked by the arrow on top; and b) Reed thermal enhancement factor, η for the data shown in (a). Representative St_L values are noted along the plot and are color-coded based on Re and marked in (b).*

presence of these reeds in Figure 5.10a and the variations of thermal enhancement factor with flow power in the presence of the reeds in Figure 5.10b.

In the absence of reeds, *Nu* increases with $\widehat{W}_{pp}$ and the curve of the base flow diverges downwards relative to the reed curve for *Re* < 7,000 and exhibits close match with the variations in the laminar flow of Kakaç et al. (1987) for which $Nu_{\text{lam}} \sim (\widehat{W}_{pp})^{0.15}$. For *Re* > 7,000, the slope of the base flow curve increases, and it approaches the curve of the reed data as the base flow apparently transitions to turbulence and the transitional flow domain moves upstream in the channel (as observed by the streamwise variations of $\hat{k}_{\text{m}}$ between *Re* = 7,000 and 12,000 in Figure 4.19). For *Re* > 12,000 ($\widehat{W}_{pp}>4\cdot10^{9}$), the base flow and the reed curves nearly coincide and exhibit close match with that of a fully turbulent channel flow of Promvonge et al., (2008) for which $Nu_{\text{turb}} \sim (\widehat{W}_{pp})^{0.29}$**.** The choice of *Re* = 7,000 to represent the transitional flow is based on the experimental data of Hartnett et al. (1962), and transition in the base flow is marked by a vertical dashed line in Figure 5.10a. In the presence of reeds, the global Nusselt number increases with the St_{L} and flow power (from left to right in Figure 5.10a at each *Re*). Note that the reed data are color coded (the color map shown at the bottom of Figure 5.10) based on their Reynolds numbers. It is remarkable that the variations of *Nu* with $\widehat{W}_{pp}$ in the presence of the reeds appear to collapse at all *Re* on a single curve for which $Nu\sim(\widehat{W}_{pp})^{0.25.}$ The curve for the base flow approaches the reed curve asymptotically for *Re* > 12,000. That the variations of *Nu* with $\widehat{W}_{pp}$are similar between the reeds and that of a fully turbulent base flow corroborate the findings in §4.4 that the reed accelerates the transition to turbulence in the

channel. In fact, for $\widehat{W}_{pp} < 4 \cdot 10^9$ (Re < 12,000 in the base flow), Nu is higher relative to the base flow for an invariant flow power which leads to $\eta > 1$.

Similar to Figure 5.9-b.2, the variation in reed thermal enhancement factor, η with flow power is shown in Figure 5.10b for the color coded Reynolds numbers of Figure 5.10a (St_L for selected reeds is marked to the right of the symbols in Figure 5.10b for reference). At Re = 1,500, η increases marginally as the flow power increases from η = 1.5to 1.55 for St_L between 0.6 and 2.6 because the base flow and reed curves slightly diverge as the flow power increases (cf. Figure 5.10a). However, for 3,000 ≤ Re ≤ 7,000 η decreases as flow power (and St_L) increases because the base flow and reed curves converge towards each other, and for Re = 9,000, $\eta \sim 1$ as the base flow and reed curves overlap. It is noted that for an identical increase in St_L ($\Delta St_L = 2$), the decrease in η is significantly lower at Re = 3,000 than Re = 5,000. In fact, $\eta\,(St_L)$ decreases from 1.8 (0.5) to 1.7 (2.6) at Re = 3,000 and from 1.7 (0.3) to 1.14 (2.3) at Re = 5,000**.** As the curves of Nu vs $\widehat{W}_{pp}$ for the base flow and the reed (at Re = 7,000) converge in Figure 5.10a, the changes in η with St_L are much smaller and $\eta\,(St_L)$ decreases from 1.14 (0.42) to 1.02 (1.8). These data indicate that while the reed's efficiency reaches a peak at Re = 3,000, the sensitivity of η to changes in St_L is, in fact, stronger when the base flow is transitional at Re = 5,000. Even though $\eta \sim 1$ at Re = 9,000, the reed still enables an increase in Nu relative to the base flow at the same Re (cf. Figure 5.10a).

In the investigations presented here, the reeds nearly spanned the full height of the channel (H_s/H = 0.9). Limited investigations were also conducted using reeds of variable

span at *Re* = 5,000 and are discussed in Appendix B and show that while the flow losses decrease with the span of the reed so does the heat transfer enhancement.

5.5 Variation of the Channel Width

The investigations so far have focused on characterization of the effects of the reed on the flow and heat transfer within a characteristic high aspect ratio channel over a broad range of flow speeds, heating power, and reed dimensions while keeping the channel's dimension unchanged. Although detailed variations of channel width are beyond the scope of the present work, this section explores briefly whether the results obtained so far can be scaled when the channel's (high) aspect ratio is varied. To this end, it is checked whether the results obtained with the present $H/W = 5$ aspect ratio can be extended to aspect ratio $H/W = 10$ ($H = 25$, $W = 2.5$, and $L = 250$ mm, described in Chapter II) that are characteristic of low-*Re* heat exchangers (e.g., Bar-Cohen et al., 2002).

To begin with, scaling of the heat transfer as measured by the global Nusselt number (*Nu*) and global channel losses as measured by *f* in channels with $H/W = 5$ and 10 is demonstrated in the absence of the reeds. Based on the dimensionless parameters discussed in §4.1, each channel length is scaled with its width such that $L/W = 50$ in both the $H/W = 10$ and 5 channels and the variations of *Nu* and *f* with *Re* in the base flow of the two channels are shown in Figures 5.11a and b, respectively, for $\dot{Q}_{\text{heater}}'' = 1.6$ KW/m^2. These data show that *f* decreases, and *Nu* increases with *Re* in both channels. While the magnitude of *f* is nearly identical in the two channels at all *Re*, the magnitude of *Nu* is up to 20% lower in the narrower ($H/W = 10$) channel. As discussed in Chapter II, since in the narrower ($H/W = 10$) channel the global Nusselt number is calculated using the average of the local

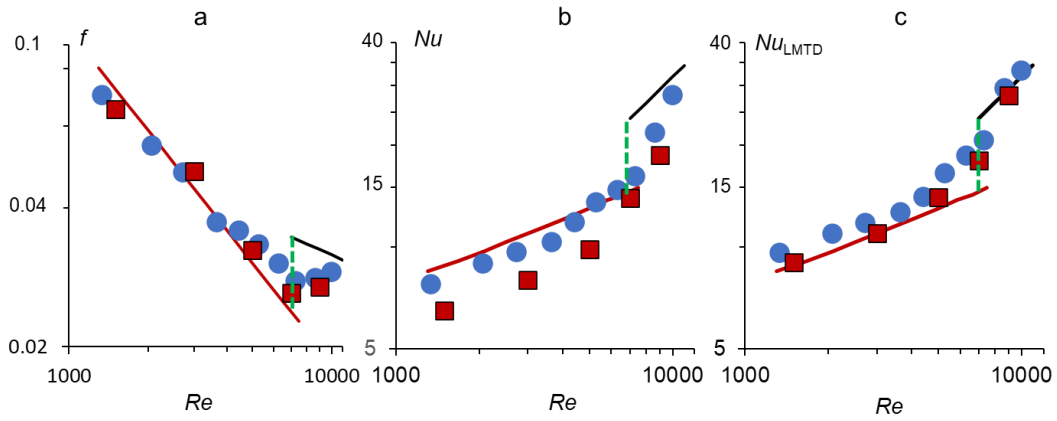

Figure 5.11. *Variation with Re in the base flow of the friction factor f (a), and the global Nusselt number Nu (b) based on internal measurements within the channels, and of the global Nusselt number based on LMTD, Nu_{LMTD} (c) for the H/W* = 10 (■) and 5 (●) *channels at* $\dot{Q}_{heater}$" = 1.6 KW/m^2. *The solid lines denote data for* ***laminar*** *(Kakac, 1967) and* ***turbulent*** *(Hartnett, 1962) flows. The critical Reynolds number for transition to turbulence is marked by a green dashed line based on the data of Hartnett et al. (1962).*

Nusselt numbers at three streamwise panels compared to six panels in the wider (H/W = 5) channel, these discrepancies are attributed to the lower spatial resolution of the temperature data in the narrower channel. Figures 5.11a and b (respectively) also show comparisons of the friction factors and global Nusselt numbers (based on internal measurements, cf. §5.1) in the two channels with the available literature which includes the laminar and turbulent flow data of Kakaç et al. (1987) and Hartnett et al. (1962) for a channel of aspect ratio H/W = 5. For Re < 5,000, the friction factors in the two channels (H/W = 5 and 10) closely resemble the laminar flow data. For 5,000< Re < 10,000, the channel flow transitions to turbulence which increases the friction factor relative to the laminar flow and as the Reynolds number increases, the streamwise domain of transitional flow increases until the friction factors of the base flow asymptotically approach the levels of the fully turbulent channel flow at Re = 10,000. Similar trends were evident in the comparisons of Nusselt

number data in the two channels with the literature albeit the deviations from the laminar flow occur at Re = 7,000.

The global Nusselt numbers of the base flows in the two aspect ratio channels were also compared using a low-resolution technique based on logarithmic mean temperature differences (*LMTD*) of the channels' inlet and exit wall and air temperatures (described in §6.1) which is widely used in heat transfer studies of fin channel arrays. Figure 5.11c shows that the *LMTD* yields a reasonable agreement between the Nusselt numbers of the base flow in the two channels. It is noted that the Nusselt numbers obtained based on *LMTD* are higher than using the internal measurements in both the channels since they only take into account the inlet and exit temperatures and are therefore biased upwards due to the high heat transfer at the channel inlet. Using *LMTD* measurements, both the channels show reasonable agreement with the laminar and fully turbulent flow data by Kakaç et al. (1987) and Hartnett et al. (1962) except for 5,000 < Re < 8,000 where the differences are ostensibly due to changes with Re in the streamwise and spanwise extent of transitional flow in the channel.

In the presence of reeds, based on Equation 4.1, the channel and reed lengths L/W and L_s/W were kept fixed in the two channels (H/W = 5 and 10) and the scaling of the reed driven heat transfer enhancement was checked at Re = 1,500, 3,000, 5,000, 7,000 and

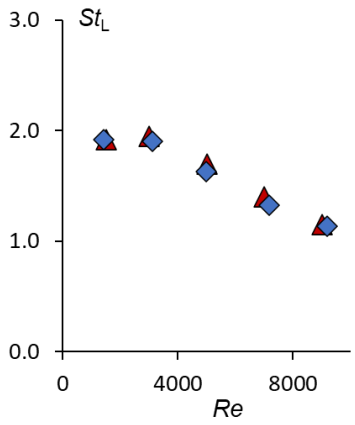

Figure 5.12. *Variation of St_L with Re for reeds with L_s/W = 20 in the H/W* = 10 (▲) *and* 5 (♦) *channels*

9,000. In addition, the reed St_L for a given *Re* was kept the same in the two channels by varying the reed thickness. However, St_L values varied with *Re* such that at each Reynolds number reeds of length, L_s/W = 20 oscillated at their critical speeds. Figure 5.12 shows the variation of St_L with *Re* for the reeds in the two channels.

The variation with *Re* of the reed-enhanced heat transfer and associated channel losses in the *H/W* = 5 and 10 channels are shown in Figures 5.13a and b in terms of the ratios relative to the base flow of the global Nusselt numbers Nu/Nu_b and friction factors f/f_b for heat flux $\dot{Q}_{heater}$" = 1.6 KW/m^2. These data show that at a fixed *Re* and St_L, Nu/Nu_b and f/f_b are nearly identical in the two channels. Between *Re* = 1,500 and 5,000 the reed oscillations lead to increases in Nu/Nu_b and f/f_b from 1.9 to 2.3 and from 2.9 to 4, respectively, but at *Re* = 9,000 Nu/Nu_b and f/f_b decrease somewhat from 2 and 3.6 at *Re* = 7,000 to 1.7 and 3.4, respectively, as the base flow transitions to turbulence. Figure 5.13c shows the similarity in reed efficiency between the two channels through the variation of the thermal enhancement factor, η with *Re*. Similar to the Figure 5.10b, the peak η occurs at *Re* = 3,000 and decreases to 1.05 at *Re* = 9,000.

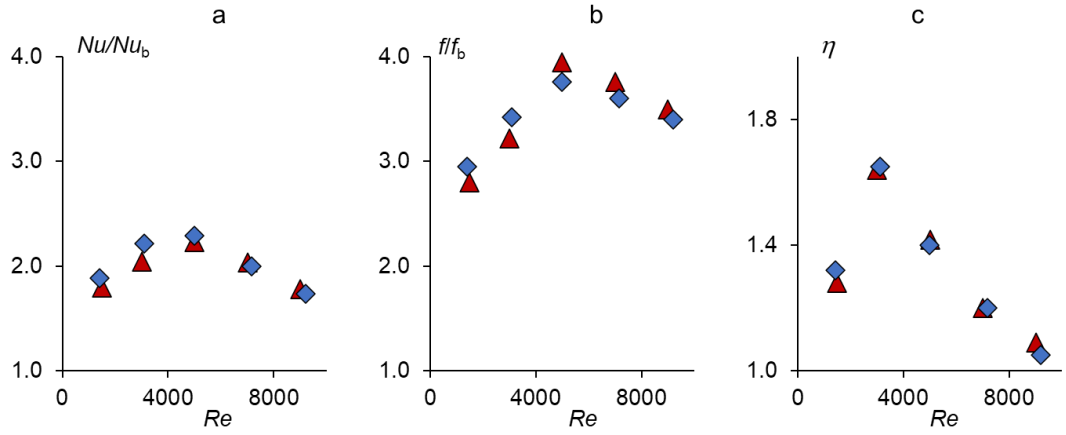

Figure 5.13. *Variation with Re of Nu/Nu$_b$ (a), f/fb (b), and thermal enhancement factor (c) for reeds with L_s/W = 20 in the H/W* = 10 (▲) *and 5* (♦) *channels at* $\dot{Q}_{heater}$" = 1.6 *KW/m*^{2}

The variations of *Nu*/*Nu*$_b$ with *Re* were also computed using *LMTD* (Figure 5.14b) and compared with the earlier calculations based on the internal measurements (repeated for reference in Figure 5.14a**)**. These results show that the reed-enhanced heat transfer in the two channels are identical when computed based on internal measurements and *LMTD* when the length of each reed is scaled with the channel width and St_L and *Re* are invariant. However, these data also show that *Nu*/*Nu*$_b$ computed based on LMTD is *lower* compared

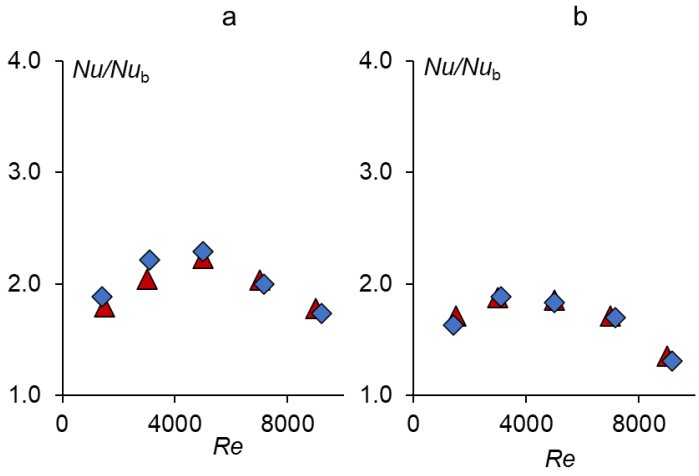

Figure 5.14. *Variation with Re of Nu/Nu$_b$, based on internal measurements (a) and on LMTD (b) for reeds discussed in. Figure 5.13 in the H/W* = 10 (▲) *and 5* (♦) *channels.*

to Nu/Nu_b computed based on the internal measurements within the channel. For example, at Re = 1,500 and 5,000 Nu/Nu_b = 1.6 and 1.83 using *LMTD* and 1.8 and 2.3 using internal measurements indicating that the heat transfer enhancement by the reed is under-predicted when *LMTD* is used.

The measurements in the isolated channels used a single reed within the channel and showed that the reed-enhanced heat transfer diminishes downstream of the reed. The effect of placing multiple reeds along the channel were explored in the H/W = 10 channel and are discussed in Appendix C.

CHAPTER VI

A. IMPLEMENTATION OF REEDS IN FIN ARRAYS

Overview

The system-level scaling of reed-enhanced heat transfer in the isolated channel described in Chapter V was assessed in models of the fin arrays of heat exchangers. The scaling was assessed in arrays of channels of $H/W = 5$ ($W = 5$ mm) using variations of Nusselt numbers and friction factors with the reed Strouhal number at Re = 1,500, 3,000 and 4,500. In addition, since the reeds were mounted externally to the fin array owing to practical considerations, the effect of the reed offset upstream from the start of the fin array on heat transfer enhancement was also assessed.

6.1 The Fin Array Setup

The fin array comprises 9 fin channels of aspect ratio $H/W = 5$ ($W = 5$ mm, $H = 25$ mm and $L = 200$ mm) and includes 10 aluminum fins each $t_{fin} = 0.4$ mm thick that are machined using a wire EDM process onto a 3.125 mm thick base plate. A thin film heater is attached to the bottom of the base plate as shown in Figure 6.1a. The fin array is placed within an acrylic rectangular enclosure that forms the top, bottom and side walls of the array, provides some thermal insulation, and is connected upstream to a rectangular offset section (Figure 6.1c) whose thickness was varied (d_{offset} =20 and 30 mm) to change the streamwise position of the reed in the fin channels. Upstream of the rectangular offset, there is a mounting fixture for that supports the reeds 5.4 mm apart on mounting plates (28 x 5 mm, 0.125 mm thick) within each fin channel as shown in Figure 6.1b. It should be

noted that in the absence of the offset sections, the reeds are mounted 6 mm upstream of the fin array by the thickness of the mounting fixture. The mounting fixture is connected to a 3:1 contraction with an exit measuring 50.8 x 25.4 mm (Figure 6.1c). The mass flow

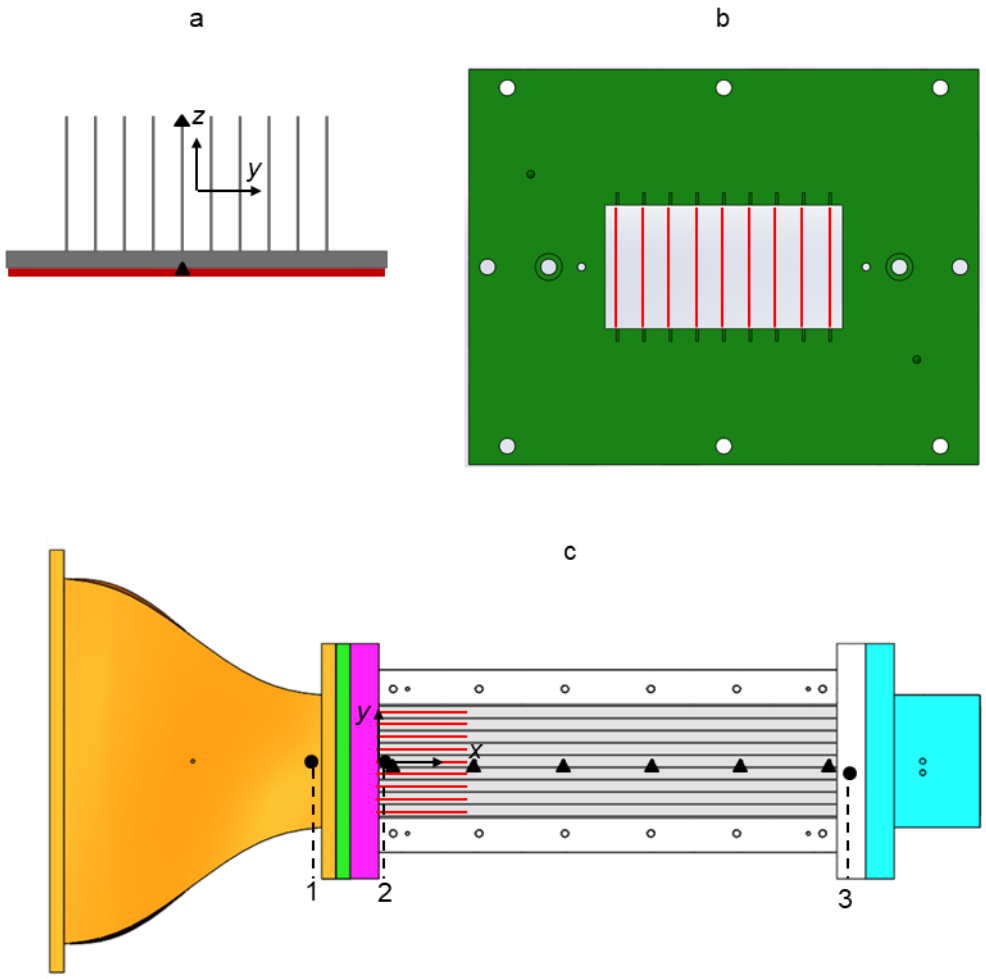

Figure 6.1. *a) Front view of the fin arrays showing the thin film heater attached from below to the base plate of the fin array and the spanwise locations of two streamwise arrays of equally-spaced (38.5 mm apart) thermocouple sensors that are attached along the top and below the 5th fin from the left ($\hat{y}$ = -0.5) in notches along its top edge and within grooves in the base plate; b) Front view showing the mounting fixtures for the reeds upstream of the fin array; and c) Top view of the assembled test setup showing (from left to right) the* ***contraction****, the* ***reed mounting fixture****,* ***offset section****, the acrylic channel, the fin channel array and the* ***mixing section****. The streamwise locations of pressure ports labeled 1,2 and 3 (●) and the thermocouple sensors over and below the 5th fin (▲) are also shown in (c)*

rate ($\dot{m}$) of the cooling air within the assembly is metered upstream of the contraction using a thermal mass flow meter.

The heat transfer measurements are conducted using the streamwise distribution the fin temperatures $T_w(\hat{x},\ \hat{z})$ using a streamwise array of 6 equally-distributed pairs of T-type thermocouple sensors (between $3 < x < 196$ mm) that are each mounted along the top edge ($\hat{z}$ = 2.5) and bottom (within the base $\hat{z}$ = -2.5) of the 5th fin from the left in Figure 6.1a. The thermocouple sensors at the bottom of the fin are glued within grooves in the base plate before the thin film heater (Figure 6.1a) is attached. The thermocouples at the top edge of the 5th fin are attached within v shaped notches (1 mm deep) using adhesive.

The gauge static pressure was measured at the static pressure ports on the top surface of the assembly as shown in Figure 6.1c (marked by 1, 2 and 3) and the channel's friction factor was calculated using the measured pressure drop between the pressure taps 2 (near the inlet of central fin channel, fifth channel from left in Figure 6.1a, $\hat{x}$=0.5) and 3 (at the exit of central channel, $\hat{x}$ = 40) for comparison with the isolated channels in Chapter V. The combined pressure drop across the reeds and the fin channels [i.e. between taps 1 (at the exit of the contraction) and 3 in Figure 6.1c] was used to calculate the friction factor in the presence of the reed in §6.4.

The periphery of the acrylic enclosure was insulated using glass fiber sheets (12.7 mm thick) which spanned the length of the fin channels and have thermal conductivity comparable to the air insulation gap used in the isolated channels. In contrast to isolated channels, where the heat dissipated to the air was calculated by subtracting the insulation losses from the heater power (cf. §5.1), the heat dissipated to air was calculated by

measuring the increase in the thermal energy ($\dot{m}\bullet\tilde{C}_p\bullet\Delta T_a$) of the air flow (as discussed in §6.2). To this end, it is necessary to measure the flow velocity and temperature distributions at the exit of the fin channels. However, since the flow velocities and temperatures vary somewhat between the channels, a straight section for mixing the channel flows ($L_{\text{mixing section}}/W = 5$) is used at the exit of the fin array (Figure 6.1c). The distributions of the flow velocity and temperature were measured downstream of the exit of the mixing section to calculate the heat dissipated to the air in the fin array. To minimize heat losses from the mixer, it was also insulated using glass fiber sheets. The insulation losses from the mixing section were measured using four pairs of thermocouple sensors. Each wall of the mixing section had a pair of T-type thermocouples attached at its center and across the thickness of the wall which were used to measure the conduction losses across its walls (similar to measurements of insulation losses in the isolated channels as discussed in Chapter 2). It was found that the maximum insulation losses from the mixing section were about 0.5% of the overall heater power $\dot{Q}_{\text{heater}}$.

The velocity and temperature profiles downstream of the mixing section were measured using a pitot tube and a T-type thermocouple sensor mounted on a computer-controlled traverse in the *y*-*z* plane. Measurements are acquired on a rectangular 11 x 6 grid which covered the cross-section of the exit plane of the mixing section (measuring 50 mm x 25 mm in the *y* and *z* directions, respectively) with increments $\Delta y = 10$ and $\Delta z = 5$ mm. At each grid point, the velocity and temperature data were sampled at 10 Hz and for 10 secs and the data were used to compute the time averaged streamwise velocity u_e and temperature $T_{a,e}$.

6.2 Calculations of the Heat Transfer in the Fin Array

The heat dissipated to the air in the fin array is computed by assessing the increase in bulk mean temperature of the air across the fin array. To this end, air temperature near the inlet of the fin array (assuming a uniform distribution of flow velocity and temperature), $T_{a,i}$ is measured $10W$ upstream of the array and the exit bulk mean temperature, $T_{m,e}$ is measured using integrated velocity and temperature profiles obtained downstream of the mixing section. The heat dissipated in the fin array to the air $\dot{Q}_{air}$ is computed as:

$$\dot{Q}_{air} = \dot{m} \cdot C_p(T_{m,e} - T_{a,i})$$

$T_{m,e}$ is the bulk mean temperature at the exit (y-z) plane of fin array defined as:

$$T_{m,e} = \iint (u_e/U) \cdot T_{a,e} \cdot d\hat{y}d\hat{z}$$

where U is the average flow speed within the fin array. An estimate of $T_{m,e}$ was calculated just downstream of the exit mixer using the y-z distributions of air velocity, u_e and temperature, $T_{a,e}$, obtained on a 11 x 6 grid (cf. Section 6.1).

While the heat transfer in isolated channels was characterized through the variations in local Nusselt numbers using "internal measurements", the spatial resolution of wall and flow temperatures limits the use of "internal measurements" in fin arrays. Following conventional methodology used in heat transfer studies on fin arrays, the global Nusselt numbers were calculated based on the lower resolution *LMTD* methodology using the temperature distributions along the bottom of the instrumented fin. The present *LMTD* methodology is similar to the procedure described by Naphon et al.(2009). For a given fin

temperature distribution $T_w(x)$ and total heat flux to the air, $\dot{Q}_{air}^{"}$, the global heat transfer coefficient, h_{LMTD}, is defined based on Newton's law as

$$h_{LMTD} = \frac{\dot{Q}_{air}^{"}}{LMTD}$$

$$LMTD = \frac{(\Delta T_1 - \Delta T_2)}{\log(\Delta T_1 / \Delta T_2)}$$

$$\Delta T_1 = T_w(x_0) - T_m(x_0)$$

$$\Delta T_2 = T_w(x_e) - T_m(x_e)$$

where *LMTD* is the logarithmic mean temperature difference, $T_w(x_0)$ and $T_w(x_e)$ are the fin bottom temperatures and $T_m(x_0)$ and $T_m(x_e)$ are the bulk mean air temperatures at the fin array inlet (x_o) and exit (x_e) respectively. In addition, $T_m(x_0) = T_{a,i}$ and $T_m(x_e) = T_{m,e}$ and $T_{a,i}$ and $T_{m,e}$ are measured upstream and downstream of the fin array respectively as discussed earlier. The global Nusselt number based on the LMTD methodology is

$$Nu_{LMTD} = h_{LMTD} \cdot D_h / k_a$$

Before calculating Nu_{LMTD} for the fin array, a representative comparison is shown between internal measurements and *LMTD* methodology in the absence and presence of selected reeds ($L_s/W = 20$) in the $H/W = 5$ isolated channel through variations with *Re* of the global Nusselt numbers *Nu* and Nu_{LMTD} as shown in Figure 6.2. These data show that for $1{,}000 < Re < 10{,}000$ while in the absence of the reeds the global Nusselt numbers based on

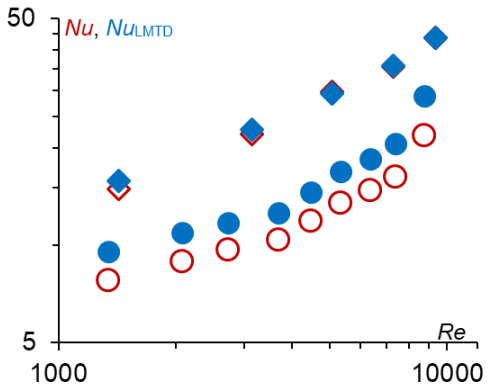

Figure 6.2 *Variation with Re of the global Nusselt numbers calculated using internal measurements* (*Nu*) *and LMTD* (Nu_{LMTD}) *in the absence* (○, ●) *and presence of reeds* (◊, ♦) *of length* $L_s/W = 20$ *in the* $H/W = 5$ *isolated channel.*

LMTD are on an average 15% higher than when using on internal measurements, the two methods yield nearly identical global Nusselt numbers in the presence of the reeds. Hence, as discussed in §5.5, the Nusselt number enhancement due to the reeds is under-predicted when using LMTD methodology. *Although LMTD technique only approximates the "true" variations of the global Nusselt numbers, it is used in the current fin array studies since the local variations in Nusselt numbers could not be obtained due to limitations of access to local wall and air temperatures inside the fin array*.

6.3 Scaling between Isolated Channels and Fin Arrays

The heat transfer and losses were compared between isolated channels and fin arrays in the base flow and in the presence of reeds at Re = 1,500, 3,000 and 4,500. Similar to the measurements in the H/W = 5 isolated channel, the heater power was varied in the fin arrays such that maximum fin temperature $ITD_{max} = 40^0$C in both the absence and presence of the reeds. It is noted that owing to limitations of the heater power in the fin array ITD_{max} could only be set to a maximum of 40°C in the fin array compared to 60°C in the isolated channels. A comparison between the effects of setting ITD_{max} to 40°C and 60°C in the isolated channel for the base flow and in the presence of the reeds at Re = 1,500, 3,000 and 4,500 is included in Appendix C and shows that Nu and f are the same for the two temperatures indicating that the isolated channel data at ITD_{max} = 60°C can be used as a proxy for measurements at ITD_{max} = 40°C.

To begin with, Figure 6.3 shows the variation of the top and bottom fin temperatures in the absence of the reed for Re = 1,500, 3000 and 4,500 for $\dot{Q}_{heater}$ = 73.2, 99.0 and 136.9

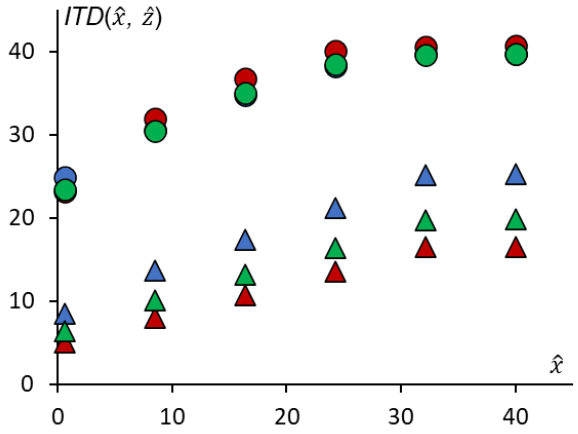

Figure 6.3. *Streamwise variation of the fin temperatures* ITD_t *(*$\hat{z}$ *= 2.5* ▲*)*and ITD_b *(*$\hat{z}$ *= -2.5,* ●*) in the base flow for Re = 1,500* (●, ▲)*, 3,000*(●, ▲), *4,500* (●, ▲) *for H/W = 5 and* ITD_{max} *= 40°C.*

W. The respective heat dissipated to the air in the fin array was $\dot{Q}_{air}$ = 65.9, 90.1 and 126.2 *W*. As evident in Figure 6.3 for all *Re*, the bottom and top fin-temperatures (ITD_b and ITD_t) increase in the streamwise direction (similar to the trend seen in isolated channels cf. Figure 5.2) and become nearly streamwise-invariant for $\hat{x} > 30$. However, ITD_t is lower than ITD_b throughout the channel length due to conduction resistance across the fin height and is affected by the fin efficiency, η_{fin} is defined as (Incropera et al., 2002)

$$\eta_{fin} = \tanh(mH)/(mH)$$

$$m = \sqrt{\frac{h_m P_{fin}}{k_{al} A_{fin}}}$$

where h_m is the average heat transfer coefficient based on LMTD, and $P_{fin} = 2(L+t_{fin})$ and $A_{fin} = L \cdot t_{fin}$ are the perimeter and area of the *x*-*y* cross-section of the fins, respectively. The Nusselt number Nu_{LMTD} was calculated based on ITD_b using LMTD and fin efficiency correction as described by Teertstra et al. (1999) was applied to obtain an estimate of the isothermal Nusselt number defined as $Nu_T = Nu_{LMTD}/\eta_{fin}$. *It should be noted that this correction accounts for spanwise temperature variations due to the fin's thermal conductivity and enables scaling of channel's heat transfer if a different fin material is used*. Figure 6.4a shows the variation of Nu_{LMTD} and Nu_T with *Re* in the base flow and they are compared with Nu_{LMTD} in the base flow of the isolated channel (where $\eta_{fin} = 1$). While Nu_{LMTD} for the fin array and isolated channel are nearly identical, Nu_T in the fin array is up to 25% higher (at *Re* = 4,500) than in the isolated channel ostensibly because the length of

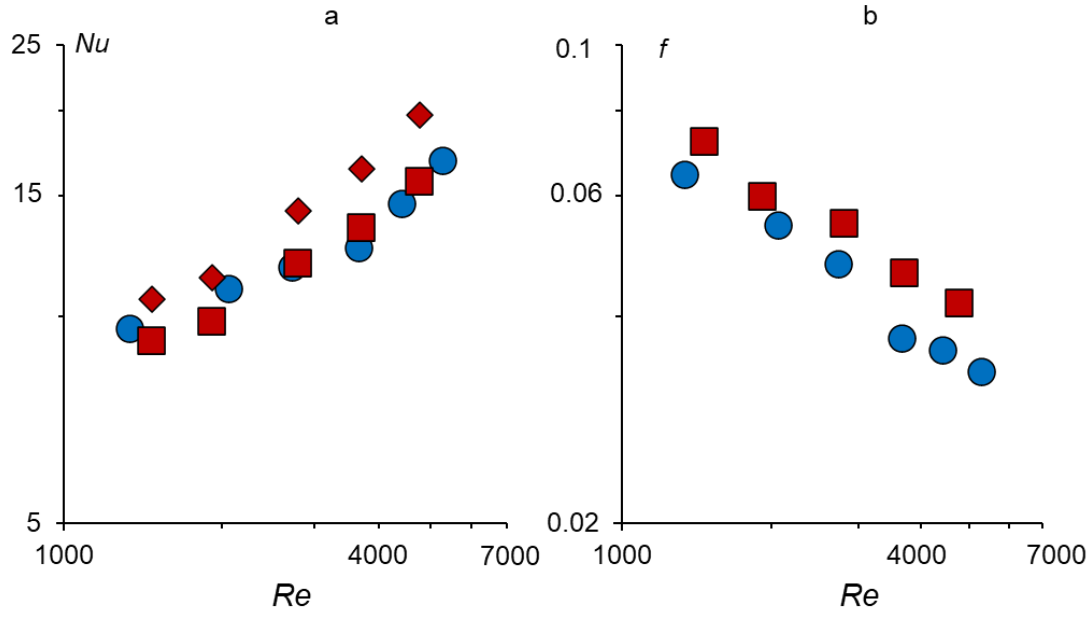

Figure 6.4. *Variation with Re of a)* Nu_{LMTD} (■) *and* Nu_T (♦) *for the fin array* (ITD_{max} = 40°C) *and* Nu_{LMTD} (●) *of the isolated channel* (ITD_{max} = 60°C)*; and b) friction factor, f for the fin array* (■) *and isolated channels* (●) *of H/W = 5.*

the fin array channels (L/W = 40) is 20% shorter than in the isolated channels (L/W = 50). As shown by Kakaç et al. (1987), for laminar developing flows, Nu and f decrease as $(L/W)^{-1}$ owing to streamwise thickening of thermal boundary layers. The differences in Nu between fin array channels and the isolated channel can therefore be accounted for by scaling Nu with L/W. A comparison between the isolated channel and the fin array channels shows that the respective $Nu \cdot L/W$ are 260 and 254 for Re = 1,500 and 440 and 450 at Re = 4,500. The variation of friction factor f with Re (Figure 6.4b) shows a monotonic decrease for both the isolated channel and the fin array channels and the differences between them can be accounted for by a respective similar scaling with channel length ($f \cdot L/W$ = 1.8 and 1.73 at Re = 1,500 and $f \cdot L/W$ = 1.07 and 1.03 at Re = 4,500).

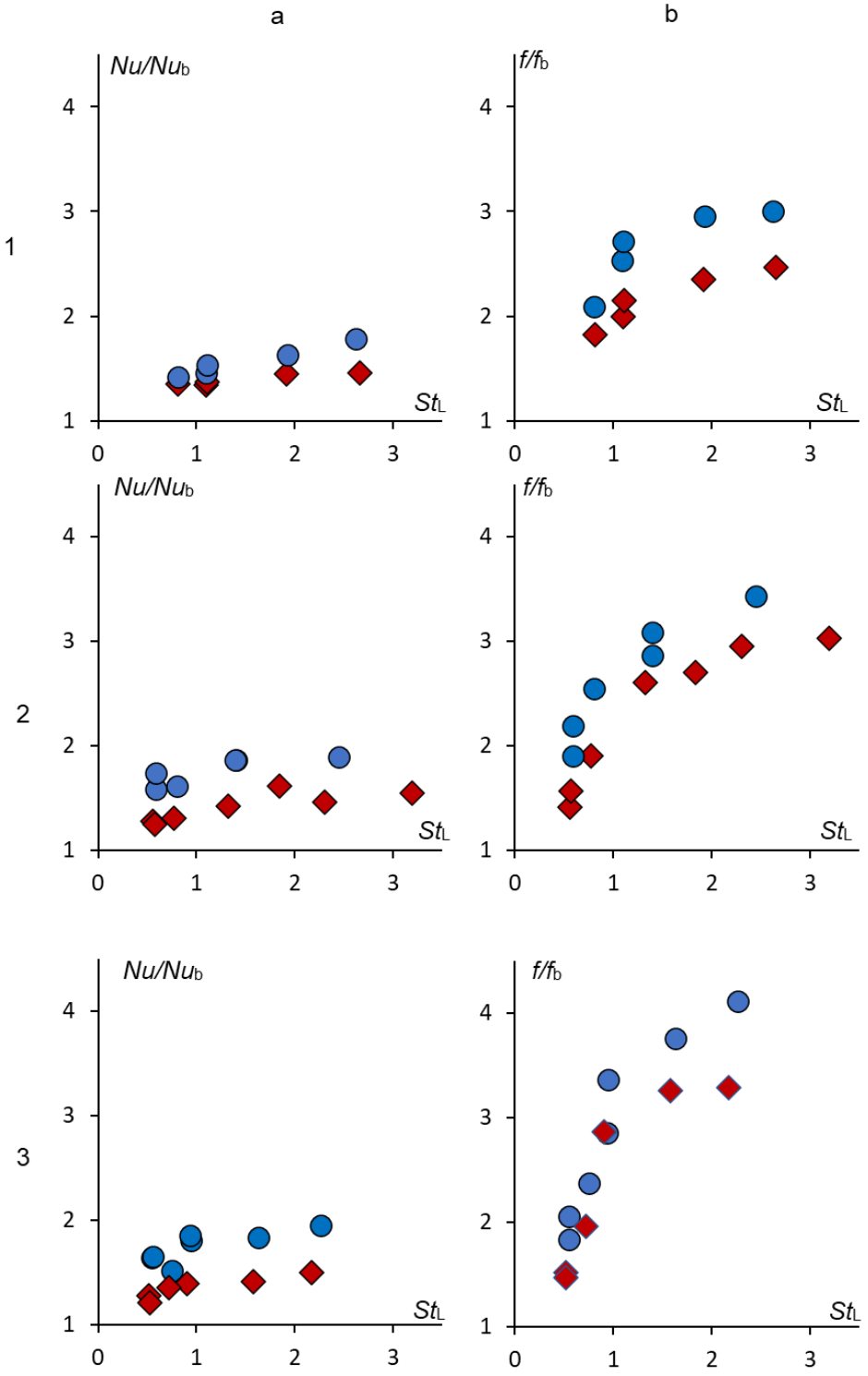

Figure 6.5. *Variation with reed Strouhal number, St_L of Nu/Nu_b and f/f_b for the fin array (♦) and the isolated channel (●) at Re = 1,500 (a.1 and b.1), 3,000 (a.2 and b.2) and 4,500 (a.3 and b.3). Channel aspect ratio is H/W = 5 and ITD_{max} is the same as Figure 6.4.*

Following the comparison of the base flow heat transfer between the isolated channel and the fin array, attention is shifted to comparisons of heat transfer enhancements and channel loss increments in the presence of the reeds for the Reynolds numbers tested in the base flow. Similar to the base flow, the temperature variations along fin height in the presence of reeds are accounted for by using the fin efficiency η_{fin} (cf. Figure 6.4) to obtain an isothermal estimate of Nusselt number. Following the discussion of Figures 5.9-a.1 and b.1, the variations in the ratios of Nusselt numbers, Nu/Nu_b and friction factors f/f_b with St_L are assessed in the fin array and compared with the isolated channel at Re = 1,500 (Figures 6.5-a.1 and b.1), 3,000 (Figures 6.5-a.2 and b.2) and 4,500 (Figures 6.5-a.3 and b.3). At Re = 1,500, while f/f_b is smaller in the fin-array at all St_L (f/f_b is 12.5 and 12% smaller at St_L = 0.8 and 2.6 respectively), Nu/Nu_b is nearly identical between the fin-array and the isolated channels for $St_L < 1.92$ beyond which it is noticeably smaller in the fin arrays (for e.g., Nu/Nu_b is 15% smaller in the fin arrays at St_L = 2.6). Similar to Re = 1,500, at Re = 3,000 (Figures 6.5-a.2 and b.2), a lower f/f_b is evident for the fin-array as compared to the isolated channel at all St_L (f/f_b is 20% and 16% smaller at St_L = 0.55 and 2.30 respectively). In addition, lower Nu/Nu_b is now evident at all St_L in the fin array as compared to the isolated channel (Nu/Nu_b is 18 and 20% smaller at St_L = 0.55 and 2.30 respectively). At Re = 4,500, the reduction in Nu/Nu_b in the fin array is 23 and 22.5% and f/f_b is 18 and 22% at St_L = 0.51 and 2.2, respectively. These data indicate that the increment in channel losses (as measured by f/f_b) are smaller in the fin array as compared to the isolated channels at all Re and St_L. This is because the channel losses in the absence of the reed are higher in the fin array (cf. Figure 6.4b) and the channel losses (f) in the presence of the reed only depend on the Strouhal number of the reed (cf. §4.5) which are kept

identical between the isolated channels and fin arrays. The heat transfer enhancement (Nu/Nu_b) due to the reed is nearly identical between the fin array and the isolated channels at the lower Reynolds number (Re = 1,500) and lower Strouhal numbers ($0.5 < St_L < 1.92$). However, at the higher Reynolds numbers of 3,000 and 4,500, Nu/Nu_b values are smaller in fin arrays as compared to the isolated channel at all Strouhal numbers.

To investigate the cause of lower reed-enhanced heat transfer in the fin arrays compared to the isolated channels at higher Reynolds numbers of 3,000 and 4,500, the enhancement by two reeds having the same planform dimensions ($L_s/W = 10$) was compared at different Reynolds numbers: Reed I which operated at Re = 1,500 and St_L = 0.8 (cf. Figure 6.5-a.1) and has nearly identical Nu/Nu_b in the fin array and in the isolated channel, and Reed II which operates at Re = 4,500, St_L = 2.2 (cf. Figure 6.5-a.3) and for which Nu/Nu_b is 22% lower in the fin array compared to the isolated channel. The streamwise variations of thermal resistances near the top and bottom of the fin were

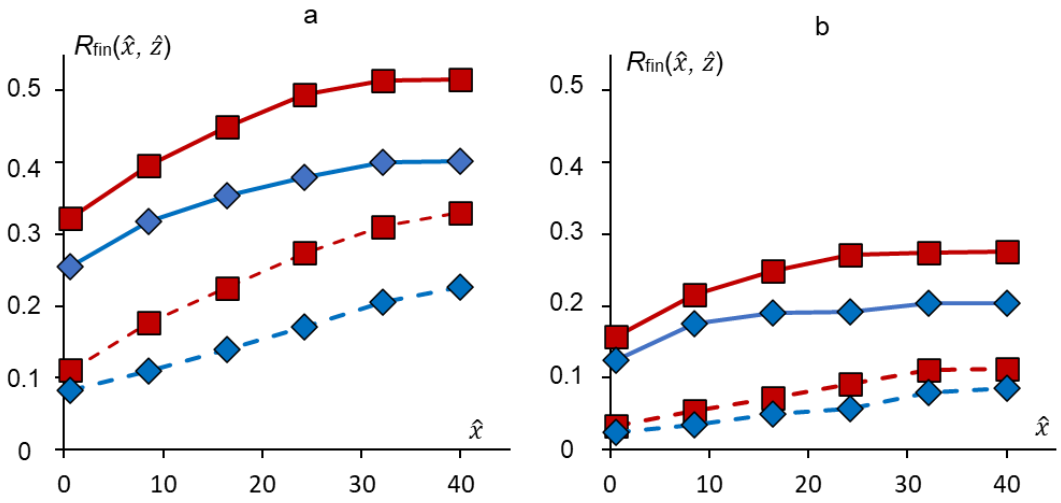

Figure 6.6. *Streamwise variation of the bottom ($\hat{z}$ = -2.5, solid lines) and top ($\hat{z}$ = 2.5, dashed lines) fin resistances $R_{fin}(\hat{x}, \hat{z})$ in the base flow (■) and in the presence of the reed (♦) a) Reed I, Re = 1,500, St_L = 0.8 (cf. Figure 6.5-a.1), and b) Reed II, Re = 4,500, St_L = 2.2 (cf. Figure 6.5-a.3)*

assessed in the absence and presence of reed I (Figure 6.6a) and reed II (Figure 6.6b). The fin thermal resistance $R_{fin}(\hat{x}, \hat{z})$ is defined as:

$$R_{fin}(\hat{x}, \hat{z}) = ITD(\hat{x}, \hat{z})/\dot{Q}_{heater}$$

While Figure 6.6a shows that in the presence of Reed I**,** both the top and bottom fin resistances decrease by nearly identical amounts (relative to the base flow), for $\hat{x} > 10$, Figure 6.6b shows that reductions in top fin resistance is nearly negligible due to Reed II. These data indicate that at the higher *Re*, most of the heat transfer enhancement (due to decrease in thermal resistance) occurs at the fin base and a there is negligible heat transfer enhancement due to lower fin *ITD*s near the fin top (as evident in Figure 6.4). It is conjectured that the reduction in overall lower Nu/Nu_b compared to the isolated channel is due to lower *ITD*s near the top of the fins in the fin array while in the isolated channel *ITD* is uniform.

The efficiency of reed in the fin array and the isolated channel are compared using the variations of Nusselt numbers with normalized flow power, $\hat{W}_{pp}$ between the base flow and in the presence of reed and is shown in Figure 6.7. This analysis follows the procedure discussed in connection with Figure 5.10. These calculations use the isothermal estimate of Nusselt number, Nu_T, in the fin array (Figure 6.7a) whereas Nu_{LMTD} is used in the isolated channel (Figure 6.7b) since the spanwise temperature variations are negligible (the

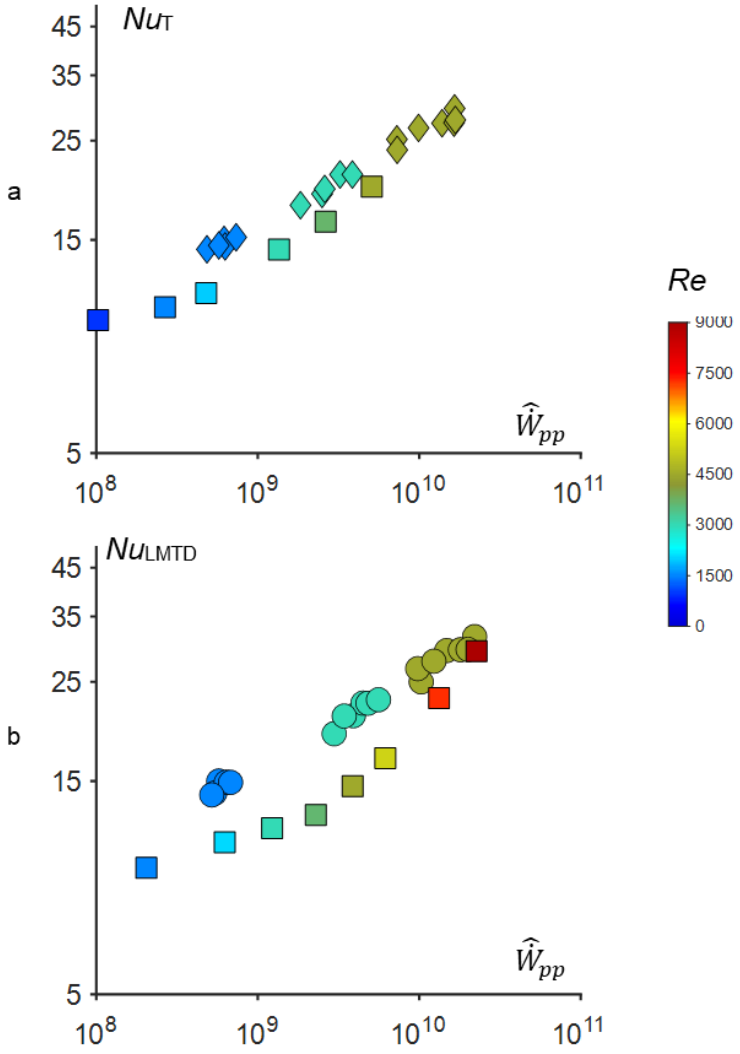

Figure 6.7 *Variation with normalized flow power, $\hat{W}_{pp}$ of a) Nu_T in the fin array and b) Nu_{LMTD} in the isolated channel in the base flow (■) and in the presence of reeds (♦, ●) at Re = **1,500**, **3,000**, **4,500**. The base flow and reed symbols are color coded based on the Reynolds number and the color bar is shown on the right.*

reed and base flow in Figures 6.7a and b are color coded by *Re*). In the presence of reeds, the Nusselt numbers and $\hat{W}_{pp}$ at each Reynolds number (*Re* = 1,500, 3,000 and 4,500) increase with the reed Strouhal number. Comparison of Figure 6.7a and 6.7b shows that in the absence of the reeds, the Nusselt number for a fixed flow power is higher in the fin array than in the isolated channel (e.g. for the base flow at $\hat{W}_{pp} = 0.5 \cdot 10^9$ and $5 \cdot 10^9$ respectively, the Nusselt numbers are 11.5 and 19.7 in the fin array and 11 and 16.9 in the isolated channels). This can be expected since the inlet velocity fluctuations in the fin arrays are higher due to the abrupt entrances compared to the smooth entrances in the isolated channel. However, in the presence of reeds, variations of Nusselt number with flow power are nearly identical in the fin array and the isolated channels (at $\hat{W}_{pp} = 0.5 \cdot 10^9$ and $5 \cdot 10^9$ respectively, the Nusselt numbers are 14.1 and 22.8 in the fin array and 14 and 22.3 in the isolated channels). The similarity between the isolated channels and fin arrays show that the channel thermal characteristics (Nusselt number and the flow power) in the presence of reed only depend upon the Reynolds number and the Strouhal number and are independent of entrance conditions. Similar to the isolated channel, the reed heat transfer efficiency in fin array is evident from Figure 6.7a which shows that at a fixed flow power the Nusselt number increases in the presence of the reed relative to the base flow.

Similar to the analysis in §5.4, two measures are calculated to compare the reed efficiency between the isolated channel and the fin array namely, the reed thermal enhancement factor η, and the COP_{ratio} (at a fixed Nusselt number). At *Re* = 1,500 (in the presence of the reed), in the fin array $\eta \approx 1.25$ and $COP_{\text{ratio}} \approx 2.5$ (at all St_L) while for the isolated channel $\eta \approx 1.28$ and $COP_{\text{ratio}} \approx 4$. At *Re* = 3,000, in the fin array, η and COP_{ratio}

are 1.2 and 1.9 at St_L = 0.58 and decrease to 1.1 and 1.15 at St_L = 3.2 whereas in the isolated channel, η and COP_{ratio} are 1.5 and 2.6 at St_L = 0.5 and decrease to 1.35 and 1.85 at St_L = 2.5. These comparisons were not possible at reed *Re* = 4,500 since the flow power in the base flow and in the presence of the reed could not matched due to limitation of the blower.

These data suggest that the reed efficiency is similar between the fin array and the isolated channel at *Re* = 1,500 (which is within the range of *Re* at which industrial scale heat exchangers operate). At the higher *Re* (*Re* = 3,000), the efficiency of the reed in the fin array is lower than in the isolated channels since the reed-enhanced heat transfer is lower (as also discussed in connection with Figure 6.6).

6.4 Limited Investigations of External Reed Mounting

While in the isolated channel the reeds were mounted within the channel (Chapter II), the implementation of reeds in fin arrays of heat exchangers will require external mounting, upstream of the fin array as discussed in §6.1. In addition to the offset provided by the reed mounting fixture (d_{offset}/W = 1.2, Figure 6.1) the reeds were also offset by additional spacers with d_{offset}/W =4 and 6 that were used along with reeds of length L_s/W = 5.2 and 10 in the H/W = 5 fin array. Reeds of length, L_s/W = 10 were selected since they operated at low St_L and therefore had a significantly lower friction factor and nearly identical Nusselt number enhancement as longer reeds (cf. Figure 6.5). The shorter reeds were selected to determine whether the Nusselt number enhancement remained the same as with the longer reeds. These offsets were selected since $d_{offset}/W < 1$ would have made little difference since the reed is adhered to the mounting post along 1W of its length and therefore contributes marginally to losses or heat transfer, and $d_{offset}/W > 6$ was deemed unreliable

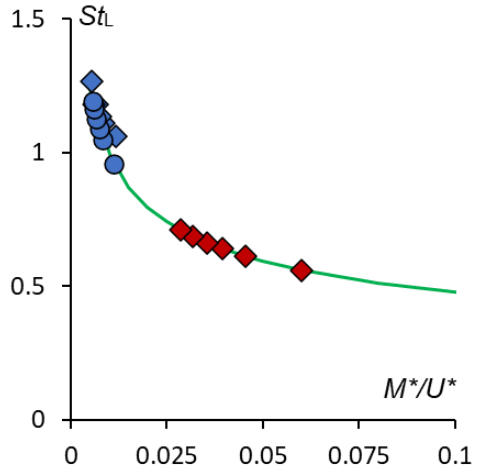

Figure 6.8. *Variation of strouhal number, St_L with M*/U* for reeds of length L_s/W = 10 , and thickness t_s = 12.7 μm and offset d_{offset}/W = 1.2 (♦) and 6 (●) and L_s/W = 5.2 with d_{offset}/W = 1.2(♦). The green curve is $St_L = 0.23(M^*/U^*)^{-0.33}$based on the isolated H/W = 5 channel data (Figure 4.26c).*

since the reed could be displaced out of the fin channels. Also, it was found that the differences in reed oscillation frequency and the channel friction factor between offsets of d_{offset}/W =4 and 6 are negligible and discussions of d_{offset}/W =4 were omitted in the present discussion. Given the interest in industrial heat exchangers the range of Reynolds numbers $1{,}000 < Re < 2{,}000$ was selected.

The effect of reed offset was assessed for reeds of thickness t_s = 12.7 μm using two sets of measurements: a) the reed length was fixed (L_s/W = 10) while varying the offset (d_{offset}/W = 1.2 and 6) and b) the reed length within the channel (L_s-d_{offset}/W = 4) was fixed using reed length, L_s/W = 10 and d_{offset}/W =6 and reeds length L_s/W = 5.2 and d_{offset}/W =1.2. The effect of offset was assessed by measurement of changes in the reed oscillation frequency followed by measurements of the changes in friction factor and Nusselt numbers. As discussed in §6.1, the combined pressure drop across the reed and fin channels (between points 1 and 3 in Figure 6.1a) was used to calculate the friction factor, *f* and, as discussed in connection with Figure 6.7, Nu_T was used as an isothermal estimate of the Nusselt number. Figure 6.8 shows the variation of the St_L with M^*/U^* and includes comparison with the corresponding fitted data of the isolated channel H/W = 5 (cf. Figure 4.26c). These data show a good agreement with the isolated channel despite the variations in offset and length (note that L_s/W = 5.2 reed oscillates at a lower St_L corresponding to higher M^*/U^* than L_s/W = 10) .

Figures 6.9-a.1 and b.1 show the variation of *f* and Nu_T with *Re* in the absence and presence of the reeds discussed above. In the presence of reeds, *f* and Nu_T are higher than in the base flow over the range of Reynolds numbers tested. For L_s/W = 10 both *f* and Nu_T are lower for the reeds with d_{offset}/W =6 compared to the d_{offset}/W =1.2 for

1,000 < *Re* < 2,000. For reeds with lengths L_s-d_{offset} /W = 4 within the channel, f is marginally lower in the presence of L_s /W = 5.2 reed (d_{offset} /W =1.2) than the L_s /W = 10 reeds (d_{offset} /W = 6) but Nu_T is the same between the two reeds for *Re* < 1,300 and marginally higher for the L_s /W = 5.2 reed for *Re* > 1,500. As expected, due to the lower Strouhal number and for a fixed offset (d_{offset} /W =1.2), the shorter reed L_s /W = 5.2 has

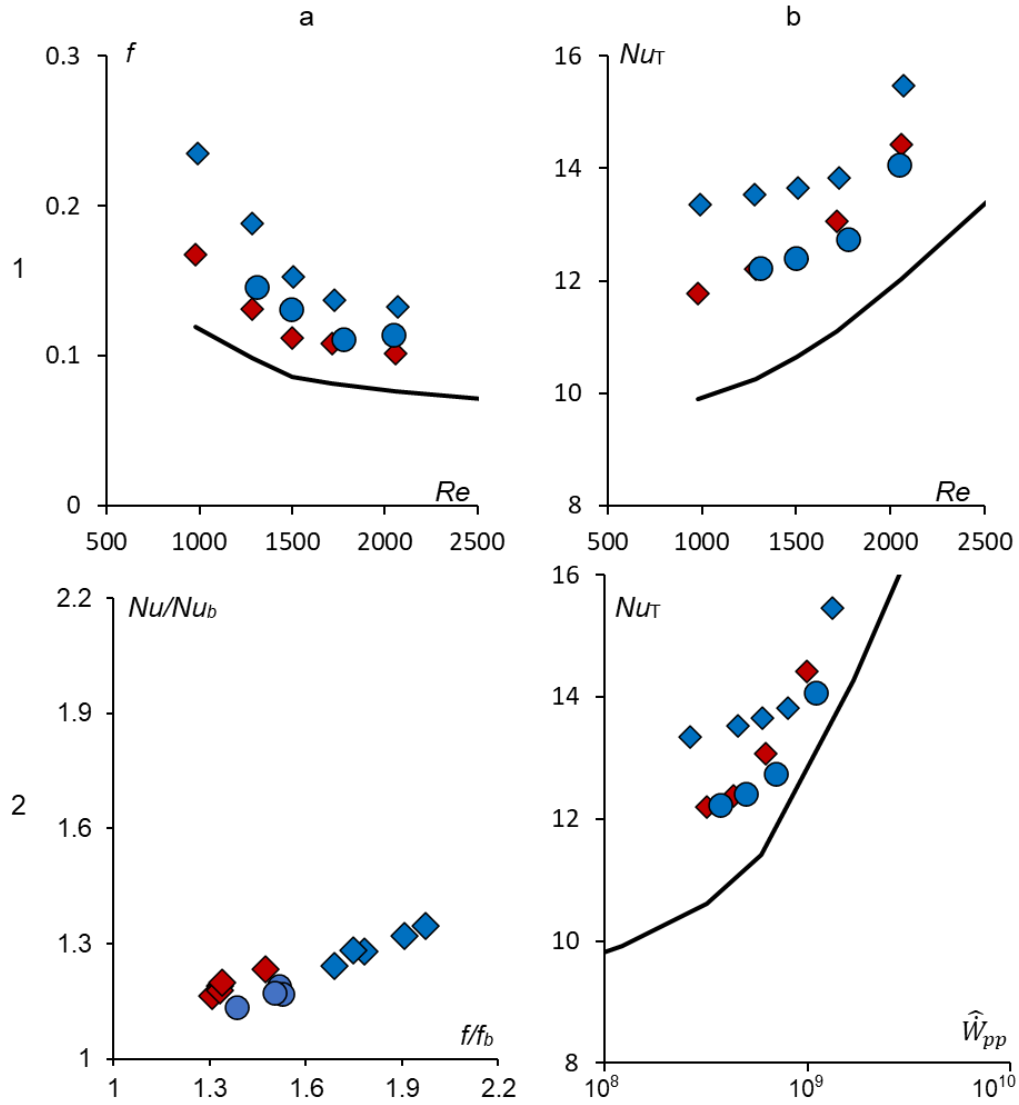

Figure 6.9. *Variation with Re of friction factor f (a.1) and* Nu_T *(b.1); and the variation of* Nu/Nu_b *with* f/f_b *(a.2) and of* Nu_T *with flow power,* $\widehat{W}_{pp}$ *(b.2) in the base flow (shown by solid black lines) and in the presence of reeds:* $L_s/W = 10$, $t_s = 12.7$ *μm* , $d_{offset}/W = 1.2$ (♦) *and 6* (●), *and* $L_s/W = 5.2$ *and* $d_{offset}/W = 1.2$ (♦).

lower f and Nu_T for all Re . The variation of Nu/Nu_b with f/f_b is assessed in Figure 6.9-a.2. While a higher offset in the presence of $L_s/W = 10$ reed decreases f/f_b, it also decreases the Nu/Nu_b. For reeds with $d_{offset}/W = 1.2$ and 6, the ratios vary linearly as $Nu/Nu_b = 0.33f/f_b + 0.67$. In comparison, the $L_s/W = 5.2$ reed with $d_{offset}/W = 1.2$ (which has a nearly identical length within the channel as the $L_s/W = 10$ reed with $d_{offset}/W = 6$) appear to have marginally higher Nu/Nu_b at the same f/f_b.

The efficiency of the reeds is also assessed through the variations of Nusselt number with flow power in the base flow and in the presence of the reeds as shown in Figure 6.9-b.2. These data show that the reeds increase the Nusselt number relative to the base flow at a fixed flow power. At any fixed flow power, the $L_s/W = 10$ reeds with $d_{offset}/W = 1.2$ have the highest Nusselt number and hence efficiency. As an illustration, the maximum thermal enhancement factor, η which occurs at $\hat{W}_{pp} = 2.6 \cdot 10^8$ is 1.26 and 1.15 respectively for $d_{offset}/W = 1.2$ and 6 (for $L_s/W = 10$ reeds). The maximum COP_{ratio} in the presence of reeds which occurs at $Nu = 13.4$ are 3 and 1.33 respectively for $L_s/W = 10$ reed with $d_{offset}/W = 1.2$. In addition, $L_s/W = 5.2$ reed with $d_{offset}/W = 1.2$ has lower η than the $L_s/W = 10$ with $d_{offset}/W = 6$ for $\hat{W}_{pp} < 8 \cdot 10^8$ ($Re < 1{,}500$) but beyond that the thermal enhancement factors are nearly equal.

These data show that while the losses can be reduced when the reed mounting is offset upstream of the channel, the decrease in Nusselt number is not insignificant and therefore reeds with $d_{offset}/W = 1.2$ perform better in terms of η and COP than with $d_{offset}/W = 6$.

CHAPTER VI

B. SYSTEM LEVEL PERFORMANCE ENHANCEMENT

The reed-enhanced heat transfer in model fin arrays (cf., Chapter VI.A) can be utilized to assess potential performance improvements in large-scale systems such as air-cooled condensers that utilize finned airside heat exchangers.

As discussed by Bustamante et al. (2016), conventional air-cooled condensers (ACCs) have been hindered by high air-side thermal resistance and poor air thermal capacity. To enable efficient operation of the condensers, the heat transfer between the condensing steam and the air-side medium must be significantly enhanced while maintaining reasonable air-side pressure drop. The air side pressure drop in a typical A-frame air-cooled condenser system is dominated by a number of flow losses outside of the finned heat exchanger (represented by the finned tube bundle in Figure 6.10) that include losses across and downstream of the air fan and inlet and exit losses of the heat exchanger itself (as shown schematically in Figure 6.10). Because these losses scale with the square

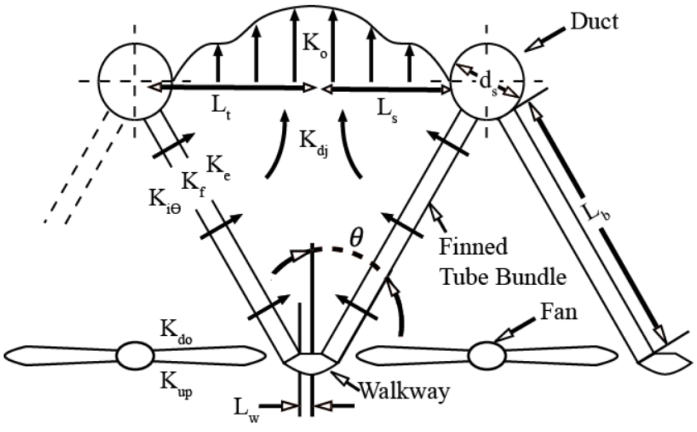

Figure. 6.10*. Schematic rendition of an A-frame air-cooled condenser indicating various air-side losses throughout the system (Kroger, 2004).*

of the air speed, reduction in the volume flow rate of air that is necessary for a given heat dissipation can lead to significant savings in the power required for driving air through the entire cooling system.

The following section includes a brief description of a geometrically scaled fin array model of an air-cooled condenser followed by an estimate of the reduction in system volume flow rates and the losses that can achieved for a fixed heat dissipation by using reeds.

6.5 Estimated Reed-Enabled Reduction in ACC Losses

Following the ACC investigations by Bustamante et al. (2016), a fin array model based on an ACC cell as described in Section 1.2 of their study is used to model the fins of their heat exchanger**.** The fin array model comprises two aluminum fin arrays (fin thickness, t_{fin} = 0.4 mm on a 3.125 mm thick base) that are assembled in a back-to-back configuration with thin-film heaters sandwiched between their base plates as shown in

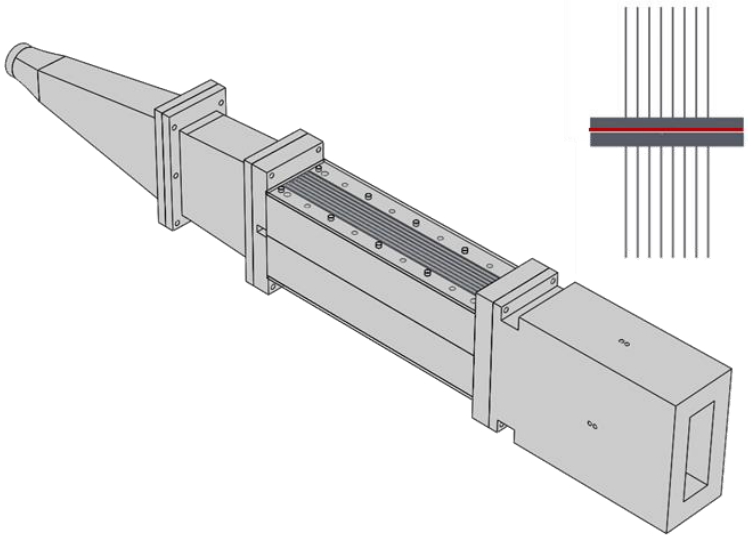

Figure. 6.11. *The double fin array facility with a back-to-back fin array cross-section and thin film heater shown at upper right.*

Figure 6.11. In the present design, each fin array has 7 channels of width, W = 2.5 mm, aspect ratio, H/W = 10, and length, L/W = 66. The fin arrays are bolted together using acrylic surfaces on the outside which form the insulating bounds of the heat sink. Cooling air is supplied through a duct which transitions from a round inlet to two rectangular flow paths that match the height and width of each of the fin arrays as shown in Figure 6.11. The reeds used in this investigation were fabricated from polyester film (t_s = 50 μm, L_s/W = 20). Each reed is adhered to a stainless-steel mounting plate (28 x 5 mm, 0.125 mm thick) and the ends of the mounting plates recess into a reed mounting fixture (12 mm thick) immediately upstream of the heat sinks such that they are aligned with the cross-streamwise centerline along the height of each channel (similar to Figure 6.1a). The air flow to the assembly is regulated using a thermal mass flow controller and is varied to yield channel Reynolds number within the range $750 \leq Re \leq 5000$. The inlet air temperature ($T_{a,i}$) is measured using a thermocouple sensor. The streamwise temperature distribution T_w along the bottom of one of the fins adjacent to the center channel is measured using an array of six equally-spaced ($\Delta\hat{x} = 12.7$) thermocouple sensors within the base of each heat sink, starting at $\hat{x}$ = 1.3 (immediately downstream from the inlet to the heat sink). Similar to the fin array in §6.1, an insulated mixing section is attached downstream of the fin array with a cross section that matches the exit of the dual fin array and $L_{mixingsection}/W$ = 5, which allows

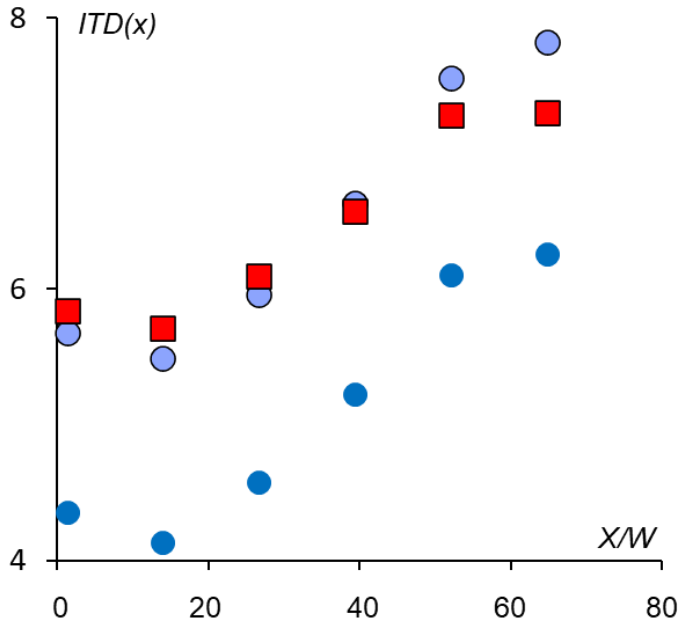

***Figure 6.12**. Streamwise variation of fin base ITD at $\dot{Q}_{heater}$ = 17.3 Watts for base flow at Re = 3,200 (■) and with reeds (L_s/W = 20) at Re = 2,200 (●) and 3,200 (●) and St_L = 2.*

for mixing between the air flows at the fin channel exits. The insulation losses from the mixing section were measured and were lower than 0.005 $\dot{Q}_{heater}$ (cf., §6.1). Similar to the procedure used in §6.2, the heat dissipated to the air is calculated using the increment in bulk mean temperature of the air through the fin array. The bulk mean temperature at the exit of the fin array $T_{m,e}$ is estimated from a surface integral of the temperature and velocity profiles measured on a 11 x 11 *y*-*z* grid (Δy = 2.1 mm, Δz = 5.7 mm) over the exit cross-section of the mixing section (similar to §6.2). The pressure drop across the fin array is measured using static pressure taps on the top surface of the fin array assembly 1 mm upstream of the reed mounting fixture and 1 mm downstream of the dual fin array.

Figures 6.12 and Table 6.1 outline the procedure that is used to obtain the heat dissipation of the base flow at lower flow rates in the presence of reeds along with estimates of the changes in system losses at *Re* = 3,200. The reed length and Strouhal number (L_s/W = 20 and St_L = 2) were selected based on the earlier tests in isolated channels of identical

aspect ratio, $H/W = 10$ (cf. Figure 5.12). The changes in system losses in the presence of reeds were also estimated at lower and higher base flow Reynolds numbers (1,000 and 4,500).

Figure 6.13 shows the streamwise variations of the fin *ITD* in the base flow at $Re = 3{,}200$ and in the presence of the reed at $Re = 2{,}200$ and 3,200 (similar studies were also performed for reed and base flow at base flow Reynolds numbers of 1,000 and 4,500). Compared to the base flow, at $Re = 3{,}200$ the fin *ITD* decrease in the presence of reed, but when the Reynolds number in the presence of reed is reduced to 2,200 the fin *ITD* is matched with base flow. In addition to the similar fin temperature distribution, the heat dissipation to the air in the absence of the reed at $Re = 3{,}200$ and in the presence of the reed at $Re = 2{,}200$ are equal ($\dot{Q}_{air} = 14.9$ Watts). These data show that in the presence of reed, the required Reynolds number for a fixed heat dissipation and fin *ITD* distribution can be reduced which

Table. 6.1. *The losses inside and outside of the fin array (cf. Figure 6.10) for the base flow and in the presence of the reeds discussed in Figure 6.13 at identical fin ITD and heat dissipation.*

Source of Losses outside fin array	Loss Coefficient, K	Base Flow $Re = 3{,}200$ Pressure Drop (Pa)	Reed $Re = 2{,}200$ Pressure Drop (Pa)
K_{up}	0.30	135.9	64.2
K_{do}	0.39	176.6	83.5
K_{dj}	1.75	47.4	22.4
K_{o}	8.26	223.4	105.6
$K_{i\theta} + K_{e}$	8.55	630.6	298.0
Losses outside fin array Total		1213.9	573.8
Loss inside fin array		161	212
System losses		1375	785.8

leads to a reduction of 31% in the air volume flow rate of the base flow at *Re* = 3,200. The effect of this reduction in volume flow rate on system losses at in the base flow at *Re* = 3,200 and in the presence of reeds at *Re* = 2,200 is shown in Table 6.1. The sources of the losses outside the fin array are detailed in Figure 6.10 and the corresponding loss coefficients are obtained from Kroger, 2004. As evident in Table 6.1, even though the losses within the fin array are higher in the presence of the reeds, the losses outside the fin array are significantly lower due to the lower volume flow rate. As a result, the system losses in the presence of the reed are 43% lower than in the base flow. The reductions in system flow rate and losses in the presence of reed increase with the Reynolds number of the base flow from 23.65% and 19% at *Re* = 1,000 to 38% and 41% at *Re* = 4,500.

Alternatively, at a given *Re*, the *ITD* in the presence of the reeds can also be matched to the *ITD* of the base flow by increasing the heater power. Figure 6.13 illustrates this effect at *Re* = 3,200, for base flow at $\dot{Q}_{heater}$ = 17.3 Watts and reeds at $\dot{Q}_{heater}$ = 17.3 and 21.5 Watts. The reduction in fin *ITD* at $\dot{Q}_{heater}$= 17.3 Watts in the presence of reeds can be

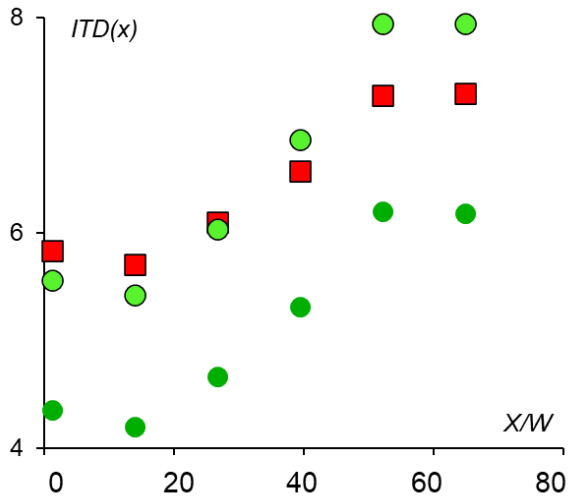

Figure 6.13 *Streamwise variation of fin base ITD at Re = 3,200 for the base flow at* $\dot{Q}_{heater}$ *= 17.3 Watts (■) and in the presence of the reeds* in *Figure 6.12 at* $\dot{Q}_{heater}$ *= 17.3 Watts (●) and 21.5 Watts (●).*

compensated for by increasing the heater power to $\dot{Q}_{heater}$ = 21.5 Watts. Thereby, in the presence of the reeds the heat dissipated to air at *Re* = 3,200 and at the same *ITD* as in the base flow increases by 27% from 14.9 to 18.95 Watts.

In summary, these data indicate that ACC system-level heat transfer performance can be enhanced by using self-oscillating reeds in two ways (at a given fin temperature, *ITD*): ***i.*** *Fixed heat dissipation* at lower volume flow rate of cooling air with reduced air path system losses; or ***ii.*** *Increased heat dissipation* to the air at a given system volume flow rate.

CHAPTER VII

CONCLUSIONS

7.1 Summary of Findings

The interactions of aero-elastically oscillating reeds with air flow in high aspect ratio rectangular channels was investigated experimentally with specific emphasis on the flow evolution and on heat transfer enhancement in heated channels. Details of the reed motion and the formation and advection of small-scale vortical motions within channel models were investigated using imaging of the reeds and 2-D PIV along with hot wire anemometry. The local and global heat transfer coefficients in the absence and presence of the reeds were computed along with the associated flow losses to determine the efficiency of the heat transfer enhancement. The scaling of the present results was assessed by comparing the reed driven heat transfer and associated losses with corresponding setups in arrays of fin channels.

Dynamics of Reed Motion

The reed motion within the channel is characterized by its critical speed, oscillation frequency, the dominant bending modes and time-dependent distributions of the reed's mechanical energy. The effects of the proximity of the channel walls to the reed on these parameters were investigated in channel aspect ratios H/W = 1, 5 and 10. It was shown that the reed's critical speed $U_{critical}$* measured by tracking the motion near the tip decreases at diminishing rates with increasing reed mass ratio M*, and for M* > 1.5, $U_{critical}$* becomes nearly invariant with H/W (at $U_{critical}$* ~ 12). The reed's oscillation frequency characterized

by its Strouhal number St_L depends on M^* and the reduced channel speed U^* and decreases with increasing M^*/U^*. It was shown that while for $H/W = 1$, $St_L = 0.23(M^*/U^*)^{-0.25}$ as the channel aspect ratio increases to $H/W = 5$ and 10, St_L becomes nearly invariant and $St_L = 0.23(M^*/U^*)^{-0.33}$.

The effect of the proximity of the channel walls on the reed modes is compared for a reed of a given length L_s between the $H/W = 1$ and 5 channels for which $U_{critical}^*$ is nearly invariant using conditionally-averaged traces of the reeds' centerline (along their midspan) during the oscillation cycle. To this end, L_s which is equal to $L_s/W = 1.8$ and 10, in the low- and high-aspect ratio channels $H/W = 1$ and 5, respectively is selected. While in the $H/W = 1$ channel the modal interactions between this reed and the channel walls are limited to its tip, they extend $0.1L_s$ upstream of the tip in the higher aspect ratio channel. The reed's dominant bending modes are computed using proper orthogonal decomposition (POD) which shows that the reed's first two modes capture approximately 95% of the total modal energy. These data indicate that the effective oscillating segment of the reed is "hinged" $0.44L_s$ upstream of its tip in the higher aspect ratio channel resulting in a marginally higher oscillation frequency. Distributions of the reed's mechanical energy show that it is dominated by the kinetic energy which is at least four orders of magnitude higher than the elastic potential energy. The *s*-*t* distributions of reed's elemental kinetic energy $\delta(KE)^*(s, t)$ demonstrate the temporal propagation of travelling waves along the reed length during the cycle, albeit the domain of propagation is shorter in $H/W = 5$ channel consistent with the shorter oscillating segment. The cyclic variations of the integrated kinetic energy of the reed demonstrate that for a given channel flow speed, the integrated

kinetic energy of the reed at any instant in the cycle is smaller in $H/W = 5$ channel due to the lower amplitude of cross-stream reed motion.

Evolution of the Reed-Induced Flow Structures

The flow structures induced by the interactions between the reed and the channel flow are first assessed in the $H/W = 1$ channel using conditionally-averaged PIV measurements that are acquired locked to the cross-stream position of the reed just upstream of its tip. The reed shape and motion are clearly coupled to the flow over both sides and are accompanied by modulation of the pressure gradients and vorticity distributions along the reed and the channel's side walls. Vorticity shedding by the reed is dominated by its concave surface as it is moving towards either one of the walls, the sense of the shed vorticity is determined by the sense of the boundary layer vorticity along this surface and it switches its sense as the concave surface switches sides. As the reed approaches a wall, the shed vortex interacts with the vorticity layer on the channel's wall resulting in time periodic modulation (acceleration and deceleration) of the flow within wall boundary layer at the frequency of the reed. The corresponding time-averaged levels of fluctuation kinetic energy of the flow downstream of the tip are significantly higher than in the base flow but lower in the high aspect ratio channels where the excursions of the reed are lower and decrease monotonically with downstream distance due to dissipation.

The vortical structures shed downstream of the reed lead to formation of a hierarchy of small-scale motions whose spectral content are captured using hot-wire measurements downstream of the reed's tip. The spectra on the channel's centerline near the reed tip exhibit peaks at the reed's oscillation frequency and its higher harmonics and the dominant spectral peak occurs at twice the reed oscillation frequency due to alternate shedding of CW and CCW vortices from its surfaces twice per cycle (similar spectral measurements in vicinity of the channel's wall show a spectral peak at the reed's oscillation frequency

corresponding to the shedding of a reed vortex once per cycle). Similar to the decay of the kinetic energy of the fluctuations, the spectral peaks decrease significantly in the streamwise direction near both the centerline and the channel walls indicating small-scale dissipation.

The effects of the proximity of the channel walls to the reed on the flow induced structures was also investigated in the higher aspect ratio channel $H/W = 5$ using the same reed length and channel flow speed. In comparison to the low aspect ratio channel where the interactions between the reed and wall bound vorticity concentrations are limited to its tip, in the high aspect ratio channel, these interactions also occur upstream of the tip which leads to formation of additional spanwise vorticity concentrations on channel walls that are interlaced within the vortices that form due to interactions at the tip. These additional vortices separate from the walls due to adverse pressure gradients imposed by the reed upstream of its tip and in contrast to the low aspect ratio channel modulate the wall vorticity layer at twice the reed frequency.

The Time-Averaged Flow Field

The time-averaged effects of the reed on the mean and fluctuating flow fields are characterized in detail in the high aspect ratio channel ($H/W = 5$) over a range of Reynold numbers and reed planform shapes (L_s/W, H_s/W) and Strouhal numbers (St_L), and for a few reed streamwise locations (x_0/W).

The power to drive the reed motion and the associated small scale motions is extracted from the mean flow which at a given Reynolds number (or channel mass flow rate) is manifested by an increase in streamwise mean pressure gradients (over the base

flow). The increase in magnitude of streamwise pressure gradient is significantly higher along the reed than downstream of the reed. While the higher increase in pressure drop along the reed is associated with the energy required to sustain the energy invested in the reed motion, the marginal increase in pressure drop downstream of the reed compared to the base flow is associated with the advection of the vortical structures which are produced near its tip.

The advection of the induced vortical structures downstream of the reed leads to changes in the mean and fluctuating flow fields that are assessed from 2-D PIV data. The changes in mean flow downstream of the reed are illustrated in changes in cross-stream distributions of streamwise and cross stream velocity components, spanwise vorticity, and of the second moment of velocity fluctuations. In addition, the evolution of channel's flow field is investigated using an energy balance of the mean and fluctuating components of its kinetic energy in the base flow and in the presence of the reed.

These measurements were first conducted at Re = 2,000 when the base flow is laminar to delineate the differences in the channel flow due to the presence of the reed and assess the dominant terms in the flow's kinetic energy budgets. In the presence of the reed, $\widehat{\overline{u'u'}}$ is an order of magnitude larger than $\widehat{\overline{v'v'}}$ and $\widehat{\overline{u'v'}}$. Cross stream profiles of $\widehat{\overline{u'u'}}$ show peaks at y = 0 and ±0.35W which are associated with the time-periodic disruptions of wall boundary layer due to the reed-wall interactions. Downstream of the reed tip, $\widehat{\overline{u'u'}}$ decreases due to dissipation but at higher streamwise rates near the channel center than near the walls and near the channel's exit, $\widehat{\overline{u'u'}}$ is higher near the walls than at its center. The budget of the mean kinetic energy $\widehat{M}$ computed using its material rate of change shows

that in the absence of the reed there is streamwise acceleration at the channel center that is characteristic of a developing inlet flow in which the wall boundary layers thicken with streamwise distance. In the presence of the reed, the elevated pressure gradients near its tip (relative to base flow) increase the kinetic energy of the flow at the channel's center and subsequently the elevated second moment of velocity fluctuations lead to a rise in the mean kinetic energy near the walls. Near the channel's exit the cross-stream distribution of $\widehat{M}$ in the presence of reeds asymptotes to its level in the base flow while its higher levels near the walls are still apparent and manifested by increased momentum and vorticity levels. The fluctuating kinetic energy budget shows that the material rate of change of $\widehat{M}_{\mathrm{f}}$ occurs primarily due to a balance between the small-scale viscous dissipation $\widehat{D}_{\mathrm{vf}}$ and pressure fluctuations $\widehat{T}_{\mathrm{pf}}$ and that the elevated levels of second moment of velocity fluctuations in the presence of the reed are sustained by the pressure fluctuations. As might be expected, the spanwise variations in the mean and fluctuating flow fields that are symmetric about mid span show that the effects of the reed are not spanwise uniform near the tip, probably due to formation of streamwise vortices of alternating sense along its outboard edges as the reed oscillates towards and away from the top and bottom wall. The cross stream distributions of the fluctuation kinetic energy, k_{f} near the tip intensify significantly near the top and bottom walls but decrease rapidly in the streamwise direction.

The variations in channel flow fields are also assessed at higher Reynolds numbers spanning transitional and turbulent flows in the base flow and in the presence of reeds of a fixed length and Strouhal number. While the base flow is laminar at Re = 2,000, it transitions to turbulence at about Re = 7,000 and the onset of transition moves upstream as the Reynolds number is further increased and at Re = 12,000 the turbulent flow becomes

nearly fully-developed near the channel exit. The spectral content of the base flow increases significantly as the Reynolds number increases, with a few spectral peaks that correspond to transitional instabilities in the flow and a pronounced spectral decay in the dissipative sub-range with slopes of -3, and -5/3 at *Re* = 7,000, and 12,000, respectively. As the Reynolds number increases, the reed accelerates the transition to turbulence as is evident from cross stream distributions of the mean streamwise velocity and fluctuation kinetic energy $\hat{k}_{\mathrm{f}}(\hat{y})$ and the cross-stream averaged fluctuation kinetic energy $\hat{k}_{\mathrm{m}}$ and small-scale dissipation $<\hat{D}_{\mathrm{vf}}>$ at Reynolds number of 5,000, which are already similar to the corresponding averages in the base flow at *Re* = 12,000 near the channel's exit. From a spectral standpoint, compared to the base flow, the presence of the reed leads to a marked broad-band increase in spectral power at low and transitional Reynolds numbers with multiple spectral peaks at the reed's oscillation frequency and its higher harmonics. As the base flow undergoes transition the broad band increase in spectral power is lower but still quite pronounced and is coupled with multiple spectral peaks at the harmonics of the reed oscillations that are as high as 3 orders of magnitude above the local broad band levels. These observations show similarity to pulsatile flows where the transition to turbulence is triggered at low Reynolds number by interactions between the base flow and the imposed flow pulsations.

Considering the evolution of the inlet flow within the channel, the streamwise position of the reed was varied in limited experiments to explore the effect of the location of its oscillating tip as the flow becomes fully-developed. These data indicate that when the tip of the reed is placed at streamwise position where the base flow is already

asymptotically turbulent, the streamwise decay of the reed-induced oscillations is higher and therefore its streamwise domain of influence is shorter.

One of the central elements of the present investigations was the role of the reed's oscillation frequency as captured by its Strouhal number on the evolution of the flow in the channel with specific emphasis on the balance between pressure drop and attained heat transfer. These effects were explored for $0.46 < St_L < 3.22$ (using reeds of different lengths and thicknesses) and Reynolds numbers up to 10,000 in the $H/W = 5$ channel. The present investigations showed that the reed-induced *changes* in the velocity field and the associated distributions of $\hat{k}_m$ and $<\widehat{D}_{vf}>$ follow a similar pattern. The induced changes downstream of the tip first increase with St_L followed by streamwise diminution at a rate that also increases with St_L so that ultimately these changes become invariant with St_L just upstream of the channel's exit. The present investigations also demonstrated that the flow losses within the channel in the presence of the reed as manifested in the channel's friction factor $f = \Delta P/(0.5 \cdot \rho_a \cdot U^2 \cdot L/D_h)$ vary primarily with St_L such that $f = 0.1 \cdot (St_L)^{0.5}$ and f is nearly independent of the channel's Reynolds number. These findings suggested that at a given Reynolds number, heat transfer in the presence of the reed may be only weakly dependent on its Strouhal number and therefore the reed can be operated at a low Strouhal number with minimal loss in heat transfer enhancement but significant reduction in pressure losses.

Heat Transfer enhancement in isolated channels

Heat transfer enhancement by the reed was studied in the $H/W = 5$ channel in which the side walls were heated such that the maximum temperature difference between the walls (at mid span) and inlet air temperature ITD_{max} was kept fixed. The local heat transfer

coefficients, $h(x)$ and Nusselt numbers $Nu(x)$ were calculated using the local wall and air temperatures along the channel.

In the base flow, $ITD\,(x)$ increases monotonically and reaches ITD_{max} near the channel exit but in the presence of reeds there is a reduction in the local wall temperature at the same heater power and hence the heater power is increased to maintain the same ITD_{max}. Although near the channel exit the wall temperatures are nearly the same in the absence and presence of reed, the channel wall temperatures in the presence of the reed are lower even for the increased heater power. The combined effect of higher heat dissipation to air and lower wall temperatures in the presence of reeds leads to increments in local $Nu(x)$ relative to the base flow throughout the measurement domain with peaks near its tip and a streamwise decay downstream. The ratio of local Nusselt numbers, $Nu(\mathrm{x})$ near the reed tip between the presence and absence of reed (at fixed length and Strouhal number) at Re = 2,000 and 7,000 are 1.8 and 2.45 but at Re = 12,000 this ratio diminishes to 1.4. These changes are commensurate with the induced changes in small-scale motions as depicted by the changes (relative to the base flow) in bulk mean fluctuation kinetic energy, $\Delta\hat{k}_{\mathrm{m}}$. Furthermore, the present findings indicate that for transitional base flow Reynolds numbers, the changes in local Nusselt numbers, ΔNu, due to the reed solely depend on $\Delta\hat{k}_{\mathrm{m}}$ and this dependence goes as $\Delta Nu \sim (\Delta\hat{k}_{\mathrm{m}})^{0.8}$.

The thermal performance of the reed is assessed by considering the balance between the reed-driven increase in channel losses and the enhancement in heat transfer. An important finding of the present investigation is that by reducing the reed's Strouhal number its thermal performance can be substantially improved since the channel losses in

the presence of the reed decrease significantly with only a marginal decrease in heat transfer increment. Consequently, the thermal enhancment factor, η increases with decreasing Strouhal number. The present data show that the reeds yield up to 41% and 22 % higher η than conventional dimples and vortex generators, respectively.

Scaling of the Reed's Heat Transfer Enhancement

When the heat transfer in the $H/W = 5$ channel was compared with the $H/W = 10$ channel for the same St_L and Re it was shown that Nu/Nu_b, f/f_b, and η are identical when the lengths of the reed and the channels are scaled the same. The performance of the reed in the isolated $H/W = 5$ channel was also compared with its performance in a fin array having the same cross sectional dimensions and similar length ($L/W = 40$). The performance was assessed using *LMTD* and was adjusted to obtain an estimate of the isothermal Nusselt number. The reed-enhanced heat transfer enhancement (Nu/Nu_b) due to the reed in the fin array is nearly identical to the isolated channel at $Re = 1{,}500$ and $0.5 < St_L < 1.92$ but is lower than the isolated channel at $Re = 3{,}000$ and 4,500 at all Strouhal numbers because there is negligible heat transfer enhancement near the tip of the fins due to the lower fin *ITD*s. It is noted that at $Re = 1{,}500$ (the range of industrial scale heat exchangers) the reed thermal enhancement factor in the fin array is similar to the isolated channel.

While in the isolated channel the reeds were mounted within the channel, the implementation of reeds in fin arrays of heat exchangers require external mounting which was achieved with an offset upstream of fin array channels. The oscillation frequency of the externally mounted reeds in the fin array is invariant with changes in offset length and

the reed Strouhal number only varies with M^*/U^* in good agreement with the isolated channel. The measurements of Nusselt numbers and friction factors for externally mounted reeds showed that while the friction factor can be reduced when the reed mounting is offset upstream of the channel, the decrease in Nusselt number is not insignificant and therefore reeds with lower offset perform better in terms of η and COP.

7.2 Summary of Insights

Characteristics of reed oscillations

Reeds (or flags) cantilevered in free gas or liquid flow can be destabilized by coupling of pressure and surface perturbations owing to flow nonuniformities that overcome the bending rigidity. When these reeds are mounted and oscillate within channels, the proximity of the walls leads to additional viscous forces that can modify the reed's critical speed but their relative effect depends on the reed's mass ratio, M^*:

a. For $M^* > 1$, the reed's critical speed, $U_{critical}^*$, in channels is nearly identical to free air because wall interactions are limited to the vicinity of its tip. Because these interactions do not change significantly with increasing channel aspect ratio, $U_{critical}^*$ does not change significantly with channel aspect ratio.
b. For $M^* < 1$, $U_{critical}^*$, is significantly higher in channels than in free air although its variation with channel aspect ratio is negligible because the bending rigidity which scales as $(t_s/L_s)^3$ is small when $t_s < \rho_a \cdot L_s/\rho_s$ or $L_s > \rho_s \cdot t_s/\rho_a$.
c. For $M^* > 1.5$, $U_{critical}^*$ is invariant with M^* which means that the (dimensional) critical speed, $U_{critical} \sim (E/\rho_a)^{0.5}(t_s/L_s)^{1.5}$, depends only on the reed's material

properties and geometry, and on air density. *These data can be used to predict the critical speed of reeds for which* $t_s > 1.5\rho_a \cdot L_s/\rho_s$ or $L_s < 1.5\rho_s \cdot t_s/\rho_a$.

The reed's oscillation frequency above its critical speed is affected by the presence of channel walls. In free air, the oscillation frequency is determined by the balance between the aerodynamics loads and the reed's inertia. The variations in the reed's oscillation frequency in the presence of walls are assessed using its dimensionless frequency or Strouhal number (St_L). In free air, St_L only depends on M^* and varies as $M^{*-0.5}$ whereas within channels St_L depends on M^* and U^* and varies as $(M^*/U^*)^{-n}$ ($n = 0.25$ for $H/W = 1$ and $n = 0.33$ for $H/W = 5$ and 10). Since U^* is also the ratio of the reed's elastic potential energy and the kinetic energy of the flow with which it interacts, U^* affects its mode shapes and wall interactions and thereby the resulting viscous damping of the reed oscillations which modifies the Strouhal number.

Mechanisms of Reed-Enhanced Heat Transfer in High Aspect Ratio Channels

Upstream of the reed's tip: The strength of the vorticity layers along the channel walls is modulated at the reed oscillation frequency by imposed changes in the streamwise pressure gradients in the flow's cross sections over the two surfaces of the reed. The modulation of the vorticity concentrations and flux along the heated channel walls modifies the thickness of the thermal boundary layers and thereby increases the local heat transfer coefficient along the reed. The effects of the reed's frequency and amplitude are evident by the dependence of the local Nusselt number on the reed's Strouhal number indicating that the local heat flux can be modified by tuning the reed frequency through its geometrical and structural properties.

Downstream of the reed: The oscillations of the reed lead to the formation and shedding of a hierarchy of small-scale vorticity concentrations whose interactions with the embedding flow enhances small-scale motions as manifested by broad-band spectral peaks in the velocity spectra that are otherwise absent in a laminar base flow. These small-scale motions disrupt the wall thermal boundary layers downstream of the reed and increase the cross-stream mixing between the hot fluid near the walls and cold fluid away from the walls. Even though the magnitude of the reed-induced flow perturbations decreases in the streamwise direction due to viscous dissipation, the streamwise momentum and vorticity flux near the wall are significantly higher than in the base flow leading to sustained higher heat transfer coefficient that is independent of the reed's Strouhal number.

Evolution of small-scale motions downstream of the reed: The interactions of the reed with the developing inlet flow in the channel can accelerate transition to turbulence. The hierarchy of the reed-induced vortical structures couples to the natural base flow receptivity during the transition process. In the present channel inlet flow this acceleration is manifested by the similarity of cross-stream distributions of the streamwise velocity and fluctuating kinetic energy at the channel exit at transitional Reynolds number to corresponding distributions of the base flow when it is turbulent at *Re* = 12,000. The reed-induced increases in bulk-mean fluctuation kinetic energy $\hat{k}_{\mathrm{m}}$ and in small-scale dissipation surpass the natural increases with *Re* in the base flow due to transition which has significant implications on the extent of the streamwise domain over which the reed increases heat transfer.

***Streamwise domains of reed enhanced heat transfer*:** At low Reynolds numbers when the high aspect ratio channel flow is characteristically laminar, the reed-enhanced heat transfer

persists through the channel exit ($28W$ for $L/W = 5$), and the present data indicates that the increase in the heat transfer coefficient is expected up to four times this distance (about $100W$). This suggests that the channel length can be increased at lower Reynolds numbers although such an increase is limited by the increase in wall temperature. At higher Reynolds numbers past transition, the streamwise domain of effectiveness decreases owing to the natural evolution of small-scale motions in the base flow but still with significant increases in the global heat transfer.

Efficiency of the Reed Driven Heat Transfer Enhancement Reed-driven heat transfer enhancement is also accompanied by an increase in flow pumping power since the power required to drive the reed motion is extracted from the flow. The efficiency of using reeds is assessed using the thermal enhancement factor, η, which is the ratio of Nusselt numbers in the presence and absence of the reeds at the same flow power. The Nusselt number in the presence of the reed at laminar Reynolds number is higher than in the base flow at the same flow power such that $\eta > 1$ and is higher than other heat augmentation techniques. Furthermore, as the reed's Strouhal number decreases, the needed flow power decreases and hence the thermal enhancement factor increases. When the base flow becomes asymptotically turbulent the thermal enhancement factor approaches 1, and the present study suggests that the limit of the efficiency of using reeds occurs at Re~9,000.

Implementation of Reeds in fin arrays The findings of the reed enhanced heat transfer in isolated channels were implemented in fin arrays showed that reeds operating at $St_L < 1.9$ can be used to enhance heat transfer in the fin array with the same efficiency as in the isolated channel for $Re < 1{,}500$. Although the reed enhances the heat transfer at higher Re,

the efficiency is lower compared to the isolated channels apparently owing to the reduced fin *ITD*s along the fin height due to conduction resistance.

***Performance Enhancement in Large Scale Heat Exchangers*:** The present findings were used to demonstrate that the system level performance of large-scale heat exchangers can be improved significantly using reed-enhanced heat transfer. The fan power in an air-cooled condenser operating at a given heat dissipation can be reduced by up to 64% by decreasing the cooling air mass flow rate by up to 38% and overall system pressure drop by 41%. Alternatively, for a fixed air mass flow rate, reed actuation can enhance heat dissipation per unit area and therefore, for a fixed system heat dissipation, the plot area can be decreased with significant infrastructure savings.

Limitations of the Current Study

1. The current study only resolved the dominant bending modes of the reed based on the time-traces of reed. As indicated by higher critical speeds for reeds with $M^*<1$, torsional modes might exist along the reed and were neglected in the current study.
2. The present 2-D PIV measurements do not capture the evolution of streamwise concentrations of vorticity that evolve along the spanwise edges of the reed and can impact the heat transfer.
3. In the study on the fin array, isothermal estimates of Nusselt numbers were obtained based on the fin efficiency which assumes negligible variations of heat transfer coefficient and air temperature along the fin height and length. This limitation can be potentially overcome using numerical modelling to extract better isothermal estimates of Nusselt numbers in the fin array.

APPENDIX A

KINETIC ENERGY BUDGET ANALYSIS

A.1 Simplifications for Obtaining Mean Kinetic Energy Budget using 2-D PIV Data

This section describes the assumptions and calculations used to obtain the mean kinetic energy budget from the 2-D PIV data at $z = 0$ as discussed in §4.3 in connection with Equation 4.1. Equation A.1 shows the traditional 3-D budget of the mean kinetic energy (per unit mass), $E = 0.5\ (\bar{u}^2 + \bar{v}^2 + \bar{w}^2)$, (Pope, 2000a), in terms of its substantial derivative or material rate of change of the mean kinetic energy.

$$\frac{DE}{Dt} = \frac{\partial}{\partial x_j}\left(-\frac{p\bar{u}_j}{\rho_a} + 2\vartheta\bar{u}_i S_{ij} - \overline{u_i' u_j'}\bar{u}_i\right) - 2\vartheta S_{ij}S_{ij} + \overline{u_i' u_j'}S_{ij} - g\frac{\bar{\rho}}{\rho_a}\bar{w} \tag{A.1}$$

where $u_1 = u$, $u_2 = v$, and $u_3 = w$, and S_{ij} is the symmetric part of the mean strain rate

$$S_{ij} = 0.5\left(\frac{\partial u_i}{\partial x_j} + \frac{\partial u_j}{\partial x_i}\right)$$

It is assumed that $\bar{w} = 0$ and $\partial/\partial z = 0$ at $z = 0$ (due to spanwise symmetry), ρ_a and the streamwise pressure gradient $\partial p/\partial x$ = constant (based on the pressure distributions in Figure 4.6), $\partial p/\partial y << \partial p/\partial x$ (changes in cross stream momentum and viscous stresses are smaller than the streamwise components as $\bar{v} << \bar{u}$ in the region downstream of the reed

tip, cf. Figure 4.8) and hence $\partial p/\partial y$ is neglected. Additionally gravitational changes, $-g\frac{\bar{\rho}}{\rho_a}\bar{w}$ (Term VI on R.H.S of Equation A.1) are neglected to obtain Equation 4.1.

First, the mean kinetic energy at $z = 0$ can be simplified as $E = 0.5\ (\bar{u}^2 + \bar{v}^2)$. The Left hand side can be simplified as follows by neglecting temporal changes as this is a steady state equation:

$$\frac{DE}{Dt} = \frac{\partial E}{\partial t} + \bar{u}_i\frac{\partial E}{\partial x_i} = \bar{u}\frac{\partial E}{\partial x} + \bar{v}\frac{\partial E}{\partial y}$$

Term I on the right hand side of Equation A.1, i.e. $\frac{\partial}{\partial x_j}\left(-\frac{p\bar{u}_j}{\rho_a}\right)$, or the transport of the mean kinetic energy by the mean pressure, T_p, is simplified using continuity equation ($\frac{\partial u_j}{\partial x_j} = 0$) as follows:

$$\frac{\partial}{\partial x_j}\left(-\frac{p\bar{u}_j}{\rho_a}\right) = -(\frac{p}{\rho_a})\frac{\partial u_j}{\partial x_j} - (\bar{u}_j/\rho_a)\frac{\partial p}{\partial x_j} = -1/\rho_a(\bar{u}\frac{\partial p}{\partial x} + \bar{v}\frac{\partial p}{\partial y})$$

Term II on the right hand side of the Equation A.1, i.e, $\frac{\partial}{\partial x_j}\left(2\vartheta\bar{u}_{\mathrm{i}}S_{\mathrm{ij}}\right)$, or the transport of the mean kinetic energy by the viscous shear stresses, T_v, is simplified as:

$$\frac{\partial}{\partial x_j}\left(2\vartheta\bar{u}_{\mathrm{i}}S_{\mathrm{ij}}\right) = 2\vartheta(\frac{\partial}{\partial x}(\bar{u}S_{11} + \bar{v}S_{21}) + \frac{\partial}{\partial y}(\bar{u}S_{12} + \bar{v}S_{22}))$$

Term III on the right hand side of the Equation A.1, i.e, $\frac{\partial}{\partial x_j}\left(-\overline{u_{\mathrm{i}}'u_{\mathrm{j}}'}\bar{u}_i\right)$, or the transport of the mean kinetic energy by the second moment of velocity fluctuations, T_R, can be simplified as

$$\frac{\partial}{\partial x_j}\left(-\overline{u_i{}'u_j{}'}\bar{u}_i\right) = \frac{\partial}{\partial x}\left(-\overline{u'u'}\bar{u} - \overline{u'v'}\bar{v}\right) + \frac{\partial}{\partial y}\left(-\overline{u'v'}\bar{u} - \overline{v'v'}\bar{v}\right)$$

Term IV on the right hand side of Equation A.1, i.e, $-2\vartheta S_{ij}S_{ij}$, or the dissipation of mean kinetic energy by viscous shear stresses, D_v, can be simplified by using $S_{23} = S_{31} = S_{33} = 0$ as $\bar{w} = 0$ and $\partial/\partial z = 0$ at $z = 0$ and using symmetry $S_{23} = S_{32} = 0$ and $S_{13} = S_{31} = 0$, $S_{12} = S_{21}$.

$$-2\vartheta S_{ij}S_{ij} \;=\; -2\vartheta\left(S_{11}{}^2 + 2S_{12}{}^2 + S_{22}{}^2\right)$$

Finally, Term VI in Equation A.1 i.e $\overline{u_i{}'u_j{}'}S_{ij}$ or shear production of fluctuation kinetic energy by second moment of velocity fluctuations can be simplified as

$$\overline{u_i{}'u_j{}'}S_{ij} = \overline{u'u'}S_{11} + 2\overline{u'v'}S_{12} + \overline{v'v'}S_{22}$$

It should be noted that while these assumptions were found reasonable near the channel center span (z = 0), near the channel and top and bottom walls due to significant variations along the channel span, these assumptions are no longer valid.

A.2 Simplifications for Obtaining Fluctuating Kinetic Energy Budget using 2-D PIV Data

This section describes the assumptions and calculations used to obtain the fluctuating kinetic energy budget from the 2-D PIV data at $z = 0$ as discussed in §4.3 in connection with Equation 4.2. Equation A.2 shows the traditional 3-D budget of the fluctuating kinetic energy (per unit mass) $k_f = 0.5\ (\overline{u'^2} + \overline{v'^2} + \overline{w'^2})$ (Pope, 2000a) in terms of its substantial derivative or material rate of change of the fluctuating kinetic energy, k_f.

$$\frac{\mathrm{D}k_f}{\mathrm{D}t} = -\frac{\partial}{\partial x_j}\left(\frac{\overline{p'u_j'}}{\rho_a} - 2\vartheta\overline{u_i' e_{ij}} + 0.5 \cdot \overline{u_i'^2 u_j'}\right) - 2\vartheta\overline{e_{ij}e_{ij}} \quad \text{(A.2)}$$

$$- \overline{u_i u_j} S_{ij} - g\alpha\overline{w'T'}$$

where e_{ij} is the symmetric part of the fluctuating strain rate. In addition to the assumptions made in connection with Equation A.1, it is assumed that $e_{12} = e_{23} = e_{31}$ and $w' \sim v'$ based on statistically isotropic cross stream and spanwise velocity fluctuations (Delafosse et al., 2011). Additionally, the buoyancy term in Equation A.2 ($-g\alpha\overline{w'T'}$) is neglected to obtain Equation 4.2.

First, the fluctuating kinetic energy at $z = 0$ can be simplified as $k_f = 0.5\,(\overline{u'^2} + 2\overline{v'^2})$. The left hand side can be simplified as follows by neglecting temporal changes as this is a steady state equation:

$$\frac{Dk_f}{Dt} = \frac{\partial k_f}{\partial t} + \bar{u}_i\frac{\partial k_f}{\partial x_i} = \bar{u}\frac{\partial k_f}{\partial x} + \bar{v}\frac{\partial k_f}{\partial y}$$

Term I on the right hand side of Equation A.2, i.e, $-\frac{\partial}{\partial x_j}\left(\frac{\overline{p'u_j'}}{\rho_a}\right)$, or the transport of the fluctuating kinetic energy by the pressure fluctuations is calculated as a balance between the right hand side and left hand side of Equation A.2 since the instantaneous pressure data is not available. Term II on the right hand side of the Equation A.2, i.e $-\frac{\partial}{\partial x_j}\left(-2\vartheta\overline{u_i' e_{ij}}\right)$, or the transport of the fluctuating kinetic energy by the fluctuating viscous shear stresses, T_{vf}, is simplified as:

$$\frac{\partial}{\partial x_j}\left(2\vartheta\overline{u_\iota{}'e_{\iota J}}\right) = 2\vartheta\left(\frac{\partial}{\partial x}\left(\overline{u'e_{11}} + 2\overline{v'e_{12}}\right) + \frac{\partial}{\partial y}\left(\overline{u'e_{12}} + \overline{v'e_{22}} + \overline{v'e_{12}}\right)\right)$$

Term III on the right hand side of the Equation A.1, i.e, $-\frac{\partial}{\partial x_j}\left(0.5 \cdot \overline{u_\iota{}'^2 u_J{}'}\right)$, or the transport of the fluctuating kinetic energy by the second moment of velocity fluctuations, T_{Rf} can be simplified as

$$-\frac{\partial}{\partial x_j}\left(0.5 \cdot \overline{u_\iota{}'^2 u_J{}'}\right) = 0.5\left[\frac{\partial}{\partial x}\left(\overline{u'^3} + \overline{u'v'^2}\right) + \frac{\partial}{\partial y}\left(2\overline{v'^3} + \overline{v'u'^2}\right)\right.$$

Term IV on the right hand side of Equation A.2, i.e, $-2\vartheta\overline{e_{\iota J}e_{\iota J}}$, or the dissipation of fluctuating kinetic energy by fluctuating viscous shear stresses, D_{vf}, can be simplified by based on the technique used by Delafosse et al. (2011)

$$-2\vartheta\overline{e_{\iota J}e_{\iota J}} = -\vartheta\left(2\overline{\left(\frac{\partial u'}{\partial x}\right)^2} + 2\overline{\left(\frac{\partial v'}{\partial y}\right)^2} + 3\overline{\left(\frac{\partial u'}{\partial y}\right)^2} + 3\overline{\left(\frac{\partial v'}{\partial x}\right)^2} + 2\overline{\left(\frac{\partial v'}{\partial x} \cdot \frac{\partial u'}{\partial y}\right)}\right)$$

Finally, Term VI in Equation A.1, i.e, $-\overline{u_{\mathrm{i}}{}'u_{\mathrm{j}}{}'}S_{ij}$, or shear production of fluctuation kinetic energy by second moment of velocity fluctuations or $T_{\mathrm{pf}} = -T_{\mathrm{p}}$.

APPENDIX B

SUPPLEMENTAL PARAMETRIC INVESTIGATIONS

B.1 Spanwise Variations in the Base Flow

The spanwise variations in mean flow field in the absence and presence of reed in the $H/W = 5$ channel were obtained using PIV. As an illustration of these variations for the base flow, Figure B.1 shows the cross-stream profiles, $\hat{\bar{u}}(\hat{y})$ as obtained at $Re = 2{,}000$ and $\hat{x} = 18$, for five spanwise locations along the channel height, $\hat{z} = 0, \pm1, \pm2$ (top and bottom channel walls are at $\hat{z} = \pm2.5$). Figure B.1 shows that the spanwise variations in the flow fields are negligible in the absence of the reed at $Re = 2{,}000$, indicating a predominantly 2-D laminar flow.

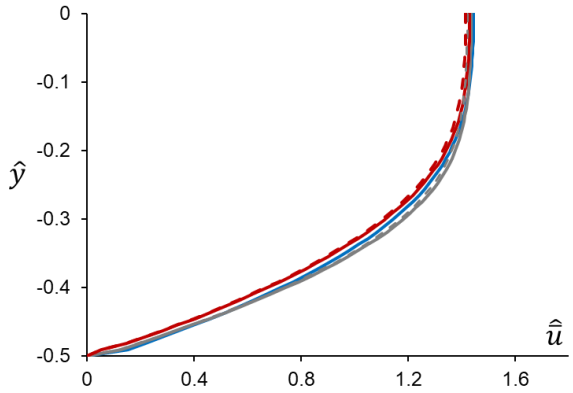

Figure B.1 *Cross-stream distributions ($-0.5<\hat{y}<0$) of streamwise velocity ($\hat{\bar{u}}$) for the base-flow at $\hat{x} = 18$ for $Re = 2{,}000$ obtained in high aspect ratio channel of width $W = 5$mm for $\hat{z} = 0, \pm1, \pm2$. The distributions for $\hat{z} \geq 0$ are shown with solid lines and for $\hat{z} \leq 0$ are shown with dashed lines.*

B.2 Limited Investigations on Streamwise Location of Reed at Re = 5,000 in H/W = 5 Channel

As the characteristics of mean and fluctuating flow fields vary streamwise in the channel, the effect of streamwise location of the reed in the channel on small-scale interactions was also analyzed through limited investigations in a predominantly laminar flow (Re = 5,000) in H/W = 5 or 5-mm wide channel. Reeds of length, L_s/W = 10, H_s/H = 0.9 and t_s = 25.4 μm were tested at Re = 5,000 for three streamwise locations such that the tip is at $\hat{x}_{tip}$ = 16, 26 and 48.

A characterization of the base flow at Re = 5,000 is done by comparison with that at Re = 2,000 and 7,000 through the cross-stream profiles of streamwise velocity, $\hat{\bar{u}}$ and fluctuation kinetic energy, $\hat{k}_f$ at $\hat{x}$=18, 30 and 42 as shown in Figure B.2. The variations

with *Re* of the base flow $\hat{\bar{u}}$(y) distributions at $\hat{x}$ = 18 (Figure B.2-a.1) shows that at *Re* = 5,000, $\hat{\bar{u}}$(y) distributions are closer to *Re* = 2,000 than 7,000 for $|\hat{y}|$>0.25, and fall in

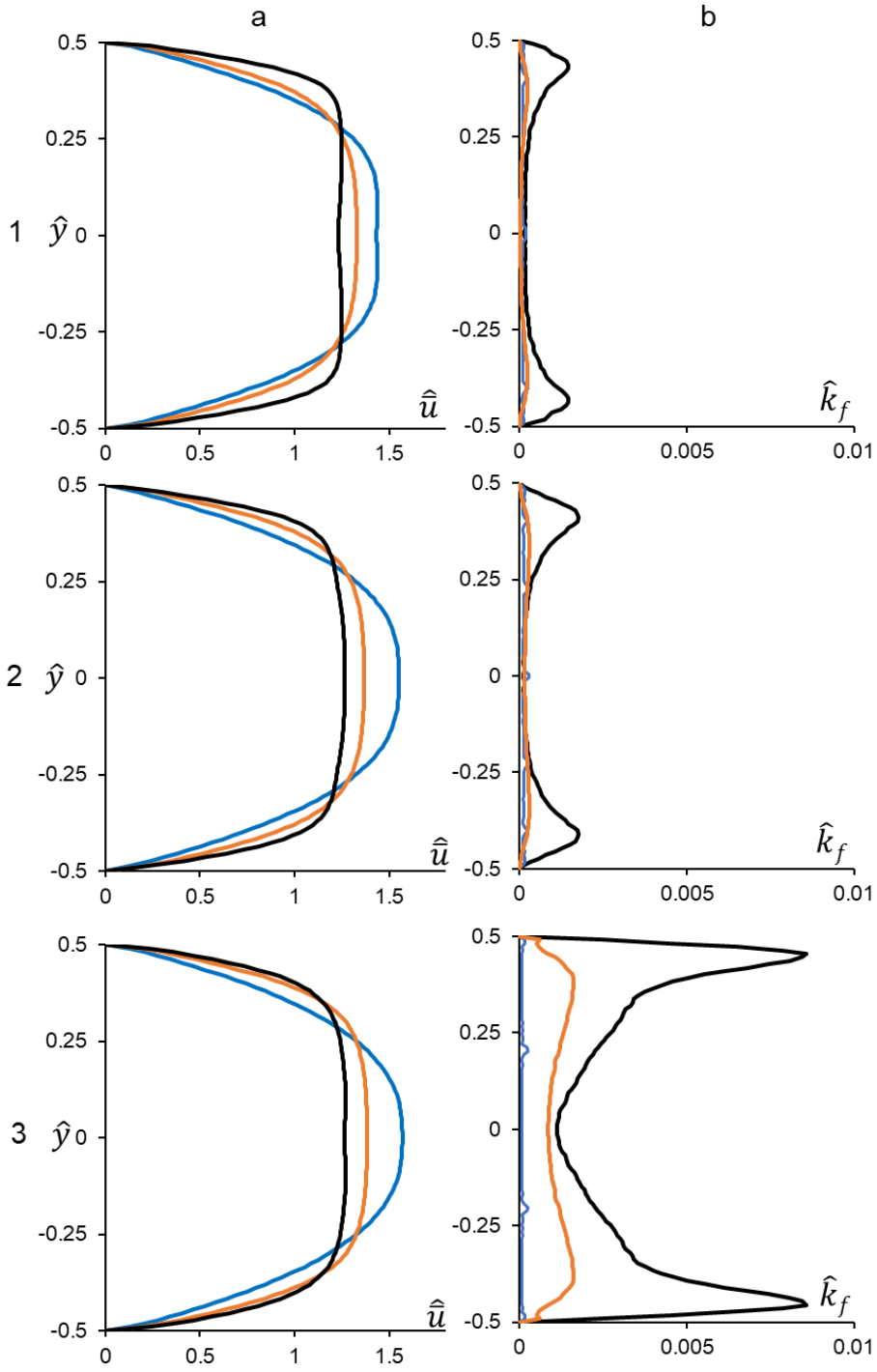

Figure B.2 *Cross-stream distributions* (*at z = 0*) *of* $\hat{\bar{u}}$ *and* $\hat{k}_f$ *(columns a and b respectively) at Re =* ***2,000****,* ***5,000*** *and* ***7,000*** *for the base flow at* $\hat{x}$ *= 18, 30 and 42* (*row 1, 2 and 3 respectively*).

the mid-range between the two *Re* for $|\hat{y}|<0.25$. As evident in Figure B.2-a.2, the $\hat{k}_f(y)$ distributions are also significantly smaller for $|\hat{y}|>0.25$ at *Re* = 5,000 than 7,000 (and similar to *Re* = 2,000) which could lead to lower cross-stream mixing and hence explain the smaller $\hat{u}(y)$. While similar trends can be seen at $\hat{x}=30$ in the $\hat{u}(y)$ and $\hat{k}_f(y)$ distributions (Figures B.2-a.2 and b.2), at $\hat{x}=42$, the base flow $\hat{k}_f(y)$ (Figure B.2-b.3) increases at *Re* = 5,000 and 7,000 and $\hat{u}(y)$ is similar for $|\hat{y}|>0.3$ between *Re* = 5,000 and 7,000. It should be noted that for $|\hat{y}|<0.3$, $\hat{u}(y)$ is still higher for *Re* = 5,000 than 7,000 and ostensibly this could be due to the spanwise differences in the base flow. These data

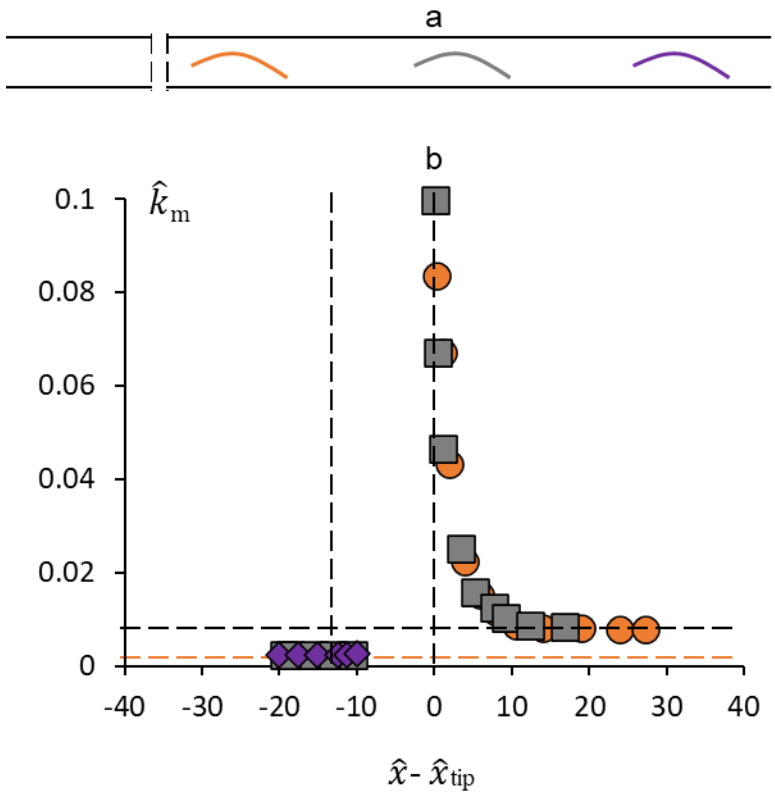

Figure B.3 *a) schematic of the streamwise locations of the reeds (L_s/W = 10 and thickness, t_s = 25.4 μm) with $\hat{x}_{tip}$ = **16**, **26** and **48** (the channel is not to scale). b) Variation of $\hat{k}_m$ (at z = 0) with the (normalized) distance from reed tip, $\hat{x}$-$\hat{x}_{tip}$ for reeds with $\hat{x}_{tip}$ = 16 (●), 26 (■) and 48 (♦) at Re = 5,000 (vertical dotted lines show reed's streamwise extent). The horizontal black and orange dotted lines show the asymptotic value $\hat{k}_m$ = 0.008 (cf. Figure 4.20) and the maximum value of $\hat{k}_m$ in the base flow at Re = 5,000 respectively.*

indicate that at *Re* = 5,000, while the fluctuating kinetic energy, $\hat{k}_f(y)$ is similar to that at *Re* = 2,000 for $\hat{x} \leq 30$ indicating a predominantly laminar base flow, further downstream, the base flow transitions and the $\hat{\bar{u}}(y)$ distributions are similar near the wall ($|\hat{y}|>0.3$) to that at *Re* = 7,000, but with smaller $\hat{k}_f(y)$.

Post characterization of the base flow at *Re* = 5,000, attention is shifted to the role of the streamwise location of the reed on the small-scale motions downstream of its tip as it interacts with a streamwise developing and transitioning but predominantly laminar base flow. $St_L = 0.9$ and $f_{osc} = 180$ *Hz* for all the reeds at *Re* = 5,000 regardless of the streamwise location which shows that the streamwise development of the underlying base flow has no influence on the reed oscillation frequency. Figure B.3 shows the streamwise variations of the cross-stream integral measure of the energy of small-scale motions, $\hat{k}_m$, (taken at channel mid-span, $z = 0$) in the absence and presence of reed for $\hat{x}_{tip} = 16$, 26 and 48. It should be noted that the streamwise distance from the reed tip, $\hat{x}$-$\hat{x}_{tip}$, was chosen as the x-axis to assess the streamwise variations relative to the reed (reed's streamwise extent is marked with vertical dashed lines in Figure B.3, where no PIV data could be taken). The streamwise variations of $\hat{k}_m$ (and its magnitude) for the base flow are discussed in detail in Figure 4.25 and are repeated for reference using the horizontal orange line. Upstream of the reed ($\hat{x}$-$\hat{x}_{tip} < -10$), the streamwise variations of $\hat{k}_m$ for $\hat{x}_{tip} = 26$ and 48 show that $\hat{k}_m$ in the presence of reed is nearly equal to that of the base flow indicating that the perturbations upstream of the reed (if any) are small. It should be noted that since the reed's tip for $\hat{x}_{tip} = 48$ was nearly at the channel exit, no PIV data was obtained downstream of the reed tip. While $\hat{k}_m$ for $\hat{x}_{tip} = 26$ is 20% higher than for reed with $\hat{x}_{tip} = 16$ for a small region in the vicinity of tip ($\hat{x}$-$\hat{x}_{tip} < 0.4$), immediately downstream ($\hat{x}$-$\hat{x}_{tip} = 0.4$), $\hat{k}_m$ is identical

between the two reeds and further downstream decreases at identical rates such that they reach the asymptotic levels, $\hat{k}_m \sim 0.008$ which were also observed for the reeds at *Re* = 7,000 and 12,000 as discussed in connection with Figure 4.19. That the streamwise variations of $\hat{k}_m$ downstream of the reed are nearly independent of the streamwise location of the reed at *Re* = 5,000 also means that it might be advantageous to place the reed near the channel entrance in order to increase the streamwise extent of reed induced small-scales.

The effect of reed location in the channel on heat transfer enhancement is also studied for reeds discussed in Figure B.4 at $ITD_{max} = 60^oC$. Figure B.3a shows the streamwise variation of local Nusselt number in the absence and presence of these reeds. $Nu(x)$ is identical in the absence and presence of reed with $\hat{x}_{tip} = 48$, upstream of the reed ($\hat{x} < 38$) as there are negligible increments in small-scales upstream of the reed. By comparing

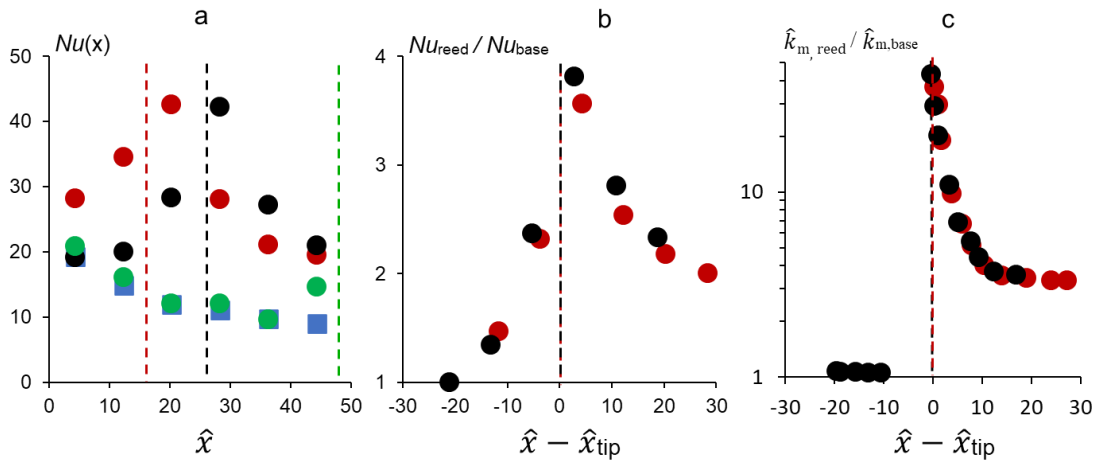

Figure B.4. *a) Streamwise Variation of local Nusselt number, Nu(x) in the absence (■) and presence of reeds ($H_s/H = 0.9$, $L_s/W = 10$, $St_L = 0.9$) with tip locations $\hat{x}_{tip} = 16$ (●), 26 (●), and 48 (●) for $ITD_{max} = 60^oC$ and Re= 5,000 in 5 mm channel; Variation of b) ratio of local Nusselt number, Nu_{reed}/Nu_{base} and c) ratio of bulk mean fluctuation kinetic energy, $\hat{k}_{m,reed}/\hat{k}_{m,base}$ in the presence and absence of reeds with streamwise distance from the reed-tip, $\hat{x}$-$\hat{x}_{tip}$ for $\hat{x}_{tip} = 16$ and 26. The tip-locations are shown through dotted lines.*

reeds with $\hat{x}_{tip} = 16$ and 26, the streamwise variations of $Nu(x)$ along the reed and downstream appear similar and vary with the distance from the reed-tip. In fact, the increments in local Nusselt number over the base, Nu_{reed}/Nu_{base}, due to these two reeds (Figure B.4b) depends only on the streamwise distance from the reed-tip, $\hat{x} - \hat{x}_{tip}$ and decreases as $(\hat{x} - \hat{x}_{tip})^{-0.3}$ downstream of the reed-tip The similarity between streamwise variations of Nu_{reed}/Nu_{base} can be attributed to the fact that the ratio of fluctuation kinetic energies between the reed and base flow $\hat{k}_{m,reed}/\hat{k}_{m,base}$ are identical upstream and downstream of the reed for the two reeds as shown in Figure B.4c. Overall, for the reeds with $\hat{x}_{tip} = 16$, 26 and 48, the increments in global Nu due to the reeds over the baseflow or Nu/Nu_b are 2.36, 2.16 and 1.32 whereas the increments in friction factor, f/f_b are 3.95, 3.71 and 3.18 respectively.

B.3 Limited Investigations on Reed Span

The dynamics of channel flow in the presence of reed is also affected by the reed-span. In this section, limited investigations were performed on the influence of reed-span at Re = 5,000 in the 5 mm channel on the small-scales downstream of the reed and along the channel span. The small-scale evolution downstream of the reed-tip is analyzed through the x-y distributions of $\hat{k}_f$ taken at the channel mid-span (z = 0) using time-average PIV at preset streamwise stations (cf. figure 4.8) for a representative Re = 5,000 and reeds of length, L_s/W = 10 ($\hat{x}_{tip}$ = 16) and span, H_s/H = 0.9 [figure B.5-i(a-f)], 0.5 [figure B.5-ii(a-f)] and 0.16 [figure B.5-iii(a-f)] as shown schematically in figure B.5-iv. It should be noted

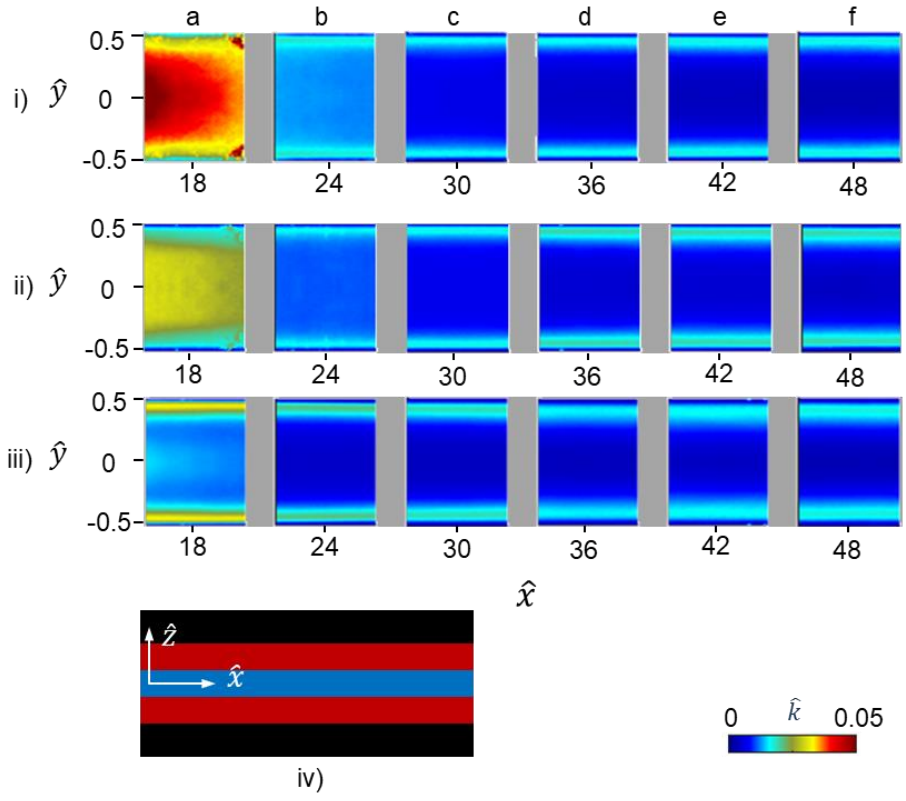

Figure B.5 *$\hat{x}$ - $\hat{y}$ distributions of the normalized fluctuating kinetic energy ($\hat{k}_f$) measured using PIV (cf. figure 4.2) in the presence of the reeds of length L_s/W = 10, thickness, t_s = 38.1 μm and span, H_s/H =* ***0.9*** *[i-(a-f)],* ***0.5*** *[ii-(a-f)] and* ***0.16*** *[iii-(a-f)]; iv) shows a schematic of the reeds in the $\hat{x}$ - $\hat{z}$ plane.*

that the strouhal number, St_L of these reeds are 0.7, 0.5 and 0.2 respectively. Near the reed-tip ($\hat{x} = 18$), while $\hat{k}_f$ peaks at the channel center and decreases towards the wall for $H_s/H = 0.9$ and 0.5 [figure B.5-i(a) and B.5-ii(a)], $\hat{k}_f$ peaks near the wall and decreases towards the channel center and the wall for H_s/H=0.16 [figure B.5-iii(a)]. While the fluctuating kinetic energy near the reed-tip decreases significantly as the reed-span reduces, for $\hat{x} \geq 30$ the cross-stream distribution of turbulent kinetic energy is nearly invariant with reed span. Similar to the studies in § 4.4 and 4.5, the streamwise variations of bulk mean fluctuating kinetic energy, $\hat{k}_m$ at the channel center for the reeds discussed in Figure B.4 and the baseflow are analyzed in figure B.6a. The data in the absence of the reed and for reed with span $H_s/H = 0.9$(dubbed "full-span reed") has been discussed in connection with Figure 4.25 and has been repeated for reference. As the reed's span decreases, the fluctuation kinetic energy near the reed-tip ($\hat{x} = 18$), reduces significantly from $\hat{k}_m \sim 0.05$ for reed span $H_s/H = 0.9$ to $\hat{k}_m \sim 0.015$ for reed span $H_s/H = 0.16$. However, 14*W*

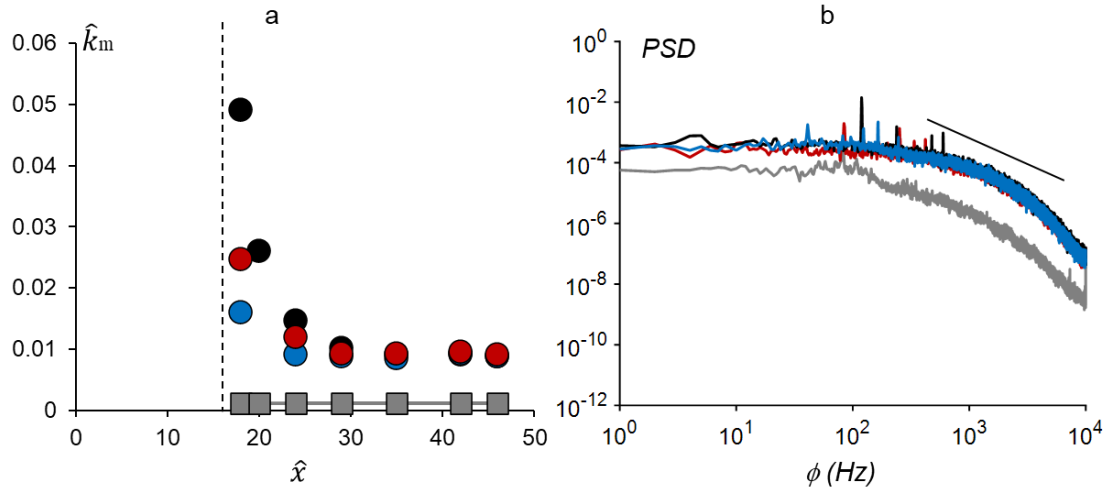

Figure B.6 *a) Streamwise Variation of the fluctuation kinetic energy ratio, $\hat{k}_m$ in the absence (■) and presence of reeds (cf. figure B.5) of span H_s/H = 0.9 (●), 0.5 (●), 0.16 (●); b) power spectra of streamwise velocity fluctuations at channel's exit for base and in the presence of reeds of span* ***0.9****,* ***0.5*** *and* ***0.16****. The solid line denotes -5/3 slope. The reed tip's streamwise location is marked using dashed line in (a).*

downstream of the reed tip at $\hat{x}$ = 30, all the reeds regardless of their span attain nearly identical fluctuation kinetic energy, $\hat{k}_m \sim 0.008$. It should be noted that further downstream, the changes in fluctuation kinetic energy in the presence of reeds are marginal and the $\hat{k}_m$ levels at the channel exit ($\hat{x}$ = 48) match those of the asymptotically turbulent channel flow as discussed in connection with Figure 4.19.. These data show that the small scales downstream of the reeds of shorter span are weaker in intensity but also dissipate at slower rates due to the lower St_L and lower span. The spectra of the streamwise velocity fluctuations at the channel exit (figure B.6b) for the reeds of varying span clearly shows that the small-scales farther downstream of the reed are identical in magnitude and spectral composition for all the reeds despite the fact that their St_L and spans are different indicating that they only depend on *Re*.

The differences in small-scales due to the reed span were also assessed through the spanwise variations of the increment in bulk mean fluctuation kinetic energy , $\Delta\hat{k}_m$ relative to the base flow for reeds of span, H_s/H = 0.9 (figure B.7a) and 0.16 (figure B.7b)

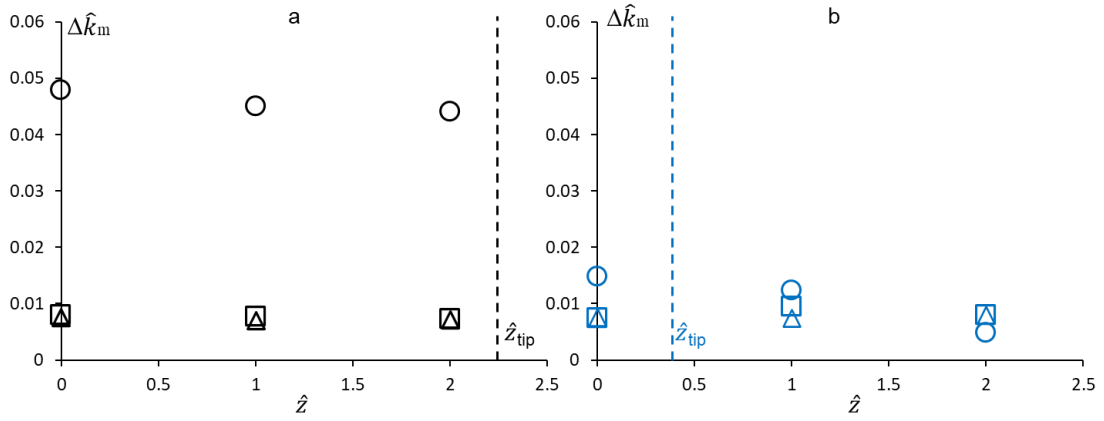

Figure B.7 *Spanwise variation of relative increment in bulk mean fluctuating kinetic energy, $\Delta\hat{k}_m$ at $\hat{x}$ = 18, 36 and 48 for reeds of length L_s/W = 10, thickness, t_s = 38.1 μm and span a) H_s/H = 0.9 (○, □,Δ) and b) 0.16 (○, □, Δ) for Re = 5,000. The dotted lines represent the spanwise edge of the reed-tip.*

downstream of the reed tip at $\hat{x}$ = 18, 36, and 48. While negligible spanwise variations exist for H_s/H = 0.9 or a "full-span" reed at all streamwise stations, a spanwise decrease can be seen for the "short-span" reed or H_s/H=0.16 at $\hat{x}$ = 18. It is remarkable that even though the reed's spanwise extent is only $\hat{z}$ = 0.4 (as shown through the dotted lines in Figure B.7b), an increment in fluctuation kinetic energy $\Delta\hat{k}_m$~0.004 can be obtained near the channel side-walls ($\hat{z}$ = 2) relative to the base-flow. It is also interesting that while the fluctuation kinetic energy for the "short-span" reed decreases streamwise at the spanwise center ($\hat{z}$ = 0), it increases streamwise near the side wall ($\hat{z}$ = 2) (cf. Figure B.7b) such that near the channel exit ($\hat{x}$ = 48), the spanwise variations are negligible and $\hat{k}_m$ is equal to the full span reed. It is hypothesized that since the distance between the side wall and the spanwise edge of the reed is higher and St_L is smaller for the "short-span" reed, the tip-vortices convect towards the top and bottom walls downstream of the reed-tip and dissipate at smaller rates thereby increasing the energy of small-scales.

While the heater transfer studies in Chapter V were carried out for "full-span" reeds or $H_s/H = 0.9$, numerical studies by Rips et al., (2020) on reeds ($L_s/W = 2$, $H_s/H = 0.125$, 0.5 and 0.875) and operating at constant wall temperatures have shown that reducing the reed-span significantly reduces the heat transfer enhancement, Nu/Nu_b and η in the channel by suppressing the 3-dimensional structures (resembling tip-vortices) which exist along the channel span. Consistent with the PIV studies on the reed-span, the global heat transfer characteristics for reeds of length, $L_s/W = 10$ and span $0.16 < H_s/H < 0.9$ at $ITD_{max} = 60^oC$ and $Re = 5{,}000$ were also studied in the 5 mm channel (Figure B.8). Figure B.8-a and b show that while the ratio of global Nusselt number in the presence and absence of reed or Nu/Nu_b increases linearly with reed span, the ratio of friction factors f/f_b increases quadratically with reed span. It should be noted that the St_L increases nearly linearly with reed span (base-flow is shown for reference through the green symbol in Figures B.7-a through B.8-c). It is conjectured that the channel losses increase quadratically with reed-span due to increase in St_L and the increase in viscous losses along the reed span. The

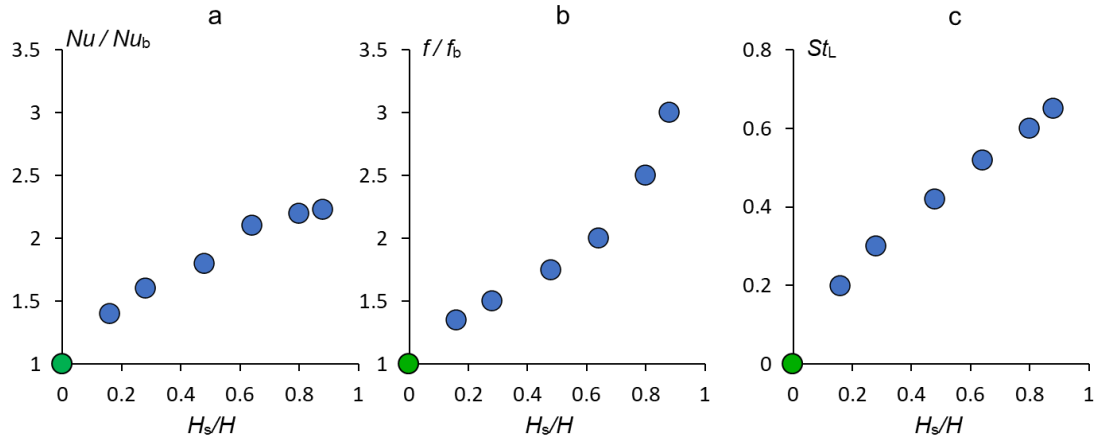

Figure B.8. *a) Variation with the reed-span, H_s/H of a) increment in global Nusselt number, Nu/Nu_b b) increment in friction factor, f/f_b and c) strouhal number, St_L for reeds of length $L_s/W = 10$, at $ITD_{max} = 60^oC$ and $Re = 5{,}000$ in 5 mm channel. The base-flow at $Re = 5{,}000$ is shown for reference* (●)

increase in Nu/Nu_b with reed-span has been shown by Rips et al.(2020) to be due to strengthening and increase in spanwise extent of tip-vortices with reed-span. A comparison of these variable-span reeds (of fixed length and variables) with "full-span" reeds of the same length (cf. Figure 5.10) is performed in Figure B.9. Figure B.9-a and b show the variation of Nu/Nu_b and f/f_b with St_L for the full-span and variable span reeds. While Nu/Nu_b for variable span reeds ($H_s/H < 0.9$) are significantly smaller than the full-span reeds for $St_L < 0.5$ ($H_s/H < 0.48$), f/f_b for variable span reeds are marginally smaller than the full-span reeds for all St_L due to the lower blockage in the channel. The thermal performance is also compared between the variable span and full-span reeds at identical flow power (cf. Figure 5.10) and the variation of Nu with the normalized fluid pumping power, $f{\cdot}Re^3$ is shown in Figure B.9-c in the absence and presence of reeds in connection with Figure B.9-b. The differences in Nu at identical $f{\cdot}Re^3$ seem to be small between variable and full-span reeds but decreases significantly for variable span reeds for

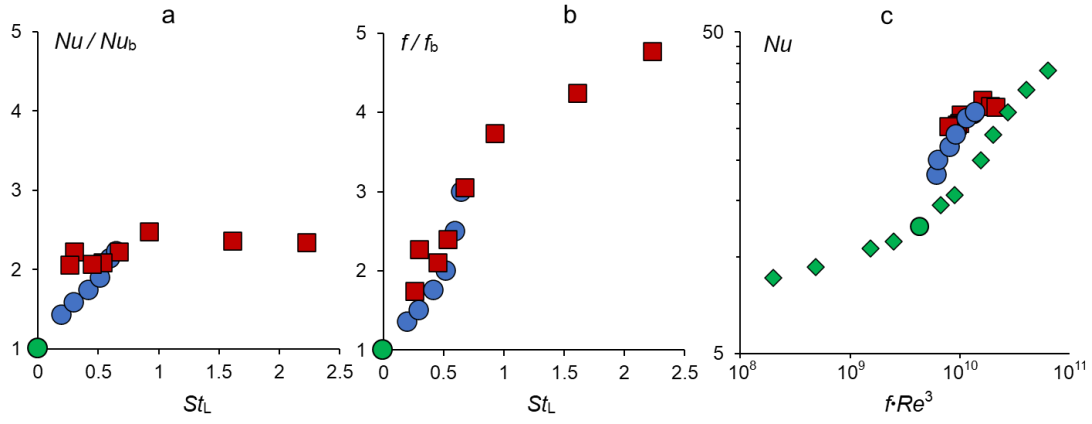

Figure B.9. *a) Variation with St_L, of a) increment in global Nusselt number, Nu/Nu_b and b) increment in friction factor, f/f_b for "full-span" reeds or $H_s/H = 0.9$ (■, cf. Figure 5.10) and variable span reeds (●, cf. Figure B.8); c) Variation of Nu with flow power $f{\cdot}Re^3$ in the absence (♦) and presence of "full-span" and "variable-span" reeds in the 5 mm channel. The base-flow or absence of reeds is shown for reference (●)*

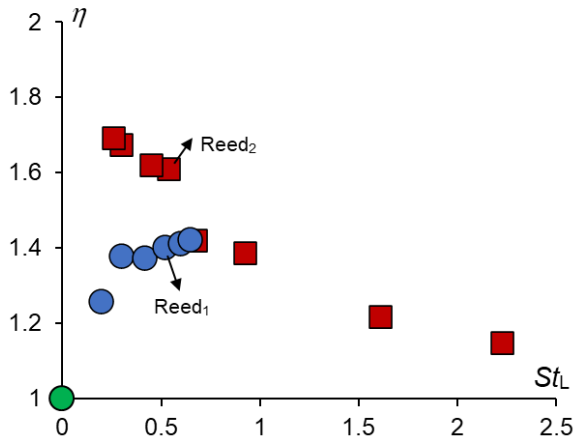

Figure B.10. *a) Variation of thermal enhancement factor, η with St_L, for "full-span" (■) and variable span reeds (●) as discussed in Figure B.9; The base-flow or absence of reeds is shown for reference (●). For length $L_s/W = 10$, and $St_L = 0.5$, a reed of span $H_s/H = 0.64$ ($Reed_1$) and a "full span" reed ($Reed_2$) are marked.*

$f{\cdot}Re^3 < 10^{10}$ ($H_s/H < 0.5$) due to the reduction in Nu by weakening of tip-vortices. The thermal performance of the variable and full span reeds were compared using the thermal enhancement factor, η which is the ratio of Nusselt numbers in the presence and absence of reeds at a fixed flow power (cf. § 5.4). The variations of η with the reed strouhal number St_L for the variable and full span reeds have been shown in Figure B.10. The data for full span reeds in Figure 5.10 has been repeated for reference. The thermal performance of full span reeds is higher than the variable span reeds at all St_L and the differences between the full span and variable span reeds increase as the St_L decreases. For a fixed reed length ($L_s/W = 10$) and strouhal number ($St_L \sim 0.5$), a reed of span $H_s/H = 0.64$ (or $Reed_1$) and a full span reed or ($Reed_2$) as shown in Figure B.10 were compared and η for $Reed_1$ and $Reed_2$ are 1.4 and 1.61 respectively. This indicates that the "tip vortices" in the presence of full span reeds lead to enhancement in thermal performance of the reeds.

APPENDIX C

EFFECT OF MULTIPLE REEDS AND LIMITED VARIATIONS IN WALL *ITD*

C.1 Effect of Multiple Reeds

As the small-scales dissipate downstream of the reed, it was considered plausible to implement multiple reeds in the channel in order to reinforce the intensity of the small-scales. As an illustration, reeds of span, H_s/H = 0.9 and length, L_s/W = 18.8 were tested in the 2.5 mm channel (L/W = 100 and H/W = 10) at Re = 2,000 and $\dot{Q}_{heater}" = 1.6\ KW/m^2$. Three reed-tip locations, $\hat{x}_{tip}$ = 30.8 (configuration I), 50.8 (configuration II) and 70.8 (configuration III) and 4 combinations of these configurations (Configuration I & II, configuration I & III, configuration II & III and configuration I, II & III) were tested as shown in Figure C.1. Figure C.2 shows an example through the variation of local Nu(x) calculated using Method I in the absence (base-flow) and presence of configuration I, II

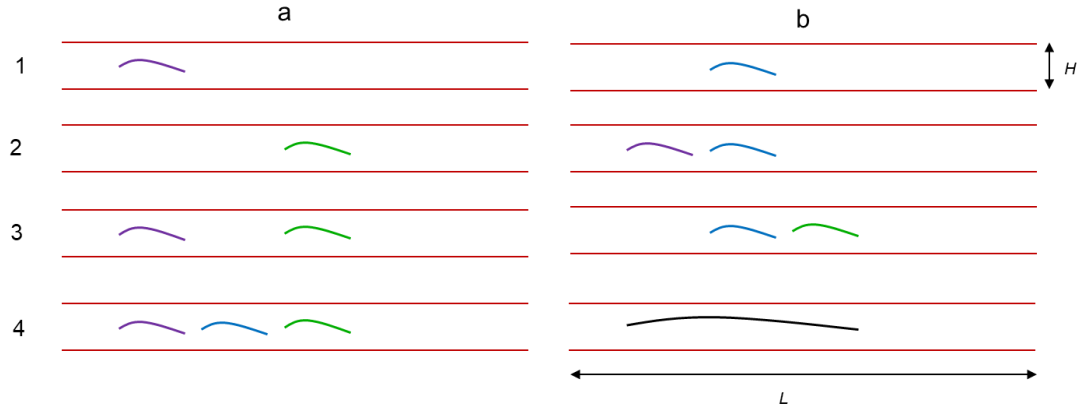

Figure C.1. *Schematic of a 2.5* X *250 mm channel with reeds of span, H_s/H = 0.9, length, L_s/W = 18.8 with tip-locations $\hat{x}_{tip}$ = 30.8,(a1, configuration I), 50.8 (b1, configuration II), 70.8 (a2, configuration III) and combinations of the configurations (b2 to a4); reed of length, L_s/W = 58.8 (configuration IV)which covers the combined channel length of the three configurations is shown in b4.*

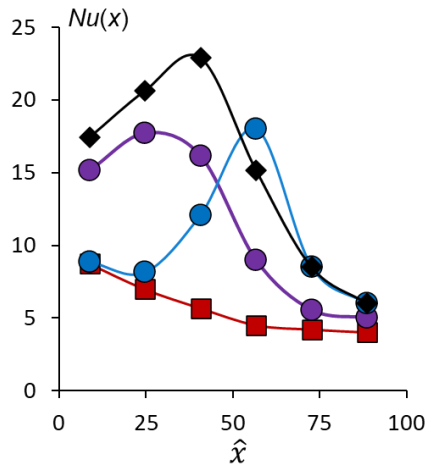

Figure C.2. *Streamwise variation of local Nu(x) in the absence (■) and presence of configuration I (●), II (●) and I&II (♦) reeds as discussed in connection with Figure 5.17 in the 2.5 mm channel at Re = 2,000 for* $\dot{Q}_{\text{heater}}$*" = 1.6 KW/m*^{2}

and configuration I & II reeds. It should be noted $St_L = 1.5$ for all the reed configurations. The peak *Nu*(x) for configuration I &II reeds which occurs midway between the two reed-tips at $\hat{x} = 40.8$ is higher than the peak *Nu*(x) for either of the single reed configurations and *Nu*(*x*) is higher along the length of the upstream reed and slightly lower for the

Table C.1. *Global Nusselt number, channel friction factor increments over the base-flow, and thermal enhancement factor,* Nu/Nu_b*,* f/f_b *and* η *for the reed configurations discussed in Figure C.1*

Configuration	Nu/Nu_b	f/f_b	η
I	2.2	2.4	1.6
II	1.9	2.3	1.5
III	1.8	2.2	1.4
I&II	2.8	3.2	1.9
I&III	2.8	3.3	1.9
II&III	2.5	3.3	1.7
I,II&III	2.7	3.9	1.8
IV	2.5	3.2	1.7

downstream reed near its tip. Overall, Nu/Nu_b, f/f_b for configuration I are 2.15 and 2.4, for configuration II are 1.9 and 2.3, and for configuration I&II are 2.83 and 3.17. A comparison between the thermal performances of the configurations described in Figure C.1 is performed through the thermal enhancement factor, η as shown in Table C.1. These data indicate that a maximum thermal enhancement of $\eta = 1.9$ can be obtained by using either configuration I & II or configuration I&III reeds which is 18% higher than that of a single reed (configuration I) and 11% higher than using three reeds in tandem (configuration I, II & III).

C.2 Comparisons between ITD_{max} = 40^{0}C and 60^{0}C in the H/W = 5 Isolated Channel

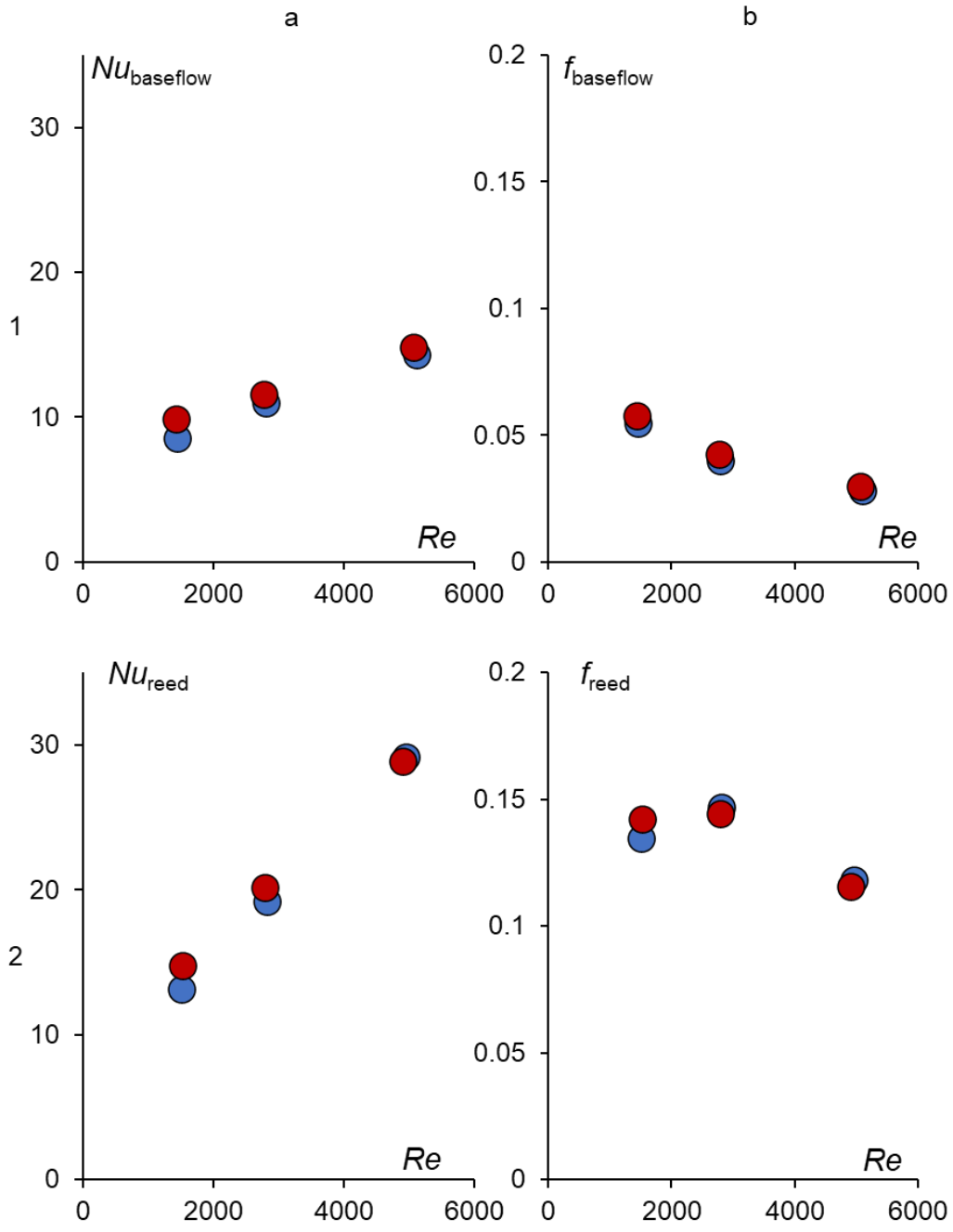

Figure C.3. *Variation of global Nusselt number (based on LMTD) and channel friction factor with Re at ITD_{max} = 40^{0}C (●) and 60^{0}C (●) in the absence of reeds (Figures a.1 and b.1) and in the presence of reeds of length, L/W = 10 (a.2 and b.2) in the isolated 5 mm wide channel.*

As discussed in §6.2, for comparison of isolated channels with the fin array, the data in isolated channel for $ITD_{max} = 60^0$C was used as a proxy for $ITD_{max} = 40^0$C. In this section it is shown that the channel Nusselt numbers and friction factors are identical for the two *ITD*'s in the absence and presence of the reeds ($L/W = 10$) for Re = 1,500, 3,000 and 4,500. The variations of Nusselt numbers (based on method II) and friction factors in the absence of the reeds are shown in Figures C.3-a.1 and b.1 and in the presence of reeds are shown in Figures C.3-a.2 and b.2 respectively. Reasonable agreement can be found in f and Nu between $ITD_{max} = 40^0$C and 60^0C at all Re in the absence and presence of reeds.

REFERENCES

Acikalin, T. and Garimella, S. V., *Analysis and Prediction of the Thermal Performance of Piezoelectrically Actuated Fans*, *Heat Transfer Engineering*, pp. 487–498, 2009.

Adrian, R. J., Particle-Imaging Techniques for Experimental Fluid Mechanics, *Annual Review of Fluid Mechanics*, vol. **23**, no. 1, pp. 261–304, 1991. DOI: 10.1146/annurev.fl.23.010191.001401

Alben, S., Flag Flutter in Inviscid Channel Flow, *Physics of Fluids*, vol. **27**, no. 3, from http://dx.doi.org/10.1063/1.4915897, 2015. DOI: 10.1063/1.4915897

Alben, S. and Shelley, M. J., Flapping States of a Flag in an Inviscid Fluid: Bistability and the Transition to Chaos, *Physical Review Letters*, vol. **46**, no. 5, pp. 3–6, 2014. DOI: 10.1103/PhysRevLett.100.074301

Argentina, M. and Mahadevan, L., Fluid-Flow-Induced Flutter of a Flag, *Proceedings of the National Academy of Sciences of the United States of America*, vol. **102**, no. 6, pp. 1829–34, 2005. DOI: 10.1073/pnas.0408383102

Bar-Cohen, A. and Iyengar, M., Design and Optimization of Air-Cooled Heat Sinks for Sustainable Development, *IEEE Transactions on Components and Packaging Technologies*, vol. **25**, no. 4, pp. 584–91, 2002. DOI: 10.1109/TCAPT.2003.809112

Biswas, G., Mitra, N. K. and Fiebig, M., Heat Transfer Enhancement in Fin-Tube Heat Exchangers by Winglet Type Vortex Generators, *International Journal of Heat and Mass Transfer*, vol. **37**, no. 2, pp. 283–91, 1994. DOI: 10.1016/0017-9310(94)90099-X

Brzozowski, Dan, PIV Error Analysis, no. 1, pp. 1–5, 2009.

Brzozowski, Daniel, Dynamic Control of Aerodynamic Forces on a Moving Platform Using Active Flow Control, no. December, pp. 1–198, 2011.

Bustamante, J. G., Rattner, A. S. and Garimella, S., Achieving Near-Water-Cooled Power Plant Performance with Air-Cooled Condensers, *Applied Thermal Engineering*, vol. **105**, pp. 362–71, from http://dx.doi.org/10.1016/j.applthermaleng.2015.05.065, 2016. DOI: 10.1016/j.applthermaleng.2015.05.065

Carruthers, A. C. and Filippone, A., Aerodynamic Drag of Streamers and Flags, *Journal of Aircraft*, vol. **42**, no. 4, pp. 976–82, 2005. DOI: 10.2514/1.9754

Çengel, Y. A., and Cimbala, J. M. T. A.-T. T.-, Fluid Mechanics : Fundamentals and Applications LK - Https://Gatech.on.Worldcat.Org/Oclc/56481360, 2006.

Chen, J., Müller-Steinhagen, H. and Duffy, G., Heat Transfer Enhancement in Dimpled Tubes, *Applied Thermal Engineering*, vol. **21**, pp. 535–47, April 1, 2001. DOI: 10.1016/S1359-4311(00)00067-3

Delafosse, A., Collignon, M. L., Crine, M. and Toye, D., Estimation of the Turbulent Kinetic Energy Dissipation Rate from 2D-PIV Measurements in a Vessel Stirred by an Axial Mixel TTP Impeller, *Chemical Engineering Science*, vol. **66**, no. 8, pp. 1728–37, 2011. DOI: 10.1016/j.ces.2011.01.011

Doaré, O., Mano, D. and Carlos Bilbao Ludena, J., Effect of Spanwise Confinement on Flag Flutter: Experimental Measurements, *Physics of Fluids*, vol. **23**, no. 11, pp. 1–4, 2011. DOI: 10.1063/1.3662127

Eloy, C., Souilliez, C. and Schouveiler, L., Flutter of a Rectangular Plate, *Journal of Fluids and Structures*, vol. **23**, no. 6, pp. 904–19, 2007. DOI: 10.1016/j.jfluidstructs.2007.02.002

Elyyan, M. A., Rozati, A. and Tafti, D. K., Investigation of Dimpled Fins for Heat Transfer Enhancement in Compact Heat Exchangers, *International Journal of Heat and Mass Transfer*, vol. **51**, no. 11–12, pp. 2950–66, 2008. DOI: 10.1016/j.ijheatmasstransfer.2007.09.013

Fernández, J. L. and Poulter, R., Heat Transfer Enhancement by Means of Flag-Type Insert in Tubes, *International Journal of Heat and Mass Transfer*, vol. **30**, no. 12, pp. 2603–9, 1987. DOI: 10.1016/0017-9310(87)90141-4

Fiebig, M., Kallweit, P., Mitra, N. and Tiggelbeck, S., Heat Transfer Enhancement and Drag by Longitudinal Vortex Generators in Channel Flow, *Experimental Thermal and Fluid Science*, vol. **4**, no. 1, pp. 103–14, 1991. DOI: 10.1016/0894-1777(91)90024-L

G. A. Tetlow and A. D. Lucey, Motions of a Cantilevered Flexible Plate in Viscous Channel Flow Driven by a Constant Pressure Drop, *Training*, vol. **25**, no. January, pp. 463–82, 2009. DOI: 10.1002/cnm

Gerty, D., Fluidic Driven Cooling of Electronic Hardware Part I: Channel Integrated Vibrating Reed Part II: Active Heat Sink, Georgia Institute of Technology, 2008.

Gerty, D., Gerlach, D. W., Joshi, Y. K. and Glezer, A., Development of a Prototype Thermal Management Solution for 3-D Stacked Chip Electronics by Interleaved Solid Spreaders and Synthetic Jets, *Collection of Papers Presented at The 13th*

International Workshop on THERMal INvestigation of ICs and Systems, THERMINIC, no. September, pp. 156–61, 2007. DOI: 10.1109/THERMINIC.2007.4451769

Gillespie, M. B., Black, W. Z., Rinehart, C. and Glezer, A., Local Convective Heat Transfer from a Constant Heat Flux Flat Plate Cooled by Synthetic Air Jets, *Journal of Heat Transfer*, vol. **128**, no. 10, pp. 990–1000, 2006. DOI: 10.1115/1.2345423

Han, J. C. and Park, J. S., Developing Heat Transfer in Rectangular Channels with Rib Turbulators, *International Journal of Heat and Mass Transfer*, vol. **31**, no. 1, pp. 183–95, 1988. DOI: 10.1016/0017-9310(88)90235-9

Han, L. S., Hydrodynamic Entrance Lengths for Incompressible Laminar Flow in Rectangular Ducts, *Journal of Applied Mechanics*, vol. **27**, no. 3, pp. 403–9, from https://doi.org/10.1115/1.3644015, September 1, 1960. DOI: 10.1115/1.3644015

Han, S. and Feeny, B., Application of Proper Orthogonal Decomposition to Structural Vibration Analysis, *Mechanical Systems and Signal Processing*, vol. **17**, no. 5, pp. 989–1001, 2003. DOI: 10.1006/mssp.2002.1570

Hartnett, J. P., Koh, J. C. Y. and McComas, S. T., A Comparison of Predicted and Measured Friction Factors for Turbulent Flow through Rectangular Ducts, *Journal of Heat Transfer*, vol. **84**, no. 1, pp. 82–88, 1962. DOI: 10.1115/1.3684299

Hidalgo, P., Herrault, F., Glezer, A., Allen, M., Kaslusky, S. and Rock, B. S., Heat Transfer Enhancement in High-Power Heat Sinks Using Active Reed Technology, *16th International Workshop on Thermal Investigations of ICs and Systems, THERMINIC 2010*, pp. 165–70, 2010.

Hidalgo, P., Jha, S. and Glezer, A., Enhanced Heat Transfer in Air Cooled Heat Sinks Using Aeroelastically Fluttering Reeds, *THERMINIC 2015 - 21st International Workshop on Thermal Investigations of ICs and Systems*, vol. **2015**, no. October, pp. 1–6, 2015. DOI: 10.1109/THERMINIC.2015.7389627

Honohan, A. M., The Interaction of Synthetic Jets with Cross Flow and the Modification of Aerodynamic Surfaces, no. April, pp. 1–283, from http://hdl.handle.net/1853/20836, 2003.

Hussain, A. K. M. F. and Reynolds, W. C., The Mechanics of an Organized Wave in Turbulent Shear Flow. Part 2. Experimental Results, *Journal of Fluid Mechanics*, vol. **54**, no. 2, pp. 241–61, 1972. DOI: 10.1017/S0022112072000667

Incropera, F. P. and DeWitt, D. P., *Fundamentals of Heat and Mass Transfer LK - Https://Gatech.on.Worldcat.Org/Oclc/45951568*, *TA - TT* -, New York SE - xix, 981 pages : illustrations (some color) ; 26 cm + 1 computer disc (4 3/4 in.) with user's guide: J. Wiley, from http://catdir.loc.gov/catdir/toc/onix06/2001017854.html, 2002.

Kakaç, S. (Sadık), Shah, R. K. and Aung, W., *Handbook of Single-Phase Convective Heat Transfer*, Wiley, accessed March 25, 2020, from https://inis.iaea.org/search/search.aspx?orig_q=RN:18090434, 1987.

Kearney, J. M., AERODYNAMIC CONTROL USING DISTRIBUTED ACTIVE BLEED Proposal for Doctoral Research, no. Carr 1988, pp. 1–18, 2013.

Kenyu Oyakawa, Yoshiharu Kawajou, Izuru Senaha, Minoru Yaga, I. M., Heat Transfer Enhancement in a Parallel Plate Duct by an Oscillating Thin Plate Insertion, *Heat*

Transfer- Japanese Research, vol. **25**, no. 8, p. 14, 1996.

Kornecki, A., Dowell, E. H. and O'Brien, J., On the Aeroelastic Instability of Two-Dimensional Panels in Uniform Incompressible Flow, *Journal of Sound and Vibration*, vol. **47**, no. 2, pp. 163–78, 1976. DOI: 10.1016/0022-460X(76)90715-X

Kota, K., Hidalgo, P., Joshi, Y. and Glezer, A., Thermal Management of a 3D Chip Stack Using a Liquid Interface to a Synthetic Jet Cooled Spreader, *15th International Workshop on Thermal Investigations of ICs and Systems, THERMINIC 2009*, no. October, pp. 186–91, 2009.

Kroger, D. G., Air-Cooled Heat Exchangers and Cooling Towers : Thermal-Flow Performance Evaluation and Design, 2004.

Lambert, T. J., Vukasinovic, B. and Glezer, A., Aerodynamic Flow Control of Wake Dynamics Coupled to a Moving Bluff Body, *8th AIAA Flow Control Conference*, no. December, 2016. DOI: 10.2514/6.2016-4081

Ligrani, P. M., Oliveira, M. M. and Blaskovich, T., Comparison of Heat Transfer Augmentation Techniques, *AIAA Journal*, vol. **41**, no. 3, pp. 337–62, 2003. DOI: 10.2514/2.1964

Mahalingam, R., Rumigny, N. and Glezer, A., Thermal Management Using Synthetic Jet Ejectors, *IEEE Transactions on Components and Packaging Technologies*, vol. **27**, no. 3, pp. 439–44, 2004. DOI: 10.1109/TCAPT.2004.831757

Mahmood, G. I. and Ligrani, P. M., Heat Transfer in a Dimpled Channel: Combined Influences of Aspect Ratio, Temperature Ratio, Reynolds Number, and Flow

Structure, *International Journal of Heat and Mass Transfer*, vol. **45**, no. 10, pp. 2011–20, 2002. DOI: 10.1016/S0017-9310(01)00314-3

Mehta, R. D., and Bradshaw, P., Design Rules for Small Low Speed Wind Tunnels., *Aeronautical Journal*, 1979.

Mendonca, T. R. F., Pinto, M. F. and Duque, C. A., Least Squares Optimization of Zero Crossing Technique for Frequency Estimation of Power System Grid Distorted Sinusoidal Signals, *2014 11th IEEE/IAS International Conference on Industry Applications, IEEE INDUSCON 2014 - Electronic Proceedings*, 2014. DOI: 10.1109/INDUSCON.2014.7059443

Naphon, P. and Khonseur, O., Study on the Convective Heat Transfer and Pressure Drop in the Micro-Channel Heat Sink, *International Communications in Heat and Mass Transfer*, vol. **36**, no. 1, pp. 39–44, from http://dx.doi.org/10.1016/j.icheatmasstransfer.2008.09.001, 2009. DOI: 10.1016/j.icheatmasstransfer.2008.09.001

Park, S. G., Kim, B., Chang, C. B., Ryu, J. and Sung, H. J., Enhancement of Heat Transfer by a Self-Oscillating Inverted Flag in a Poiseuille Channel Flow, *International Journal of Heat and Mass Transfer*, vol. **96**, pp. 362–70, from http://dx.doi.org/10.1016/j.ijheatmasstransfer.2016.01.043, 2016. DOI: 10.1016/j.ijheatmasstransfer.2016.01.043

Pope, S. B., *Turbulent Flows*, Cambridge University Press, accessed November 17, 2020a, from https://www.cambridge.org/core/product/identifier/9780511840531/type/book,

2000.

Pope, S. B., *Turbulent Flows*, Cambridge: Cambridge University Press, from https://www.cambridge.org/core/books/turbulent-flows/C58EFF59AF9B81AE6CFAC9ED16486B3A, 2000b.

Premaratne, P., Tian, W. and Hu, H., Analysis of Turbine Wake Characteristics Using Proper Orthogonal Decomposition (POD) and Triple Decomposition, *46th AIAA Fluid Dynamics Conference*, no. June, pp. 1–16, 2016. DOI: 10.2514/6.2016-3780

Promvonge, P. and Thianpong, C., Thermal Performance Assessment of Turbulent Channel Flows over Different Shaped Ribs, *International Communications in Heat and Mass Transfer*, vol. **35**, no. 10, pp. 1327–34, from http://dx.doi.org/10.1016/j.icheatmasstransfer.2008.07.016, 2008. DOI: 10.1016/j.icheatmasstransfer.2008.07.016

Raffel, M., Willert, C., and K., *J. Particle Image Velocimetry: A Practical Guide.*, 1998.

Rips, A., Shoele, K. and Mittal, R., Heat Transfer Enhancement in Laminar Flow Heat Exchangers Due to Flapping Flags, *Physics of Fluids*, vol. **32**, no. 6, from https://doi.org/10.1063/1.5142403, 2020. DOI: 10.1063/1.5142403

Sandham, N. D. and Kleiser, L., The Late Stages of Transition to Turbulence in Channel Flow, *Journal of Fluid Mechanics*, vol. **245**, pp. 319–48, 1992. DOI: 10.1017/S002211209200048X

Shah, R. K. and London, A. L., Chapter II - Differential Equations and Boundary Conditions, R. K. Shah and A. L. B. T.-L. F. F. C. in D. London, Eds., Academic

Press, from http://www.sciencedirect.com/science/article/pii/B9780120200511500073, pp. 5–36, 1978.

Shelley, M. J. and Zhang, J., Flapping and Bending Bodies Interacting with Fluid Flows, *Annual Review of Fluid Mechanics*, vol. **43**, no. September, pp. 449–65, 2011. DOI: 10.1146/annurev-fluid-121108-145456

Shelley, M., Vandenberghe, N. and Zhang, J., Heavy Flags Undergo Spontaneous Oscillations in Flowing Water, *Physical Review Letters*, vol. **94**, no. 9, 2005. DOI: 10.1103/PhysRevLett.94.094302

Shih, C. and Ho, C. M., Vorticity Balance and Time Scales of a Two-Dimensional Airfoil in an Unsteady Free Stream, *Physics of Fluids*, vol. **6**, no. 2, pp. 710–23, 1994. DOI: 10.1063/1.868310

Shoele, K. and Mittal, R., Computational Study of Flow-Induced Vibration of a Reed in a Channel and Effect on Convective Heat Transfer, *Physics of Fluids*, vol. **26**, no. 12, 2014. DOI: 10.1063/1.4903793

Shoele, K. and Mittal, R., Flutter Instability of a Thin Flexible Plate in a Channel, *Journal of Fluid Mechanics*, vol. **786**, pp. 29–46, 2015. DOI: 10.1017/jfm.2015.632

Sparrow, E. M., Hixon, C. W. and Shavit, G., Experiments on Laminar Flow Development in Rectangular Ducts, *Journal of Basic Engineering*, vol. **89**, no. 1, pp. 116–23, from https://doi.org/10.1115/1.3609536, March 1, 1967. DOI: 10.1115/1.3609536

Sreenivasan, K. R., On the Scaling of the Turbulence Energy Dissipation Rate, *Physics of Fluids*, vol. **27**, no. 5, pp. 1048–51, 1984. DOI: 10.1063/1.864731

Syred, N., Khalatov, A., Kozlov, A., Shchukin, A. and Agachev, R., Effect of Surface Curvature on Heat Transfer and Hydrodynamics within a Single Hemispherical Dimple, *Journal of Turbomachinery*, vol. **123**, no. 3, pp. 609–13, 2001. DOI: 10.1115/1.1348020

Takeishi, K., Kawahara, G., Wakabayashi, H., Uhlmann, M. and Pinelli, A., Localized Turbulence Structures in Transitional Rectangular-Duct Flow, *Journal of Fluid Mechanics*, vol. **782**, pp. 368–79, 2015. DOI: 10.1017/jfm.2015.546

Tanaka, T., Itoh, M., Hatada, T. and Matsushima, H., Influence of Inclination Angle, Attack Angle, and Arrangement of Rectangular Vortex Generators on Heat Transfer Performance, *Heat Transfer - Asian Research*, vol. **32**, no. 3, pp. 253–67, 2003. DOI: 10.1002/htj.10089

Taneda, S., Waving Motions of Flags, *Journal of the Physical Society of Japan*, vol. **24**, no. 2, p. 10, 1968.

Teertstra, P., Yovanovich, M. M., Culham, J. R., and Lemczyk, T., Analytical Forced C o Nvec t Io n Mo Deling of Plate Fin Heat Sinks, *15th IEEE SEMI-THERM Symposium*, pp. 34–41, 1999.

Tiggelbeck, S., Mitra, N. K. and Fiebig, M., Comparison of Wing-Type Vortex Generators for Heat Transfer Enhancement in Channel Flows, *Journal of Heat Transfer*, vol. **116**, no. 4, pp. 880–85, 1994. DOI: 10.1115/1.2911462

Trip, R., Kuik, D. J., Westerweel, J. and Poelma, C., An Experimental Study of Transitional Pulsatile Pipe Flow, *Physics of Fluids*, vol. **24**, no. 1, 2012. DOI: 10.1063/1.3673611

Vukasinovic, B., Rusak, Z. and Glezer, A., Dissipative Small-Scale Actuation of a Turbulent Shear Layer, *Journal of Fluid Mechanics*, vol. **656**, pp. 51–81, 2010. DOI: 10.1017/S0022112010001023

Watanabe, Y., Suzuki, S., Sugihara, M. and Sueoka, Y., An Experimental Study of Paper Flutter, *Journal of Fluids and Structures*, vol. **16**, no. 4, pp. 529–42, 2002. DOI: 10.1006/jfls.2001.0435

Wells, C. V, Principles and Measurement Un in Research and Lications of Ty Analysis Ration Third Annual Infrared Radiometric Sensor Calibration Symposium Utah State University Logan , Utah, no. November, 1992.

Westerweel, J., Theoretical Analysis of the Measurement Precision in Particle Image Velocimetry, *Experiments in Fluids*, vol. **29**, no. SUPPL. 1, 2000. DOI: 10.1007/s003480070002

Williams, A., *Structural Analysis*, *Structural Analysis*, 2009.

Wiltse, J. M. and Glezer, A., Direct Excitation of Small-Scale Motions in Free Shear Flows, *Physics of Fluids*, vol. **10**, no. 8, pp. 2026–36, 1998. DOI: 10.1063/1.869718

Wygnanski, I. J. and Champagne, F. H., On Transition in a Pipe. Part 1. The Origin of Puffs and Slugs and the Flow in a Turbulent Slug, *Journal of Fluid Mechanics*, vol. **59**, no. 2, pp. 281–335, from https://www.cambridge.org/core/article/on-transition-

in-a-pipe-part-1-the-origin-of-puffs-and-slugs-and-the-flow-in-a-turbulent-slug/EDF674FFD2DEDE5D6DC3DF9E67C7415D, 1973. DOI: DOI: 10.1017/S0022112073001576

Yu, Y., Liu, Y., and Amandolese, X., A Review on Fluid-Induced Flag Vibrations, *Applied Mechanics Reviews*, January 1, 2019.

Yu, Y., Liu, Y. and Chen, Y., Vortex Dynamics and Heat Transfer behind Self-Oscillating Inverted Flags of Various Lengths in Channel Flow, *Physics of Fluids*, vol. **30**, no. 4, from http://dx.doi.org/10.1063/1.5022723, 2018. DOI: 10.1063/1.5022723

Zanoun, E. S., Kito, M. and Egbers, C., A Study on Flow Transition and Development in Circular and Rectangular Ducts, *Journal of Fluids Engineering, Transactions of the ASME*, vol. **131**, no. 6, pp. 0612041–410, 2009. DOI: 10.1115/1.3112384

Zhang, J., Childress, S., Libchaber, A. and Shelley, M., Flexible Filaments in a Flowing Soap Film as a Model for One-Dimensional Flags in a Two-Dimensional Wind, *Nature*, vol. **408**, no. 6814, pp. 835–39, 2000. DOI: 10.1038/35048530

VITA

Sourabh Kumar Jha was born in Jamshedpur, India to Mr. Awadhesh Kumar Jha and Mrs. Meena Jha. He grew up with an older sister Mrs. Alka Mishra. Sourabh received his Bachelors and Masters in Mechanical Engineering from National Institute of Technology, Trichy in 2010 and Indian Institute of Science, Bangalore in 2013. In the Fall of 2013, he decided to pursue his doctorate in Mechanical Engineering under the guidance of Professor Ari Glezer at the Georgia Institute of Technology. A short seven years and six months later, he earned his Ph.D in March 2021 and will join Boston Consulting Group, Atlanta as a management consultant.